Power and Energy Management Strategies for Stand-alone Renewable Energy with Storage Systems

Thesis
Submitted in partial fulfilment of the requirements
for the award of the degree of

Doctor of Philosophy
in
Electrical Engineering

Ramesh Gugulothu
(Roll No. 718020)

Under the Supervision of
Dr. Bhookya Nagu
Associate Professor

Department of Electrical Engineering
National Institute of Technology Warangal
(An Institute of National Importance)
Warangal - 506004, Telangana State, India
July- 2023

APPROVAL SHEET

This thesis entitled " **Power and Energy Management Strategies for Stand-alone Renewable Energy with Storage Systems"** by **Ramesh Gugulothu (Roll No.718020)** is approved for the degree of Doctor of Philosophy.

Examiners

_____

_____

Supervisor

Dr. Bhookya Nagu
Associate Professor
EED, NIT Warangal

Chairman

Dr. S. Srinivasa Rao
Professor
EED, NIT Warangal

Date.———————-

**Department of Electrical Engineering
National Institute of Technology Warangal
Warangal - 506004, Telangana State, India**

DEPARTMENT OF ELECTRICAL ENGINEERING
NATIONAL INSTITUTE OF TECHNOLOGY WARANGAL

CERTIFICATE

This is to certify that the thesis entitled " **Power and Energy Management Strategies for Stand-alone Renewable Energy with Storage Systems**", which is being submitted by Mr. **Ramesh Gugulothu (Roll No.718020)**, is a bonafide work submitted to National Institute of Technology Warangal in partial fulfilment of the requirements for the award of the degree of **Doctor of Philosophy** in Electrical Engineering. To the best of my knowledge, the work incorporated in this thesis has not been submitted elsewhere for the award of any degree.

Place: Warangal
Date:

Dr. BHOOKYA NAGU
(Thesis Supervisor)
Associate Professor
Dept. of Electrical Engineering
NIT Warangal
Warangal – 506004,
Telangana State.

DECLARATION

This is to certify that the work presented in the thesis entitled " **Power and Energy Management Strategies for Stand-alone Renewable Energy with Storage Systems**" is a bonafide work done by me under the supervision of **Dr. Bhookya Nagu,** Associate Professor, Department of Electrical Engineering, National Institute of Technology Warangal, India, and was not submitted elsewhere for the award of any degree. I declare that this written submission represents my ideas in my own words, and where others ideas or words have been included, i have adequately cited and referenced the original sources. I also declare that I have adhered to all principles of academic honesty and integrity and have not misrepresented or fabricated, or falsified any idea, date, fact, or source in my submission. I understand that any violation of the above will be a cause for disciplinary action by the institute and can also evoke penal action from the sources that have not been properly cited or from whom proper permission has not been taken when needed.

Place: Warangal   **G.RAMESH**

Date: (Roll NO:718020)

ACKNOWLEDGMENTS

I acknowledge my gratitude to all my teachers and colleagues at various places for supporting and cooperating with me to complete the work.

I express my deep sense of gratitude and reverence to my beloved parents **Shri. Gugulothu Thansingh** & **Smt. Chandu**, my wife **Smt. Lalitha**, my daughter **G. Tanusri** & my son **G. Manvik**, my brother **Shri.G. Srinivas**, parent-in-laws **Shri. B. Ravoji** & **Smt. Laxmi**, my sister **Smt. G. Devi**, my brother-in-law **Shri. L. Harilal**, **Mr. B. Rajendar**, for their sincere prayers, blessings, constant encouragement, shouldering responsibilities, and moral support rendered to me throughout my life; my research would not have been possible without them. I heartily acknowledge all my relatives for their love and affection for me.

I would like to express my greatest admiration to all **my family members** for the positive encouragement they showered on me throughout this research work. Without my family's sacrifice and support, this research work would not have been possible. It is a great pleasure for me to acknowledge and express my appreciation to all my well-wishers for their understanding, relentless support, and encouragement during my research work. Last but not least, I wish to express my sincere thanks to all those who helped me directly or indirectly at various stages of this work.

Above all, I express my deepest regards and gratitude to **"ALMIGHTY"** whose divine light and grace showered on me the perseverance, inspiration, faith, and strength to keep the momentum of work high during tough phases of research.

Ramesh Gugulothu

ABSTRACT

There is growing concern in society regarding the adverse effects associated with the use of fossil fuels, particularly oil, coal, and gas. The curiosity about utilizing renewable and clean energy is consistently growing, leading to the emergence of new energy systems as a significant scientific and technological breakthrough.

Currently, manufacturers of different energy components, including solar panels, fuel cells, DC-DC converters, and others, are encountering challenges in terms of optimization, control, and durability. These challenges are also being experienced by various industrial sectors. In order to develop innovative and effective energy solutions that can compete in the energy sector, it is crucial to address these issues. In addition, renewable energy sources depend on several uncontrollable factors, such as geographical location and weather conditions. To effectively manage the variability of energy availability, it is recommended to integrate multiple energy sources and implement efficient energy management strategies. The approach known as hybridization is a suitable method for designing efficient energy solutions.

The objective of this thesis is to tackle the challenges related to hybridization, power, and energy management. To provide more clarity, we are investigating a hybrid system that comprises of both photovoltaic solar panels and a fuel cell. The system is designed to incorporate converters and a storage system, which includes batteries and supercapacitors. The goal is to develop control strategies that can efficiently harness the maximum power from designated sources and optimize the overall energy system to meet load requirements. Our approach focuses on implementing highly effective energy management strategies and power point tracking algorithms.

The main objective for Standalone DC microgrids often have challenges in energy management for a long time horizon due to uncertain renewable energy sources and volatile loads. This work presents a centralized energy management strategy (EMS) for a standalone DC microgrid with solar PV, fuel cells, and a battery energy storage system (BESS). The proposed EMS method is designed to improve the longevity of BESS, reliability, and reduce the hydrogen intake. In the proposed EMS, the PV system de-rating method is used to overcome the deep charging of battery under low-demand conditions. The fuel cell power supply is varied using a reverse sigmoidal function of the Batterys state of charge (SoC). This improves the hydrogen fuel efficiency and also helps in minimizing deep discharge of the battery under heavy loading conditions. The centralized EMS is fed with load power, battery SoC, and individual source power information. Consequently, the EMS provides decisive commands to the individual source local controller to control the respective output power. The efficacy of the proposed EMS under multiple operating conditions is evaluated in both simulation environment and on a hardware prototype of a DC microgrid.

The second objective is to effectively regulate and maintain the stability of the output voltage,

which is accomplished by implementing a control loop. The objective has been successfully achieved by considering a realistic model of the converter.

A comprehensive energy management strategy was developed after conducting a thorough inspection of each component and considering MPPT (maximum power point tracking). To demonstrate the importance of different strategies and the feasibility of our approach, we recommend using simulation and experimental results obtained from simulators.

After conducting a thorough inspection of each component and considering MPPT (Maximum Power Point Tracking), a comprehensive energy management strategy was devised. In order to demonstrate the significance of various strategies and the practicality of our approach, we propose the use of simulation and experimental results using simulators.

Contents

List of Figures

xiv

List of Tables

Abbreviations & Symbols

List of Abbreviations

BESS	Battery energy storage system
DGM	Deficient generation mode
EGM	Excess generation mode
EMS	Energy management strategy
MPPT	Maximum power point tracking
PV	Photovoltaic
A	Activation area of the FC ($232cm^2$)
ALO	Ant- lion optimizer
ANFIS	Artificial neuro fuzzy inference system
ANN	Artificial neural network
BESS	Battery energy storage system
BLDC	Brushless DC electric motor
BW	Band width
CSO	chicken swarm optimization
DE	Differential evolution
EMS	Energy management strategy
ESSs	Energy storage systems
EVs	Electrical vehicles

F	Faraday constant ($96487C$)
FC	Fuel cells
FSS	Fixed step size
GWO	Grey wolf otimizar
HESS	Hybrid energy storage system
HHV	Higher heating value
INCO	Incremental conductance
INRE	Incremental Resistance
LED	Light emitting diode
LHV	Lower heating value
MPP	Maximum power point
MPPT	Maximum power point tracking
MWC	Membrane water content(λm)
n	Number of electrons contained in the reaction
P&O	Perturb and observe
PEM	Proton exchange Membrane
PEMFC	Proton exchange membrane fuel cell
PID	Proportional integral derivative
PM	Phase margin
PSO	Particle swarm optimization
PV	Photovoltaic
R	Universal constant of gas ($8.314/K.mol$)
RESs	Renewable energy sources
SC	Super-capacitor

SCA	Sine cosine algorithm
SSA	Slap swarm algorithm
T	Temperature (343K)
VSS	Variable step size
WCA	Water cycle algorithm

List of Symbols

D	set of Duty cycle
d	Duty ratio
d_i^K	Actual value
d_i^{K+1}	Upgraded value
D_{bat}	Battery duty cycle
d_{best}	Best function
D_{pv}	PV duty cycle
D_{pv}^{old}	Previous duty cycle of the PV
d_{worst}	Worst function
e^-	Electron
H_2	Hydrogen gas
H_2O	Water content
i_{bat}	Battery output current
i_{fc}	Fuel cell current
k_i	Integral controller gain
k_p	Proportional controller gain
N_{FC}	Total number of fuel cell

O_2	Oxygen gas
P^*_{fc}	Fuel cell power
P_FC	Fuel cell output power
P_{H2max}	Maximum safe pressure of the cylinder
P_{batt}	Battery output power
P_{bat}	Battery output power
P_{fcmax}	Fuel cell maximum output power
P_{fcmin}	Fuel cell minimum output power
P_{H_2}	Hydrogen gas pressure
P_{H2min}	Minimum hydrogen gas pressure
P_{load}	Load output power
P_{O_2}	Oxygen gas pressure
P_{pv}	PV output power
Ph_2	Hydrogen partial pressure
Ph_{2max}	Maximum safe pressure of the cylinder
Ph_{2min}	Minimum hydrogen gas pressure
Po_2	Oxygen gas partial pressure
SoC	State of charge
SoC_{max}	Maximum limit of SoC
SoC_{min}	Minimum limit of SoC
V_{dcref}	Reference voltage signal
V_{dc}	DC link voltage
V_{FC}	Fuel cell output voltage
V_{pv}	PV output voltage

DC	Direct current
α	Saturation constant
β	Mid value of SoC limit
ΔG	Gibbs free energy in (J/mol),
ΔP_{diff}	Power difference in PV power and load power
ΔS	Entropy change of value
ΔV	Change in voltage
a	The ideality constant factor of a diode
C_{batt}	Bidirectional converter output capacitor
C_{bat}	Bidirectional converter output capacitor
Co_2	Oxygen concentrate $(molcm^-3)$
d_{batt}	Bidirectional converter change in duty
D_{bat}	Bidirectional converter duty
d_{bat}	Bidirectional converter change in duty
E_{batt}	Energy released by the BESS
E_{Nerst}	Reversible open-circuit output voltage
$E_{optbatt}$	Optimum energy released by the BESS
$f(x)_{best}$	Best candidate obtains the best value of $f_{(x)}$
$f(x)_{worst}$	Worst candidate obtains the worst value of $f_{(x)}$
f_{LPF}	Low pass filter's transfer function
$G_{\Delta vdbat}$	Duty to voltage control transfer function
$G_{i_{bat}^* dbat}$	Duty to current control transfer function
i_{batt}^*	Filtered BESS current (A)
i_L	Limiting current

I_o	Saturation current of the array
$I_{(pv,cell)}$	The current obtained by sun's radiation
i_{batt}	Actual BESS current (A)
i_{batt}^*	Battery reference current
i_{bat}^*	Battery reference current
I_d	The diode current of Shockley
I_{FC}	Fuel cell current
i_{fc}	Fuel cell current
i_{Lbatt}	Bidirectional converter inductor current
i_{Lbat}	Bidirectional converter inductor current
i_{load}	Load current
I_O	The diode's saturation current
I_{pv}	Photovoltaic (PV) current of the array
i_{pv}	PV current
k	The Boltzmann constant $(1.38065031023 \ J/K)$
L_{batt}	Bidirectional converter inductance
L_{bat}	Bidirectional converter inductance
$L_{io,cl}$	Current loop gain of closed loop system
$L_{io,op}$	Current loop gain of open loop system
$L_{vo,op}$	Voltage loop gain of open loop system
N_p	Parallel connections of cells
N_s	Cells connected in series
$P_{battref}$	Battery reference power
P_{batt}	Actual battery power

P_{scref}	Actual SC reference power
P_{sc}	SC power
P_{total}	Total load power provided by HESS
Q	BESS capacity (Ah)
q	The charge of electrons $(1.60217646 \times 1019C)$
Q_T	Total charge stored by internal of SC (Coulomb)
$r_1, and r_2$	Random numbers
R_C	Lead contact resistance
R_M	Resistance of the fuel cell
r_m	Electrolyte membrane resistance $\Omega.cm$
R_p	The equivalent parallel resistance of the array
R_s	The equivalent series resistance of the array
R_{batt}	BESS internal resistance (■)
$SoC_{batt_{max}}$	Battery maximum SoC
$SoC_{batt_{min}}$	Battery minimum SoC
$SoC_{sc_{min}}$	supercapacitor maximum SoC
$SoC_{sc_{min}}$	supercapacitor minimum SoC
T	Settling time
T	The temperature of the p–n intersection (in Kelvin)
t_m	Thickness of the electrolyte membrane $(0.0178cm)$
T_o	Reference temperature $(298K)$
U	Optimum point
V_t	The thermal voltage of the array
V_{act}	Activation drop

v_{batt}	Bidirectional converter battery voltage
v_{bat}	Bidirectional converter voltage
v_{cbat}	Bidirectional converter capacitor voltage
V_{cell}	Fuel cell single voltage
V_{con}	Concentration loss
V_{ohmic}	Ohmic loss
vc_{sc}	Bidirectional converter capacitor voltage

Chapter 1

Introduction

1.1 Introduction

The rise in energy consumption, which is now met by fossil fuels, is linked to living standard that have resulted in environmental damage, global warming, carbon emissions, and illnesses. According to studies, the demand for energy would increase by 45% by 2030, especially for fossil fuels. This increase in demand is a result of changing demographics such as population expansion, unequal income distribution across many nations, economic in security, and several other ecosystem processes that support the continued use of fossil fuels. The depletion of fossil fuel supplies and the rise in energy demand cause price hikes, which encourage energy providers to seek out alternative energy sources subsidised by government regulations, such as Feed-in-Tari (FIT) program's for photovoltaic system in india. Unfortunately, the price of energy generated from renewable sources is now greater than the price of conventional energy. Since sources of renewable energy are rarely competitive with traditional energy sources, the present economic incentives are inadequate on their own to promote energy conservation efforts. This is because rapid, worldwide development and deployment of WWSGs (Wind, Water, Solar, Geothermal) face significant economic, budgetary, political, and geographical challenges. Despite this, research into developing renewable energy sources is making progress, and the evolution of these sources has become more and more apparent.

1.2 Energy and hybrid system

Humanity needs three different kinds of energy forms to sustain its existence. Electrical, mechanical, and thermal kinds of energy fall under this category. The most convenient kind of energy is electrical because it can be moved, changed, and stored with ease. Because of this, industries fight to create the "best" product for the customer. The science underlying producing components for renewable energy sources is becoming more developed. All manufacturers and consumers strive for high system efficiency. Solar panel manufacturers are working to create the most energy-efficient panels, while power converter and semiconducting manufacturers are focused on creating quick and loss-free switching electronics. Fuel cell manufacturers are also working to develop an ideal design with the longest lifespan. The necessity for sustainable storage for renewable sources is driving energy storage system technology to its maximum

efficiency levels. Depending on the battery type and its desired use, modern battery design techniques demand a smart charging method.

The dis-advantage of renewable sources are largely dependent on climatic conditions and cannot be reliable for user applications. However, the issue of energy interruption might be resolved by utilizing various renewable energy sources and choosing systems that support one another so that the need for power supply is constant and uninterrupted. Thus, the field of renewable energy is gravitating toward hybrid systems (HS) and associated management methods.

1.3   Hybrid System Concept

Three of the most promising renewable energy generation technologies include hydrogen-based (fuel cell) power production, solar and wind power production. The most ambitious estimate has been obtained for photovoltaic (PV) and wind power production. Because of the various benefits they provide, including minimal noise, high efficiency, and reduced emissions of polluting gases,fuel cells (FC) exhibit significant potential to be sustainable power sources. Each of the above technologies, therefore, has distinct drawbacks. For instance, while the production of FC requires fuel, that of solar and wind energy depends on climatic conditions. However, combining many energy sources into a hybrid system (HS) can address the aforementioned issues. A system based on many resources provides better quality and more consistent power to meet load demand than one based on a single resource. A system that uses a variety of renewable energies may fill the energy gap left by a single source and supply all of the energy required during the course of a complete day. Additionally, when the sources of energy are controlled effectively, HS enables larger energy densities. For instance, the PV source may be operated throughout the day to charge/store batteries, provide loads, and restore FC and batteries for use at night. Consequently, HS energy has attracted research interest on a global scale. Higher energy productivity is also made possible by a control mechanism applied to each renewable power source that makes up HS. In order to harvest the most power possible from renewable energy sources, this method involves positioning them.

In the beginning, procedures like photovoltaic panels or wind turbines were the focus of the difficulty of obtaining the greatest power from renewable energy sources. This issue was covered in a number of studies [1–3]. The best value for a function may be found using a variety of techniques [4, 5]. FC are now viewed as a possible alternative strategy for producing electrically sustainable energy sources for fixed and mobile use. The excellent efficacy and environmentally-friendly attributes are accountable for this result. Similar to other manufac-

2

turing applications, reducing the entire system, optimizing fuel usage, and maximizing power extraction are key technological difficulties that must be overcome for FC to be a practical future option.

1.4   Literature survey

In the past few decades, a number of maximum power point tracking (MPPT) approaches have been used to collect power from the PV array with the use of power electronic converters. Depending on their performance, the parameters taken into account by the approaches change. The hill climbing (HC) and perturb and observe (P&O) algorithms are among these strategies that are most frequently used because of their simplicity. [1]. To achieve MPP, both algorithms operate according to a similar concept. The P&O technique operates with a PV system voltage via perturbation, whereas the HC method periodically supplies power by perturbing the duty cycle to the converter. To achieve MPP, control parameters (such as duty cycle or voltage) can be raised or lowered based on power levels. It is simple to identify oscillations close to the steady-state point, or MPP, as well as power loss while monitoring owing to elegant performance of the HC and P&O algorithms. It can exhibit minimal oscillations and slow down reaction time if the perturbation step size is small, and vice versa.

 Kollimalla, Sathish Kumar, Mishra, and Mahesh Kumar, proposed a two-stage MPPT approach developed by [2] for the tunable perturbation size for sudden changes in irradiation.The proposed method had the following features: continuous tracking of MPP all through normal tasks. .Rapid transient performance when sudden working condition violations.
.The provision of configurable perturbations that decreases variation close to the MPP.
The above properties may be achieved via variable perturbation, controller design, and current variation. The method has a faster response time than incremental conductance approach and negligible changes around MPP. Unlike artificial neural network (ANN) and fuzzy logic control (FLC)-based methods, the suggested approach did not need massive data for training or heavy computing at different levels. Research confirmed the simulation and showed the algorithm's quicker response time.

Femia, N. and Granozio, proposed the challenge of P&O approach for PV system improvement as given by [3]. A variation in step size (Δd), which linearly reduces with increasing tracking power of a photovoltaic system, was employed to substitute for conventional fixed duty cycle step size. With regard to tracking power requirements and maximal power point consistency, the user can enhance the constant (Δd) P&O results under uniform solar irradiance circumstances(conditions). By changing the disturbance step size, some enhancements to P&O

3

method have been suggested. These techniques' primary weakness is that those who cannot acquire global power control during partial shaded condition(PSC). Similar to the P&O technique, incremental conductance (IC) has limitations in terms of accuracy, beginning tracking efficiency, and failure to track global peak (GP) whenever the PV system is being shaded in [4]. It achieves MPP whenever the P-V graph slope is zero.

Xiao and Dunford (W.G.) introduced MAHC, a modified adaptive hill climbing method [5]. Parameter optimization was applied to achieve static and dynamic appropriateness. To eliminate tracking variance, control mode change was designed. Simulation and testing validated this technique's enhanced tracking effectiveness. By setting the step change of variation to 0.4%, the MAHC approach reduces steady state loss and speeds convergence by 34.62% compared to adaptive hill climbing (AHC). Power loss between steady-state and tracking would be a concern with the MAHC. Shaded PV systems did not employ MAHC.

Balasubramanian, Indu Rani, and Ilango Ganesan [6] explored how partially shaded conditions impact electrical supply. Different shading styles were examined for load demand transfer. Load point MPP for a converter's effectiveness differed from PV array MPP. In partially covered scenarios, the converter's power supply curve monitoring wouldn't verify maximum load demand transfer. Once they looked at output attributes' global point tracking, hardware and simulation showed maximum power demand transfer.

Abdelghani Harrag and Sabir Messalti ,to improve MPPT in photovoltaic systems is suggested [7] combining a step size variable P&O with an evolutionary technique. GA adjusted the PI controller's amplification to optimize the perturbation step size for MPPT's P&O approach, resulting in an optimal duty cycle for the power converter. The described approach has issues with quickly shifting irradiation levels. The proposed system's modeling confirmed efficiency gains. To investigate the reactivity under transitory conditions and abrupt air circulation, irradiations were randomly altered. The suggested approach was compared to the P&O technique with a set step size. The recommended method reduced ripple, response time, and inaccuracy while increasing robustness.

De Oliveira, Fernando M. and Oliveira, [8], established a single-phase, photovoltaic system with the capacity to filter active electricity. To solve the issue of mismatching under partially shaded circumstances, GMPPT technique was used with PSO. The P&O MPPT strategy was linked to the PSO GMPPT's success. In contrast to P&O MPPT strategy, which increased the effectiveness of the suggested photovoltaic system, the particle swarm optimization GMPPT

4

method consistently achieved GMPP under various working circumstances. The findings of modeling and testing have demonstrated excellent achievement for PSO GMPPT in contrast to P&O maximum power point for a photovoltaic system with a utility grid under partly shaded conditions of PV system.

Sarah Lyden, Haque, and Md. Enamul [9] proposed an evolutionary MPPT approach for determining PV system GMPPT in various conditions. The effectiveness of the recommended approach and the behavior of P&O and PSO maximum power points under similar irradiation circumstances were evaluated to monitor the GMPP against real solar irradiance data. In simulations, the approach responded quickly to GMPP, outperforming expectations. The approach yielded accurate and fast GMPP, but required more computational complexity than P&O algorithm and memory storage for each cycle, unlike PSO algorithm.

Zhu et al. exploited hill climbing to decrease MPP oscillation and enhance tracking system performance [10]. Adaptive hill climbing makes diverging from MPP location easy under cumulative irradiance change. The matalb/simulink modeling research recommends a modified hill climbing method: The proposed technique can improve speed response and reduce steady-state changes in an atmosphere with step-change irradiation level compared to the conventional hill climbing approach. It can also solve the flexible hill climbing issue, which departed from the MPP the spot while working under solar insolation variation. Power outages during transients and oscillations that don't reach steady-state limit are drawbacks of the enhanced hill climbing approach. This method wasn't tested.

Ishaque and Kashif developed a deterministic PSO (DPSO) method to enhance the traditional PSO technique [11]. The key is to remove the random number from the PSO movement equation's acceleration component. After a thorough analysis of P-V behavior under partial shadowing, the largest movement variance is limited to a set value. Without random variables and one component, the inertia weight must be modified, hence the DPSO approach was utilized. Although the article eliminates arbitrary production variables to boost PSO efficiency, DPSO still has a motion constraint. Previous particles under the recommended DPSO approach depend on Photovoltaic system and MPP fluctuations, according to experiments. Local MPP may fail due to velocity restrictions (LMPP).

Liu, Yi-Hwa, and Huang's optimization methods, including particle swarm optimization (PSO), improved global MPP efficacy by adjusting three parameters two acceleration coefficients (C_1 and C_2) and one weight factor (w) for optimal iteration q. This technique aims to provide a

dependable, system-independent optimization mechanism for PSC-operated centralized power generation systems. The PSO basic architecture has been changed to address the practical issues of partially shadowed electrical generating systems. Better monitoring has shown that the recommended technique should produce GMPP in less than 27 iterations. This system's practicality is often tested in an experimental environment employing the four shading patterns.

T. Sudhakar Babu, N. Rajasekar and K. Sangeetha, introduced an efficient approach to compute initial duty cycle for rapid convergence, decreased oscillations around maximum power, and natural tracking fluctuations to increase PSO efficiency [12]. Furthermore, the global peak power was tracked under different climactic conditions. The drawbacks of the proposed Modified PSO (MPSO) method is that the initial values depend on the PV system, and during dynamic cases, the proposed algorithm was considered without re-initializing the parameters to see the efficiency of the recommended MPSO algorithm.

Jiang and Douglas proposed an MPPT-based ant colony optimization (ACO) approach for a large PV system in shadowed situations [13]. This method is fast, originally considers independent particles, and does not need PV array knowledge. Simulations of different shading patterns show that the proposed MPPT for PV array works under transient and fixed irradiation. The analysis shows that the proposed approach outperforms P&O, CVT, and PSO MPPT algorithms, while requiring less iterations. Because ACO was not used in a physical model, this approach has one drawback. Each cycle, the system had to compute more as additional controlled variables were engaged. Five variables were set upon activation.

Sundareswaran, Kinattingal, Sankar, and Peddapati, looked at GMPP tracking in a PV power generation system and recommended a new solution based on artificial bee colony (ABC) [14]. The simulation results performed on two distinct configurations of differing shading patterns explicitly show that the proposed ABC algorithm outperforms the current PSO and enhanced P&O approaches. The limitation of this method is that it takes more time to reach the global MPP with the proposed algorithm when the population size reaches six.

Many other meta-heuristic algorithms [15], such as genetic algorithm [16], artificial bee colony [14], grey wolf optimization (GWO) [17], ant colony optimization [17], flower pollination algorithm [18], overall distribution of PSO [19], leader particle swarm optimization [20], fibonacci search (FS) [21], extremum seeking control (ESC) [22], artificial neural network (ANN) [23] and improved cuckoo search [24], hybrid adaptive P&O and PSO [25], the hybrid enhanced leader PSO-P&O [26], have been proposed to track GMPP for a PV system that has MLP dur-

ing partially shaded conditions. But all these algorithms optimize tuning parameters that need to be properly selected; otherwise the optimization algorithm may increase the tracking time or may be stuck at any local peak point.

Venkata Rao Ravipudi [27], proposed Jaya algorithms which do not require any parameter tuning for tracking GMPP. This method is proven to track fast speed & and exhibits less oscillatory behaviour steady-state at GMPP compared to PSO. Nevertheless, this method may still take significant time compared to conventional methods and is highly dependent on the initial particle.

Shams Immad, and Mekhilef, used a meta-heuristic-based modified butterfly algorithm (MBOA) [28] and a radial movement optimization (ARMO) [29] MPPT tracking algorithm. The proposed algorithm effectively works for optimal tracking under partial shading conditions and fast-varying loads. But the tracking speed and accuracy of these methods are highly sensitive to the optimization parameter, which should be properly selected for best results.

Ali Amjad , and Almutairi, K, proposed soft computing and optimization algorithms that are used to implement GMPP [30]. All the soft computing GMPPT techniques are favorable for finding GMPPT for most PSC, but they are computationally inefficient. Consequently, these methods are executed at a predetermined time, which may lead to inefficient tracking performance under fast irradiance variation.

Podder and Amit Kumer Roy offered machine learning-based MPPT tracking methods. Neural networks are used to monitor MPP in PV systems [31]. The main drawback of this method is that it needs exact data to give optimal values, but the bayesian fusion technique (BFT) quantifies parameter uncertainty (maximum values) and gives the distribution of parameter values (uncertainty), while the neural network gives only optimal values with respect to data. When data is available, both the neural network and BFT give accurate results. The bayesian fusion strategy, prominent in machine learning, has not been studied for MPPT. This method finds the global optimum as an unimportant function in few evaluations. Gaussian process design for uncertain consequences is a common strategy. GP designs provide estimated and uncertain information for feature vector function evaluations, revealing the greatest power point [32].

Similar to photovoltaic and wind turbine systems, maximum power tracking (MPT) methods are required for FC to trace MPP and exhibit improved efficiency at any constant hydrogen pressure and oxygen partial pressure.

7

L. Egiziano and A. Giustiniani propsed perturb and observe (P&O) algorithm-based MPPT technique for a grid-connected FC system [33] similarly, in P&O algorithm, MPPT was applied to a FC designed for charging EV through a soft switching DC/DC converter.

Karami Nabil, and Khoury [34] used conventional P&O and incremental conductance (INCO) methods for MPPT in FC systems. However, the conventional methods mostly exhibited steady-state oscillations around MPP. Further, the INCO-based strategy does not guarantee optimal solution for any sudden or large operational changes.

Hanane Hassani and Faika Zaouche compared P&O, INCO, and incremental resistance (INRE) approaches in PEMFCs [35], revealing INRE's increased tracking responsiveness under various operating situations. Applying P&O and INCO MPPT approaches to FC-powered EVs enhances driving range and performance. Each strategy has limits. The fixed step size (FSS) causes P&O to fluctuate around MPP, causing energy loss. Additionally, lesser convergence prevents P&O from detecting MPP in rapid environmental changes like temperature and membrane water content. The INCO MPPT technique is more complex than P&O but effective at handling rapid changes. FSS fluctuations make this strategy less efficient.

Pi-Yun Chen, and Kuo-Nan Yu,Used a novel technique reduce steady oscillation in the conventional MPPT technique; more recently, an innovative fractional-order INCO technique with variable step size (VSS) was reported [36]. This approach outperformed P&O and INCO in terms of dynamic, steady-state reactions and can be used with reduced sampling points and without the use of air pressure and moisture measurements, which results in cost savings. It was determined that the new MPPT improved FC efficacy as much as traditional techniques by decreasing excessive power loss.

Qi Li and Weirong Chen, designed the FC/battery energy storage system (BESS) system and assessed it by providing a P&O algorithm to increase the FC accomplishment power [37]. To maximize the overall output power from a PEMFC, a controller design technique comprising implicit model prediction using an oxygen supply reference regulator was proposed.

N. Bizon, [38] showed a bi-buck approach may be used to track the MPP of FC. The MPPT was intended to be integrated with a combination of FC/Wind approach to enhance the power generated, and the efficacy of MPPT used for an FC was increased to 99.41%. To enhance the system effectiveness, the FC power and utilization efficiency were improved using a global extremum searching algorithm [39], and the overall efficiency was also enhanced raised in the
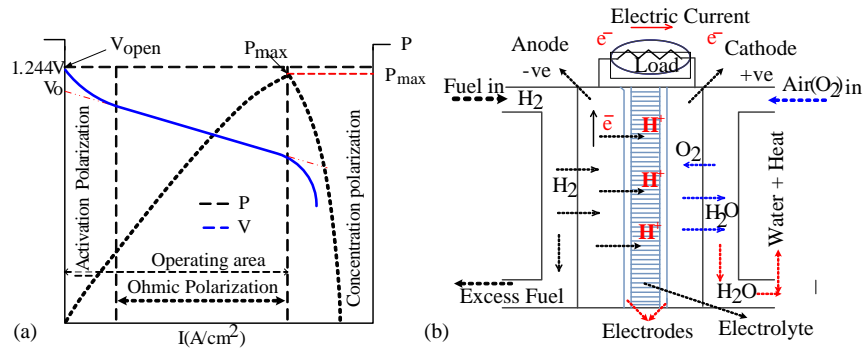
Figure 1.1: Fuel cell (a) $P - I$ and $V - I$ characteristic (b) functional diagram

region [1%, 2.1%], four control methodologies were designed for regulating the energy of an FC hybrid power generator that increased the total energy of FC by 12% when compared to standard approaches.

Saugat Bhattacharyya, and Amit Konar [40], enhanced the efficiency of MPPT utilized in FC using a fractional-order high pass filter. The MPPT integrated with PEMFC was simulated using the water cycle algorithm (WCA) [41].

Aly Mokhtar, Rezk,and Hegazy, proposed an optimized fuzzy logic MPPT [42], where a meta-heuristic-based differential evolution (DE) technique is optimally used to design the feature set of the fuzzy logic controller which helps to enhance tracking efficiency, and has low ripple at the peak point for FC system. However, DE contains several user-defined parameters, such as (population size, mutation, crossover, etc) and influences the membership function.

Ahmed Fathy, Mohammad Ali and Abdelkareem, implemented slap swarm algorithm (SSA) [43] to obtain as much power as possible from FC. In this, SSA was used to obtain the estimate of the voltage point corresponding to the MPP and then the voltage was regulated using a PID control strategy to achieve maximum power of a PEMFC. However, in FC, the MPPT is made effective through a current controller rather than a voltage controller. Never theless, SSA-PID is not simple to implement in real time. This is mainly because the peak power characteristics are observed against varying current, as seen in Fig. 1.1(a).

Derbeli, and Mohamed, came up with a technique to address a current estimator using curve fitting technique and obtain MPP reference current; the reference current was tracked using high order sliding control [44] for fast-tracking of MPP in an FC. Sliding control is highly dependent on sliding surface and might cause increased steady state oscillations.

9

Reddy, K., Natarajan, and Sudhakar, a proposed an MPPT depending on the adaptive neuro-fuzzy controller [45];it was also developed to improve the efficacy of PEMFC used in EVs, but training the neural system and developing fuzzy rules was challenging. Similarly, ANN-based MPPT techniques were proposed for regulating PEMFC. ANFIS, on the other hand, required an extreme amount of data and memory for training. [46].

Nirmalya Mallick and V. Mukherjee, proposed a modified P& O MPPT algorithm [47] in combination with a closed-loop fuzzy logic control to obtain the exact global peak point with reduced steady oscillations. However, extensive data was necessary for training. Other than conventional, ANN, and fuzzy logic-based MPPT techniques, meta-heuristics-based optimization techniques have been widely used for MPPT due to their superior tracking speed and accuracies.

Ahmadi, S., Abdi, Sh. Kakavand, and Madjid [48], developed combined particle swarm optimization (PSO)- PID controller-based MPPT in which the PSO provides the reference current corresponding to the MPP point of FC to the PID controller, which controls fuel output current tracking MPP. However, in PSO-PID approach, the PID controller gain tuning is crucial and plays a vital role in tracking speed.

Luta, Doudou N. and Raji Atanda K, proposed mamdani's fuzzy theory and the results of these theory were compared with PSO-based MPPT algorithms for FC [49]. In this, the authors observed that PSO-based MPPT outperformed the mamdani fuzzy-basis MPPT in terms of rising time and overshoot. For instance, a sine cosine algorithm (SCA) approach was used with PID design in [50] for MPPT tracking.

Kumar Sonu, Shaw,and Binod [51], employed ant-lion optimizer (ALO) approach for constructing the maximum power point PID controller. However, the sine cosine algorithms (SCA) and ALO techniques require more computation time, and their implementation is rather difficult.

Priyadarshi, Neeraj, Azam, Farooque and Solanki, for determing MPPT of an FC-based electric car, chicken swarm optimization (CSO) technique [52]. Furthermore, a bi-directional converter with a neutralized zero-current controller was fitted to reduce switching operation losses and improve efficiency. Although the given technique outperforms many traditional approaches, CSO seems to have poor convergence rate.

Derbeli, Mohamed and Barambones [53], proposed MPPT for PEMFC which depends on esti-

10

mating the reference current using a back stepped technique to extract optimum power from the fuel cell and Lyapunov study was carried out to analyze the tracker's reliability.

S. M. Nasiri, and Avanaki I, [41], presented a water cycle algorithm(WCA)-PID MPPT based technique for PEMFC. WCA was used to calculate the voltage during peak power, while the proportional controller was used to adjust the duty cycle of the boost converter. However, WCA showed its advantages over P&O but MPPT had some limitations during the tracking stages.

K.P.S. Rana, Vineet Kumar and Nitish Sehgal, proposed a grey wolf optimizer (GWO) based optimization for tuning the PID controller [54] to make the FC change in output power to make current ratio zero i.e, $\frac{dP}{dI} = 0$. Moreover, GWO had poor accuracy and sluggish convergence.

Samal Sarita et al. [55] found that MPPT may boost efficiency by 94.5% in FC applications compared to no MPPT operation. Additionally, few writers have developed improved MPPT approaches for FC to improve tracking performance and accuracy. For considerable FC performance, MPPT approaches are evaluated using tracking speed, FC power ripples, and computational loads. The bulk of meta-heuristic MPPT methods tracked peak power points using PID controllers. Due to its dependence on PID controller gains, MPPT tracking is less efficient.

Wang Caisheng, Nehrir, and M. Hashem, came up with several hybrid system (HS) approaches. Their methods for handling the sources, used HS. Each technique has a unique characteristic that depends on the use, i.e., kind of loads, climate maps, accessibility of the power grid, and commercial data.For instance, the authors of [56] describe an HS, which consists of a battery, electrolyzer, photovoltaic, fuel cell (FC), and wind power. It is recommended that FC serve as a backup power supply because of its limited lifespan. The kind of loading used greatly affects the lifespan of PEMFC, according to the latest FC literature. In [57], the researchers evaluated PEMFC's endurance to load on/off switching and observed a fall in kinetic energy in addition to an increase in transportation losses for specific electrode types.

Marrony, and Mathieu, [58], reported that after 500 hours of electrical cycling in comparison to a constant current situation, hydrogen crossover increased significantly. An identical technique was recommended by authors, who took out the battery. They thus evaluated continuous load usage and ignored the impact of machine-starting current surges in their investigations. The requirement power cannot be maintained in a quick step rise or decrease due to the sluggish reaction properties of FC. In order to increase the systems' transient response properties, batteries are used. The use of an HS with a battery and an SC is recommended by authors in [59].

11

Agbossou, K, Kolhe, M. and Hamelin [60], offer a standalone renewable system that stores energy using hydrogen. Even though the device is capable of operating on its own, the DC link voltage exhibits significant fluctuations that may be damaging to the quality of electricity.

Frances Airan and Asensi Rafael, designed DC microgrid, where power fluctuations are governed by three aspects [61]: (i) power exchange variability, (ii) power variations in power sources and (iii) storage systems, and sudden changes in DC load. An efficient EMS is required to handle power fluctuations and provide energy balance in the long term.

Vega-Garita Victor, Sofyan Muhammad Faizal, and Narayan developed an EMS for integrated PV battery modules [62] using three architectures: AC-coupled, DC-coupled, and inline. These designs have seven operational modes, and EMS controls PV system and battery power depending on them. A coordinated approach for BESS, PV sources, and load management took into account battery state-of-charge (SoC) and power restriction, however a PV power regulation that might create deep charging difficulties in BESS during standalone operation was not addressed.

Alahmadi Ahmad Aziz Al and Belkhier Youcef created an intelligent EMS for a hybrid wind/PV/battery DC microgrid using FO-PID and fuzzy logic controllers [63]. Renewable MPPT employs fractional-order PID control, and fuzzy logic control tunes FO-PID gains. DC Bus Signaling (DBS) uses bus voltage to communicate between sources in a DC microgrid's power management EMS. The EMS for PV/storage-based microgrid, described in [64], uses petri-net modeling to assess source conditions. Using petri-nets models, energy management systems use PV, batteries, and ultra-capacitors for long-term energy supply and rapid dynamic power control.

Mousa Marzband Seyedeh and Samaneh Ghazimirsaeid, worked on the uncertainty of power generation from PV and wind sources. The issue of power supply regulation between the fuel cell systems and storage systems is challenging and requires special attention while designing energy management strategies [65]. In [66], a multi-objective optimization approach was developed to properly coordinate the system. The seamless power supply for electric vehicles is provided by the battery, SC, and PEM fuel cells.However, the fuel cell is operated independently of the battery SoC.

12

Hanane Hassani, Faika Zaouche and Djamila Rekioua, designed an energy management method for a photovoltaic system with BESS and fuel cells [67], where a fuzzy logic controller (FLC) was used to maximize PV power. The excess solar electricity was utilized to operate an electrolyzer to generate H_2 and also to store energy in BESS. However, the development of the membership function was not properly designed, and the system's operation under extreme conditions, such as extreme SoC, was not considered. Similarly in [68], a combined and dynamic rule-based power regulation of an off-grid solar/wind and HESS consisting of a lithium-ion, a lead-acid battery, and an SC was developed.

Chafiaa Serir, Djamila Rekioua and Nabil Mezzai, developed an energy management system for photovoltaic (PV) and wind power systems, along with battery storage to fulfill load requirements [69]. A field-oriented control (FOC) technique of an induction motor (IM) powered by a PV system used to manage DC bus voltage. While both sources are renewable, meeting the load requirements under all conditions might be challenging.

L. Valverde, F. Rosa and A.J. del, used a DC microgrid with voltage management techniques and power balance limitations to minimize fuel exhaustion and increase performance in [70]. The functioning of the fuel cell is managed via an on-off switch using a threshold control technique based on the battery SOC. A predictive power management technique for switching the fuel cell and batteries based on predicted load demand and renewable energy source output power was proposed [71]; However, the switching strategies might generate unnecessary transients in the microgrid.

Shehata, Emad G, Gaber, Maged S. and Ahmed, presented an EMS for DC microgrid based on a multi-agent system implemented with java agent development Framework (JADE), and PI controllers, serving as EMS but this method is highly communication sensitive [72].

Amin et al. developed a model-based prediction control technique to regulate DC bus voltage and limit battery and fuel cell currents [73].An extremum seeking control technique uses average power balancing to reduce the battery stack and efficiently run the fuel cell stack. These energy management technologies promote power balance. Modern hydrogen gas DC microgrid studies have been conducted. These approaches are computationally expensive and need high controller computing capacity due to technological constraints. However, the EMS does not completely address fuel cell operating efficiency or coordinated control goals. Since fuel cells cost more to generate than other distributed generation methods, efficiency affects system efficiency and economics.

13

Table 1.1: BESS versus SC capabilities. [76]

S.No.	Parameters	Supercapacitor	Lead acid BESS
1.	Particular power density	<10000W/kg	<1000W/kg
2.	Particular energy density	1-10 Wh/kg	10-100 Wh/kg
3.	Life cycle	>500000	1000
4.	Efficiency	85%-98%	70%-85%
5.	Charging time	0.3-30 s	1-5 h
6.	Discharging time	0.3-30 s	0.3-3 h

Sathish Kumar et al. found that BESS has great energy storage capacity but poor power density [74]. To satisfy changing load demand, BESS may experience significant stress and internal temperature due to its poor power density. Especially in nanogirds, discharge/charge rates may not be enough to handle unexpected big load shifts. Additionally, low load factor in modest residential loads increases discharging/charging cycles, reducing BESS lifespan. BESS is often used for long-term low power needs because to its high energy density. SC has high power density but low energy density. SC is often employed in microgrids and nanogrids to stabilize power fluctuations caused by variable generation and loads [75]. SC retains electricity as static charge. Due to poor energy density, it cannot meet load requirements for lengthy durations. The Table 1.1 compares the characteristics of BESS and SC.

Patrick T. Moseley, accounted for the inherent limitations of BESS and SC, and that any one system alone cannot meet high power, and high energy demands simultaneously. As a result, to ensure the combined benefits of both high energy density, and high power density, a BESS-SC hybrid storage energy system (HESS) is employed to have:

- Increased BESS lifespan,

- Reduction BESS size, and cost

- Imposing low strain on BESS, and

- Ensuring better power balance between power generation, load requirement, as well as remote region power applications [77].

Gee, Anthony M. Robinson,and Francis V. P. reported many feasible configurations of BESS-SC HESS to achieve the benefits of both battery and SC systems [78]. In authors came up

with several control methods for HESS to list some objectives of the controllers proposed in the papers cited so far [79].

Mendis, N. Muttaqi, K. M. and Perera, S, discussed the purpose of integrating an SC and BESS for wind power applications [80]. The cost and implementation evaluation of HESS was investigated while showing reduced BESS costs with improved efficiency without considering SC. The details the SC and BESS control to minimize current stresses in the system.

Gee, Anthony M. Dunn, and Roderick W, proposed BESS life enhancement in wind energy systems using SC, and also an active current-filtering approach [81]. To control and decrease the power discharging flow rate from the source during rapidly fluctuating load demand, a HESS based strategy is detailed in [82].

Ming Ding, and Bo Wang Zhong, proposed adaptive charge and discharge rate limit regulation for BESS [83]. An adaptive rate-limit approach for batteries was designed to protect the main power supply during rapid load transient conditions and energy management strategies(EMS) for reducing pulse load demand in a microgrid system is proposed [84].

Singh, Prashant Lather, and Jagdeep singh [85], proposed a sliding mode technique (SMT) was proposed for DC link voltage management and adaptive power sharing in HESS-based DC microgrids. This approach efficiently minimizes battery stress through diverting uncompensated BESS current to its supercapacitor device, and proposes an energy management strategy for a PV with HESS. In this, the EMS selects the operating conditions of three main sources depending on the conditions and calculates the reference power for each source.

Fakham, Hicham Lu, francois,and Bruno [86],proposed a renewable grid-cconnected system with HESS management method, emphasizing high battery SoC and excess charge restrictions. A power management system based on model prediction for SC-battery hybridization in a DC grid scenario was presented in [87]. The major benefit of this technique is that it provides a consistent way for designing a control method that ensures the SC-battery hybrid operates within specified limitations. The conventional model predictive method, which is based on a discrete model of such a control scheme and objective functions, is computationally expensive.

Hredzak, Branislav and Agelidis, Vassilios G. [88],developed a low-complexity control method for a hybrid BESS-SC dc power supply. The main advantage is that it can achieve performance equivalent to that with lower complexity and computational burden.

Mendis, Muttaqi, and Perera discovered that most HESS control methods [89] assume batteries meet average power needs and SC supports transient power needs. For this, the power demand is separated into two categories: lower-frequency (average element) and higher-frequency (transient element). SC delivers higher-frequency power, whereas BESS gives lower-frequency power. Many controller systems ignored BESS's discharging and charging rate limit regulation and decomposition pattern. Discharging and charging rates may surpass the battery's power restrictions, causing BESS to function at its maximum pace. This stresses BESS, shortening its lifespan.

Wu, Ding, Todd, Rebecca, and Forsyth Andrew J, proposed to control BESS's charge/discharge rate limit by using EMS [90]. The authors used a linear rate limitation control scheme with rate-limit functionalities that provide a consistent rate limit. However, this has poor response time and a complicated design for an optimal solution.

1.5   Motivation

From the literature review on the different MPPT techniques for solar photovoltaic, proton exchange membrane fuel cells (PEMFC), and energy management strategies with optimal battery management, the following observations are drawn:

According to the literature study above, traditional algorithms like P&O, HC, and IC are easy to apply for maximum power tracking in single peak curves and their enhancement approaches [1–3,5]. However, they have drawbacks. In the short term, they may induce steady-state oscillation and power loss. Due to their set step size, they degrade system efficiency and are unsuitable for PV array partial shading conditions (PSC). Variable step size approaches also lose power. We developed Global Maximum Power Point Tracking (GMPPT) methods under partial shading [9] PSO. The proposed GMPPT techniques use PV module open circuit voltage. System-dependent methods may not always work, particularly in extended PV systems [11]. Under partial shading, these techniques may find a local maximum power point (MPP) instead of the global MPP.

Under PSC, evolutionary optimization methods including PSO,DPSO, ACO, ABC, FS, ANN, ARMO, and MBOA track global peak power well. These approaches have been widely investigated and described [9,11,13,14,21,23,28,29]. However, the proposed approaches take population size into account, which might make testing computationally intensive. Tuning parameters delay algorithm convergence. The technique fails to identify the optimal value throughout iterations in references [9,23]. According to [28], literature-proposed approaches use more tuning parameters during PV pattern dynamic change under PSC. MPP are limited in [11,13], therefore the search will go beyond its abilities. A limited number of control parameters reduces tracking time and iterations to attain the global peak. It also improves the system. The algorithm must balance exploration and exploitation to improve PV system performance.

The microgrid is expected to offer significant generation, control, and operational strategy capabilities, even if it only serves a small portion of the load. Therefore, it is crucial to integrate an energy management system (EMS) into power networks, especially when they are connected to a microgrid. The Energy Management System (EMS) allows for the efficient and coordinated management of power produced from distributed sources within the microgrid. The main goal of the EMS is to effectively manage the distributed sources in the microgrid, ensuring that the required power is supplied to the load at the lowest operating cost. The EMS should have a variety of functionalities in order to improve system reliability and power quality. Some of the benefits of implementing this technology include the elimination of dump loads, peak shaving, improved power quality, load leveling, enhanced transient stability, voltage regulation, and

17

uninterrupted power supply. Incorporating an intermittent source like a PV generator into the microgrid necessitates the presence of a PV output smoothing function in the EMS.

Several EMS have been recommended over the years, including coordinated EMS, centralized EMS, and smart energy management systems [84–86]. Many EMS systems prefer operating the microgrid with the lowest possible operating cost, which is determined by a specific operating strategy. Furthermore, the longevity of energy storage systems (BESS) in microgrids and the de-rating of PV systems have been neglected by many researchers. Additionally, in order to ensure more reliable operation, it is recommended to calculate the optimal solution for microgrids. Several researchers have directed their attention towards the utilization of mathematical techniques such as linear programming (LP), mixed integer linear programming (MILP), and sequential quadratic programming to address the energy management problem in microgrids [87, 88, 90]. There is a lack of literature on the comparative study of energy management methods in addressing the improvement of BESS longevity, reliability, PV system de-rating method, and reduction of hydrogen intake operation in microgrids.

Addressing all these limitations, the present work is based on a centralized energy management strategy (EMS) for a standalone DC microgrid with solar PV, fuel cells, and a battery energy storage system (BESS). The proposed EMS method is designed to improve the longevity of BESS, reliability, and reduce hydrogen intake. In the proposed EMS, the PV system de-rating method is used to overcome the deep charging of batteries under low-demand conditions. The fuel cell power supply is varied using a reverse sigmoidal function of the battery's state of charge (SoC). This improves the hydrogen fuel efficiency and also helps in minimizing deep discharge of the battery under heavy loading conditions.

The inclusion of a battery energy storage system (BESS) in a microgrid has a significant impact on the microgrid's overall performance, especially in terms of its operational performance. Furthermore, there are only a few articles in the literature that discuss the lifetime of battery energy storage systems (BESS). This is an important aspect in addressing the issue of deep charging of batteries under low-demand conditions and minimizing deep discharge of the battery under heavy loading conditions in microgrid operations [74, 75] [77], [78–80]. Furthermore, the literature articles discuss the longevity of Battery Energy Storage Systems (BESS) methods, specifically focusing on the economic operation of microgrids using one approach. In order to effectively operate the microgrid and enhance the longevity of the Battery Energy Storage System (BESS), it is crucial to accurately evaluate the BESS's longevity when used in the microgrid under the proposed operating strategy.

18

The proposed work presents a centralized energy management strategy (EMS) for a standalone DC microgrid with solar PV, fuel cells, and a battery energy storage system (BESS). The proposed EMS method is designed to improve the longevity of BESS, reliability, and reduce the hydrogen intake. In the proposed EMS, the PV system de-rating method is used to overcome the deep charging of battery under low-demand conditions. The fuel cell power supply is varied using a reverse sigmoidal function of the battery's state of charge (SoC). This improves the hydrogen fuel efficiency and also helps in minimizing deep discharge of the battery under heavy loading conditions.

1.6   Objectives of the thesis

The objective of this research is to propose a new energy management strategy for the development of stand-alone renewable energy systems with storage. For achieving it, a few objectives are defined::

1. The bayesian fusion technique (BFT) can be employed to enhance the tracking performance of a photovoltaic (PV) system operating under partial shading conditions (PSC). By effectively managing the uncertainties in the input data, the BFT enables the selection of the optimal tracking solution through informed decision-making.To achieve the global peak of multiple P-V curves and enhance the exploration process.

2. The objective of this study is to improve the tracking performance of a fuel cell system by developing a maximum power point tracking (MPPT) approach based on the jaya algorithm for proton exchange membrane fuel cells (PEMFC). This approach achieves its objective by utilizing a reduced number of control parameters and eliminating the need to modify any existing control parameter. The approach incorporates a suitable search strategy that reduces the required number of iterations for identifying the global peak in temperature fluctuations, membrane water content, oxygen partial pressure, and hydrogen partial pressure curves. Furthermore, the particles initially employed in this procedure are not dependent on the fuel cell system.

3. The proposed standalone microgrid energy management system (EMS) aims to achieve the following key objectives: The purpose of implementing a de-rating strategy in a photovoltaic (PV) system is to efficiently address the issue of excessive battery charging during periods of low load.The power output of the fuel cell is adjusted based on the state of charge (SoC) of the battery. This is done to optimize the use of hydrogen fuel when the load on the system is light or medium, and to prevent excessive discharge of the battery when the load

19

is heavy. The regulation of battery energy storage system (BESS) state of charge (SOC) is achieved through the utilization of a reverse sigmoidal function-based fuel cell output power. The reliability has been improved through the implementation of a strategy that involves adjusting the pressure of hydrogen and oxygen in the fuel cell. Increasing the fuel cell output power would allow for the operation of the fuel cell at its maximum power point (MPP) in order to fulfill the additional load demand.

4. An optimization technique has been developed to address the regulation of adaptive charge discharge rate limit. The primary goal of the proposed control schemes is to optimize the energy charge and discharge from the battery energy storage system (BESS) during transient conditions by utilizing the charge and discharge rate limitation of the BESS.The objective is to enhance the efficiency of the battery energy storage system (BESS) by optimizing the duration during which it is discharging and charging at its maximum achievable rate, utilizing an energy management system (EMS). To address the issue of excessive battery charging during periods of light load, a recommended solution involves implementing a photovoltaic (PV) system de-rating approach. This approach aims to mitigate the deep charging of the battery.

The objective of the research effort is to attain optimal global maximum power point tracking (GMPPT) performance for photovoltaic (PV) systems and fuel cells. Additionally, the project aims to ensure efficient energy management of hybrid systems and enhance the longevity of batteries.

1.7   Organization of thesis

The thesis has been organized into the following seven chapters.

Chapter-1: Introduction: This chapter includes an introduction to MPPT controllers for solar photovoltaic (PV) applications, fuel cell systems, a literature review based on GMPPT for a solar PV array under PSC, MPPT for fuel cell system, and energy management strategy to optimize battery storage device under transient condition. The motivations based on the literature survey led to research objectives.

Chapter-2: Generalizations for modeling hybrid systems: This chapter includes sources of renewable energy that help compensate the suggested HS globally and are mathematically modelled. The differences between various types and attributes of PV panels, FC stacks, and battery models are highlighted in this chapter.

Chapter-3: MPPT based solar photovoltaic system: Explains in detail the proposed bayesian

fusion technique (BFT) algorithm and the essence of power tracking: it presents a summary of MPPT techniques that have been documented in the literature choice of methodology, its benefits when searching for optimal solutions in solar PV operations to extract maximum power. It also provides information on the PV array structure of three series panels connected with PSC, the simulation result of the proposed BFT over JAYA, PSO, and incremental conductance algorithms, and comparisons with other algorithms.

Chapter-4: MPPT based fuel cell system: Explains benefits of the proposed jaya algorithm for overall optimization. Detailed explanations of the fuel cell under various operating situations are provided. A summary of MPPT techniques that have been documented in the literature is given in the survey on MPPT techniques and choice of methodology. The proposed algorithm's performance in comparison to PSO and P&O algorithms in simulations and experiments is check. The performance tracking capabilities of the proposed technique are compared to those of existing techniques, and a summary of the current chapter is given at the enf.

Chapter-5: Energy management in hybrid system: This chapter describes and an energy management system. It is proposed to use a battery, FC, and a hybrid standalone structure made up of a PV panel. The sources of the HS originate from the PV and FC systems which were discussed in chapters 3 and 4. The optimization of energy production is the goal of this configuration. Results from the experiments using the entire system are provided the implications discussed

Chapter-6: Energy management for battery optimization: Management of HS is explained and put it into practice in this chapter. It is proposed to use a hybrid standalone DC grid connected structure made of SC, a battery, and a PV panel. The PV system mentioned in chapter 3 serves as the HS's primary source.The excess energy is provided to a storage device, and a super-capacitor (SC) is positioned to absorb or supply for unexpected current surges. Optimizing battery charge and discharge rate limitations are given in this chapter.

Chapter-7: The overall conclusion of the proposed scope and the future work of research in the domain of energy management applications are proposed in this chapter.

Chapter 2

An Overview of Hybrid System Modelling

2.1 Introduction

A hybrid system is made up of many sources and storage options that work together to provide reliable electricity. The mathematical formulation that is used to analyze and implement the entire system must be developed, and therefore it is necessary to conduct a study on the types and specifications of the sources in order to develop and manage them all.

A PV panel is regarded as a current source, and the quantity of current it can produce is influenced by temperature and irradiance. As a result, each input is matched with a static output. The response should be based on estimating the amount of current that has been absorbed from the inputs because they are dependent on climate and therefore unpredictable. The panel need to be designed obtain better input/output gain. In order to determine the optimal operating point for each input condition, it is necessary to be familiar with the PV cell's features and model.

In a similar way, an FC is viewed as a power source, but there are several input parameters and they are all associated with one another and with output parameters. These inputs include temperature, pressure, mass flow, and output current, which would be distinguished by how dynamically it responds to changes in the input. As a result, a mathematical expression is needed to explain the relationship between output, and input power as well as the amount of time needed to attain the steady state.

The battery, which serves as the primary backup element and is thought of as the energy storage device within the HS is charged at regular intervals discharged and converted to chemical energy and vice versa. Because the conversion procedure impacts the battery's lifespan and charge capacity, it needs specific consideration.

In this chapter, the HS elements are reviewed in light of the mathematical and physical knowledge needed to comprehend the static and dynamic behaviour inside a hybrid topology. The PV, FC, battery, and SC-related information is combined in the sections that follow.
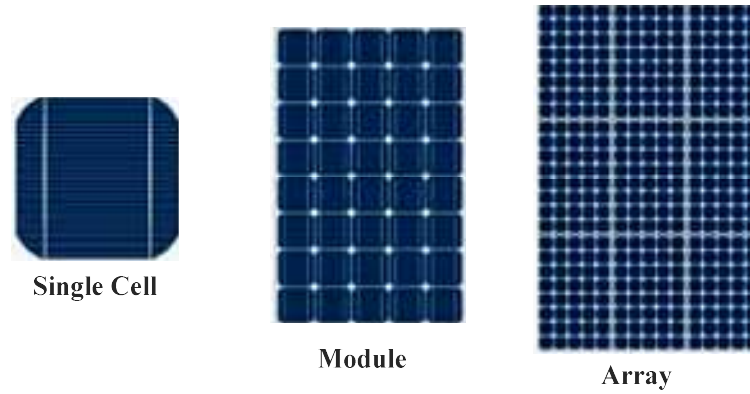
Figure 2.1: PV Cell, Module and Array
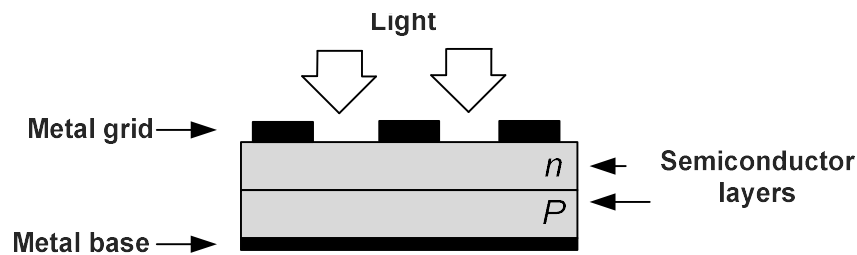
Figure 2.2: PV cell's physical composition

2.2 Solar photovoltaic system

A solar panel, also known as a photovoltaic module or panels, is a compact, integrated collection of PV cells. The PV systems are employed to supply and produce power for both domestic and industrial uses. The DC output power of solar panels is rated based on established test circumstances. To produce the necessary voltage and current, panels are arranged in an array in series and/or parallel as shown in Fig.2.1.

A single photovoltaic cell is a p-n junction formed of n and p layers, two distinct types of silicon. Valence electrons are diffuse and move from p-layer towards n-layer when both layers are linked; as a result, an electric field is formed and current passes in the load circuit. Metallic interfaces are added to both layers to collect electrons and allow current to flow. The layer exposed to radiation is connected to metallic strips that allow light to reach the cells as shown in Fig.2.2. When radiation from the sun strikes a cell's surface, photons with higher energy levels that are above the band gap of silicon cells material form a pair of electrons and produce light-generated current, which is directly proportional to the amount of solar radiation.

PV cells are available in two types, mono-crystalline and poly-crystalline solar cells. The manu-facturing of silicon, the basic component of solar cells, is where the difference first appears. By

23

employing Czochralski process, a monocrystalline silicon crystal is gently drawn from molten monocrystalline silicon to make an ingot of silicon.

Molten silicon is poured into a mould and cooled using a seed crystal to create poly-crystalline silicon. The crystal around the seed becomes homogeneous as it is cast, and it divides into several, smaller crystals, becoming "poly-crystalline."
The following aspects set those two types of cells apart from one another:

- **Price:** In terms of size, mono-crystalline photovoltaic cells are more expensive than poly-crystalline ones.

- **Efficiency:** Due to the material they are built of, mono-crystalline units are more efficient than poly-crystalline ones. In high temperature conditions, mono-crystalline frames typically perform 10% higher than poly-crystalline frames.

- **Look:** Due to its higher area efficiency, mono-crystalline solar frames are smaller in size for a given wattage compared to poly-crystalline PV frames.

- **Longevity:** Although mono-crystalline frames have a 30-year lifespan theoretically, generally warranties only cover 25 years, whereas poly-crystalline frames may easily exceed the life span of 25 years.

Overall, the manufacturing of mono-crystalline has reached an advanced state, while that of poly-crystalline is still developing. The effectiveness differences between them are closing as polycrystalline purity and manufacturing tolerances increase.

2.3 PV system modelling

2.3.1 Ideal PV cell

The circuit that corresponds to an ideal PV cell is shown in Fig.2.3. The equivalent equation (2.1), which is dependent on the semiconductor principle, quantitatively represents the I-V characteristics of a desirable PV cell [91].

$$\text{Output current}(I) = I_{pv,cell} - I_o \left[exp \left(\frac{qV}{akT} \right) - 1 \right] \tag{2.1}$$

Where, $I_{pv,cell}$ is current derived from solar radiation, I_d is current in the diode of Shockley, I_o is Saturation current of a diode, q The electrical charge of electrons (1.60217646×1019C), k The

24
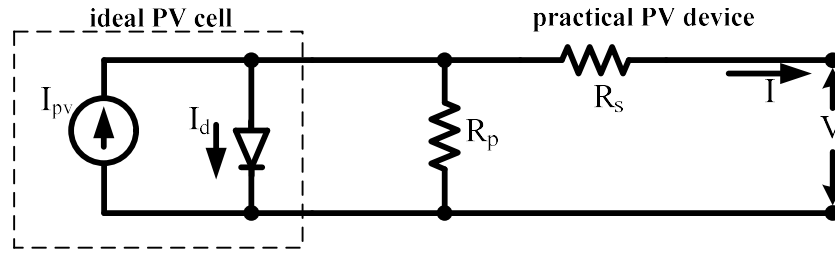
Figure 2.3: The equivalent circuit of an actual PV system

Boltzmann constant (1.3806503×1023 J/K), T The p-n junction temperature (in Kelvin),and a Diode ideality constant.

2.3.2   PV array modeling

The first equation (2.1) of the basic PV cell does not consider the I-V characteristic of a working PV array. A Typical PV system is composed of a small number of related PV cells, so that the fundamental equation (2.1) should include the following extra parameters to compensate for the terminal properties of PV system [91]:

$$I = I_{pv} - I_{o,pv} \left[exp \left(\frac{V + R_s I}{V_t a} \right) - 1 \right] - \frac{V + R_s I}{R_p} \tag{2.2}$$

Where,I_{pv} Photovoltaic (PV) array current, , $I_{o,pv}$ Array saturation current, V_t array thermal voltage, N_s Series-connected cells, N_p Parallel connections cells, R_s The equivalent resistance of the array's series circuit,and R_p The equivalent resistance of the array's parallel resistance.

If indeed the array consists of N_p solar cells, the saturation current and PV are shown as $I_o = I_{(o,cell)}\ N_p$, and $I_{pv} = I_{(pv,cell)}\ N_{(p)}$. Figure 2.4 shows the I-V curve generated by equation (2.2), which includes the short circuit points $(0, I_{sc})$, MPP at (V_{mp}, I_{mp}), and open circuit points $(V_{oc}, 0)$.

The equation(2.2) describes the single-diode model of an actual PV cell that is seen in Figure 2.4, 2.2. For the purpose of simplicity, we evaluate the single-diode technique in Figure 2.4. This approach effectively achieves a balance between adaptability and accuracy. Furthermore, this concept has been applied by several researchers in earlier research projects, which has for simplifying assumptions. This is compatible with the fundamental design an equivalent- diode current source. The single-diode model is perfect for power electronic designers who are looking for a simple and practical model to emulate PV systems in circuits.

25
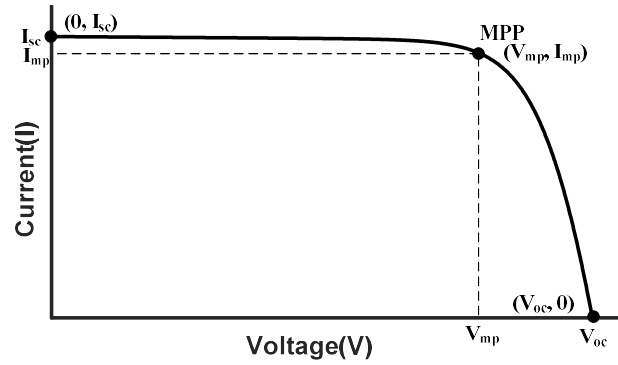
Figure 2.4: The I-V characteristics of a practical PV system

Instead of using the I-V formula, developers of PV arrays have a limited number of functional details relating to thermal and electric qualities. However, the developer's data sheets can not offer many crucial factors for changing PV array models, such as photo- generated or PV current, shunt-series resistances, diode's saturation current, diode ideality factor, and material bandgap energy.

All technical specifications for PV arrays provide the following details: The maximum power available in a realistic scenario $(P_{mpp,e})$ depends on the voltage (V_{mp}), current (I_{mp}), voltage at the open circuit at its rated voltage (V_{oc}), short-circuit state $(I_{sc,n})$,the temperature co - efficient of voltage in an open circuit (K_V), co-efficient of current (K_I) in short circuits

2.3.2.1 Fill factor

By using MPP voltage and current, V_{mp} and I_{mp}, V_{oc}, and I_{sc}, the Fill Factor (FF) may be defined as follow:

$$FF = \frac{P_{mpp}}{P_t} = \frac{V_{mp}I_{mp}}{V_{oc}I_{sc}} \tag{2.3}$$

The quality of a solar cell is measured using FF [92] . It is determined by dividing the theoretical maximum power $(V_{oc}I_{sc})$ by absolute maximum power $(V_{mp}I_{pm})$. However, this is not possible since MPP current and voltage are always lower than short circuit current (I_{sc}) , and open circuit voltage (V_{oc}) because of the diode,shunt resistor, and the series resistor,(shown Figure 2.3). Industrial solar cells often have FF greater than 0.7. The proportion of the rectangular areas shown in Figure 2.4 may also be used to graphically represent FF.

2.3.2.2 Temperature and irradiance effects

There are two key considerations that must be made: temperature and irradiance. They shift I_{sc}, V_{oc} and consequently the operational power, which have a significant impact on the properties

(a)

(b)

(c)

(d)
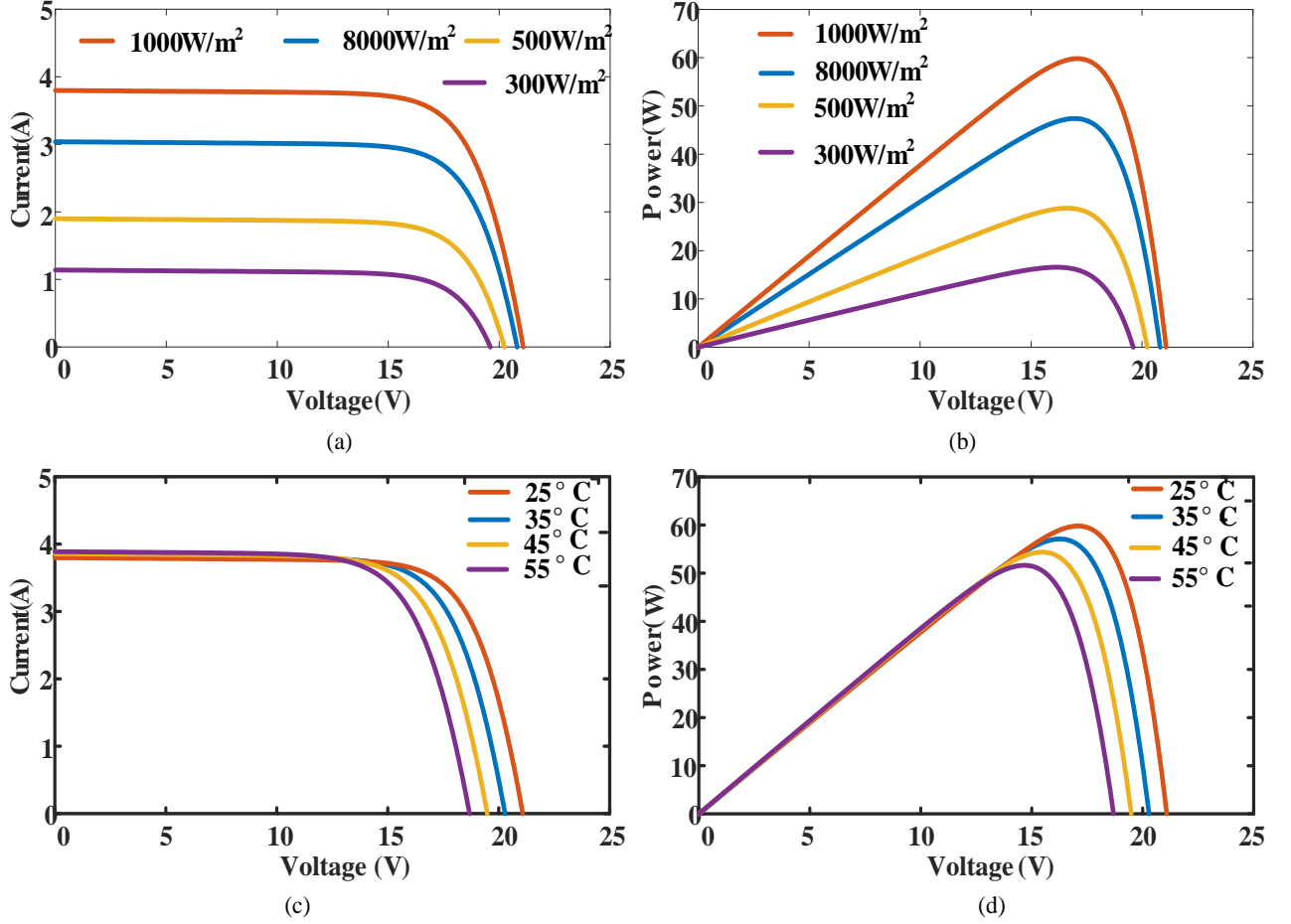
Figure 2.5: (a), (b) I-V and P-V characteristics at (25°C) for four different irradiation level. (c),(d) I-V and P-V characteristics with four different temperatures at standard irradiation $(1kW/m^2)$ of solar modules. As a consequence, MPP changes during the day, which is the major reason it needs to be monitored continuously to make sure the solar panel is getting the most power possible. The I-V and P-V graph are shown in Figure 2.5 for various solar irradiance and temperature levels. Power increases as a result of the irradiance impact since it has a positive impact on both current and voltage, which both grow even as irradiance rises. On other side, voltage is mostly impacted by temperature. The relationship shown in equation (2.4) is the linear relationship between V_{oc} and temperature:

$$(\text{Open circuit voltage})V_{oc}(T) = V_{oc}^{STC} + \frac{dV_{oc}}{dT}(T - 273.15) \tag{2.4}$$

where $T(K)$ is the solar cell temperature, $\frac{dV_{oc}}{dT}$ is the temperature difference, and V_{oc}^{STC} (V) is the V_{oc} at Standardized Temperature Condition (STC). Equation (2.4) states that the temperature has a negative influence on V_{oC} even though $\frac{dV_{oc}}{dT}$ is negative, meaning that as the temperature goes up, voltage falls. The power also falls since the current rises with temperature but only slightly and cannot make up for the drop in voltage brought on by a particular temperature rise.

27

Table 2.1: Different forms of technology' maximum current densities, band gaps, and theoretical efficiency

Material	Max. current density mA/cm^2	Band gap [eV]	Max. theoretical efficiency [%]
Silicon, Si	43.4	1.12	28
Gallium arsenide, GaAs	31.8	1.4	30
Cadmium telluride, CdTe	28.5	1.5	29
Amorphous silicon, a-Si	21.7	1.65	27

2.3.2.3 Efficiency

The efficacy of a PV cell is determined by the silicon material properties' band gap and their ability to reflect photon energy across a wide range of light. The energy gap, maximum current, theoretical efficiency of various materials commonly used at room temperature are approximated by the author in [93]and are included in Table2.1.

2.4 Fuel cell

An FC is a device that, through a chemical reaction involving oxygen or perhaps another oxidant substance, transforms the chemical energy from a fuel into electricity (see Figure 2.6). The most typical fuel is hydrogen; however, it is also occasionally necessary to use alcohols as methanol and hydrocarbons as natural gas. FC varies from batteries bank in that it needs a continual supply of fuel and oxygen to operate, but it can continuously generate power as long since the inputs are available. Table 2.3 lists the benefits and restrictions of an FC.
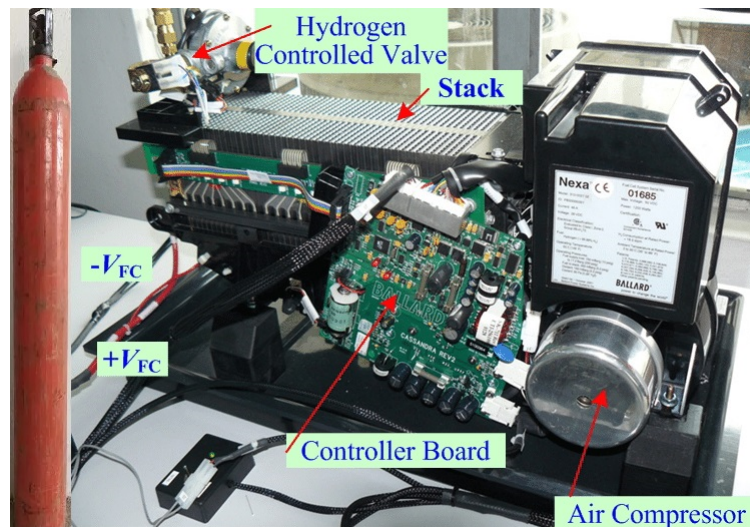
Figure 2.6: 1200 Watts NEXA fuel cell

2.5 Type of fuel cells

FCs are characterized as power generators because, so long as oxidants and fuel are available, they can run constantly. Various FC types are manufactured and used based on factors like efficiency and temperature during operation. In Table 2.2, these categories are given in the order of temperature range.

2.5.1 Proton exchange membrane fuel cell (PEMFC)

PEMFC, also described as polymer electrolyte membrane fuel cells, are a form of FC that is being developed for transportation uses in addition to portable and stationary FC purposes. Their low temperature ranges $(40 \sim 100^\circ C)$ and unique polymer electrolyte barrier are their defining features.This FC uses a fluorinated sulfonate polymeric or some similar polymer as electrolyte, which is a superb proton conductor. This form of FC produces water as a result of the chemical process within, requiring particular control for increased effectiveness. Because of membrane restrictions, the PEMFC's operating temperature range shouldn't go beyond $120^\circ C$.

2.5.2 Alkaline fuel cell (AFC)

This form of FC uses KoH as electrolyte. The alkaline KoH content determines the AFC's working temp. The concentration is approximately 85% for operations at temperatures below $120^\circ C$ and $35 to 50\%$ for operations at temperatures beyond 250°C. There are several different electro catalysts that may be utilised, and the electrolytes is kept in a matrix.

2.5.3 Phosphoric acid fuel cell (PAFC)

The 100% pure phosphoric acid used as electrolyte in PAFC and this lowers the water vapour pressure and makes control of the system easier. The operational temperature ranges between 150° to $220^\circ C$. The silicon oxide matrix is employed to hold the acid while Pt serves as the electrode material in the anode and cathode.

2.5.4 Molten carbonate fuel cell (MCFC)

Typically, a mixture of alkali carbonates serves as electrolytes in FC. The electrolytes are maintained in a ceramic $LiAlO_2$ structure. At 600∘ to $700^\circ C$, when the alkali carbonates create a high conductivity molten salt and carbonate ions provide ionic conductivity, the FC is operational. The nickel(N_i) at anode and nickel oxides at cathode are sufficient to drive the reaction

29

Table 2.2: A summary of fuel cell technology

Fuel Cell Type	Operating temperature [$^\circ C$]	Electrolyte	Electrical Efficiency [%]
PEMFC	≈ 40	Polyer	60-65
AFC	≈ 100	KoH (Potassium hydroxide)	60-70
PAFC	≈ 200	H_3PO_4 (Concentrated phosphoric)	40-45
MCFC	≈ 650	Li_2CO_3(MCFC Molten carbonate melts)	53-57
SOFC	≈ 1000	ZrO_2 (Yttrium-stabilized zirkon-dioxide)	55-65

Table 2.3: The benefits and drawbacks of an fuel cell

Advantages	High-performance and clean.
	Clean. can be utilise renewable fuels,
	Carbon-free when powered by H_2 and O_2,
	No need recharging,
	no moving components,
	No make noise.
Limitations	High cost owing to the use of precious materials such as platinum
	Requires fuel
	Reliability is still changing.
	Lifespan, especially in high temperatures
	Robustness. Many are reactive to temperature and pollution.
	Fuel density is low when compared to gasoline.
	If batteries improve enough, they may become obsolete.

at greater operating temperature for MCFC.

2.5.5   Solid oxide fuel cell for middle temperatures (SOFCMT)

This FC uses the same electrolytes and electrode components as SOFCMT. Furthermore, SOFCMT normally functions around 600° to $800^\circ C$. To encourage ionic conduction as a result, thin film is used. Alternate electrolyte substances are also being produced.

2.6   PEMFC Modelling

The complete fuel cell model has been developed and considers the auxiliary systems as shown in Figure.2.7. Fuel cells are classified according to their operating electrolyte temperature, electrodes, and use of expensive catalysts. PEMFC was chosen for this work because of its low temperature operating range of 40° to 100°C, high output power densities of as much as $2W/cm^2$, solid membranes, long cycle life, and because it has the most widely used form.

The energy provided by a fuel cell is derived from the thermodynamic energy produced by electrochemical processes within the cell. Essentially, this energy is derived by the exothermic process of releasing water content from H_2 and O_2 [54].
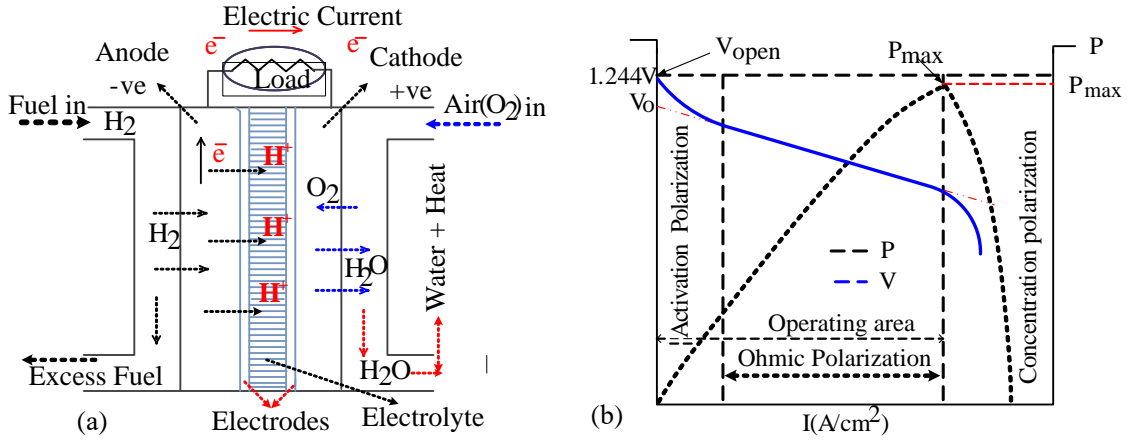
Figure 2.7: Fuel cell: (a)functional diagram, (b) $P-I$ and $V-I$ characteristic

$$H_2 + \frac{1}{2}O_2 = H_2O + Energy \qquad (2.5)$$

Above energy is known as the enthalpy of structure $H = -285.84kJ/mol$ (made reference to that as higher heating value (HHV)), and it may be categorized as thermal energy, expressed by particular entropy $\Delta S kJ/mol.K$ calculated by multiplying absolute temperature (T), and productive work, which is known as Gibbs free energies $\Delta G kJ/mol$, and can be exported as electricity; yet ΔG is restricted by the second law of thermodynamics. As a result, the amount of energy is [54]:

$$\Delta H = \Delta G + T.\Delta S \qquad (2.6)$$

Where ΔG denotes electrical work, which is described as electrical charge Q [coulombs] from across the electrostatic potential $E[V]$:

$$\Delta G = -Q.E \qquad (2.7)$$

Here Q is the number of electron molecules (n), multiplied by (Faraday standard $F = 96485$ coulombs) electron charge and ΔG is as calculated follows:

$$\Delta G = -n.F.E \qquad (2.8)$$

Because the process is exothermic, the quantities ΔG, ΔH, and ΔS become negative. As a result, the potential provided by the FC may be computed as follows:

$$E = \frac{\Delta G}{n.F} = \frac{-(\Delta H - T.\Delta S)}{n.F} \tag{2.9}$$

This quantity must be changed to account for variations in temperature and pressure of reactants relative to their rated value ($T_{ref} = 25°$, $P_{ref} = 1atm$). The consequence of temperature changes on potential is computed as follows, assuming that H and S remain consistent: [54].

$$\Delta E = \frac{\Delta G}{n.F}(T - T_{ref}) \tag{2.10}$$

From the above equation, the temperature rises, and the potential decreases since $\Delta S = -164 J/mol.K$ which is negative. Now, variations in partial pressures impact G, which is a function of specific volumetric $V[m3/mol]$ and density of pressure change dP (as $G = V.dP$), and the final solution that describes this relationship (according to the universal fundamental gas law $V = R.T/P$) is: [54].

$$\Delta G = \Delta G^o - \frac{R.T}{n.F}.Ln\frac{P_{O_2}^{0.5}.P_{H_2}^1}{P_{H_2O}^1} \tag{2.11}$$

In which $\Delta G^o = -237.17 kJ/mol$ seems to be Gibbs free energy during the standard test conditions, and $R = 8.3143 J/mol.K$. This calculation assumes that perhaps the cell is operating on clean H_2 with partial pressure PH_2 as such fuel and clean O_2 with partial pressure PO_2 as oxygen. We know that one mole of water with pressure PH_2O (the product) requires one molecule of H_2, $1/2$(half) a molecule of O_2 (i.e. reactants). As a result, the cell's potential is provided by: [94].

$$E_{Nerst} = \frac{\Delta G^o}{n.F} + \frac{\Delta S}{n.F}(T - T_{ref}) + \frac{R.T}{n.F}.ln(\frac{P_{O_2}^{0.5}.P_{H_2}^1}{P_{H_2O}^1}) \tag{2.12}$$

$$= 1.229 - 0.85 * 10^{-3}(T - 298.15) + 4.3085 * 10^{-5} * T * ln(P_{H_2} * \frac{P_{O_2}^{0.5}}{P_{H_2O}^1}) \tag{2.13}$$

This is known as the Nernst equation. This refers to the highest voltage that the FC can provide owing to losses including overpotentials, which have been divided into four distinct types:

2.6.1   Activation loss

 The above loss is recognized as the ignition spark required to initiate the reactions. It is determined using a semi-empirical equation that takes into account partial pressure (PH_2, PO_2), temperature (T), and the activator employed on the counter electrode: [95] The activation voltage drop V_{act} is given in [96].

$$V_{act} = [\xi_1 + \xi_2 T + \xi_3 T \ln(C_{O_2}) + \xi_4 T ln(I_{FC})] \tag{2.14}$$

Where ξ_i (i=1 to 4) represents the FC properties coefficients, carbon di-oxide $CO_2(atm)$ represents the carbon di oxide content in $(molcm)^-3$ provided by equation (2.15), and I_{FC} represents the FC current.

$$C_{O_2} = \frac{Po_2}{(5.08 \times 10^6) \times \exp^{(\frac{-498}{T})}} \tag{2.15}$$

2.6.1.1   Ohmic loss

V_{ohmic} is the ohmic-voltage drop, which is calculated as follows:

$$V_{ohmic} = I_{FC}(R_M + R_C) \tag{2.16}$$

The V_{ohmic} of such cells can be reduced by employing conductive substances as well as an electrolyte barrier. R_C in equation (2.16) is the edge contact resistance, which would be considered to be constant because it is independent of FC operating temperature. R_M is the PEM's resistance, which is given by an empirical formula;

$$R_M = \frac{r_m t_m}{A}, \tag{2.17}$$

$$r_m = \frac{181.6 \left[1 + 0.03(\frac{I_{FC}}{A}) + 0.0062(\frac{T}{303})^2(\frac{I_{FC}}{A})^{2.5}\right]}{\left[\lambda_m - 0.634 - 3(\frac{I_{FC}}{A})\right] \exp\left[(4.18(T - \frac{303}{T}))\right]}. \tag{2.18}$$

Where, r_m is the electrolyte barrier resistance in $(W.cm)$, t_m =(0.0178cm) is the thickness of the barrier, $A = 232(cm^2)$ is the functional region of FC, and λ_m is barrier water content with a normal value range of (0 to 14) and a relative humidity of 100%.

2.6.1.2 Concentration loss

The voltage loss (V_{con}) is caused by the overflowing of water inside FC substances [97].

$$V_{con} = \frac{-RT}{nF}(1 - \frac{I_{FC}}{i_{LA}}) \tag{2.19}$$

Where n denotes the number of electrons towards the reactions, i_L denotes the limitation current, and R denotes the gaseous universal constant.

2.6.1.3 Cross over loss

The partial pressure of (PH_2, PO_2), temperature (T), and barrier water content (λ_m) all impact FC stack voltage. Furthermore, the FC voltage exhibits drooping V-I characteristics due to a drop in voltage caused by activation, concentration, and Ohmic losses. Taking these drops into account, the FC dc voltage is signified as [46].

$$V_{cell} = E_{Nerst} - V_{act} - V_{ohmic} - V_{con} \tag{2.20}$$

The total output voltages and power of the stacked FC are calculated as follows:

$$V_{FC} = N_{FC}.V_{Cell} \tag{2.21}$$

$$P_{FC} = V_{FC}.I_{FC} \tag{2.22}$$

Where, ($N_{FC} = 35$) represents the number of FC, (V_{FC}), (I_{FC}), and (P_{FC}) represent the output power, voltage, and current of the FC stack,respectively.

2.6.1.4 Stack efficiency

Equation (2.23) may be used to calculate FC efficiency [98].

$$\eta = \mu f.\frac{V_{FC}}{1.48} \tag{2.23}$$

Where μf is the fuel utilization coefficient, which is typically within 95% of the range, and 1.48 V indicates the highest voltage attained by employing higher heating value (HHV) hydrogen pressure enthalpy. In a fuel cell with a hydrogen pressure flow rate controller, fuel consumption is kept constant. In this scenario, hydrogen is given based on the load current.

2.6.1.5   Calculating fuel cell system efficiency (η_{FC})

The standard method for calculating the efficiency of a fuel cell power plant or other electrical generation device is to divide the net electricity generated by the higher heating value (HHV) of the fuel used [99], i.e.,

$$\eta_{FCS} = \frac{\text{Electricity generated}}{\text{HHV of fuel used}} \qquad (2.24)$$

This is a reasonable method for calculating power plant efficiency because the power plant operator purchases fuel (natural gas is sold by heating value) and sells electricity. However, the maximum theoretical limit to the electrical efficiency of a fuel cell system is represented using Gibbs free energy divided by the combustion heat of the fuel. In the case of the hydrogen fuel cell, this value is Gibbs free energy/HHV ($237.2kJ/mole285.8kJ/mole = 83\%$). The use of HHV here is in keeping with the method used in the United States to calculate efficiency for internal combustion (IC) engine/generators and gas turbine/generator systems [100].

Some U.S. developers of high-temperature fuel cells, however, prefer the European convention and instead use lower heating value (LHV) of hydrogen for efficiency calculations. The Joint Army-Navy-Air Force (JANAF) tables list the Gibbs free energy for the formation of water vapor from hydrogen and oxygen as $228.6kJ/mole$, so the maximum theoretical efficiency of a complete fuel cell system based on the LHV of hydrogen is $228.6kJ/mole241.8kJ/mole$, or 94.5%. Using LHV convention for calculating the efficiency of an electrical generator always yields numbers greater than those yielded by calculations using HHV for the same system. When quoting electrical efficiency of an electric generator, it is important to indicate whether it is based on HHV or LHV calculation method.

Practical fuel cells cannot achieve maximum electrical efficiency values due to the presence of internal resistance losses and other losses. The practically calculated fuel cell efficiency using equation (2.23) for varying output power is shown in Figure.2.8(b).

A practical fuel cell operating near its maximum power output might be able to produce only $154kJ$ of electricity per mole of hydrogen consumed, with the rest of the heating value appearing as heat produced by the fuel cell. The calculation for such a fuel cell is $154kJ/mole285.8kJ/mole$ Higher heating value (HHV). However, the remaining 46% of the energy produced can be recovered from the fuel cell system as co-generated heat [99, 101].
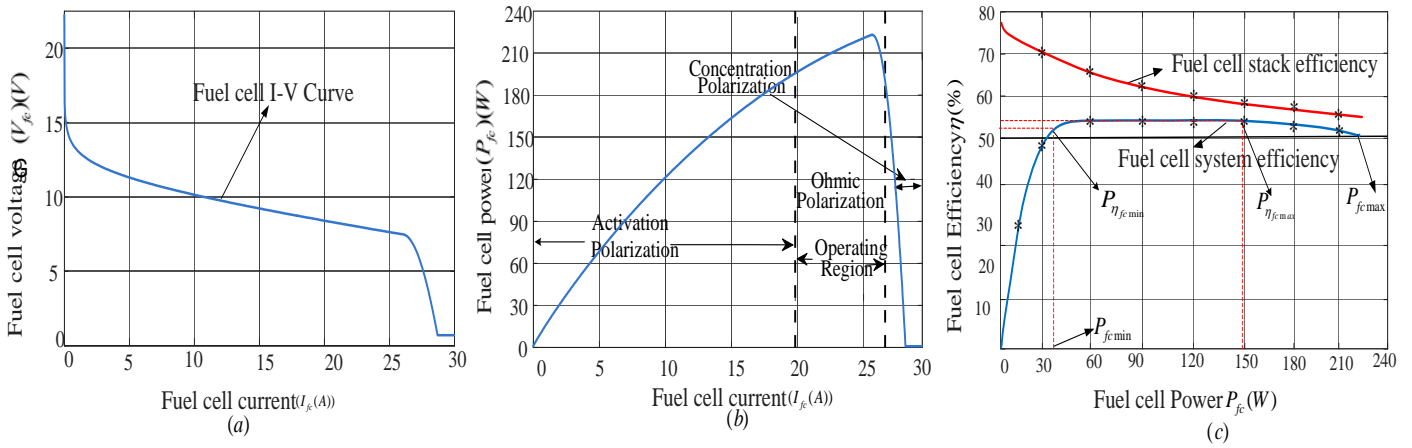
Figure 2.8: (a)$I - V$,(b) $I - P$, and(c) power- efficiency, curves of a fuel cell at constant hydrogen and oxygen gas pressure

As observed from Figure. 2.8(c). The fuel cell system efficiency is very low for the low value of output power and it is sharply increased with an increase in output power, up to a value of P_{fcmin}. Beyond the output power, although the rate of increase in efficiency with output power is positive, it is very small in magnitude. In this curve, the peak efficiency value $(P_{\eta fcmax})$ is observed when the fuel cells system output power is P_{fcmax}. On further increase of output power, the efficiency is reduced with a small negative slope. From these efficiency characteristics, it can be observed that fuel cell system efficiency is only constant when the output power of the system is between P_{fcmin} and P_{fcmax}. Even at the MPP point, the efficiency is observed to be 7% lower than its peak value. Thus, taking this advantage, the proposed strategy can be easily employed by maintaining the fuel cell's minimum power, i.e., P_{fcmin} (or power corresponding to the nose point in the efficiency curve), when batteries are overcharged and power balance is achieved by derating PV. During normal operation, the fuel cell is operating using a reverse sigmoidal function, delivering power between P_{fcmin} to P_{fcmax}. The reverse sigmoidal characteristics are modified accordingly to fit within the output power limits within these ranges.

2.7   Batteries

In solar, wind, as well as other intermittent renewable sources, battery storage offers significant advantages. In the event that the sources are generating electricity, the battery gets charged. Once the generator is no longer there, this energy is able to be released. Depending on the application, operating properties change considerably. Common uses for PV systems are illumination, telemetry, remote houses, and communications. It is necessary to take into account factors like great energy efficiency, low self-discharge, low cost, and lifespan, and also no main-

36

tenance when developing detailed specifications.

The selection of an appropriate battery for different types of fuel cell necessitates a detailed assessment of the battery's charge rate and discharge rate needs, along with load, production of solar power or other sources, working temperature, and the performance of the adapter and other parts of the system. Due to low production costs, lead-acid battery packs are frequently employed in compact stationary energy storage devices. For these purposes, maintenance-free battery packs are currently being designed. These battery packs (120-Ah size) have a self-discharge rate of about less than 5% every month, a recharge time of mostly less than 8 hours, and 1000–2000 cycles toward an 80% deep discharge. They may operate without maintenance when left unattended.

In many different applications, lead-acid battery packs are often utilised. The most popular examples are emergency and backup power, industrial trucks with equipment, and lighting, starting, and ignition (LSI) automobile use. Recently, the use of battery packs as a source of power for electric and hybrid automobiles has renewed its popularity. Major development initiatives have been started to improve the efficiency of present battery packs and create new systems that will fulfil the exacting requirements of these numerous applications.

Standard lead-acid battery packs are distinguished by higher power density, strong discharge behavior, and decent low temperature achievement as well as the capacity to be recharged. However, some batteries, such those using lithium ion technology, offer greater specific energy, greater charge storage, and many other performance improvements due to the utilization of higher energy components.

Edison developed the nickel-iron alkaline batteries in 1908 to equip the first electric cars. In the end, it was used in commercial trucks and in automobiles used for excavating minerals/coal in tunnels. Although it had longevity and durability as benefits, it rapidly decreased in popularity due being its expensive, demanding high service requirements, and poor energy density [102].

Huge manufacturing applications were the main use for such pocket-plate nickel-cadmium batteries, which have been produced since 1909. In the 1950s, the sintered-plate innovations, which boosted power capacity and density of energy, expanded the market for correspondence and aircraft engines starting using them, Later, the creation of sealed nickel-cadmium batteries made it possible for it to be widely used in portable devices as well as for other purposes.

37

Currently, the annual global market for rechargeable batteries is worth over $20 billion. The LSI battery commands a considerable market share for lead-acid batteries, which are currently most commonly used batteries.

2.7.1 Rechargeable battery categories and characteristics

The key features of rechargeable battery packs are that the discharging and charging, or the conversion of electrical energy to chemical energy and returning again, should occur almost reversibly, be efficient, and have few physical defects that might shorten cycle life. The battery cell should have the typical qualities required of a battery, including high energy, low resistance, and acceptable performance across a wide range of temperatures. Chemical activity, which can also cause cell damage, loss of life,and loss of specific energy, should be absent. The range of materials that may be effectively used in a rechargeable battery is limited by these constraints.

Several of these features may be found in lead-acid battery pack. The process of charge-discharge is virtually reversible, the device is free from harmful chemical activity, and although the lead-acid battery's is low energy density , it operates consistently across a wide range of temperatures. Its low price with excellent performance and cycle-span is a major contributor to its attractiveness and leading position.

According to the designs specified in the lead-acid battery pack the battery is available in a wide range of sizes, from 1 Ah packed tiny cells to 12,000 Ah big cells. The LSI battery used in automobiles is easily the most common and widely used. In comparison to LSI batteries, lead-acid corporate rechargeable batteries are often bigger and of superior quality. corporate batteries are used for a variety of purposes. similar stationary service, which comprises HS, telecom, utility companies for running backup and case of emergencies power supplies, UPS, and on trains, signalling and vehicle power systems.

Three various positive plate forms are used in industrial battery pack: tubular, pasted, and Plante's models, which produce active electrode materials using pure lead and are mostly used in stationary battery packs for motor power, stationary, and diesel engine cranking applications. Lead-antimony or lead-calcium metal grid alloys are used in flat-plate batteries.

Lead-acid battery packs are also used in various kinds of applications, including in submarine operations, as a backup power source for maritime applications, and in enclosed spaces, and in

coal mines where generators are not permitted. Load levelling for services and solar PV projects are two new applications that can benefit from the battery's low cost. The energy and density of energy of the lead-acid batteries will need to be increased for these purposes.

2.7.2   Battery capacity, energy and voltage

In essence, the electrode materials affect the voltage and storage of a battery. According to [102], the energy supplied by a reaction is as follows:

$$\Delta G^o = -nFE^o \tag{2.25}$$

where F is Faraday constant, n stands for the number of electrons participating in a stoichiometric process, and E^0g is the standard voltage dictated by the kind of active various materials towards the cell.

2.7.3   Theoretical capacity(Coulombic)

The entire amount of energy used in the electrochemical process is referred to as the specific capacitance, which is given in coulombs(C) or ampere-hours (Ah) for a cell. The amount of power produced by the active electro materials is directly related to the capacity. Ideally, a substance containing 1 gramme equivalent will produce $96,487C$ or $26.8Ah$.

2.7.4   Theoretical energy

The sum of battery cell voltage and capability is the theoretical energy, which is measured in Watt-hours(Wh). The greatest value that a particular electrochemistry system can give is called theoretical energy: Watt hour(Wh)=Voltage x Ampere Hour(Ah)

2.7.5   Mathematical modeling of battery pack

A cell can be represented as the equivalent circuit [102] shown in Figure 2.9. The corresponding circuit uses empirical approach to simulate the behaviour observed at the battery contacts rather than directly modelling the interior chemical properties of such lead-acid battery pack in the design. In order to simulate a 12 V automotive battery pack, the output voltage level is approximated by six, the number of series battery cells.
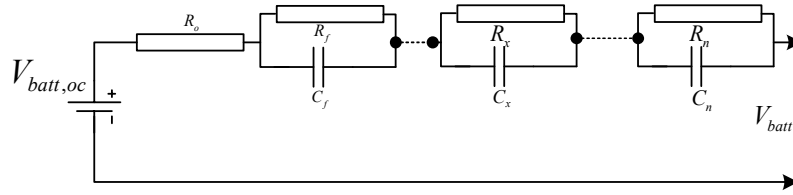
Figure 2.9: Battery equivalent circuit

Thevenin circuits [103] utilize a series resistor as well as an RC parallel system to monitor battery responses to transient loads while maintaining Voc constant. The projected battery reaction may be predicted more precisely by running more parallel RC networks.

2.7.5.1   Main branch voltage

Equation (2.26) provides an approximation of the inner electromotive force (EMF) or Voc of a single cell. In the case of a completely charged battery pack , the EMF value is taken to be constant. The State of Charge (SOC), or the amount of charge left in the battery, affects the EMF's variation with temperature [104].

$$V_{batt,oc} = V_{batt,c} - K_1(273 + \theta)(1 - SOC) \tag{2.26}$$

While $K_1(V/C)$ is a constant, (C) is the electrolytes temperature, and $V_{batt,oc(V)}$ and $V_{batt,c(V)}$ represent open-circuit voltage and full charge, respectively.

2.7.5.2   Resistance and capacitance of the main branch

Equation (2.27) provides a close approximation of the main resistance, R_k. Resistance is dependent on the battery's charge of depth(COD) which is a measurement of charge modified for discharge current flow. As the battery drains down during a recharge, the resistance has to become significantly less.

$$R_k = -K_2 ln(COD) \tag{2.27}$$

where $K_2(\Omega)$ is a constant and $R_k(\Omega)$ is the resistor of k_{th} main branch.

The source of the discharge/charge time lag seems to be capacitance, which is represented in equation (2.28). The precision of the actual battery model is influenced by an increment in R_k C_k units within the circuits.

$$C_k = \frac{T_k}{R_k} \tag{2.28}$$

40

here $C_k(F)$ denotes the capacitance of k_{th} branch and $T_k(s)$ denotes time constants of the k_{th} branch.

2.7.5.3   Resistance in the main branch

Equation (2.29) provides an approximation of the main branch resistor, R_o. As battery Capacity SOC rises, the resistance rapidly increases.

The resistance fluctuates in relation to the amount of current that flows through the major branch. The battery is mostly influenced by resistance when it is getting charged. For discharging currents, the resistance becomes comparatively negligible.

$$R_o = K_3 \frac{e^{[K_4(1-soc)]}}{1 + e^{\left(\frac{K_5 I_{batt}}{I_{norm}}\right)}} \tag{2.29}$$

where $I_{batt(A)}$ and $I_{nom(A)}$ are the major branch current and normal battery current, respectively, and K_3, K_4, and K_5 are constant parameters.

2.7.5.4   Extracted and additional charges

The charge taken out of or supplied to the batteries is a basic integration of such current pouring in and out of the major branch.

$$Q(t) = Q_{initial} \pm \int_0^t I_{batt}(\tau) d\tau \tag{2.30}$$

here $I_{batt}(A)$ is the major branch current, $Q(Amp/sec)$ is the charge obtained, $Q_{initial}$ is the initially recovered charge, τ is an integral time parameter, and $t(s)$ is the simulations duration.

2.7.5.5   Modeling of both voltage and current

The charge current, I_{batt}, is shown in Figure 2.10 and calculated as follows:

$$I_{batt} = V_{Ro} R_o = C_k \frac{dV_k}{dk} + \frac{V_k}{R_k} \tag{2.31}$$

while V_k, C_k, and R_k stand for voltage, capacitance, and resistance of k_{th} batteries branch model, and V_{R0} is the voltage between R_0 and V_k.
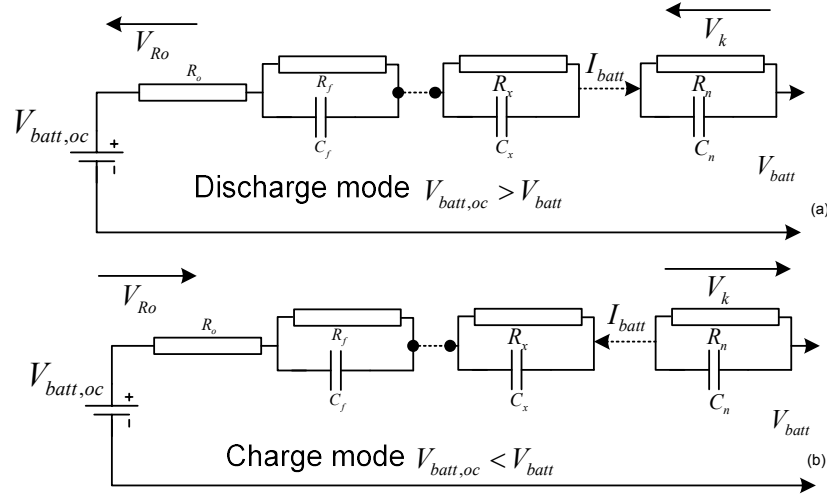
Figure 2.10: Battery equivalent circuit:(a) Discharge mode, (b) charge mode

The following equations yield voltage V_k, across k_{th} RC circuit:

$$V_k = I_{batt}R_k x \left(1 - e^{\frac{-t}{R_k C_k}} \right) \tag{2.32}$$

The battery output, V_{batt}, is written as follows when the battery is discharged (see Figure 2.10.(a):

$$V_{batt} = V_{batt,oc} - V_{Ro} - \sum_{k=1}^{n} V_k \tag{2.33}$$

The initial current given as under fully discharged condition is:

$$I_{batt} = \frac{V_{batt,oc} - V_{batt}}{R_o} \tag{2.34}$$

After the charging procedure is complete, the current becomes:

$$I_{batt} = \frac{V_{batt,oc} - V_{batt}}{R_o + \sum_{k=1}^{n} R_k} \tag{2.35}$$

Equations (2.34) and (2.35) show that the current needed by the battery is large at the start of the charging period and falls until it becomes a minimum, which is indicated by the flow of electricity within the series resistor of the major branch.

As seen in Figure 2.10.(b), the battery pack voltage is stated as follows when it is being charged:

$$V_{batt} = V_{batt,oc} + V_{Ro} + \sum_{k=1}^{n} V_k \tag{2.36}$$

42

Figure 2.11: supercapacitor
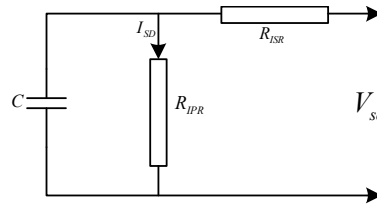
Figure 2.12: supercapacitor equivalent circuit

When a battery is completely discharged, the beginning charge current is determined as follows:

$$I_{batt} = \frac{V_{batt} - V_{batt,oc}}{R_o} \tag{2.37}$$

The following formula is used to represent the current after the charging process:

$$I_{batt} = \frac{V_{batt} - V_{batt,oc}}{R_o + \sum_{k=1}^{n} R_k} \tag{2.38}$$

Equations (2.37) and (2.38) indicate that the battery's current need is greatest at the start and lowers when the major branch capacitances in the model are completely charged.

2.8 Supercapacitors

The supercapacitor (SC), often referred to as the Electric Double-Layer Capacitor (EDLC), or ultracapacitor (UC) is distinct from a standard capacitor in that it possesses an extremely high capacitance. Additionally, EDLCs offer a far better power density than FC or traditional batteries.

The capacitance of EDLC would increase by around two or three magnitudes, although often at a lower operating voltage. It would have a capacitance of several Farads. Professional, larger EDLC capacitors may store up to 5,000 Farads of energy. They are particularly appealing for various applications, such as car, electric grids, UPS, etc., because of their unique characteris-

Table 2.4: Benefits and drawbacks of a supercapacitor

Advantages	Virtually limitless cycle life
	Relatively high power
	Charges quickly
	No end-of-fee termination is necessary.
	Easy to charge Safe
	Outstanding charge and discharge capability in low temperatures
Limitations	Low energy content,
	Discharge voltage,
	High degree of self,
	Relatively low voltage
	Increased price per watt
	Low battery cell voltage

tics. Thus, this component may be used in conjunction with a battery to provide 9high power required for the automobile to start and accelerate, which can lower the maximum output power provided by the battery and lengthen its lifespan. Table 2.4 lists the benefits and restrictions of an SC.

The traditional equivalent circuit model of a SC unit [105, 106] is composed of a capacitance (C), an identical series resistance (R_{ISR}), which simulates the self-discharging deficits, and an identical parallel resistance (R_{IPR}). Figure 2.12 provides the equivalent circuit diagram, and the following equations provide the output voltage:

$$V_{sc} = I_{sc}R_{ISR} + \frac{1}{C}\int_0^t (I_{sc} - I_{SD})dx + V_{sc}(0) \tag{2.39}$$

where V_{SC} and I_{SC} stand for SC voltage and current respectively. Self-discharge flow current is denoted by I_{SD}, while old SC prospective voltage is denoted by $V_{SC}(0)$.

44

Chapter 3

A Bayesian Fusion Technique for Maximum Power Point Tracking Under Partial Shading Condition

3.1   Introduction

Photovoltaic (PV)-based power generation has gained immense attention over the past few decades. With advancements in PV technology, PV cells have shown improved efficiency with reduced manufacturing costs [107]; also, PV systems have nonlinear characteristics that are dependent on various parameters such as irradiance, temperature, series, and parallel resistance. The power extracted from the PV panel is dependent on output voltage for a given irradiance and temperature. This output voltage of the PV panel is usually varied using a power electronic converter that interfaces with load and grid. For full utilization of the installed PV panel, a proper maximum power point tracking (MPPT) technique that extracts maximum possible power from PV systems for a particular irradiance and temperature is needed. Conventionally, the MPPT technique such as perturb and observe (P&O) [1], andincremental conductance [108] is used for PV power plants as appropriate for single peak characteristics to obtain MPPT and its improved strategies [109]. The main drawback of conventional methods is steady-state oscillations. Typically, the PV power plants are extended over a wide area by series and parallel combinations of multiple PV panels to increase the operating voltages and the capacity of the PV system. Due to the presence of multiple PV panels, there is a possibility of partial shading [110] where few PV panels get full irradiance whereas others may be shaded due to passing clouds, shading effect of trees and buildings which in turn can lead to partial shading conditions (PSC). The PV power plant under partially shaded conditions may exhibit multiple local peak(MLP) characteristics which include a global peak (GP) [111]. The conventional MPPT techniques based on the "hill-climbing" algorithm may not guarantee a global peak under these conditions and may be stuck at the local MPP. The multiple global maximum power point tracking (GMPPT) algorithms available in literature.

This chapter proposes a Bayesian fusion technique (BFT) for tracking GMPP under PSC. In this method, Bayes' theorem is applied to obtain a proper GMPP solution by combining the information obtained from two methods [112–114], i.e., incremental conductance and Jaya algo-

Table 3.1: Different patterns of the Irradiance (W/m^2) value

Module (PV)	Pattern-1 (W/m^2)	Pattern-2 (W/m^2)	Pattern-3 (W/m^2)
PV1	1000	1000	1000
PV2	1000	900	900
PV3	400	800	800
PV4	300	500	600

Table 3.2: Rating of the PV

P_{max}	V_{oc}	I_{sc}	V_{max}	I_{max}
$60W$	$21V$	$3.8A$	$17.1V$	$3.5A$

rithm for different partially shaded conditions. As the solutions from both conventional method and meta-heuristic algorithms are used, based on previous probabilities, the BFT technique can reduce overall convergence time, increase tracking accuracy, and reduce steady-state oscillation. For this reason, BFT method is more satisfactory than distribution based techniques. The BFT adopts its solution based on the inputs obtained from incremental conductance and Jaya algorithm-based tracking information, and is a step towards the best solution in the search domain.

3.2 Solar PV under partial shading condition

The Solar PV comes under partially shaded conditions (PSC) and a PV array which accommodates various PV modules that are associated in series and parallel [115]. The combination of every module generates power, which implies that the PV array power. Out of the PV module, any single PV module is shaded instead of inadequate solar irradiation to achieve output power, assume as the shaded module in different levels are shown in Table 3.1 and shaded modules are shown in Figure. 3.1 (b), In every PSC combination, the number of PV modules is associated with a series arrangement called the patterns. The remaining modules generate power and dissipate power to the load. The PV array works like current I_a but shaded modules are forced to operate in the reverse-biased operating region, and the PV array behaves like a load rather than power source [116]. This indicates more localized power loss and the hotspot will appear on an object with irreversible damage to the shaded PV module. Hence, to avoid the hotspot a bypass diode is added to the PV modules under PSC condition [117]. Bypass diode has been added in the configuration as shown in Figure.3.1 (b), to protect it from hotspot during PSC [118]; under uniform irradiation plane, the bypass diodes are forward biased. Because of bypass diodes, the multiple local peaks of the P–V curve appear under PSC. For the simulation, three partially shaded patterns were considered, i.e., GMPP at the left side of the PV curve, the middle global

46

(a)

(b)
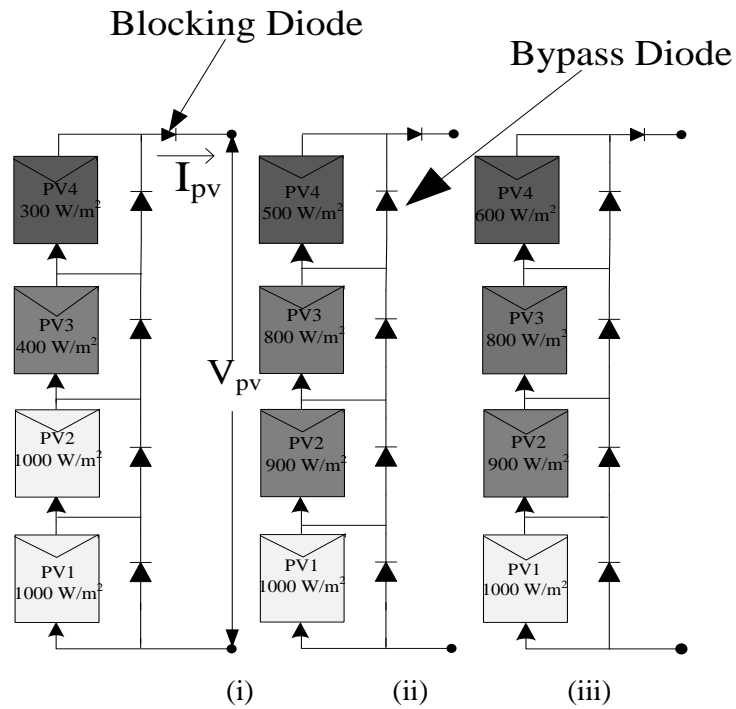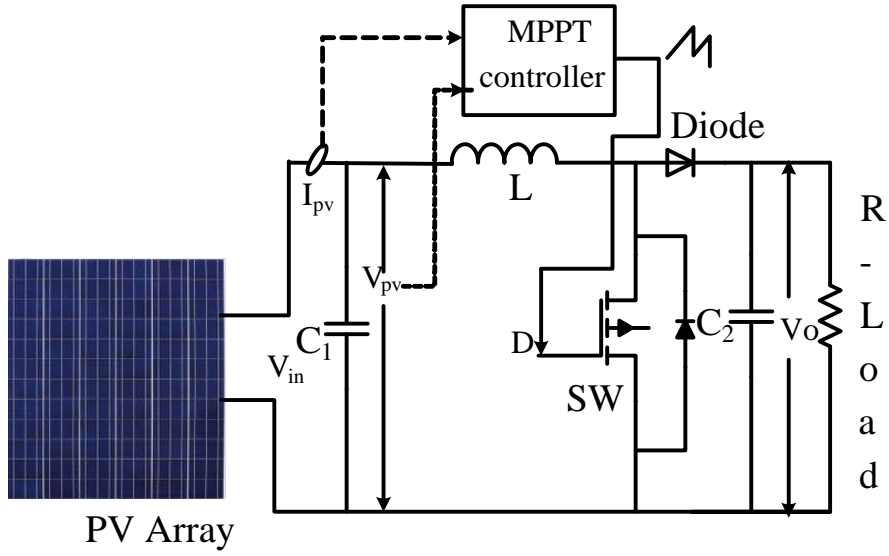
Figure 3.1: (a)Schematic diagram of PV with boost converter, (b) Three different arrangement of array configuration exposed to different levels of partially shaded condition.i.e.(i) pattern-1 (GMPP on the left side of the PV curve), (ii) Pattern-2 (middle global peak of the PV curve), (iii) pattern-3 (GMPP at right side of the PV curve)
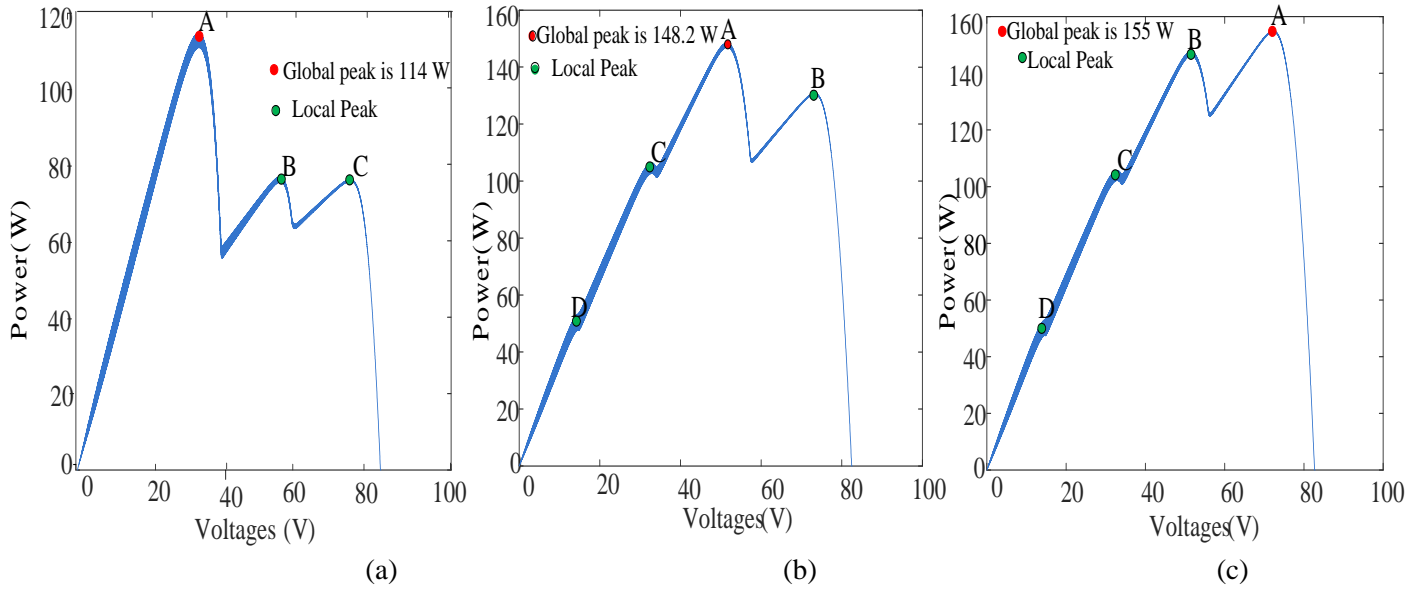
Figure 3.2: P–V curves of the partially shaded patterns; (a) GMPP on the left side of the PV curve, (b) Middle global peak of the PV curve; (c) GMPP at right side of the PV curve

peak of the PV curve, and GMPP at the right side of the PV curve. For the partially shaded condition, 4 series(4s) PV modules configuration were used as shown in Figure. 3.2.

Under normal conditions, conventional MPPT methods, which are P&O, incremental conductance methods, track the maximum power. But under the PSC it is difficult to differentiate in the middle of local maximum power point and global maximum power point (GMPP). Hence, in this chapter, some modifications have been made to eminent tracking about the GMPP under PSC.

3.3   GMPPT methods

3.3.1   Incremental conductance method

The incremental conductance MPPT method is the most frequently used method because its performance has precise regulation with low steady-state oscillation under sudden change in weather conditions. In this method, the incremental conductance ($\frac{dI}{dv}$) is compared to instantaneous conductance ($\frac{I}{V}$) [109]. The operating point at which the difference between incremental conductance and instantaneous conductance will be zero is considered to be MPP, shown in Figure.3.3. The detailed expressions that govern the incremental conductance MPPT are given by equations (3.1)-(3.5).

$$\frac{dP}{dV} = \frac{d(IV)}{dV} = I + V.\frac{dI}{dV} \tag{3.1}$$

48
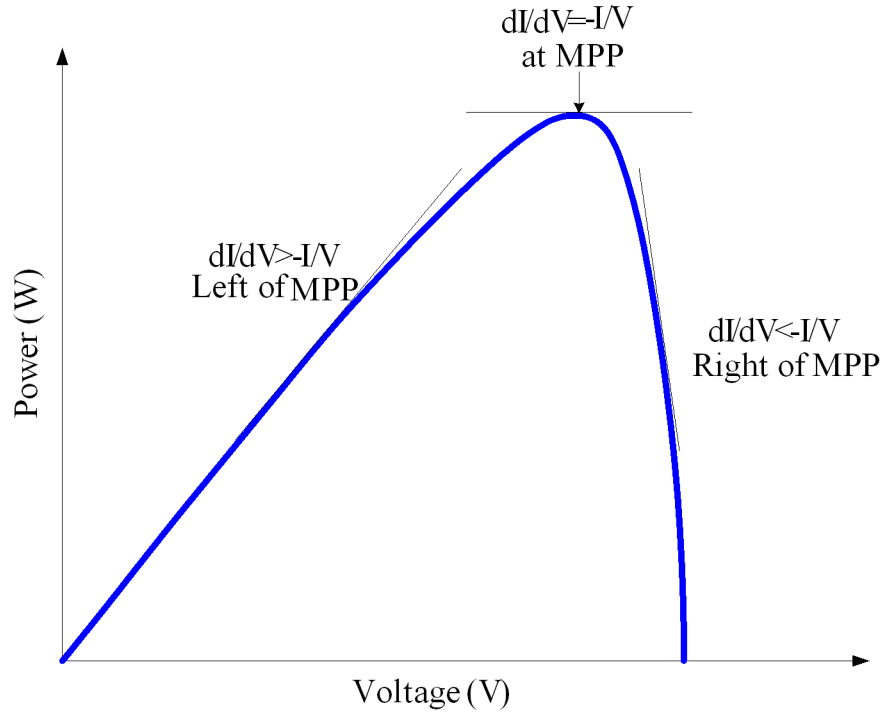
Figure 3.3: Basic P–V characteristics of incremental conductance method

The above equation can be changed into the subsequent equation

$$-\frac{I}{V} = \frac{dI}{dV} = \frac{\Delta I}{\Delta V} \tag{3.2}$$

$$\frac{dI}{dV} = -\frac{I}{V}, \tag{3.3}$$

$$\frac{dI}{dV} > -\frac{I}{V}, \tag{3.4}$$

$$\frac{dI}{dV} < -\frac{I}{V}, \tag{3.5}$$

A system to track the MPP by using an incremental conductance with a Cuk converter is presented [119]

The significant disadvantage of the above conventional technique has deviated from the maximum power point if there should be an occurrence of quickly changing weather conditions. More slow assembly, complex control hardware, and steady-state tracking oscillations around MPP are because of fixed step size. Anyway, these disadvantages are dispensed with if there is an occurrence of Jaya method.

49

3.3.2   Jaya algorithm

Jaya algorithm was developed as a meta-heuristic technique for solving optimization under constrained and unconstrained problems [120]. This method differs in algorithmic specific parameters compared to other heuristic techniques in that it has only two common parameters such as iteration and population size, and these parametric values are easily initialized. This critical improvement makes the utilization of Jaya algorithm simple and proficient.

Let us consider $P = F(X)$ as the objective function; to maximize P, $F(X)$ best and $F(X)$ worst is the description of the best values and worst values of $F(X)$ out of all candidate solutions during every iteration [121, 122]. First n number of candidate solutions are initialized and the next iteration of Jaya algorithm is updated. Let k be the candidate solution under i^{th} iteration, the modified value of k^{i+1} is calculated by using Jaya algorithm given below in Equation(3.6).

$$X_i^{k+1} = X_i^k + r_1(X_{best} - X_i^k) - r_2(X_{worst} - X_i^k) \tag{3.6}$$

where X_i^k and X^{k+1} are the present and updated values, X_{best} and X_{worst} are the best and worst solution among all candidates, r_1 and r_2 are the arbitrary numbers between $U[0,1]$, the term $r_1(X_{best} - X_i^k)$ is the solution of closer to the best, and $r_2(X_{worst} - X_i^k)$ is avoid the worst solution. This method also has fewer oscillations while tracking GMPP, and it takes more iteration to reach the GMPP. The proposed technique combined recent meta-heuristic Jaya algorithm and incremental conductance to improve maximum power point tracking with fewer oscillations and lower iterations.

3.4   Proposed Bayesian Fusion Technique for MPPT

The proposed work is based on the concept of Bayesian decision theory [114], to grow a mathematical fusion structure. This conceptualization enhances the integration of two or more MPPT tracking methods based on feature vector construction. Because of its probabilistic approach the proposed approach can easily handle the uncertainties in irradiance and temperature [123].

3.4.1   Bayesian fusion formulation

The Bayesian technique has the provision of a reverse probability that models uncertainty based on available observations (likelihood and prior knowledge). There are two different interpretations of probability theory,in which one is a frequentest interpretation that provides the probability about the frequencies of events or trials. The other one is Bayesian interpretation that

Table 3.3: Utilized algorithm and boost converter parameters are given below

Particulars	Total set of data=527, training data =80% of 527(421), testing data = 20% of 527 (106).
Bayesian Fusion	Maximum iteration=100, population size=3.
Jaya	Dinitial = 0.15, DeltaD= 0.0051
Incremental conductance	L = 5.20 mH,C1 = C2 = 10 F = 10 kHz,
Boost converter	Switch (MOSFET)
Sampling period(Ts)	for simulation Ts = 0.0023 sec

provides the probability to quantify the uncertainty about some parameters [124].
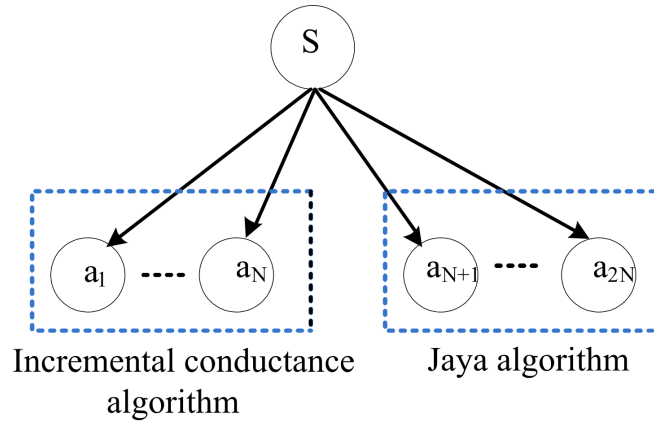
Figure 3.4: Bayesian fusion structure for MPPT information

The most commonly used statistical interpretation method is the frequentest (or classical) method. In this interpretation, the unknown parameters are assumed as constant, and they define probability based on relative frequencies of event occurrence. This limits the decision making capabilities on uncertain parametric conditions.

Bayesian fusion optimization techniques offer an alternative strategy; they treat as random parameters, and they define probability as "degrees of belief" in that probabilities are instinctive and that can make probability explanations about parameters using Bayes' theorem. Bayes theorem is intended to solve the problem after collecting the observed data events using inverse probability

Suppose an unknown state "S" needs to be identified from the data set $a = \{a_1, \ldots . a_n\}$ by using a statistical model characterized by a probability $P(\frac{a}{S})$. Bayesian philosophy is used where uncertainty concerning the parameter limitation is expressed during the probability evidence and

51

distributions. The following steps illustrate the essential fundamentals of Bayesian inference

(i). For the probability distribution "S" , there is a construct as $P(S)$ which is named as the prior distribution. This distribution communicates the probabilities (for example, on the mean, the skewness, the spread, etc.) about the given parameter before examining the given information.

(ii). For a given particular data "a", the statistical model is represented as $P(\frac{a}{S})$ is obtained to describe the distribution of S in the given data.

(iii). The probabilities about "S" are updated by combining data information from the given prior distribution, and calculation of data through posterior distribution $P(\frac{a}{S})$.

Simply, Bayes' theorem updates existing knowledge with new information. In the concept of Bayesian fusion, methods provide simple alternatives for the statistical inference all the inferences that need to be mustered against the posterior probability distribution $P(\frac{a}{S})$.

Practically, the posterior probability distribution can be obtained with a simple analytical solutions for most rudimentary problems. Sophisticated computations with the inclusion of simulation methods are a part of most Bayesian analyses. The posterior distribution from the given sample data is defined as equation (3.7)

$$P(\frac{S}{a}) = \frac{P(a/S)P(S)}{P(a)} \tag{3.7}$$

For n number of independent random variables, varies from $n = 1$ to $2N$

$$P(\frac{S}{a_n}) = \frac{P(a_n/S)P(S)}{\sum_{n=1}^{2N} P(a_n/S)} \tag{3.8}$$

Equations.(3.8) can be written as the product of the conditional probabilities

$$\frac{1}{\sum_{n=1}^{2N} P(a_n/S)}) = [P(a_n/S)P(S)] \tag{3.9}$$

$$\frac{1}{Z} = P(a_n/S) \tag{3.10}$$

For n number of independent random variables, the posterior probability is given by

$$P(\frac{S}{a_n}) = \frac{1}{Z} \prod_{n=1}^{2N} P(a_n/S)P(S) \tag{3.11}$$

52

Where $\frac{1}{Z} = \frac{1}{\sum_{n=1}^{2N} P(a_n/S)}$, $P(a_n/S)$ is the likelihood, $P(S)$ is the marginal distribution, and $P(S/a_n)$ is conditional probability.

3.4.2   Maximum power point tracking using Bayes fusion technique

The BFT-based MPP tracking technique is designed using a Bayesian network [113]. A Bayesian network is a high powered tool derived from Bayes theorem that is used for the joint probability distribution of statistics fusion. In Bayes theorem, the posterior probabilities depend on prior probability distribution. The prior probability distribution is obtained from the statistical inference collected using a set of available prior information. Using current system information, best rational assessment is applied to obtain posterior probability. The prior probabilities are continuously updated based on the previous information available and this is used to estimate new posterior probabilities using Bayes' theorem. These posterior probabilities will help in identifying if a set of information passed is either new event-information or existing event information. This complete BFT process can be segmented into two parts.

  (i). Feature vector production.

  (ii). Decision making

3.4.2.1   Feature vector production

For multiple random variables, a Bayesian network is used to move in the direction of obtaining GMPP under PSC for PV array. The proposed work was done based on joint probability distribution of statistics fusion of incremental conductance and Jaya algorithm. For better understanding, consider a PV system with four modules connected in series with each module having an input combination of voltages and currents pairs at $1000W/m^2$, and the total open-circuit voltage of the PV system being $V_{oc} = nV_{OCM}$, where (n=number of modules, nV_{OCM} is the module open circuit voltage). Now, a Bayesian network is designed and observations input nodes, i.e. $L = \{a_1....a_n\}$, are equally divided into two parts named, left nodes $\{a_1, \ldots, a_n\}$ and right nodes $R = \{a_{n+1}, \ldots, a_{2n}\}$, respectively. The left nodes $L = \{a_1, ..., a_n\}$ are assigned voltage information of individual panels when operated at MPP obtained by incremental conductance under a partially shaded condition. Similarly, the right nodes $R = \{a_{n+1}, \ldots, a_{2n}\}$ are assigned with input voltages obtained across individual panels when the PV system operates using Jaya MPP algorithm for similar partially shaded conditions. The network arrangement for Bayesian network is shown in Figure 3.4; in this network, the output node is defined as "S". After assigning values to all observation nodes, the individual nodes of the left nodes are compared with all right nodes to identify matching nodes. Then the feature vector a is formulated

using equation (3.12).

$$a(i) = a(j) = \begin{cases} 1, & \text{if } L_i = R_j \\ 0, & \text{if } L_i \neq R_j \end{cases} \forall i = 1, 2, \dots \frac{n}{2}; j = 1, 2, \dots \frac{n}{2} \qquad (3.12)$$

If any two nodes on the left and right nodes are matched, then "1" is placed in the feature vector, otherwise "0" is placed. A vector is signified by $a(t) = \{a_1(t), \dots . . a_{n(t)}\}$, where $a_i(t)$ represents the condition of *ith* node at time t.

3.4.2.2   Decision making

The sample training data sets, i.e., input combination of voltages and currents pairs (V, I) of solar cell module with different irradiance and temperature, are noted and the output at each training data sets the GMPP (output) for both Jaya and incremental conductance method. This input data set (voltage, current, and corresponding output (GMPP)) serves as data set, 80% of samples are randomly picked as training data set, and 20% samples are picked as the testing set. The training data set (input, output) is used to train the BFT.
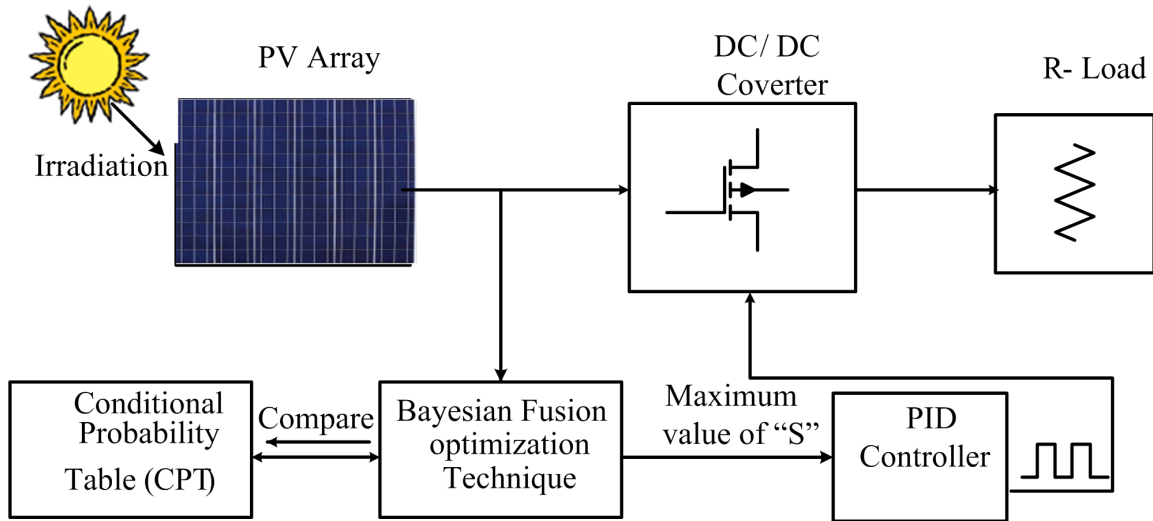
Figure 3.5: Block diagram of proposed Bayesian fusion optimized controller

As mentioned above, input nodes to be stated as $\{0 \, or \, 1\}$, and "S" has output nodes, i.e. $N_S + 1$ = 527 + 1 states, states: $S = \{s_1, \dots . . S_{NS}, NoEvent\}$. Every state $\{s_1, \dots s_{Ns}\}$ compares to an expected point on the I-V curve. The location of the output point "S" (maximum power point) is estimated from the feature vector by appropriately tuning it to BFT.

When values of "S" are given, the values of a_i are conditionally independent on "S". Hence

Measure the PV irradiance
and temperature values

Generate the feature vectors
by using incremental
conductance and Jaya MPPT
Methods

Find out the conditional
probability by using Bayesian
network

Compare the Training Table

Update the posterior
probability

Calculate the
maximum value
i.e(S)   of

probability by using

BFOT

No

Yes

Maximum state is
reached i .e .(S)

Conditional Probability Table

Irradiance	Incremental conductance	Jaya MPPT	Maximum Probability values
$1000W/m^2$	$P(A_1),..P(A_N)$	$P(A_{N+1})..P(A_{2N})$	$P(S)$
-	-	-	-
-	-	-	-
-	-	-	-
-	-	-	-
-	-	-	-
$200W/m^2$	-	-	-

Figure 3.6: Flow chart of the proposed Bayesian fusion method

55

conditional probability distribution is based on the Bayes rule, $P(S|a_1,...,a_N P(S|a_{N+1},...a_{2N})$, and this distribution can be written as the product of conditional probabilities $P(a_n S)$ using equation (3.13)

$$P(S/a_1,....a_{2N}) = \frac{1}{Z}P(s)\prod_{n=1}^{2N}P(a_n/S) \tag{3.13}$$

BFT is trained to estimate the prior and likelihood distribution and the constant value "Z" is calculated from the training data set. These distributions are used to predict the output "S" from the trained BFT. Where $\frac{1}{Z} = \frac{1}{\sum_{n=1}^{2N}P(a_n/S)}$, $P(a_n/S)$ is the likelihood, $P(S)$ is the marginal distribution, and $P(S/a_1,...a_{2N})$ is the conditional probability approximated from the training data sets. For every feature vector, the output "S" is given as a tag. The calculated conditional probability data saved in a particular table is called conditional probability table (CPT). In this method, I-V curve points are stored under different irradiation, and at temperatures under partially shaded conditions. Hence, these are used as training sets. Irradiation values were changed from $1000W/m^2$ to $200W/m^2$ with a difference of $50W/m^2$, and with temperature changed from 10 to $50°C$ with a range of $2°C$ in each combination between these groups. For PV modules, the MPP values of voltages and current combinations were taken. These samples were deployed as part of CPT training. The block diagram of the Bayesian fusion optimized proposed controller is shown in Figure.3.5, as well as in the flowchart shown in Figure. 3.6.

At this point, once the PV array system is under operating conditions, the feature vectors were determined each time as evidence. By using evidence obtaining the conditional probability as above equation(3.13), conditional probability determined to the most credible state of "S" was acquired, i.e. the most probable maximum output power with low steady-state oscillation, more tracking speed, with fewer iterations and more efficiency was observed by combining incremental conductance and Jaya algorithm was better compared to individual meta-heuristics techniques

3.5   Simulation results and discussion

A PV system with 4 PV modules configured in series is connected to the standalone loads using a boost converter shown in Figure. 3.1(a) which is considered for simulation studies. The parameters of the boost converter and algorithms data values have been shown in Table 3.3. The simulation outcome is executed by applying the proposed Bayesian fusion optimization technique (BFT) to get the global maximum power point (GMPP) in MATLAB/SIMULINK for three possible patterns shown in Table 3.2 under PSC.The performance of the proposed method is evaluated by comparing it with existing methods such as incremental conductance method, PSO method, and Jaya method. Three different case studies were performed with three

56

different partially shaded conditions of the PV system as detailed below.

Case-(i): Simulation results with GMPP at the left side of the PV curve.

Case-(ii): Simulation results with the middle global peak of the PV curve.

Case-(iii): Simulation results with GMPP at the right side of the PV curve.

3.5.1   Case-(i): Simulation results with GMPP at left side of the PV curve

In this scenario, the irradiance on each PV module is shown in Table 3.1. Here, PV module-1 and PV module-2 are considered to have the same irradiance values thus leading to three different characteristics that are generated from PV module, and the complete PV characteristics of the PV system are shown in Figure. 3.2(a). It can be observed that the maximum global peak lies on the left side of the PV curve with maximum power being 114.1 W, while the other peaks middle and right peak are local peaks (LP) of the PV array for the PV configuration. The time response of the PV output while reaching maximum peak point using incremental conductance, PSO, Jaya, and the proposed method is shown in Figure. 3.7(a). The incremental conductance algorithm was able to track a maximum power of 110.5 W with the tracking time being 0.39 s. Moreover significant steady-state oscillation and power loss while tracking MPP were observed while using incremental conductance. The PSO-based MPPT method was able to extract a maximum power of 111 W in 63 iterations with a tracking time of 0.43 s. With PSO, the steady-state oscillations were significantly reduced compared to incremental conductance, but there were increased oscillations during the tracki atng period. The power extracted by at Jaya algorithm was 111 W and it took around 28 iterations with a tracking time of 0.19 s and there were fewer oscillations.

The proposed method was also able to extract 113 W with a tracking time of 0.3 sec at global peak of the left side peak. In the proposed technique, the tracking time,and steady-state power oscillations fewer compared to other methods, as observed in Figure. 3.7. There was almost no oscillatory behaviour while tracking MPP compared to incremental conductance, PSO, and Jaya technique, indicating the superior performance of the proposed Bayesian fusion technique. The relative waveforms of the voltage and current are shown in Figure. 3.7(b),(c), and analytic comparison is provided in Table 3.4

3.5.2   Case-(ii): simulation results with middle global peak of the PV curve

In this scenario, the irradiance on each PV module is shown in Table 3.1. While the four peaks
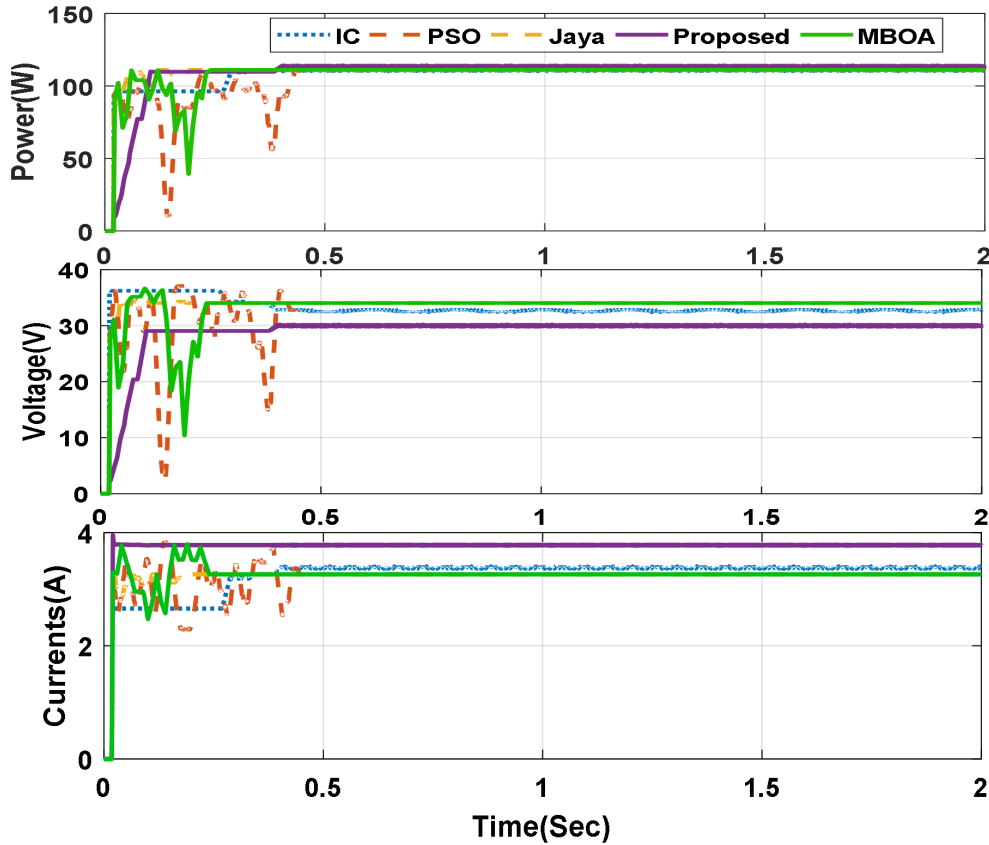
Figure 3.7: Simulation results with GMPP at left side of the PV curve

are available in the P–V curve, as shown in Figure. 3.2(b), it can be observed that a global peak exists in the middle of the PV curve, whereas the rest of the peaks lift side of the PV curve and the right side of the PV curve has been considered as local peaks, with maximum power being 148.2 W. The time response of the PV output while reaching maximum peak point using incremental conductance, PSO, Jaya, and the proposed method is shown in Figure. 3.8(a). The incremental conductance was able to track the maximum power of 147 W, with tracking time being 0.24 sec. Moreover, a significant steady-state oscillation and power loss while tracking MPP were observed while using incremental conductance. The PSO-based MPPT method was able to extract a maximum power of 147.6 W, in 79 iterations with a tracking time of 0.55 sec. With PSO, the steady-state oscillations are significantly reduced compared to incremental conductance, but there were increased oscillations during the tracking period. The power extracted by Jaya algorithm was 147.6 W and took around 28 iterations with a tracking time of 0.58 sec and there were fewer oscillations. The proposed method was able to extract 147.5 W with a tracking time of 0.27 sec global peak of the left side peak. In the proposed technique, the tracking time, and steady-state power oscillations were fewer compared to other methods as observed in Figure. 3.8. There was almost no oscillatory behaviour observed while tracking MPP as compared to incremental conductance, PSO, and Jaya technique, indicating the supe-

58

rior performance of the proposed Bayesian fusion technique. The relative waveforms of voltage and current are shown in Figure. 3.8(b),(c), and analytic comparison is provided in Table 3.4.
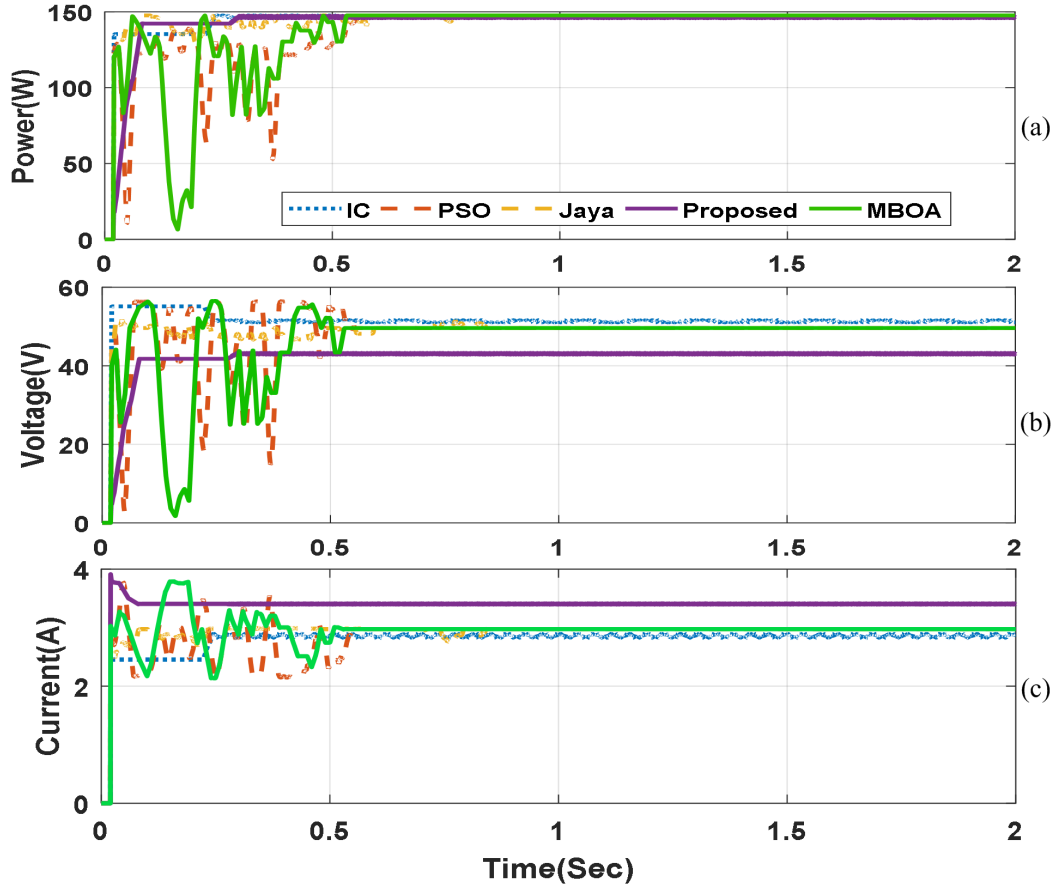
Figure 3.8: Simulation performance with middle global peak of the PV curve

3.5.3 Case-(iii): Simulation results with GMPP at right side of the PV curve.

In this scenario, the irradiance on each PV module is shown in Table 3.1. While the four peaks are available in the P–V curve, as shown in Figure. 3.2(c), it can be observed that a global peak exists at the middle of the PV curve, whereas the rest of the peaks on the left side of the PV curve and right side of the PV curve have been considered as local peaks, with maximum power is being 155 W. The time response of the PV output while reaching maximum peak point using incremental conductance, PSO, Jaya, and the proposed method is shown in Figure. 3.9(a).The incremental conductance was able to track maximum power of 153.8 W, with a tracking time 0.19 sec. Moreover a significant steady-state oscillation and power loss while tracking MPP were observed while using incremental conductance. The PSO-based MPPT method was able

Table 3.4: Simulation analysis of proposed Bayesian fusion along with incremental conductance, PSO and Jaya algorithms as for PV array systems of 4 series configurations

Methods to use produce maximum power	Rated power (W)	Power at MPP, (W)	Voltage at MPP, (V)	Current at MPP,(A)	Tracking Time at MPP, (sec)	Maximum efficiency produce from PV %
Incremental conductance method	114.1 Pattern-1	110.5	34.06	3.3367	0.39	96.84
PSO method		111	34.08	3.176	0.44	97.2
Jaya method		111	34.08	3.262	0.29	97.2
MBOA		111	33.99	3.27	0.24	97.2
Proposed method		**113**	**41.22**	**3.621**	**0.23**	**99.03**
Incremental conductance method	148.2 Pattern-2	147	50.59	2.889	0.24	99.19
PSO method		147.6	49.65	2.85	0.55	99.59
Jaya method		147.6	49.65	2.975	0.53	99.59
MBOA		147.6	49.75	2.98	0.53	99.59
Proposed method		**147.5**	**38.16**	**3.628**	**0.27**	**99.52**
Incremental conductance method	155 Patterns-3	153.8	72.5	2.13	0.19	99.22
PSO method		154.4	74.18	1.957	0.18	99.61
Jaya method		154.4	74.18	2.084	0.17	99.61
MBOA		144.6	53.47	2.71	0.89	93.29
Proposed method		**154.7**	**45.7**	**3.43**	**0.07**	**99.80**

to extract a maximum power of 154.4 W, in 26 iterations with a tracking time of 0.17 sec.With PSO, the steady-state oscillations were significantly reduced compared to incremental conductance, but there were increased oscillations during the tracking period. The power extracted by the Jaya algorithm was 154.4 W and took around 26 iterations with a tracking time of 0.18 sec and there were fewer oscillations. The proposed method was able to extract 154.7 W with a tracking time of 0.07 sec at global peak on the left side peak. In the proposed technique, the tracking time, and steady-state power oscillations were are fewer compared to other methods as observed in Figure. 3.9. There was almost no oscillatory behaviour while tracking MPP as compared to incremental conductance, PSO, and Jaya technique indicating the superior performance of the proposed Bayesian fusion technique. The relative waveforms of the voltage and current are shown in Figure. 3.9(b), (c), and analytic comparison is provided in Table 3.4.
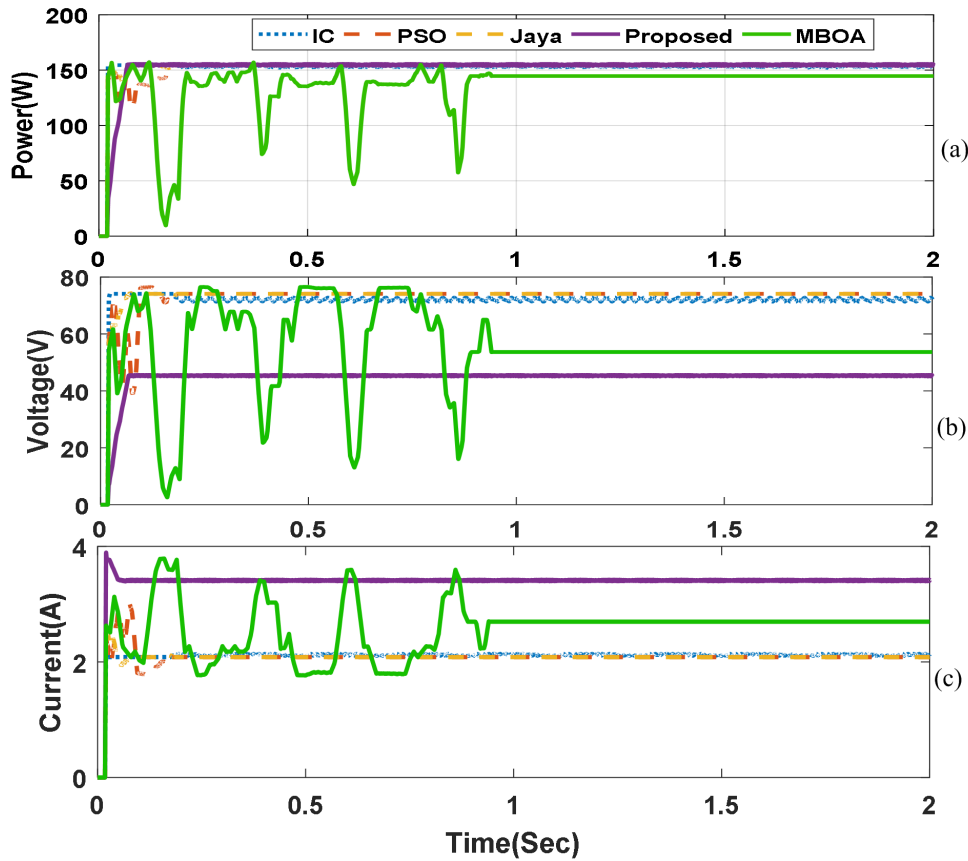
Figure 3.9: Simulation performance with GMPP at right side of the PV curve

3.6 Comparative study

The proposed method portrayed and improved tracking accuracy and speed to achieve GMPP under dynamic response; there were minimal oscillations with almost negligible steady-state

oscillation, and execution time was quicker compared to incremental conductance of [109], Jaya algorithm [26], and PSO [125] to achieve the global maximum power point tracking of the PV system. The problems in incremental conductance algorithm are step size, and instability when there is a change in irradiance due to PSC. But PSO and Jaya algorithms show more oscillations during the tracking period and PSO needs comparatively larger time and more iterations to reach GMPP. The proposed method compares with MBOA [28], as MBOA depends on one tunning parameter or one random number; whereas the proposed method does not require any tunning parameters and the random number, this makes the proposed algorithm more robust in implementation. Moreover, the average efficiency of the proposed method is almost near to that of MBOA, which is 99.45% and the response is fast to sudden load variations. When compared with ARMO [29], the proposed method has GMPP tracking capability, simple with high efficiency, more tracking speed, and less steady state oscillation with high reliability are shown in Table 3.5.
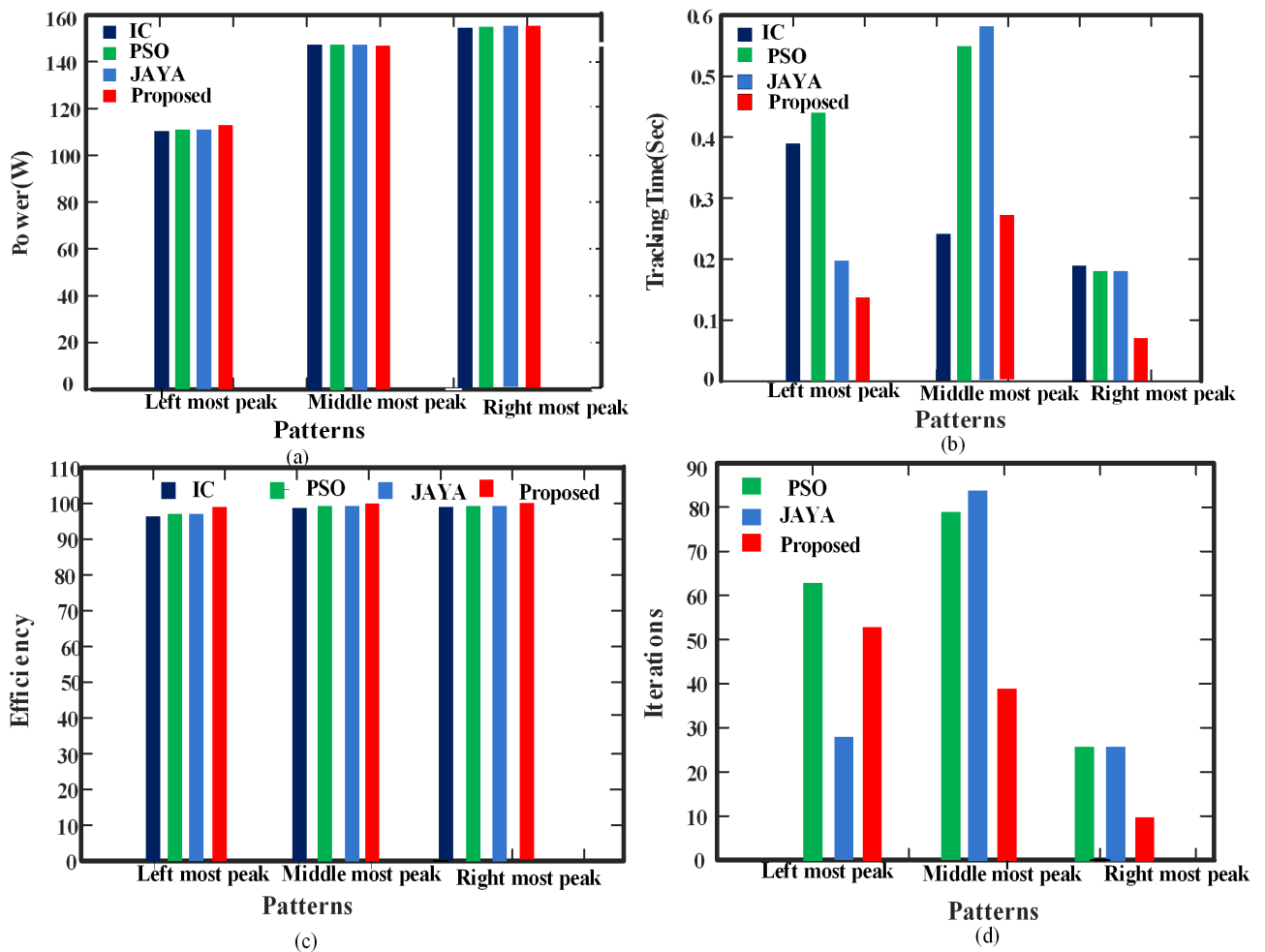
Figure 3.10: Comparative results of, (a).Power,(b).Tracking time, (c). Efficiency. (d). Iterations

The proposed BFT method is ideally suited to track the maximum power under PSC condi-

Table 3.5: Qualitative Presentation of the Proposed Bayesian Fusion with Existing GMPPT Algorithms

Type	IC [109]	PSO [20]	JAYA [121]	GWO [17]	MBOA [28]	ARMO [29]	Proposed
Number of tuning parameters	—	3	2	1	1	2	0
Number of random numbers	—-	2	2	2	1	1	0
Average MPPT Efficiency	99.55%	98.8 %	98.8%	98.75%	99.87%	99.85%	99.85%
Response to load variation	Slow	slow	slow	slow	fast	fast	Very fast
simplicity	simple	medium	medium	medium	medium	medium	simple
Tracking speed	High	medium	medium	medium	medium	simple	simple
Steady state fluctuation	Yes	No	No	No	No	No	No
GMPPT tracking capability	No	Yes	Yes	Yes	Yes	Yes	Yes

tions. The performance of the proposed algorithm in terms of simulation results of incremental conductance, PSO, and Jaya is explained clearly. Three patterns were reviewed for comparing the generation of current (I), voltage (V), and power (P) of all four algorithms on similar time measures, shown in Figures. 3.7,3.8, and 3.9. Efficiency, tracking time, tracking power, and iterations against many patterns of the peak of the PV array of the entire four algorithms have been shown in Figure. 3.10. In Incremental conductance, tracking speed is very slow and tracking accuracy may track local MPP, where efficiency is very low and oscillation is very high compared to the proposed Bayesian fusion algorithm. When compared to PSO and Jaya algorithm, the iterations and dynamic oscillation are more compared to the proposed system, comparison of the proposed method with the existing method shown in Table 3.4.The Qualitative Presentation of the Proposed Bayesian Fusion with existing GMPPT algorithm is shown in table.3.5.

3.7 Conclusions

In this chapter, a Bayesian fusion technique-based controller for solar PV systems was designed for improved global maximum power point tracking under partially shaded conditions. The proposed method is simple to implement,highly cost-effective, and could achieve quicker and highly effective tracking performance compared to PSO, Jaya, and incremental conductance-based tracking methods. BFT was established to assist the controller in overcoming the stagnancy at the local peak position under partially shaded conditions. BFT has the provision of reverse probability that models uncertainty based on available observations. To reach GMPP, the proposed technique depicts enhanced tracking time, reduces the number of iterations, and is more efficient compared to many existing state-of-the-art techniques. This research could be expanded to cover different aspects within renewable energy areas, such as using machine learning to make a quick distinction in temperature difference(s), enabling efficient control of different hybrid renewable energy sources like solar energy, wind energy, etc.

Chapter 4

A Computationally Efficient Jaya Optimization for Fuel Cell Maximum Power Tracking

4.1   Introduction

Global warming, gradual depletion of fossil fuels, and public awareness about carbon emissions have made researchers explore alternate solutions for energy production. The use of renewable energy resources(RESs), fuel cells(FC), biogas, and energy storage systems (ESSs) are some alternate sources for power generation [126]- [127]. The use of renewable resources like FC, biogas, and energy storage devices are some such alternate sources for power generation. Among all alternate sources, FC have numerous advantages because of their modular structure that provides improved reliability, flexibility, and scalability to the desired level of power generation [48]. Additionally, electrolyzers can be used to convert surplus electricity from RES towards hydrogen fuel generation, which can be stored and used to supply power from FC during power deficient conditions [48]. The entire operation of electrolyzers and FC are pollution-free and emit almost zero greenhouse gases, as they use hydrogen fuel and atmospheric oxygen as input and produce electricity and water as output through a chemical process. The FCs have been classified into various types, including direct methanol FC, solid oxide FC, molten carbonate FC, proton exchange membrane FC (PEMFC), alkaline FC, and phosphoric acid FC. Among these,PEMFC are highly popular due to their superior performance characteristics such as quick start-up, low weight, and optimum working temperature and can be used for electric vehicles (EV) and residential applications [128]- [129]. However the parameters for determining acceptable marginal pricing in different locations [130].

In FC, the output is sensitive to changes in operating temperature [131], membrane water content(MWC), hydrogen gas pressure, and oxygen pressures [132]. For a constant temperature, MWC, hydrogen gas pressure, and oxygen partial pressures, PEMFC show non-linear $V-I$ and $P-I$ characteristics with a global peak power point for varying current as shown in Figure.4.1(a). Hence, it is desirable to operate FC at maximum power point (MPP) to have improved FC efficiency. This chapter's primary emphasis is in the creation of a heuristic optimization technique to achieve fast-tracking of global MPP with reduced oscillations in a steady state.
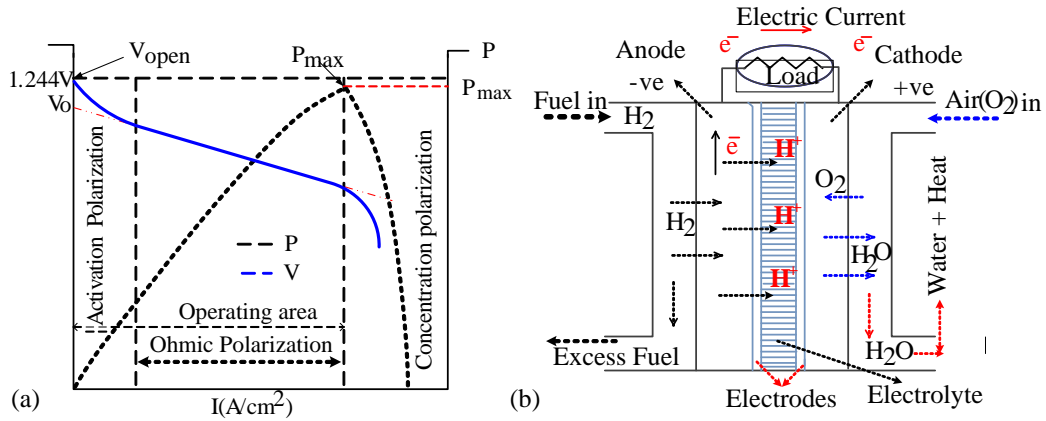
Figure 4.1: Fuel cell: (a) $P - I$ and $V - I$ characteristic, (b) functional diagram

In this work, Jaya algorithm-based MPPT tracking technique without a PID controller is developed to achieve the PEMFC's MPP. The proposed approach improves MPP tracking speed with minimal oscillations for a given hydrogen and oxygen pressure. The key contributions of this chapter are follows as:

- Development of Meta-heuristic Jaya-based MPPT technique for PEMFC presented.

- Designing Jaya algorithm for PEMFC MPPT without using any additional PID controller.

- Detailed comparisons with other methods to show the superiority of the proposed method.

- Hardware realization of the proposed approach considering various real-time disturbances and operating conditions.

4.2 PEMFC operation

In ideal conditions, the fuel cell has three different regions, *(i)*. active polarization, *(ii)*. Ohmic polarization, and *(iii)*. concentration polarization. A combination of three regions results in polarization curves and the curves have three different characteristics in $V - I$ curves as shown in Figure. 4.1 (a). The electrical energy is extracted from FC only if the current is absorbed by the loads which in turn results in a drop in FC voltage due to irreversible loss mechanisms. Ideally, the Ohmic polarization curve region exhibits inverse slope characteristics in which the FC is operated. The extension of the Ohmic polarization line towards zero current gives open-circuit voltage V_o. From the Ohmic polarization region, it is clear that power increases with an increase in current and reaches a peak and then the operation reaches the concentration region in which power decreases with increased current (as in Figure. 4.1).

Further, the $V - I$ and $P - I$ curves are sensitive to FC parameters such as temperature (T),

66
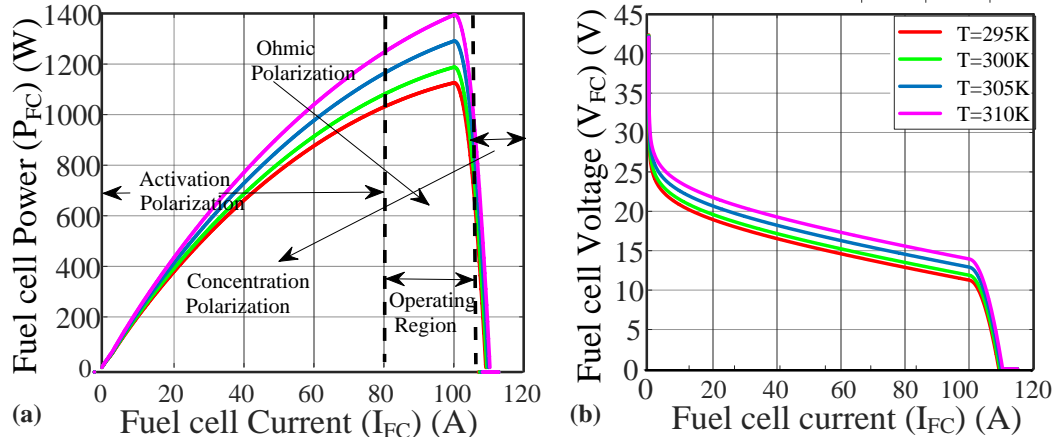
Figure 4.2: $P-I$ and $V-I$ curves at various fuel cell temperatures

membrane water content(WMC) (λ_m), hydrogen partial pressure (Ph_2), and oxygen pressure (PO_2). Figure.4.2 portrays, FC $P-I$ and $V-I$ curves for (T) is varying keeping λ_m, Ph_2 and PO_2 are constant. Similarly, the FC characteristics under varying MWC (λ_m), hydrogen gas pressure (Ph_2) with other parameters being constant are shown in Figure.4.3, and Figure. 4.4, respectively. All the curves show that the FC output power is a nonlinear function of current and the curves are highly affected by cell temperature, membrane water content(MWC), hydrogen gas pressure,and Oxygen pressure. A fast and accurate MPPT technique is required to regulate FC current so that maximum possible power can be extracted for any FC parameter variation. Thus, in this chapter, a Jaya-optimization-based MPPT control is developed, to ensure MPP operation in the Ohmic region.
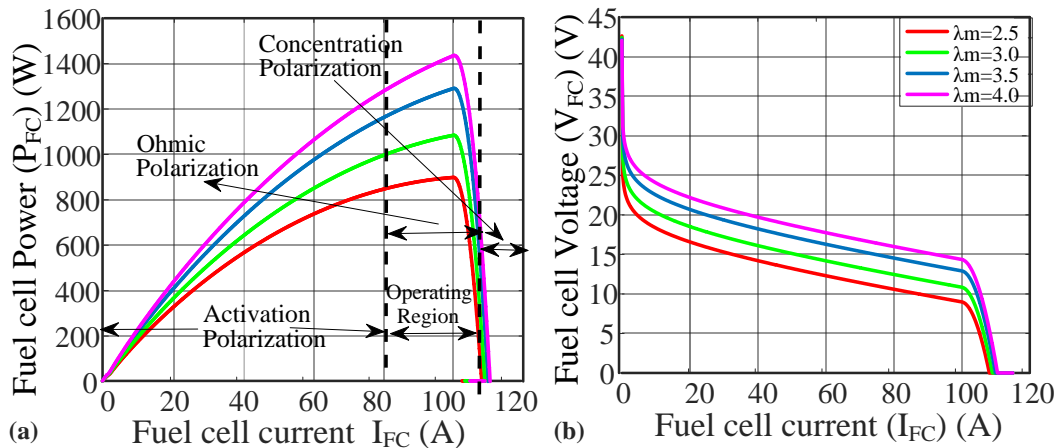
Figure 4.3: Variation in fuel cell water content affecting $P-I$ and $V-I$ curves.

4.2.1 Constructing a DC-DC converter

The fuel cells are usually connected to the DC bus through a DC/DC boost converter to ensure regulated output voltage, irrespective of load demand. The step-up interleaved converter [133]
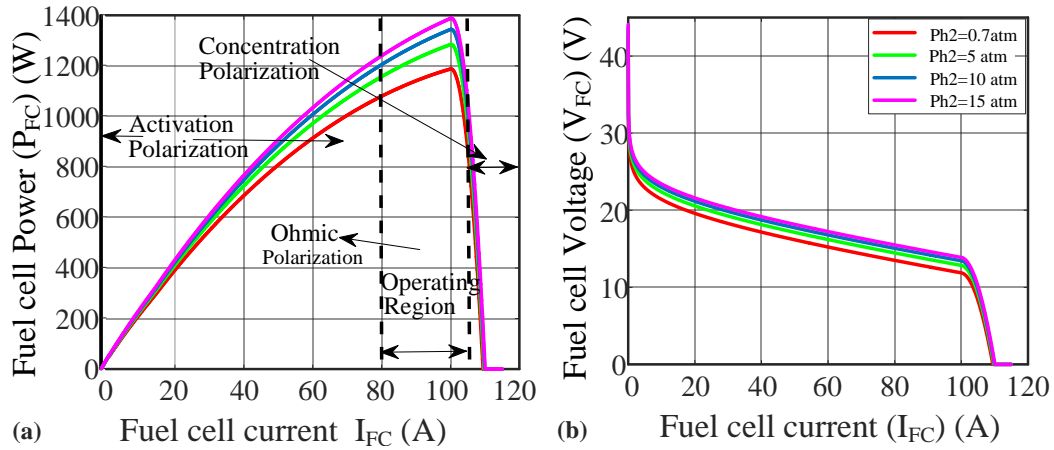
Figure 4.4: $P - I$ and $V - I$ curves of a fuel cell at various hydrogen gas pressures
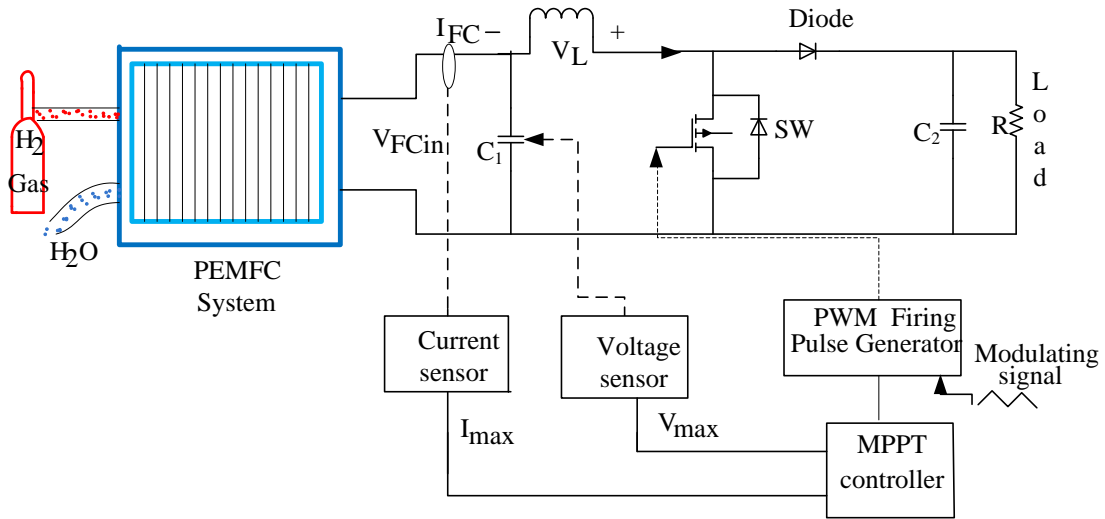
Figure 4.5: Block diagram of the proposed system setup

is also designed to ensure FC operation in the linear domain of $V - I$ characteristics as there is a possibility of damage to the electrolyte membrane when operated in the non-linear region of $V - I$ characteristics. Figure.4.5 portrays the closed-loop DC/DC converter [134]. The parameters of the power converter are tabulated in 4.1. The duty of the converter is controlled using the maximum power tracking controller. The output voltage for varying duty (d) is given by equation (4.1):

$$\frac{V_o}{V_{FC}} = \frac{1}{1-d} \tag{4.1}$$

Where V_{FC}, V_o, are the input, and output voltages, d is the Duty ratio.

Table 4.1: Parameters of the proposed method and boost converter

Particulars	Specifications
PSO	$C_1 min = C_2 min = 1$; $C_1 max = C_2 max = 2$ $W_{min} = 0.1$, $W_{max} = 1$
Boost Converter	$L = 0.4mH$, $C_{in} = C_{out} = 100 \mu F$, $F_s = 10kHz$, Variable Rheostat load:100Ω $10A$
Sampling Period	For Simulation $T_s = 10ms$, For Experimental $T_s = 200ms$

4.3   MPPT algorithm

As explained before, the MPP of the FC changes within FC variables such as T, Ph_2, PO_2, and λ_m. By using MPPT methods, one can find optimal current and voltage operating point that can be obtained so that it has maximum output power with high efficiency for a given system. In this chapter, a Jaya-based MPPT has been developed for an FC system with such a boost converter coupled to the resistive load as shown in Figure.4.5.

4.3.1   MPPT through proposed Jaya algorithm

Jaya method is a recently developed meta-heuristic technique for addressing restricted complicated non-convex optimization problems [135]. This method is different compared to other heuristic techniques as it takes only two popular parameters, namely, "number of iterations" and "population size" as inputs, and the parametric values can be easily initialized for any optimization problem making the utilization of Jaya algorithm simple and convenient.

The power output P_{FC} is considered as the objective function in the MPPT tracking of the FC. Initially, a random population set $D = \{d_1, d_2, ...d_n\}$ of size $'n'$ corresponding to duty cycle is generated. For a set of duty cycles D, the power output P_{FC} is obtained from the FC measurements. Two intermediate variables, d_{best} and d_{worst} are defined to which the best and worst function valued candidates are assigned, respectively [27], [136]. In each iteration, the population set is updated using the best and worst candidates. In Jaya algorithm, shown in Figure.4.6

, the update rule of an ith candidate in a kth iteration is given as:

$$d_i^{k+1} = d_i^k + r_1(d_{best} - d_i^k) - r_2(d_{worst} - d_i^k) \tag{4.2}$$

$$d_{i+1}^k = \begin{cases} d_i^{k+1}, & \text{if } f(d_i^{k+1}) > f(d_i^k) \\ d_i^k, & \text{if } f(d_i^{k+1}) \le f(d_i^k) \end{cases} \tag{4.3}$$

where d_i^k and d_i^{k+1} represent the actual and upgraded values, d_{best} and d_{worst} represent the best and worst responses across all the candidates, r_1 and r_2 are random numbers between $U[0, 1]$ the expression $r_1 (d_{best} - d_i^k)$ refers to the solution that is closer to the best, while $r_2 (d_{worst} - d_i^k)$ refers to the worst solution to be avoided. The termination process is met, if the maximum proportion of iterations is achieved or the difference between $|d_{best}\text{-}d_{worst}| < \varepsilon$.shown in algorithm 1.

Algorithm 1 Jaya optimization based MPPT tracking

1: **while** iter_count<iter_max **do**
2:     **initialize** n, random set $D= \{d_1, d_2, ..., d_n\}$, iter_max, iter_count
3:     **obtain** $P_{FC} = \{P_{FC}(d_i) \; \forall i = 1, 2, ..., n\}$
4:     **assign** $d_{best} = \{d \ni P_{FC}(d) = \max(P_{FC})\}$ and $d_{worst} = \{d \ni P_{FC}(d) = \min(P_{FC})\}$
5:     Update D using (4.2) and (4.3)
6:     iter_count=iter_count+1
7:     **return**(d_{best})
8: **end while**

4.4   Simulation results

The proposed method implemented for the fuel cell system designed in MATLAB/Simulink domain. The FC System includes 35 FC linked in series, a DC/DC converter, resistive load, and a maximum power tracker. To evaluate the tracking performance and steady-state behavior of the FC system using the proposed Jaya algorithm MPPT method, it is compared with traditional P&O technique and meta-heuristic-based PSO MPPT techniques by performing various case studies under different operating conditions and perturbations as given below.

Case-(i): MPPT Tracking for constant fuel cell parameter with $(T = 300K)$, $(\lambda_m = 3)$, $(Po_2 = 0.8atm)$,and $(Ph_2 = 0.7atm)$ being constant.

Case-(ii): Change in membrane water content (λ_m).

Case-(iii): Variation in fuel cell temperature (T).

Case-(iv): Variation in hydrogen gas Partial pressure (Ph_2), and oxygen partial pressure (Po_2).
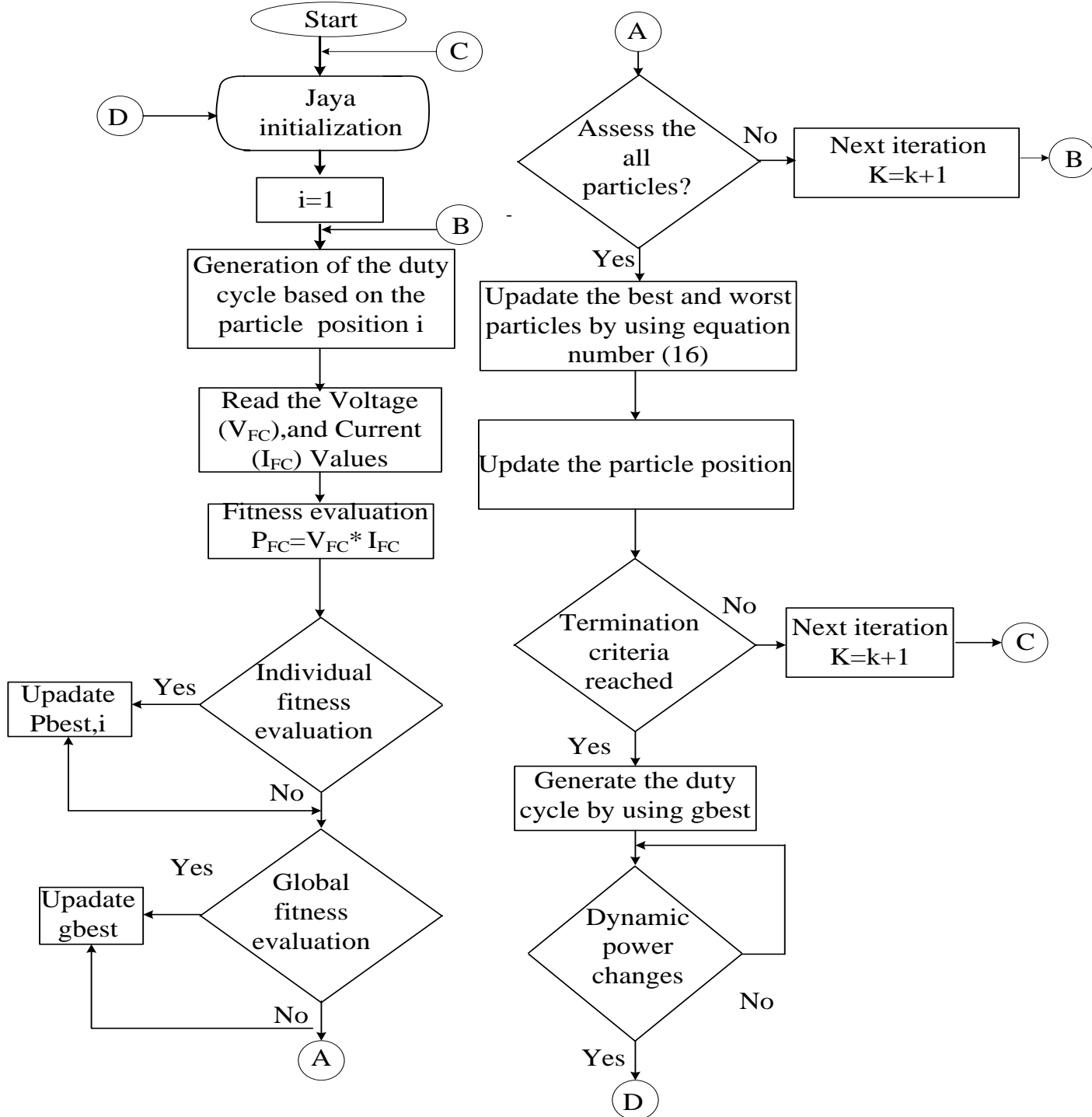
Figure 4.6: Jaya Optimization algorithm for Fuel cell

71

Case-(v): Variation in fuel cell temperature (T), membrane water content (λ_m), and hydrogen gas partial pressure (Ph_2) at the same time .

4.4.1   Case-(i): MPPT tracking for constant fuel cell parameter with $(T = 300K)$, $(\lambda_m = 3)$, $Ph_2 = 0.7atm$, $Po_2 = 0.8atm$ being constant.

In this study, fuel cell temperature $T = 300K$, MWC $\lambda_m = 3$, hydrogen gas pressure $(Ph_2 = 0.7atm)$, and oxygen partial pressure $(Po_2 = 0.8atm)$ were taken and held constant. The respective $P - I$, and $V - I$ behaviour of the FC system are shown in Figure.4.7 for the system parameters; MPPT tracking was using the done proposed Jaya algorithm, PSO, and P&O techniques as shown in Figure.4.8. From the Figure, it is noticed that P&O algorithm took a considerable amount of time to track MPP, and persistent oscillations were recorded using this algorithm due to three-step variation around the peak point.
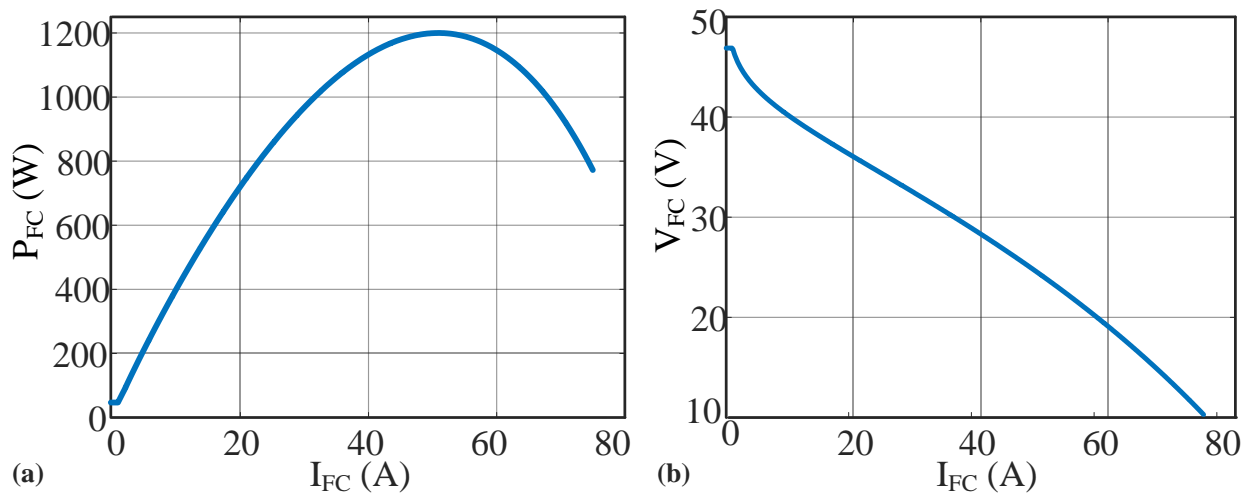
Figure 4.7: Fuel cell characteristics at $T = 300K$, $\lambda_m = 3$, $Ph_2 = 0.7atm$, $Po_2 = 0.8atm$ (a) $P - I$ curve and (b)$V - I$ curve

Although the MPPT using PSO shows a better steady-state behavior unlike P&O, the transient behavior during the MPP tracking the system behavior is oscillatory, as shown in Figure.4.8 However, the proposed Jaya algorithm-based MPPT shows better transient and steady-state behavior compared to other two methods. A detailed comparative evaluation is given in Table 4.2.

4.4.2   Case-(ii): Change in the membrane water content. (λ_m)

In this case, fuel cell parameters such as hydrogen gas pressure $(Ph_2 = 0.7atm)$, oxygen pressure $(Po_2 = 0.8atm)$, and temperature $(T = 300K)$ are kept constant at the given values, where
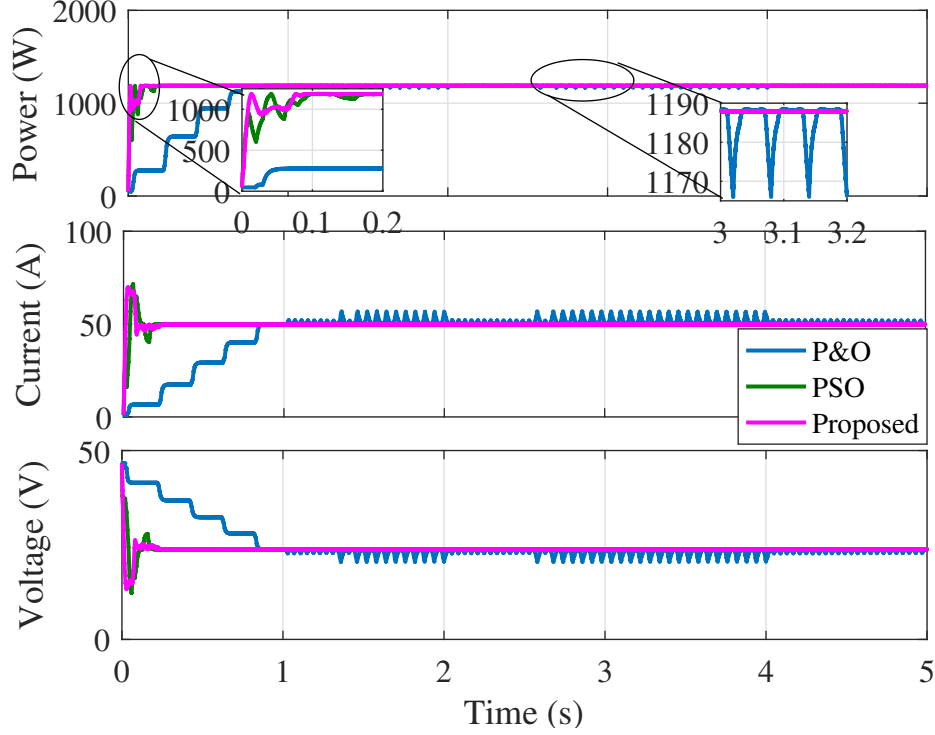
Figure 4.8: MPPT tracking of power, current, and voltage in normal operating conditions for the proposed technique, PSO, and P&O techniques

there is variation in MWC. The variation in (λ_m) as a function of time is shown in Figure.4.9,(a) in which WMC is $\lambda_m = 2.5$, and at $t = 1.5s$, the MWC of the cell is assumed to be 3.5 held at that value till $t = 3s$, after which the MWC attains a value of 2.5, and then is held constant for the rest of the simulation time.Figure.4.9 (b) portrays the Jaya algorithm-based MPP tracking process on an FC $P - I$ curve when the MWC is varied. Initially, when the MWC is at $\lambda_m = 2.5$, the FC is operating at MPP point P; later when the MWC is suddenly changed from 2.5 to 3.5, the operating point shifts from P to Q; however, as Q is not an MPP, Jaya algorithm moves the operating point from Q to R making it operate at MPP when MWC is brought back to $\lambda_m = 2.5$.The operating point shifts to a new point R from S and as S is not an MPP, Jaya algorithm tracks the MPP point and shifts operation back to point P as shown in Figure 4.9.(b) Accordingly, the time response of the output power, current, and voltage using Jaya algorithm, PSO, and P&O MPPT techniques are displayed in Figure.4.10. From the Figure,it can be observed that the proposed method has better time response, as well as tracking time as given in Table 4.2

4.4.3 Case-(iii): Variation in fuel cell temperature. (T)

In this case, fuel cell parameters such as hydrogen gas pressure $(Ph_2 = 0.7atm)$, oxygen partial pressure $(Po_2 = 0.8atm)$, and MWC $(\lambda_m = 3)$ are kept constant at the given values while there
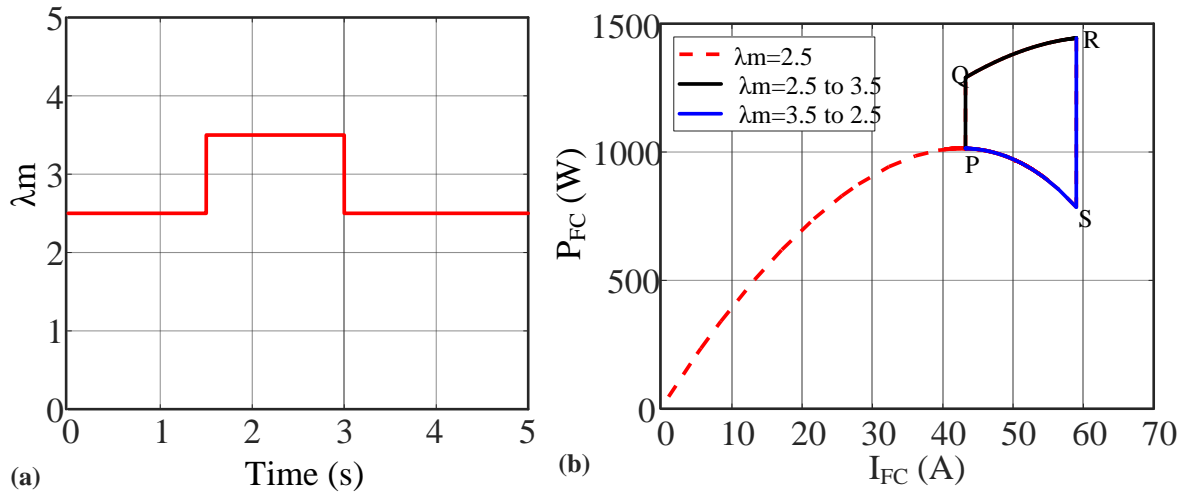
Figure 4.9: Tracking the $P - I$ characteristics of a fuel cell as water content changes (a) water content variation (b) tracing the $P - I$ curve as the water content varies.
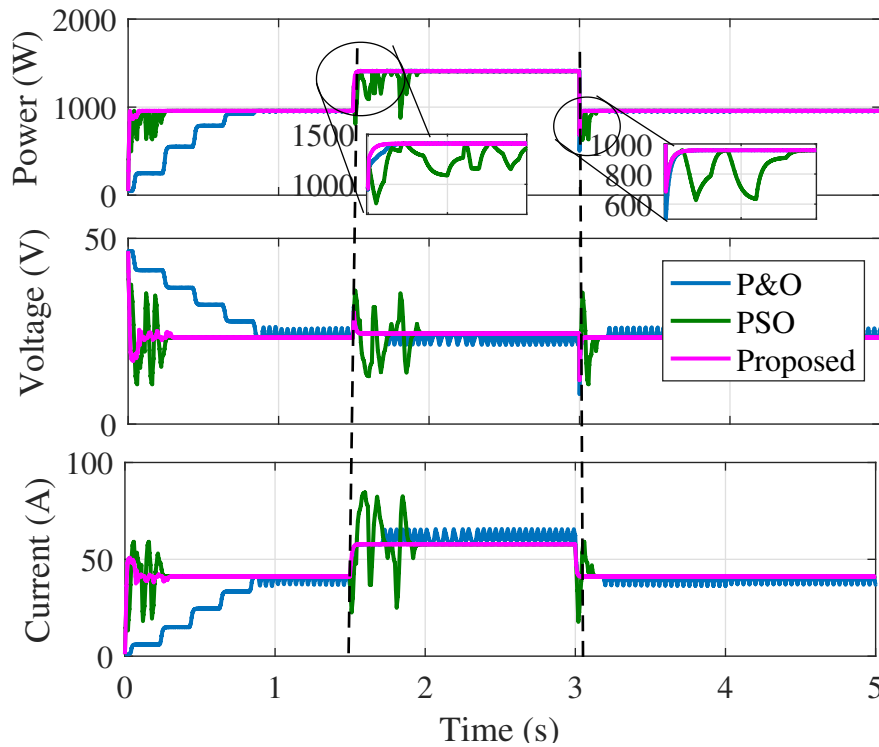
Figure 4.10: MPPT power, voltage, and current tracking for the proposed, PSO, and P&O systems with significant water content deviation
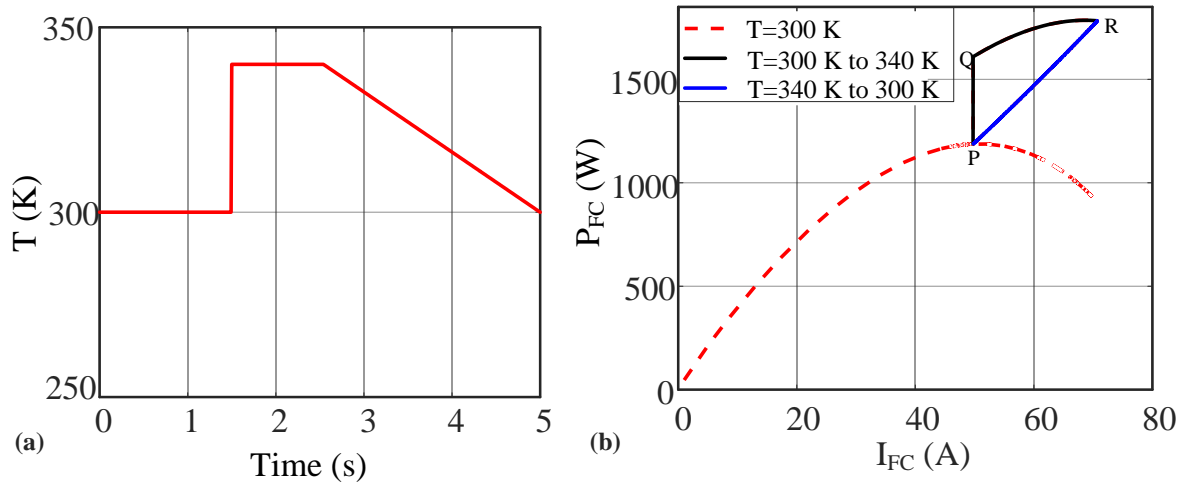
Figure 4.11: Tracking $P-I$ characteristic of a fuel cell as temperature varies: (a) temperature variation, (b)tracing the $P-I$ curve as temperature changes.
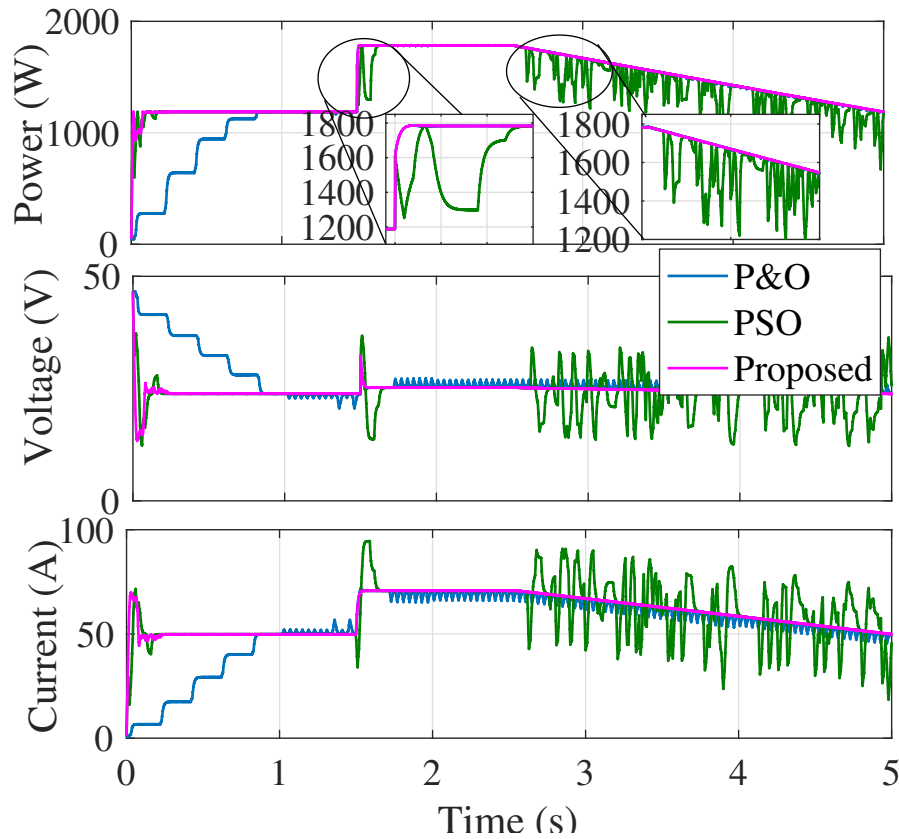
Figure 4.12: MPPT tracking of power, voltage, and current under sluggish cell temperature variation for the proposed technique, PSO, and P&O techniques

is variation in FC temperature. The variation in (T) with time is shown in Fig.4.11.(a) in which, the initial temperature is considered as $T = 300K$, and at $t = 1.5s$, the temperature of the cell is increased to $340K$ and maintained at that value till $t = 2.5s$, after which the temperature is ramped down with a slope up to $t = 5s$ till the temperature reaches $300K$, and remains so for the rest of the simulation time. Figure.4.11.(b) portrays the Jaya algorithm-based MPP tracking process on an FC $P - I$ curve when the temperature is varied. Initially, when the temperature changes from $T = 300K$ to 340, the new MPP operating point changes from P to R using Jaya algorithm, shown in Figure.4.11. (b) Accordingly, the time response of the output power, current, and voltage using Jaya algorithm, PSO, and P&O MPPT techniques is displayed in Figure.4.12. From the Figure it can be observed that the data matches what is shown in Table 4.2.

4.4.4   Case-(iv): Variation in hydrogen gas partial pressure (Ph_2), and oxygen partial pressure (Po_2).
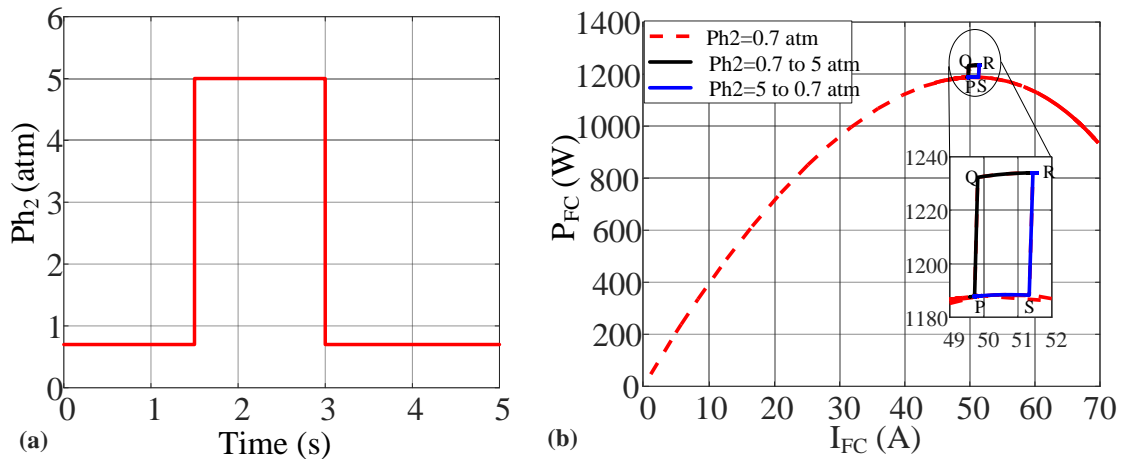
Figure 4.13: Fuel cell $P - I$ characteristic tracing change in hydrogen pressure: (a) hydrogen pressure variation, (b) tracing the $P - I$ curve as hydrogen levels vary pressure

This case deals with two different cases, case-(i) where hydrogen gas pressure (Ph_2), is constant; in this case, FC parameters such as, $Po_2 = 0.8atm$, $\lambda_m = 3$, and $T = 300K$ are kept constant at given values expect hydrogen gas pressure of FC (Ph_2), and, in case-(ii), oxygen partial pressure Po_2 is kept constant; $Ph_2 = 0.7atm$, $\lambda_m = 3$, and $T = 300K$ are held constant at the given values expect oxygen pressure Po_2 of FC. The variation in FC (Ph_2), with respect to time, is shown in Figure4.13(a) in which,initial hydrogen gas is considered as $Ph_2 = 0.7atm$, and at $t = 1.5s$, the pressure of hydrogen gas of the cell is increased to $5atm$ and held at that value till $t = 3s$; for case-4 (Po_2) the initial pressure of oxygen gas is taken to be $Po_2 = 0.8atm$, and at $t = 1.5s$, the oxygen gas of the cell is increased to $5atm$ and held at that value till $t = 3s$.
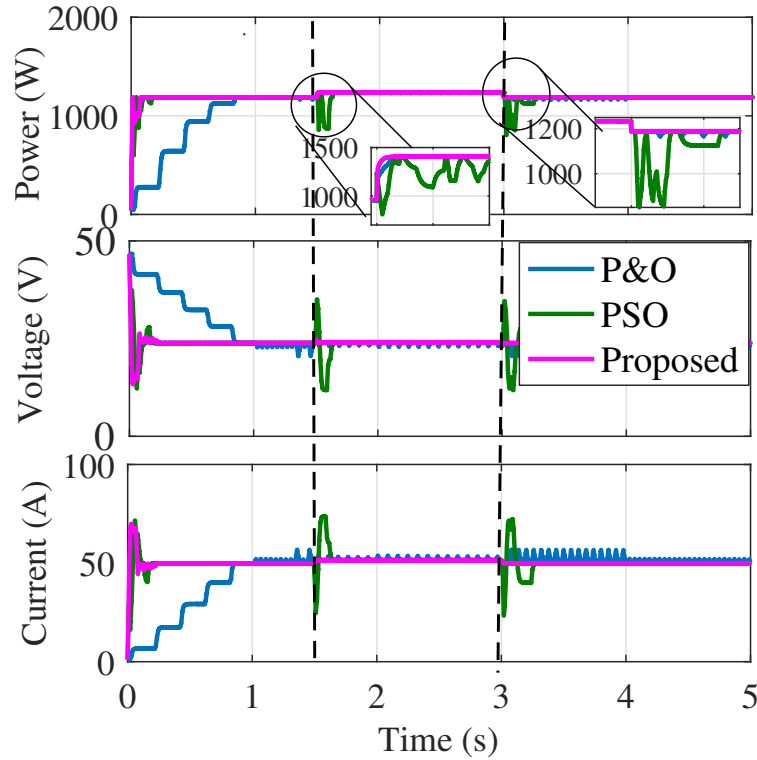
Figure 4.14: MPPT tracking of power, voltage, and current under quick deviations in hydrogen gas partial pressure for the proposed technique, PSO, and P&O techniques

The MPPs for partial pressure of hydrogen gas were determined by Jaya algorithm which tracks the MPP point and shift operation as shown in Figure.4.13(b). The workings of the proposed Jaya algorithm, PSO, and P&O MPPT techniques are displayed in Figure.4.14, when oxygen partial pressure changes as shown in Figure.4.14,in Table 4.2.

4.4.5   Case-(v): Variation of fuel cell temperature (T), membrane water content (λ_m), and hydrogen gas partial pressure (Ph_2) at the same time

In this case, the parameter Ph_2, λ_m, and T are changed during the period 1.5s to 3s as shown in Figure.4.13(a). The temperature is changed from 300K to 340K, while the variation in Ph_2 and λ_m, are considered similar to earlier case studies. The sudden changes in the given parameters impact FC MPP; consequently the time response of the output power, current, and voltage using the proposed Jaya algorithm, PSO, and P&O MPPT techniques are displayed in Figure.4.15. The P&O shows transient behavior during MPP tracking, while the system behavior is oscillatory, as shown in Figure 4.15. A detailed comparative evaluation is given in Table 4.2.

77
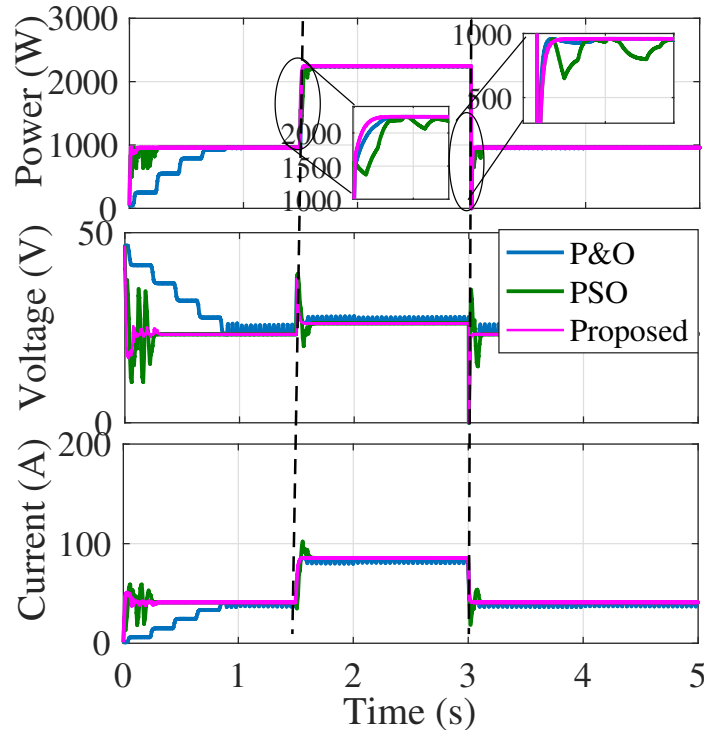
Figure 4.15: MPPT tracking of power, voltage and current under fast change of fuel cell temperature, water content, hydrogen gas partial pressure,and oxygen partial pressure for proposed, PSO, and P&O Techniques

4.5 Experimental results and analysis

The hardware prototype was developed using a fuel cell simulator linked to a power converter that provides a resistive load. The MPPT algorithm along with the converter control was realized through rapid prototype controller dSPACE ($DS1104$) which was interfaced through MATLAB/SIMULINK. The dSPACE reads the system information through analog inputs taken from the current sensor ($LA55-p$), and voltage sensor($LV25-p$), which are connected at system measuring points. This was done through a FC simulator (Magna power simulator ($XR600-9.9/415+PPPE+HS$). The complete hardware prototype model is shown in Figure.4.16 whose system electrical parameters are similar to simulation parameters given in Table 6.2. The FC simulator was loaded with a few predefined $P-I$ characteristics which were used in all case studies. To assess the efficiency of the proposed MPPT tracking scheme for FC, two different scenarios were implemented in hardware as given below:

Scenario-(i) MPPT Tracking for Constant Fuel cell Parameter ($T=300K$, $Ph_2=0.81atm$, $Po_2=0.85atm$)

Scenario-(ii) Dynamics in Fast deviation of fuel cell temperature from ($T=340K$ to $300K$), hydrogen gas partial pressure ($Ph_2=0.7atm$), and oxygen partial pressure ($Po_2=0.8atm$), are kept constant.

78

Table 4.2: Comparison of simulation control approaches with output power, tracking time, and number of iterations of the fuel cell under different conditions

Cases	Control methods	Rated Power, W	MPP power, W	MPP voltage, V	MPP current, A	Tracking time (s)	Number of iteration	Efficiency (%)
Case-1	Without MPPT	MPP= 1.2kW	980	25.01	39.22	—	—	81.6
	P&O		1113.42	23.1	48.2	0.8	–	92.78
	PSO		1125.2	23.2	48.5	0.18	6	93.76
	Proposed		**1189.7**	**23.8**	**49.99**	**0.12**	**4**	**99.14**
Case-2	Without MPPT	MPP= 1.42kW	1222.21	27.1	45.1	—	—	86.07
	P&O		1370.4	24	57.1	0.8	–	96.5
	PSO		1376.11	24.1	57.1	0.445	15	96.9
	Proposed		**1411.02**	**24.37**	**57.9**	**0.04**	**2**	**99.36**
Case-3	Without MPPT	MPP= 1.8kW	1604.5	28.1	57.1	—	—	89.13
	P&O		1665.31	24.1	69.1	0.75	–	92.51
	PSO		1743.84	25.2	69.2	0.14	5	96.88
	Proposed		**1785.6**	**25.3**	**70.58**	**0.04**	**2**	**99.2**
Case-4 (Ph2 changes)	Without MPPT	MPP= 1.24kW	1134	27.01	42.01	—	—	91.45
	P&O		1141.93	23.3	49.01	0.81	–	92.09
	PSO		1189.44	23.6	50.4	0.14	5	95.92
	Proposed		**1233.94**	**23.96**	**51.5**	**0.045**	**2**	**99.51**
Case-4 (PO2 changes)	Without MPPT	MPP= 1.22kW	1101.65	27.5	40.06	—	—	90.29
	P&O		1127.98	23.02	49	0.82	–	92.45
	PSO		1139.04	22.6	50.4	0.13	5	93.36
	Proposed		**1211.73**	**23.9**	**50.7**	**0.04**	**2**	**99.32**
Case-6 (All variations)	Without MPPT	MPP= 2.26kW	1822.4	27.2	67	—	—	80.63
	P&O		2100	26.25	80	0.81	–	92.92
	PSO		2192.4	26.1	84	0.12	4	97
	Proposed		**2259**	**26.15**	**86.4**	**0.04**	**2**	**99.95**

4.5.1   Case-(i): MPPT tracking for constant fuel cell parameter

$(T = 300K, Ph_2 = 0.81atm, Po_2 = 0.85atm)$

In this case, fuel cell $T = 300K$, $Ph_2 = 0.81atm$, and $Po_2 = 0.85atm$ are considered under
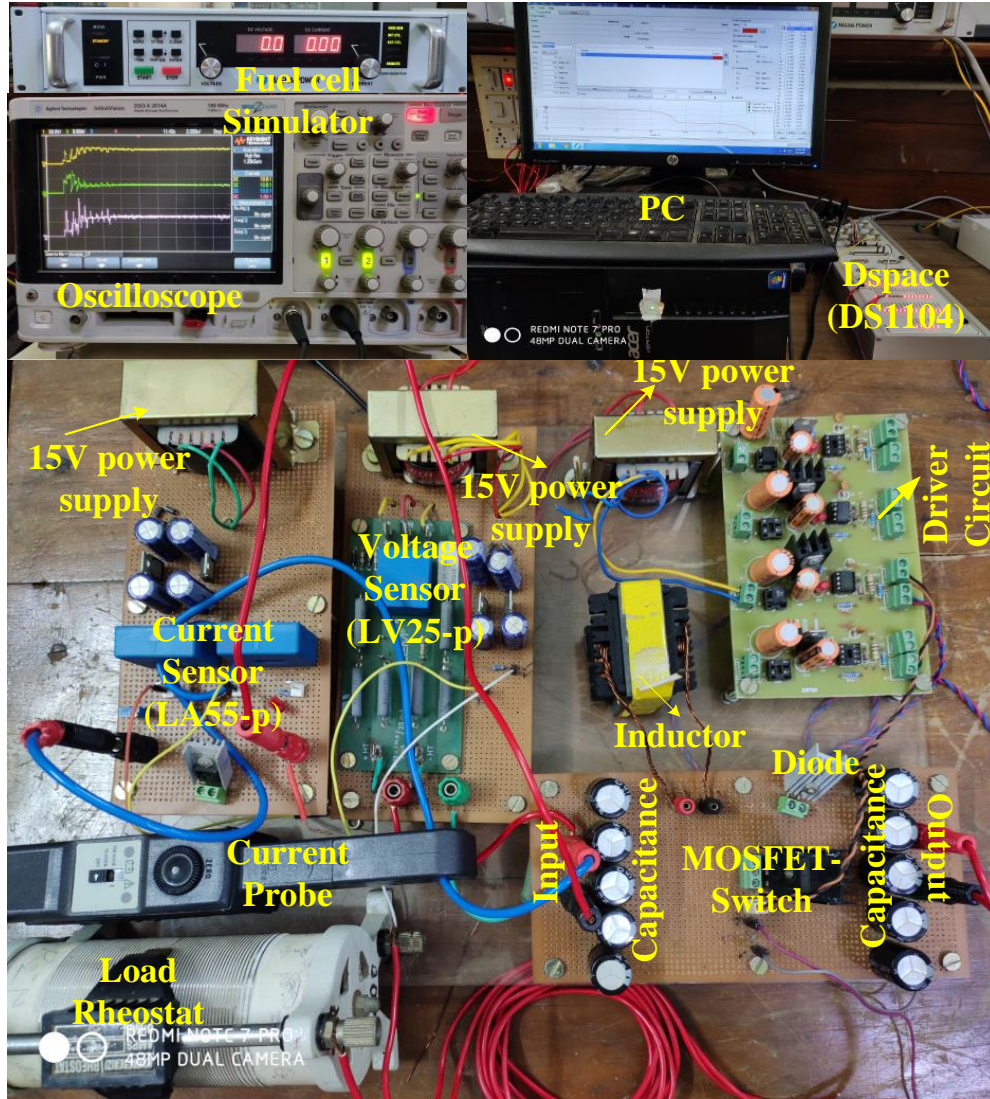
Figure 4.16: Experimental structure of the established fuel cell system.

normal operating conditions. For the FC parameters, it can be observed that the MPP of the FC curve with maximum power is 98.4W. The time response of such fuel cell tracking output using P&O, PSO, and the proposed approach even as it approached maximum point is illustrated in Figure.4.17.The P&O algorithm has fluctuating power and can monitor a maximum power of 79.9W with a tracking duration of 6s in steady state condition, as shown in Figure.4.17. The PSO-based MPPT technique is capable of extracting a maximum power of 83.3W within 4 iterations with such a tracking period of 4s, with significantly decreased steady-state oscillations than P&O but significantly higher transient oscillations when tracking the MPP, as shown in Figure.4.17.The proposed approach is the ability to extract maximum output power of 85.85W, which is slightly higher than PSO, and track MPP within 3 iterations with a tracking time of 1.75s, as shown in Figure.4.17.An analytic comparison of all three MPPT methods for this scenario is provided in Table 4.3.
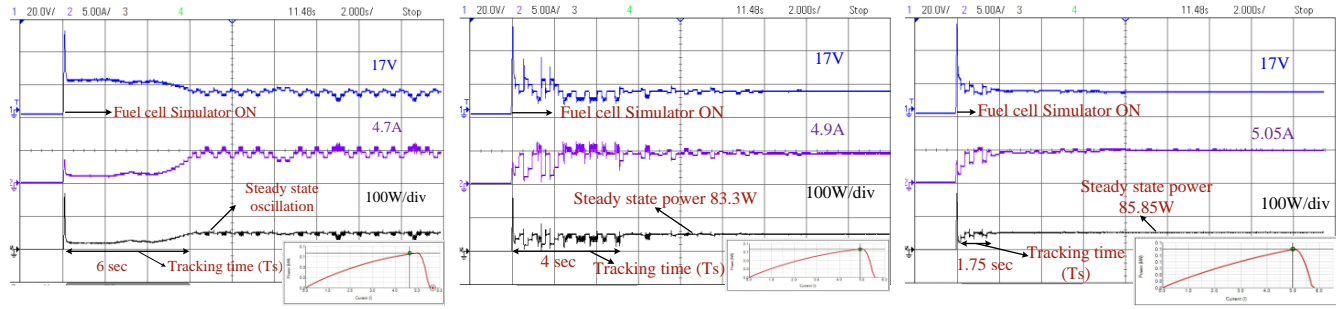
Figure 4.17: Experimental results under normal operating conditions

4.5.2 Case-(ii): Dynamics in fast deviation of fuel cell temperature ($T = 340K$ **to** $300K$)
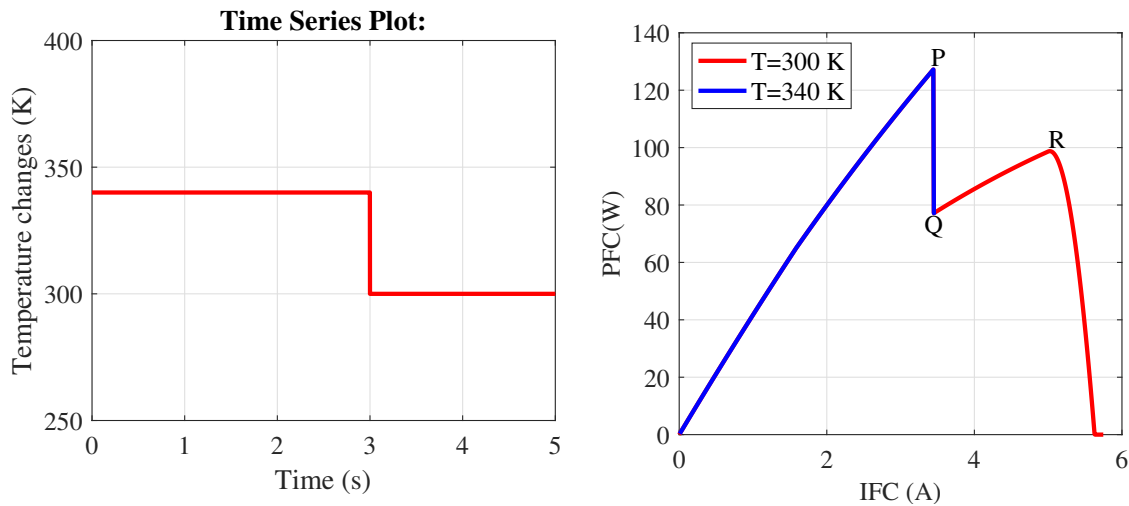
Figure 4.18: Experimental fuel cell characteristics as a function of temperature (a) temperature variation (b) $P - I$ curve

In this case, we applied sudden deviation of FC temperature for verification of the proposed Jaya algorithm on the FC system.Figure.4.18(a) shows the temperature of FC. The change in temperature proceeded from point P. The sudden temperature change ($T = 340K$ to $T = 300K$) at the operating point changes from P to Q and as Q is not an MPP, Jaya algorithm tracks the MPP point and shifts operation point to R at maximum power of ($127W$, and $98.4W$) as shown in Figure.4.18 (b). For change of temperature condition, to track the maximum power, P&O, PSO, and the proposed Jaya algorithm techniques were applied continuously to track the maximum powers using these methods, with initial tracking times shown ($112.5W, 116.84W$, and $117.5W$); the tracking times are ($0.9s, 4s$, and $3.5s$). When there are changes dramatically in the FC temperature, the algorithm re-initializes the parameters and updates the new power

81

Table 4.3: Comparison of three control approaches utilizing experimental data of output power, tracking time, and number of iterations of the fuel cell under different conditions.

Cases	Control Methods	Rated Power, W	Maximum Tracking Power W	Tracking Time,s	Number of iterations	Efficiency (%)
Case-1	P&O		79.9	6	—	81.19
Normal	PSO	98.4	83.3	4	4	84.65
condition	**Proposed**		**85.85**	**1.75**	**3**	**87.24**
Case-2	P&O		112.5	0.9	—	88.58
Fast deviation	PSO	127	116.84	4	7	92
of Temperature	**Proposed**		**117.5**	**3.5**	**5**	**92.51**
$(T = 340K)$						
Case-2	P&O		84	0.9	—	85.36
Fast deviation	PSO	98.4	84	3.5	6	85.36
of Temperature	**Proposed**		**85.6**	**2**	**3**	**86.99**
$(T = 300K)$						

based FC $(84W, 84W,$ and $85.6W)$ with a tracking time of $(0.9s, 3.5s,$ and $2s)$ Accordingly, the time response of power output, current, and voltage using the proposed Jaya algorithm, PSO, and P& O MPPT techniques are displayed in Figure.4.19. it is evident from the data that the proposed Jaya algorithm is superior to other algorithms.The comparative charts for the above two cases in terms of power, tracking time, iterations and efficiency are shown in Figure 4.20. The proposed Jaya algorithm is compared to standard MPPT algorithms in the literature, shown in Table.4.3. By comparing the present results to previous results, as shown in the table, 4.4,

Table 4.4: Comparison of the proposed Jaya algorithm with existing MPPT algorithms

Variables \Technique	P&O-INCO [137]	Fuzzy-PSO [49]	ANFIS [54]	GWO -PID [54]	Proposed Jaya method
Tracking level	Fast	Moderate	Low	Moderate	Fast
Iterations	Nil	>5	5	3	<3
Tuning Parameters	Nil	5	3	2	1
Initial particulars	Dependent	Independent	Independent	Dependent	Independent
Efficiency	Moderate	High	High	High	very high

82
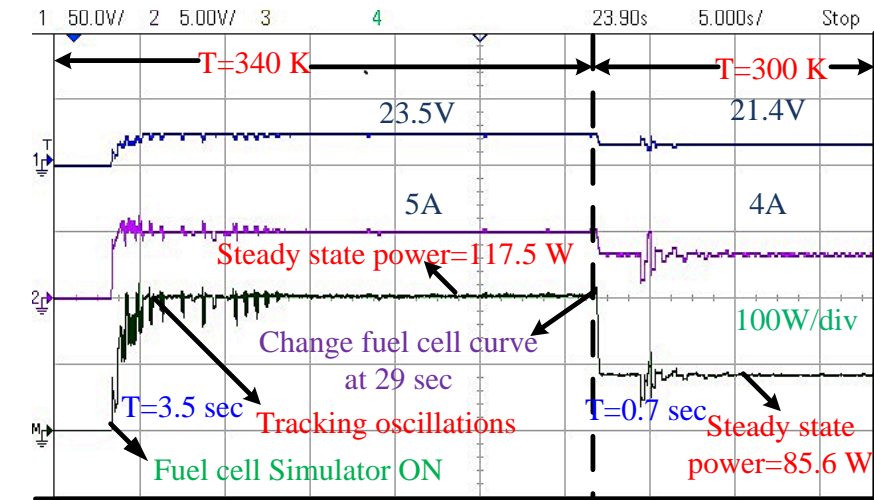
(a)
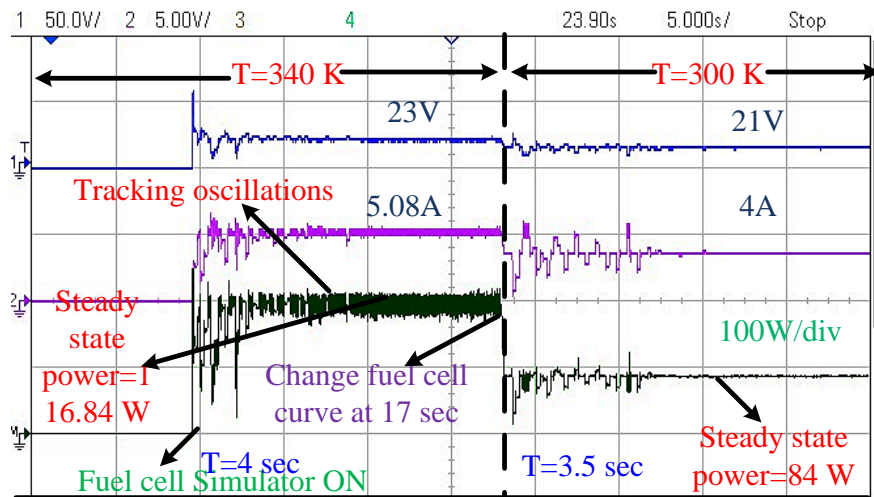
(b)
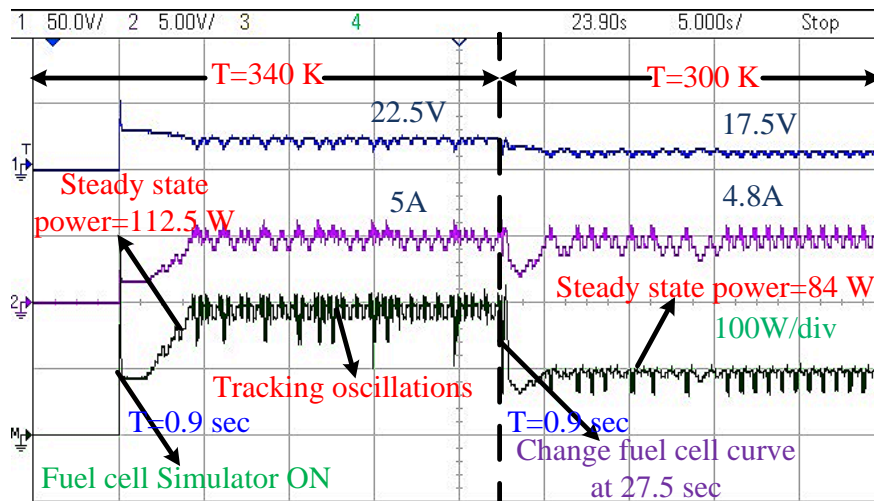
(c)

Figure 4.19: Experimental results with a fast variance of fuel cell temperature (a) P&O (b) PSO (c) Proposed
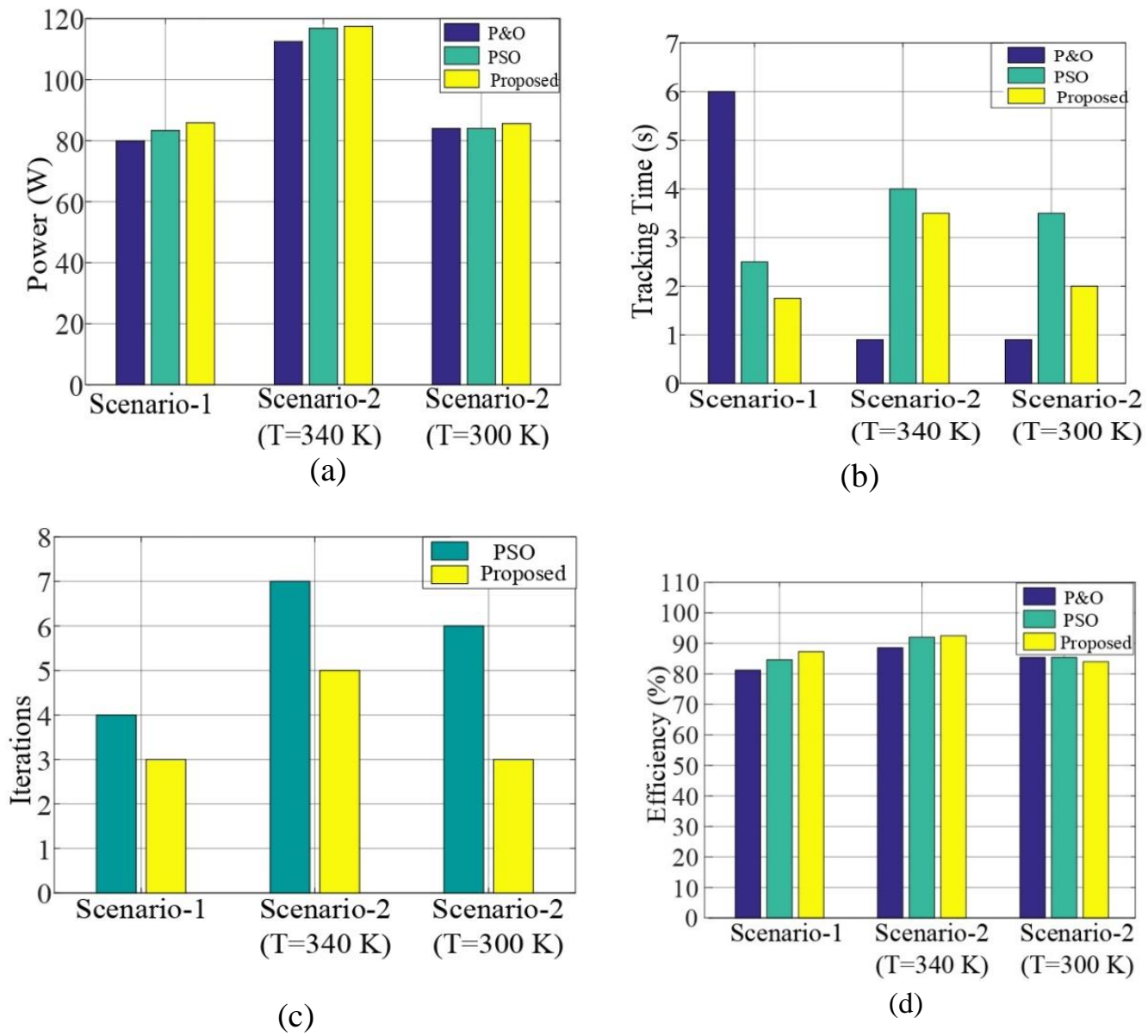
Figure 4.20: Comparative studies for: (a) power, (b) tracking time, (c) iterations, (d) efficiency

4.6   Conclusions

The Jaya algorithm-based MPPT controller of PEMFC was detailed in this chapter in the context of enchancing output power and efficiency under varying operating scenarios. When compared to certain contemporary MPPT approaches, the proposed (Jaya algorithm) technique has a greater degree of flexibility. In Jaya-based MPPT, the oscillation was observed to be minimal at a steady-state compared to P&O and PSO, as Jaya algorithm preserves global peak solution once the optimal point is achieved and until there is a change in operating conditions. The results indicated that the proposed approach is useful for tracking the optimized power of Fuel cells in an appropriate and timely manner. The performance of Jaya based MPPT was tested and evaluated using five different instances of operating conditions. The Jaya algorithm's output was compared to PSO and P&O approaches.

In the first case, a normal operating scenario, the temperature, MWC, hydrogen gas pressure, and oxygen gas pressure were $T = 300K$, $\lambda_m = 3$, $Ph_2 = 0.7atm$, and $Po_2 = 0.8atm$, respectively and were considered for which the maximum possible power of the FC and the related tracking time was obtained as $1189.7W$ and $0.12s$, respectively. The maximum power ratings obtained for PSO, P&O, and without MPPT were accordingly $1125.2W$, $1113.42W$, and $980W$. When compared to PSO, P&O, and without MPPT, the Jaya approach improved maximum power by a percentage of 5.4%, 6.4%, and 17.62%, respectively. Jaya, PSO, P&O, and without MPPT tracking algorithms relative tracking efficiency were observed to be 99.14%, 93.76%, 92.78%, and 81.6%, respectively.

Chapter 5

Energy Management Strategy for Standalone DC Microgrid System with Photovoltaic/Fuel cell/Battery Storage

5.1 Introduction

Increased focus on eco-friendly distributed generation has led to developments in microgrid systems, which provide additional reliability and flexibility over conventional power systems [138]-[139]. Microgrids are described as a cluster of distributed generation, energy storage devices, loads, and distribution networks. Microgrids can be operated in AC, DC, or AC-DC depending on the generation and nature of load [140]- [141]. However, attention to DC microgrid is increasing as it has reduced conversion stages in generation (PV, Wind, Fuel Cells, Batteries, and load) and increased efficiency in DC load appliances (LED lighting, BLDC fans, and inverter-driven appliances like refrigerators, air conditioners). But any poorly managed standalone microgrid is always prone to reliability issues and increased operational costs. To achieve improved performance, reliability, and longevity of BESS, efficient energy management strategies (EMS) are required, which regulate power flow between sources and BESS to meet the load demand.These strategies may include a state machine approach, traditional proportional-integral (PI) control, fuzzy control, external energy optimization, equivalent minimization, and frequency decoupling authority [142].

5.1.1 Features of proposed EMS and control

In this chapter, an EMS for PV/fuel cell/ battery energy storage-based DC microgrid is developed to overcome existing challenges. This approach achieves the goals in a coordinated manner while regulating the fuel cell output power based on *SOC* and regulating hydrogen pressure and oxygen pressure while maintaining pressure difference minimum to keep battery state of charge(*SoC*) within acceptable limits and also ensuring efficient operation. The approach suggested classifies the complete system operation into nine possible operating states based on the battery bank's state of charge, the system's net demand power, and source output power. The following are the key contributions of the proposed standalone microgrid EMS:

- A de-rating strategy for a PV system is designed to effectively overcome the deep charging of batteries under light load conditions.

- The fuel cell power output power is controlled as a function of the battery's SoC to optimize the effective utilization of hydrogen fuel under light/medium loaded conditions and to minimize deep discharge of the battery under heavily loaded conditions.

- A reverse sigmoidal function-based BESS SoC is used to provide smooth regulation of fuel cell output power.

- Real-time perturbations and operational conditions are considered in the hardware implementation of the proposed method.

- Improved reliability by adjusting fuel cell hydrogen and oxygen pressures to enhance the fuel cell output power, and FC is operated at the maximum power point (MPP) to satisfy additional load demand.

5.2 System configuration and control

5.2.1 DC microgrid configuration

The schematic representation of DC Microgrid with PV, fuel cell, and BESS is shown in Figure.5.1. In this scheme, the PV and fuel cell are connected to the common DC-link through respective DC/DC boost converters while BESS is connected through a DC/DC bi-directional converter. The bi-directional converter enables the charging and discharging of BESS and it is designed to tackle power mismatch between the sources (PV, fuel cell) and the load. An EMS for PV, fuel cell, and BESS is developed to minimize sources and load power mismatch to ensure longevity [143] of BESS and efficiently utilize hydrogen fuel. In the DC microgrid, the PV system is expected to operate either in MPPT or off MPPT (de-rated) based on BESS State of Charge (SoC) and load demand. The fuel cell's output power is regulated based on battery SoC. As the fuel cell output power also depends on hydrogen and oxygen pressure, the pressure is increased to a limit while keeping the pressure difference minimum to meet the additional load demand, (especially under peak load conditions). The output power of the solar PV systems, fuel cell, and BESS sources is controlled with their respective local controllers as per commands provided by the proposed EMS.

5.2.2 Solar PV local control

Solar PV systems [144–146] are usually expected to operate at MPP. However, in the standalone DC microgrid system, the PV system is expected to operate either in MPPT mode or off-MPPT (de-rated) mode, as commanded by the proposed EMS (discussed in Section.5.3). For MPPT
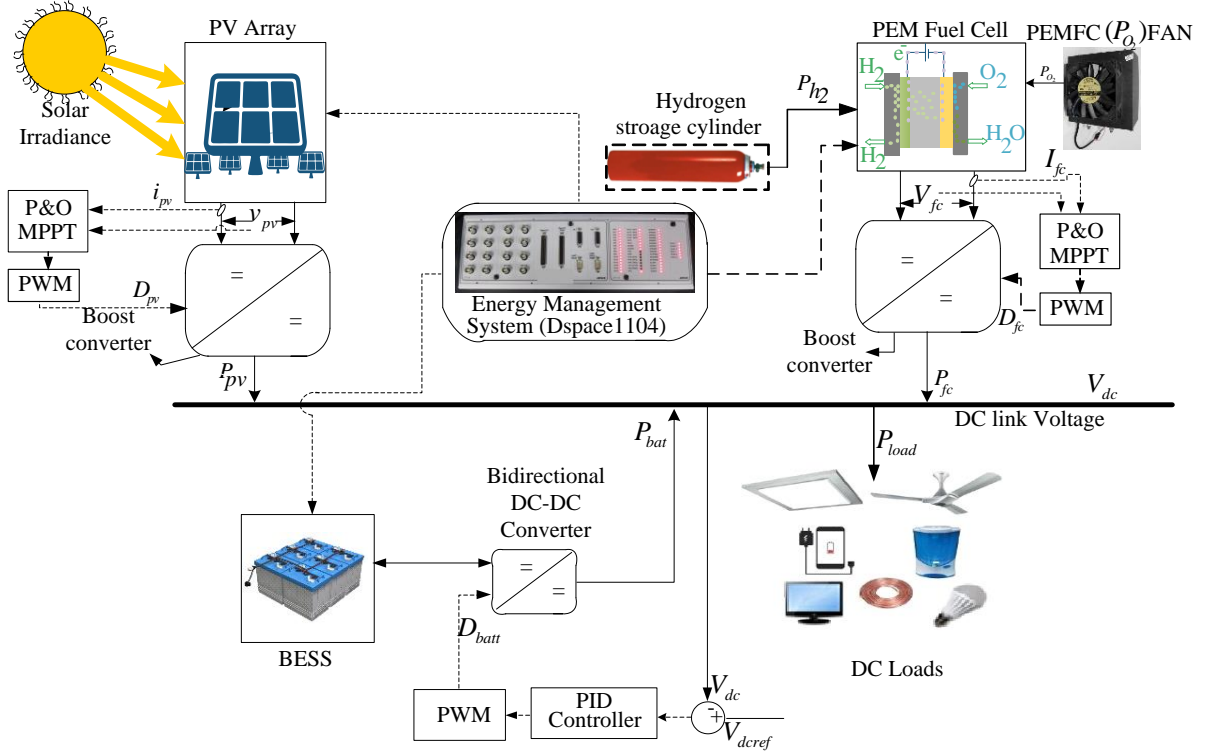
Figure 5.1: Solar PV-fuel cell-battery based standalone microgrid system with, control and energy management strategy (EMS)

operation, the conventional perturb-and-observe (flow chat) MPPT [1] shown in Figure.5.3 is used to track the maximum power point by taking V_{pv} and I_{pv} as inputs, . For off-MPPT mode, the operating point of the PV system is shifted to the right side of the MPP (as shown in Figure.5.2) that curbs PV output power to meet energy balance requirements in the system. This is achieved by varying boost converter duty cycle (D_{pv}) using conditional logic given in equation (6.1).

$$D_{pv} = \begin{cases} D_{pv}^{old} + \Delta D_{pv}, & \text{if } P_{pv} - P_{load} < 0 \\ D_{pv}^{old} - \Delta D_{pv}, & \text{else if } P_{pv} - P_{load} > 0 \\ D_{pv}^{old} & \text{otherwise} \end{cases} \tag{5.1}$$

Usually, under normal operating conditions, i.e., when $SoC < SoC_{max}$, the PV system is operated in MPPT mode by extracting maximum possible solar power. But, when $SoC \geq SoC_{max}$, the proposed EMS sends a status signal $S_{pv} = 0$ to PV controller indicating off-MPPT operation. Thus, the control now deviates from MPPT and operates at reduced output power, which is equal to load power, thereby avoiding the deep charging of the battery. It is to be noted that
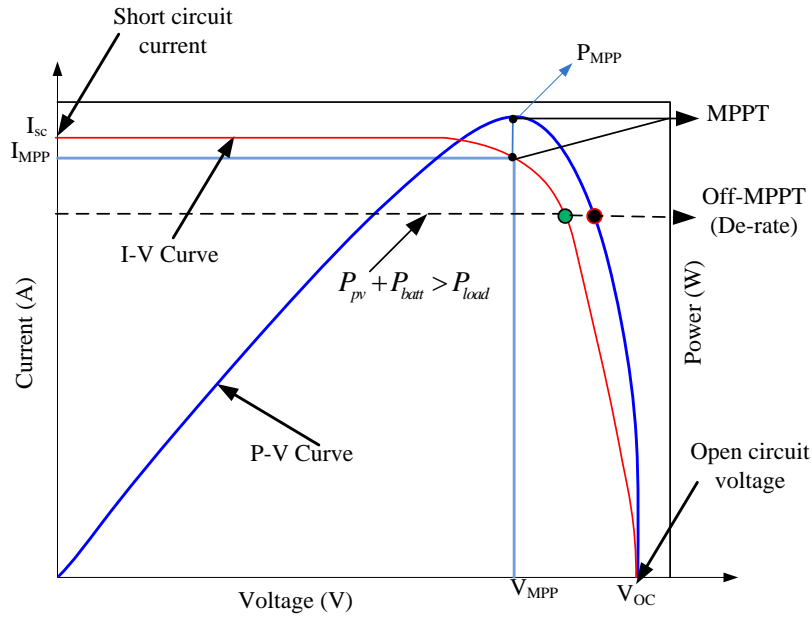
Figure 5.2: Solar P-V and V-I characteristics

during off-MPPT, PV systems are operated on the right side of the MPP curve (as shown in Figure. 5.2) so to have a low deviation in PV voltage V_{pv}. This will support stable voltage operation in the microgrid.

5.2.3 Control technique of the proton exchange membrane fuel cell (PEMFC) model

Practical fuel cells cannot achieve these maximum electrical efficiency values due to the presence of internal resistance losses and other losses. Fuel cell was efficiency calculated using equation (2.23) for varying output power as shown in Figure.5.4(b).

A practical fuel cell operating near its maximum power output might be able to produce only 154kJ of electricity per mole of hydrogen consumed, with the rest of the heating value appearing as heat produced by the fuel cell. The calculation for such a fuel cell is 154$kJ/mole$285.8$kJ/mole$ efficient (HHV). However, the remaining 46% of the energy produced can be recovered from the fuel cell system as co-generated heat [99], [101].

As observed from Figure, 5.4(c). fuel cell system efficiency is low for low value of output power and it sharply increase with an increase in output power, up to a value of P_{fcmin}. Beyond the output power, although the rate of increase in efficiency with output power is positive, it is very small in magnitude. In this curve, the peak efficiency value ($P_{\eta fcmax}$) is observed when the
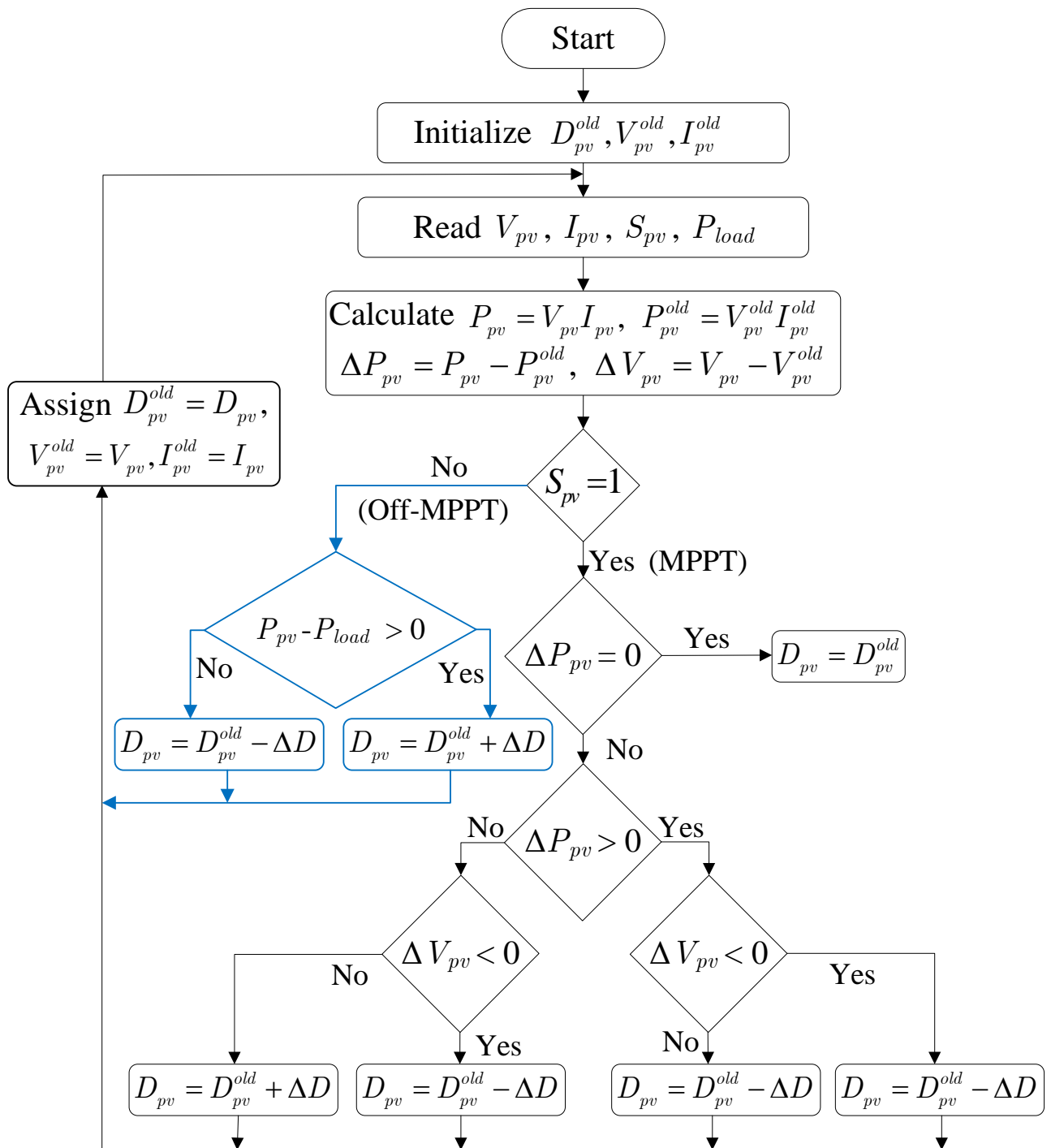
Figure 5.3: Flow Chart of P&O MPPT for PV System
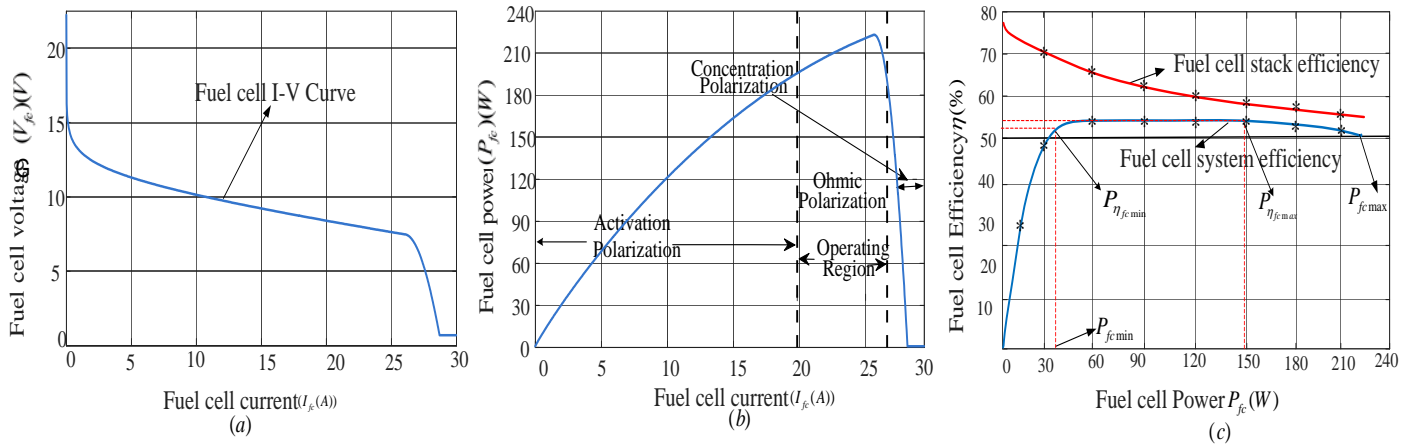
Figure 5.4: (a)$I - V$,(b) $I - P$, and (c)power- efficiency, curves of a fuel cell at constant hydrogen and oxygen gas pressure

fuel cells system output power is P_{fcmax}. On further increase of output power, the efficiency is reduced with a small negative slope magnitude. From these efficiency characteristics, it can be observed that fuel cell system efficiency is merely constant when the output power of the system is between P_{fcmin} and P_{fcmax}. Even at the MPP point, the efficiency is observed to be 7% lower than its peak value. Thus, taking this advantage the proposed strategy can be easily employed by maintaining the fuel cell minimum power, i.e., P_{fcmin} (or power corresponding to the nose point in the efficiency curve), when batteries are overcharged and power balance is achieved by derating PV. During normal operation, the fuel cell is operating using a reverse sigmoidal function, delivering power between P_{fcmin} to P_{fcmax}. The reverse sigmoidal characteristics are modified accordingly to fit within the output power limits these ranges. Further, the different efficiency curves under different operating pressures of hydrogen and oxygen are also shown in 5.5.

5.2.4   DC-Link voltage controller by using BESS

In BESS, a bi-directional DC/DC converter is employed to regulate common DC-link voltage. As BESS is regulating DC-link voltage, any power imbalance between sources and load demand is taken care of by BESS. The conventional cascaded voltage and current controller scheme [139] is adopted for BESS as shown in Figure.5.6. The measured dc-link voltage (v_{dc}) is compared with a reference voltage signal (v_{dcref}) and fed to a PI-based voltage controller. The output of the controller is considered battery reference current (i_{bat}^*) and given in equation(5.2) and (5.3);
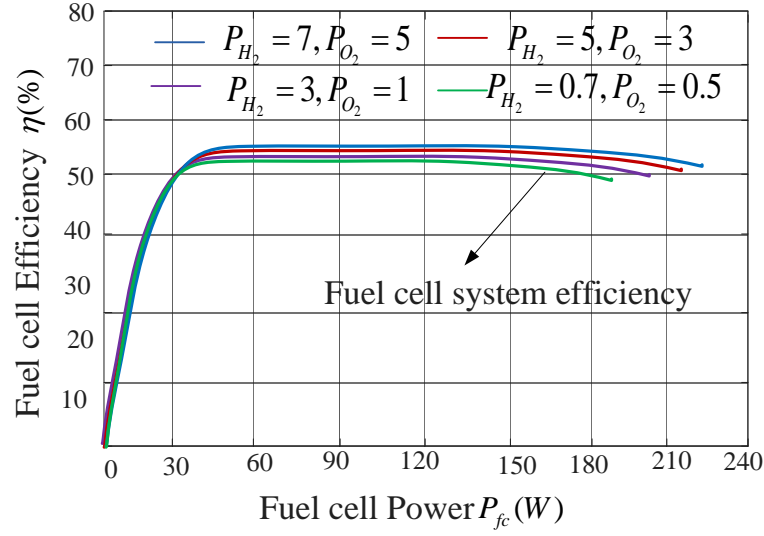
Figure 5.5: Power- efficiency, curves of a fuel cell at various hydrogen and oxygen gas pressures

$$\Delta v(t) = v_{dcref(t)} - v_{dc(t)}, \tag{5.2}$$

$$i^*_{bat}(t) = k_P \Delta v(t) + k_i \int \Delta v(t)\, dt - i_{pv(t)} - i_{fc(t)}. \tag{5.3}$$

Here k_p and k_i are the gains of voltage PI controller.

The battery reference current is limited using saturation limits to avoid any prolonged over-current that can damage BESS converter switches. The battery current (i_{bat}) measured is then compared with reference current signal (i^*_{bat}) obtained and fed to inner current PI controller which in turn provides duty-cycle (D_{bat}) as output. A PWM generator is used to generate the switching pulses that trigger bidirectional converter as per the duty cycle (D_{bat}) obtained from the controller, as shown in Figure.5.6.

5.2.4.1   Designing of BESS controller

For PI regulator of the battery, voltage controller dynamics is very slow compare to current controller dynamics, and switching frequency ($f_{sw} = 20KHz$). The current controller gains are calculated based on filter inductor inductance (L_f) and resistance (R_f) and converter switching frequency (f_{sw}). First, the current controller is designed to have a bandwidth lower than the switching frequency.

Thus, the current controller time constant (T_c) is chosen such that it greater than the settling

time of switching frequency, i.e,

$$T_c = \frac{10}{2 * \pi * f_{sw}};$$

(5.4)

The proportional(K_{pc}) and integral controller (K_{ic}) gains of current controller are calculated using the pole zero cancellation approach. The zero of PI controller ($K_{pc}s + K_{ic}$) should cancel the pole of the system due to series filter $\frac{1}{L_f s + R_f}$. Thus

$$K_{pc} = \frac{L_f}{T_c}$$

(5.5)

Where, L_f= inductance value (Henry)

$$K_{ic} = \frac{R_f}{T_c}$$

(5.6)

Where, R_f= inductor resistance (ohms)

Similarly, the voltage controller is designed with lower bandwidth than the current controller. Let T_v be time constant of voltage controller which should be greater than the settling time of the current controller. $T_v = 5$ to 10 times of T_c (settling time T_c)

Now the proportional (K_{pv}) and integral (K_{iv}) gains of voltage controller are calculated by fixing one of the gains to a constant and having time constant T_v. Thus assuming $K_{iv} = 50$, k_{pv} is calculated as follows:

$$K_{pv} = T_v * K_{iv}$$

(5.7)

It needs to be noted that if i^*_{bat} is positive while Δv is positive, the input power to the dc-link is greater than that of the output power, and vice versa. Thus the DC-link voltage is raised or reduced to make the net power imbalance and voltage deviation across the DC-link zero. Typically, when the load demand is high, and the battery SoC is greater than battery SoC_{min}, the bidirectional converter operates as in boost mode (discharging mode) supply when using power from the battery. When load demand is low, and battery SoC is less than the upper limit, the battery operates in buck mode (charging mode or floating mode).

5.3 Energy management strategy (EMS)

In this chapter, to efficiently utilize sources (PV, fuel cell, and BESS) for supplying load demand, to improve longevity, and to ensure minimum consumption of hydrogen, an EMS scheme has been proposed. Here, a rule-based controller scheme is implemented for EMS by consider-
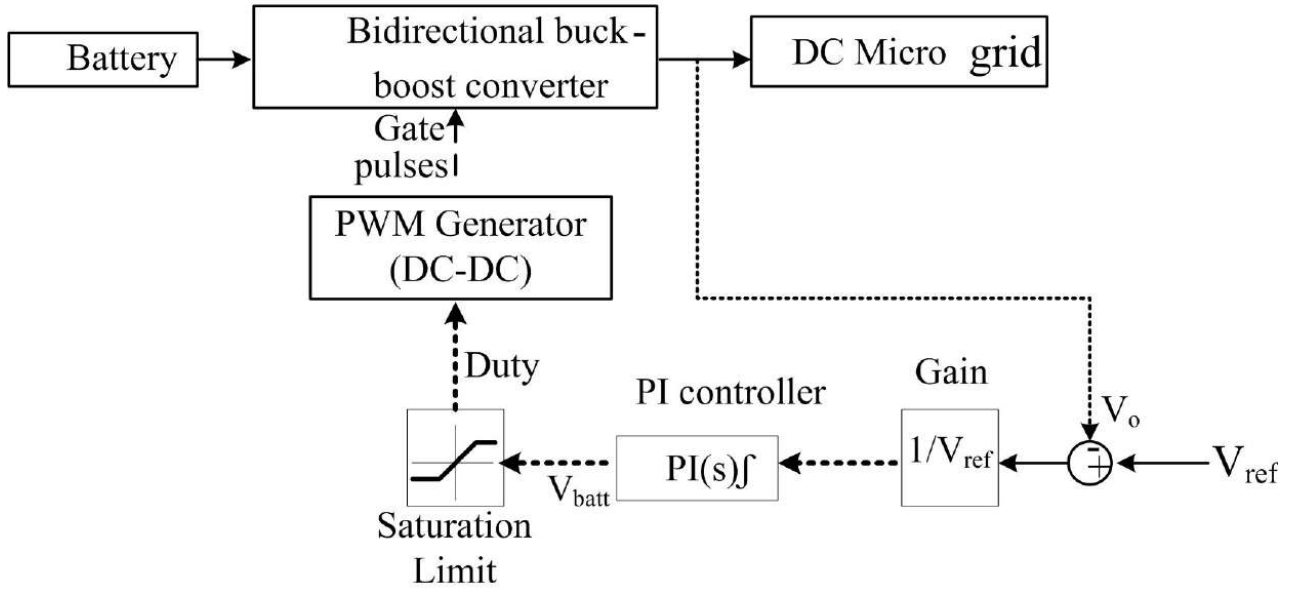
Figure 5.6: DC-link Voltage Controller by Using PI Controller

ing load (P_{load}) and battery *SoC* level. The proposed system for EMS is shown in Figure. 5.8. In EMS, Battery *SoC* is monitored and the operating points for all the sources are calculated to maintain *SoC* within limits while regulating the DC-link voltage at nominal value. In all operating conditions, S_{pv} represents PV status that is fed to PV local controller ($S_{pv} = 1$), which represents MPPT operation. while ($S_{pv} = 0$), represents off-MPPT operation. The PV system is typically operated at MPPT. For efficient operation, fuel cell is typically operated in de-rated (off-MPPT) to have not much difference of efficiency. The fuel cell operating power reference signal is obtained using a reverse sigmoidal function of battery *SoC* (shown in Figure.5.7), which is mathematically formulated as given in equation 5.8.

$$P_{fc}^* = P_{fc_{min}} + P_{fc_{max}} \frac{\exp(\alpha(\beta - SoC))}{1 + exp(\alpha(\beta - SoC)}$$ (5.8)

Here α is saturation constant, β is the mid-value of *SoC* limits (typically chosen between $45\% - 55\%$) and P_{fcmax} is the maximum possible power generation for P_{h_2} and P_{0_2} of the fuel cell. Based on power mismatch between the sources and load ($P_{pv} + P_{fc} - P_{load}$), the DC microgrid operation can be broadly classified into two different modes of operation, (i) Excess Generation Mode (EGM). and (ii) Deficit Generation Mode (DGM) as shown in Figure.5.9.

94
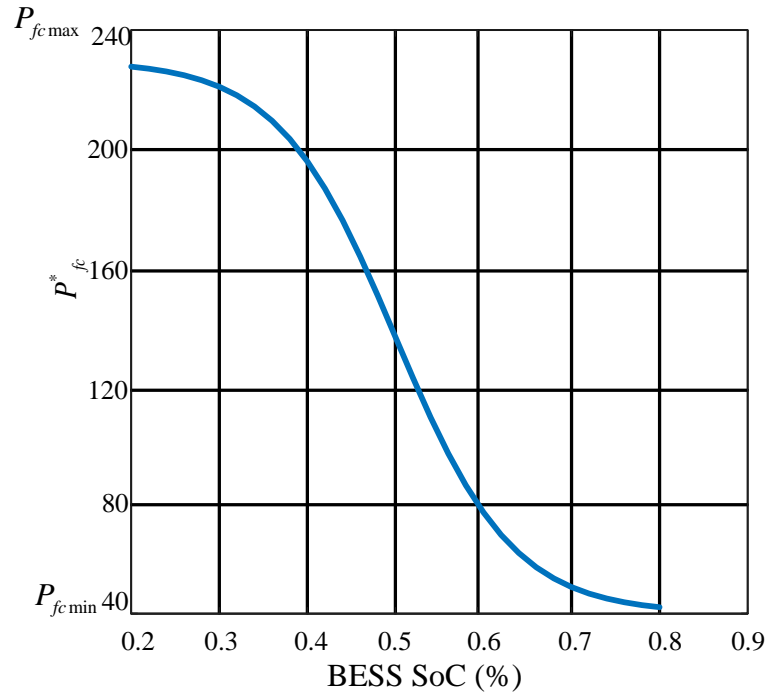
Figure 5.7: Reverse Sigmoidal Function
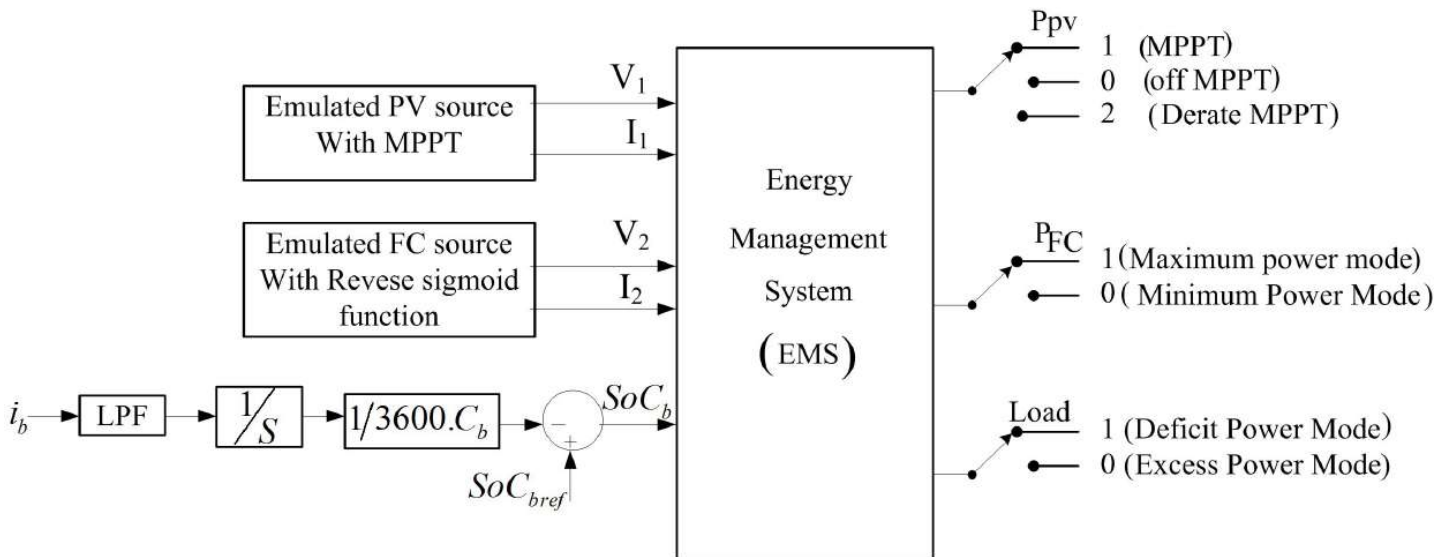
Figure 5.8: Proposed System for Energy Management

5.3.1   Excess generation modes: (EGM)$(P_{pv} + P_{fc} > P_{load})$ (modes: 1–5).

In EGM, the sum of average power from PV (P_{pv}) and fuel cell (P_{fc}) is greater than P_{load}; under this, five operating modes are possible as shown in Figure. 5.9:

Mode: 1 & 2 ($SoC \leq SoC_{min}$): In these modes, the objective of EMS is to increase *SoC* of the battery to bring it within limits. Hence, in both modes, the PV and fuel cell systems are always operated at MPP for a given solar irradiance ,hydrogen and oxygen pressure, respectively. *In mode:1*, when $P_{h_2} \geq P_{h_2max}$, $P_{o_2} \geq P_{o_2max}$ i.e., P_{h2}, P_{o2} are held constant at maximum value, which means that the fuel cell output power is at maximum rating, P_{h_2}, and P_{o_2} difference is maintained at minimum value. The fuel cell continues to operate at the same point maintaining maximum power level till *SoC* increases beyond the lower limit. *In mode: 2*, when $P_{h_2} \leq P_{h_2max}$, $P_{o_2} \leq P_{02max}$, the power of fuel cell (P_{fc}) is slightly increased as per reverse sigmoidal function given by (5.8) to operate it at maximum fuel cell power mode, hydrogen, and oxygen pressures P_{h_2max}, P_{o_2max} so as to ensure fast charging of BESS.

Mode: 3 & 4 ($SoC \geq SoC_{max}$): *In mode:3*,the PV is operated in off- MPPT (derating) mode to ensure that BESS is either in floating mode or discharging mode. *In mode: 3*, when $P_{pv} \geq P_{pv}$, i.e., the fuel cell generates derated power for supplying (P_{h_2}),with (P_{o_2}) minimum value; the EMS continues to maintain minimum power till battery *SoC* falls below SoC_{max}. *In mode:4*, when $P_{pv} \leq P_{load}$, PV operating in MPPT mode, fuel cell supplied power as per the reverse sigmoidal function (5.8), shown in Figure.5.7 to ensure that battery operates either in floating mode or in discharging mode.

Mode: 5 ($SoC_{min} < SoC < SoC_{max}$): *In mode: 5*, the PV is operated in MPPT mode while the fuel cell operates based on reverse sigmoidal function and charges the battery *SoC* to have a DC-link power balance and maintains DC link voltage nominally with reference to v_{dcref}.

5.3.2   Deficit generation modes (DGM):$(P_{pv} + P_{fc} < P_{load})$ (Modes:6-9).

In DGM, the sum of powers from the sources PV (P_{pv}) and fuel cell (P_{fc}) is less than load demand (P_{load}). Under DGM, there can be four operating modes, as shown in Figure.5.9.

Mode: 6 & 7 ($SoC \leq SoC_{min}$): The PV system and fuel cells are run at MPP in modes 6 and 7, respectively, for a given amount of solar irradiation and hydrogen and oxygen gas partial pressure. *In mode 6*, when $P_{h_2} \geq P_{h2max}$, $P_{o2} \geq P_{o_2max}$ i.e., P_{h_2}, P_{o_2} are maintained constant at maximum value; it signifies that fuel cell output power is at maximum rating, and P_{h_2}, P_{o_2}

different is kept to a minimum value. Furthermore, if the load demand is not met using both PV and fuel cells, optional loads are shed. This ensures that BESS doesn't discharge extensively.

In mode: 7, when $P_{h_2} \leq P_{h_2max}$, $P_{o_2} \leq P_{0_2max}$ the power of the fuel cell P_{fc} slightly raised according to reverse sigmoidal function provided by equation (5.8) to operate it at maximum hydrogen, and oxygen pressures Ph_{2max}, Po_{2max} so as to ensure quick charging of BESS.

Mode: 8 & 9: For *modes 8 and 9*, PV was operated at MPP in modes 8 and 9. In mode 8, battery $SoC \geq SoC_{max}$ or $SoC_{min} > SoC > SoC_{max}$; in this condition the fuel cell was supplied based on the reverse sigmoidal function shown in Figure.5.7, and the battery discharges up to above the lower limit. *In mode: 9*, when $SoC_{min} > SoC > SoC_{max}$, PV operated at MPPT mode, battery *SoC* maximum so it discharged up to the minimum level of battery,and the fuel cell provided the load power based on reverse sigmoidal function as shown in Figure.5.7; PV power,and battery power,were kept constant to maintain the load demand continuously.

5.4 Stability analysis of proposed microgrid

The stability of the DC microgrid while regulating dc-link voltage is analysed in this section. As the dc-link voltage controller remains the same in all control operating modes, stability is analysed by considering DC-link voltage as system output and its controller is designed so as to have sufficient phase margin to the system open-loop transfer function. As BESS uses bidirectional boost converters, the transfer functions of the converter system are derived from the inductor current and capacitor voltage dynamics using equation (5.9) and (5.10), respectively.

$$L_{bat}\frac{di_{Lbat}(t)}{dt} = v_{bat} - (1 - d_{bat})v_{cbat} \tag{5.9}$$

$$C_{bat}\frac{dv_{cbat}(t)}{dt} = (1 - d_{bat})i_{Lbat} - (-i_{load} + i_{pv} + i_{fc}) \tag{5.10}$$

The voltage control transfer functions [147], are generated using the state space averaging approach as follows:

$$G_{\Delta vdbat} = \frac{\Delta \hat{v}_{bat}(s)}{\hat{d}_{bat}(s)} = \frac{(1 - D_{bat})v_{dc} - L_{bat}I_{Lbat}s}{L_{bat}C_{bat}s^2 + \frac{L_{bat}i_{bat}}{V_{dc}}s + (1 - D_{bat})^2} \tag{5.11}$$

Moreover, the current control transfer function is computed as follows:

$$G_{i_{bat}^*dbat} = \frac{\hat{i}_{i_{bat}^*}(s)}{\hat{d}_{bat}(s)} = \frac{C_{obat}V_{dc}s + 2(1 - D_{bat})I_{Lbat}}{L_{bat}C_{bat}s^2 + \frac{L_{bat}i_{bat}}{V_{dc}}s + (1 - D_{bat})^2} \tag{5.12}$$
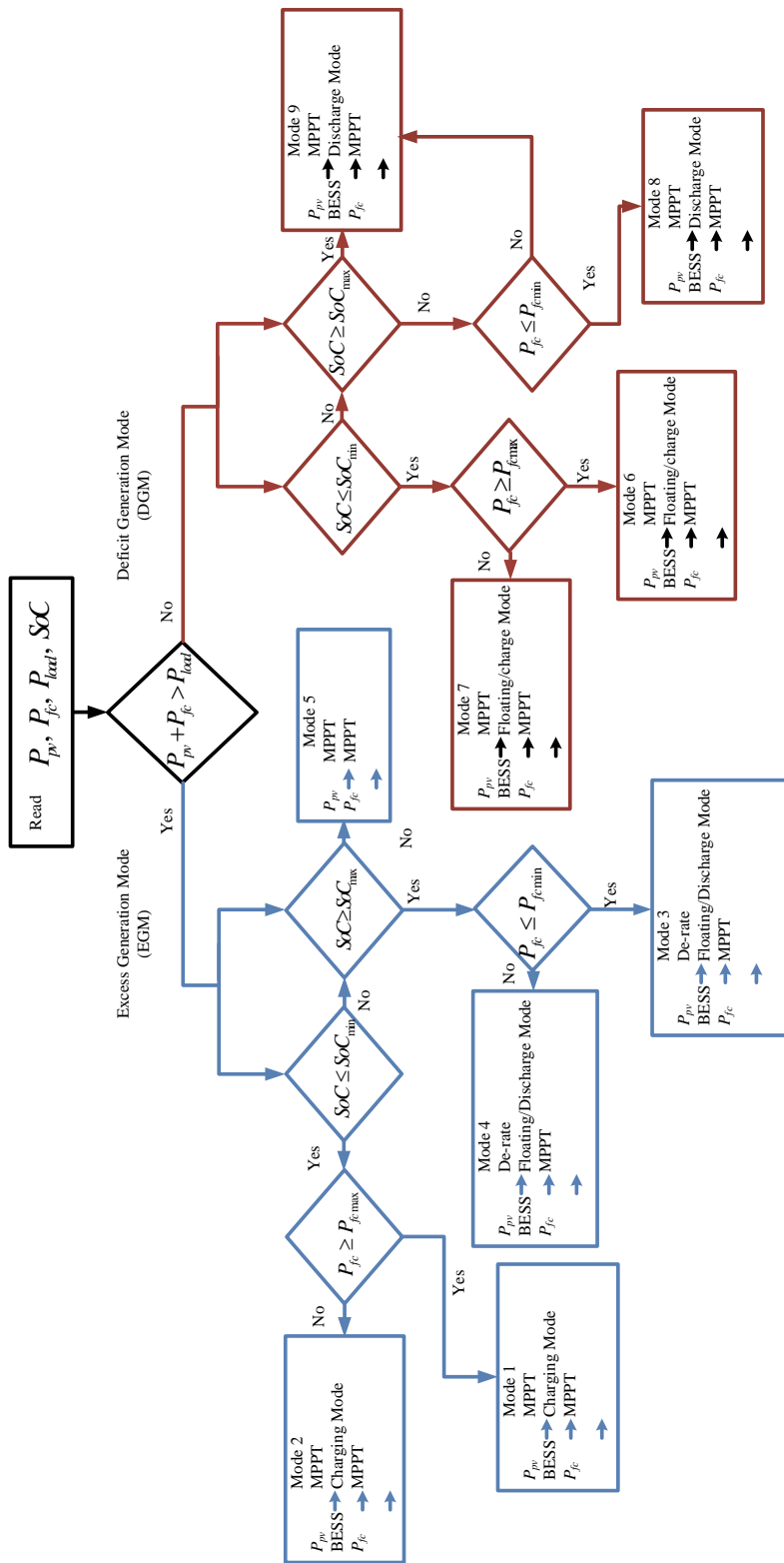
Figure 5.9: Flowchart for modes of operation in PV, fuel cell and BESS system with proposed energy management strategy.
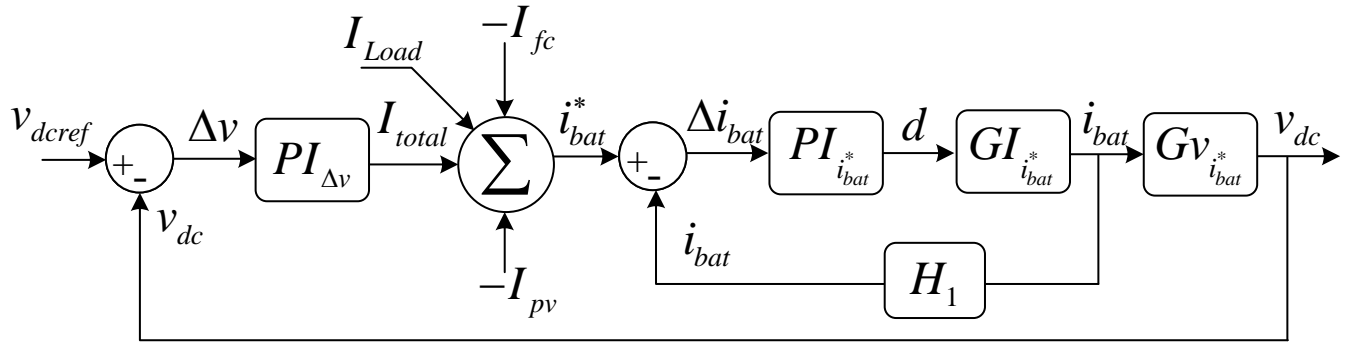
Figure 5.10: Stability analysis of feedforward loop system

The simplified transfer function model with feedback control loop of BESS system is shown in Figure.5.10. Here, it is noted that the disturbance caused by exogenous inputs (i_{pv}, i_{fc}, and i_{load}) are eliminated using the feedforward loop [147] shown in Figure. 5.10. The battery current control loop is designed for a bandwidth of $(5-10)$(bps) less than the switching frequency, so that the controller action towards switching transients is avoided. The loop gain of the battery current control loop is given by:

$$L_{i_o,op} = PI_{i^*_{bat}} \cdot GI_{i^*_{bat}} \cdot H_1 \tag{5.13}$$

and the transfer function of a closed loop current control loop is:

$$L_{i_o,cl} = \frac{PI_{i^*_{bat}} \cdot GI_{i^*_{bat}}}{1 + PI_{i^*_{bat}} \cdot GI_{i^*_{bat}} \cdot H_1} \tag{5.14}$$

The inner current controller PI gains were assigned using MATLAB/SISO toolbox. In the battery, inner current loop was designed with a bandwidth of $5000 rad/s$ to ensure fast operation of battery during load transients and the phase margin was selected as $60°$ to provide sufficient damping and exhibit stable closed-loop operation. Figure. 5.11 depicts the bode diagram for such compensated and uncompensated battery current loop systems.

Similarly, the loop gain for the simplified voltage-controlled battery system is given by equation 5.15.
$$L_{v_o,op} = L_{i_o,cl} \cdot Gv_{i^*_{bat}} \cdot PI_{\Delta v} \tag{5.15}$$

The outer voltage controller is designed with a loop bandwidth of $500 rad/s$ and phase margin of $60°$. The Bode plot with and without compensator is shown in Figure.5.11. The blue line represents the uncompensated system, whereas the red line represents the proposed accurate model [148].

99

Table 5.1: System Parameters

Parameters Name	Simulation Parameters	Experimental Parameters
Specification for Solar PV at STC ($1000W/m^2, 25°C$)		
Power at MPP (W)	54.69	70.2
Voltage at MPP (V)	16.88	31.2
Current at MPP (A)	3.24	2.25
Voltage at Voc (V)	21.1	39.36
Current at Isc (A)	3.6	2.5
No of cells	48	96
Each cell Voltage (V)	0.44	0.41
Input capacitor C_{in}	$500\mu F$	$500\mu F$
Output capacitor C_{out}	$500\mu F$	$500\mu F$
Inductot (L_{pv})	4mH,0.001X	4.5 mH
Specifications of PEMFC		
Rated Power(W)	230	50
Number of Cell	48	20
Purging at a Voltage (V)	12	12
$A(cm^2)$	27	25
$l\mu m$	127	135
$J_{max}(mA/cm^2)$	6.5	–
Ph_2 Pressure (bar)	1.00 - 5.21 (as per BESS SoC)	1.00 - 5.021
Temperature	343.15- 353.15 (K)	5° to 30°
Purity of hydrogen	> 99.995% of dry P_{h_2}	> 99.995% of dry P_{h_2}
Shut down for over current (A)	12	12
Shut down for low voltage (V)	12	12
shut down at over temp	–	65°
Time taken for start up	immediate	< 30s at ambient temp
Efficiency	46%	40%
Input capacitor C_{in}	$500\mu F$	$500\mu F$
Output capacitor C_{out}	$500\mu F$	$500\mu F$
Inductor (L_{fc})	4mH,0.001X	8.5 mH
Specification of BESS		
Battery choice	lead–acid battery	lead–acid battery
Rating in Ampere hour	120 Ah	120 Ah
Nominal Voltage	12 V	12 V
Charging rate	C/10	C/10
Capacitor (C_{bat})	$2000\mu F$	$500\mu F$
Inductor (L_{bat})	$4.8mH, 0.001X$	$7.2mH$
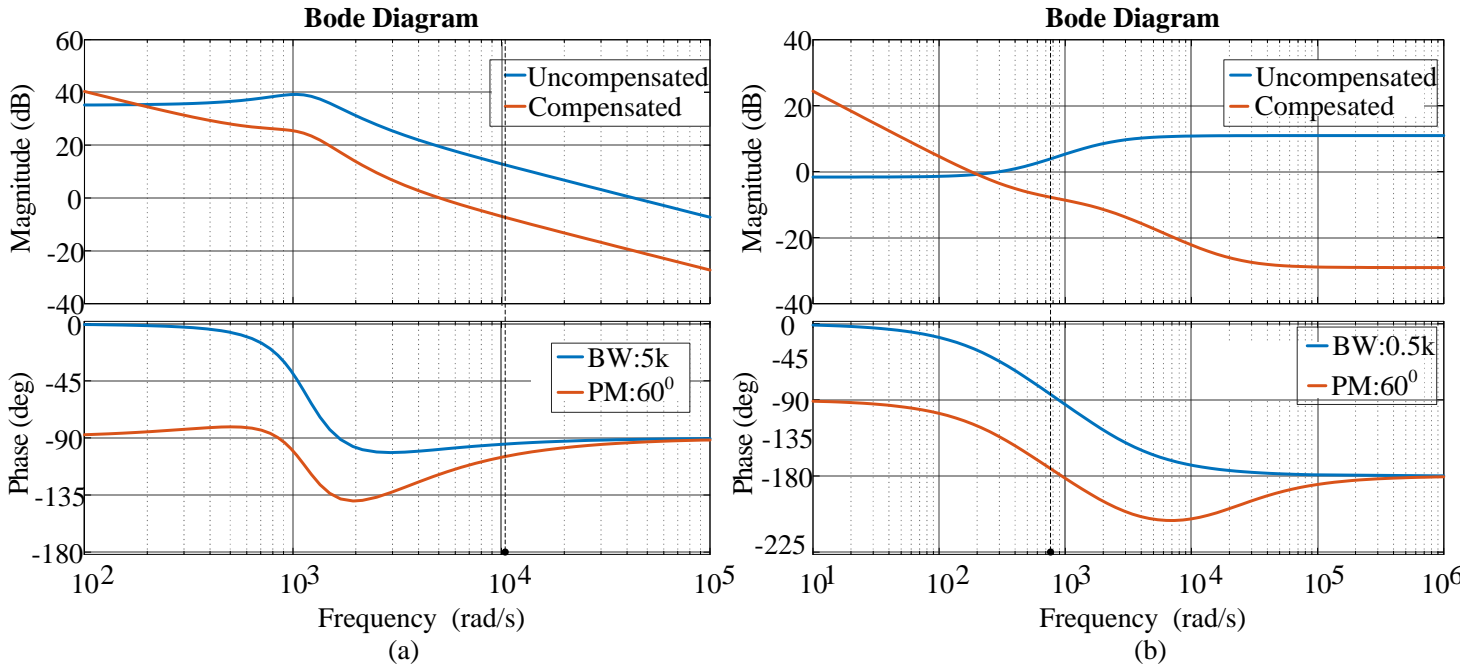
Figure 5.11: Bode plot for (a) current control loop,and (b) voltage control loop

5.5 Simulation studies

The efficacy of the proposed EMS was evaluated by simulating the DC microgrid system as shown in Figure.5.1 in MATLAB/Simulink. The specifications of the PV systems, fuel cells, and battery along with their respective converter and control parameters used in simulation studies are detailed in Table. 5.1. The fuel cell generates a maximum output power ($P_{fcmax} = 220W$) for a maximum safe hydrogen pressure range ($P_{h_2} = 5.02bar$). The hydrogen pressure of the fuel cell cylinder was controlled through pressure control valve detailed in section.5.2.3. BESS was controlled using the cascaded control loop method for DC link voltage regulation. In this, the inner current controller was tuned using pole-zero placement approach and the outer voltage controller was tuned using the symmetrical optimal method. The upper and lower limits of battery SoC were considered as $SoC_{max} = 80\%$ and $SoC_{min} = 20\%$. and the EMS was designed to operate the battery within the limit of SoC. Further, for all test scenarios, the resistive loads were considered across the DC link and BESS local controller and it was designed to maintain DC link voltage at a reference nominal value of v_{dcref}=100V.

5.5.1 Case-(i) ($SoC = 80\%$):

In this scenario, the battery SoC was close to its upper limit SoC_{max}, as shown in Figure.5.12(b). For these conditions, the performance of the proposed EMS was evaluated under varying load

Figure 5.12: BESS $SoC = 80\%$ with load changes (a) Load power (P_{load}), (b) Battery $SoC(\%)$, (c) PV power (P_{pv}), (d) Hydrogen pressure (P_{h_2}), and Oxygen gas pressure (P_{o_2}), (e) Fuel cell power (P_{fc}), and (f) DC link voltage (V_{dc})

conditions. The initial load on the DC microgrid was $P_{load} = 280W$, and battery SoC was at 80% as shown in Figure.5.12(a) and 5.12(b). As the battery SoC was at its upper limit, to avoid deep charging of the batteries, the proposed EMS, sends an $S_{pv} = 0$ signal to PV local control that makes PV operate in load follower mode for avoiding further charging of the battery. During this cycle, the hydrogen pressure is maintained at a minimum value based on reverse sigmoidal function output and the DC-link voltage is maintained at $100V$ by BESS controller. At time $t = 3.5s$, the total load P_{load} in DC microgrid is increased to $614W$(Figure.5.12(a)). As the load demand is increased, the battery starts discharging, and SoC falls below its upper limit. based on this data, the proposed EMS provides PV MPPT on signal ($S_{pv} = 1$) to PV controller and enables MPPT operation as shown in Figure.5.12(c). However, as the load $P_{load} = 614W$ is greater than PV MPP output power $P_{pv} = 430$, BESS continues to discharge by supplying $P_{bat} = 140W$. During this phase, the fuel cell is still supplying at a minimum generation of around $P_{fcmin} = 38W$ as shown in Figure.5.12(e). At $t = 9.5s$, the load demand is reduced to $280W$ which results in the battery discharging till $SoC < SoC_{max}$. When BESS SoC reaches the maximum limit, the proposed EMS sends off-MPPT signal to PV controller and makes PV operate in derated mode with output power condition $P_{pv} = P_{load}$ as shown in Figure.5.12(c). Again, at $t = 18s$, the load demand increases to $380W$, as $SoC \geq 80\%$; the PV continues to operate at off-MPPT, PV output is equal to load demand. During this phase, the battery is operated in floating mode, and the fuel cell at minimum generation mode as shown in Figure.5.12.
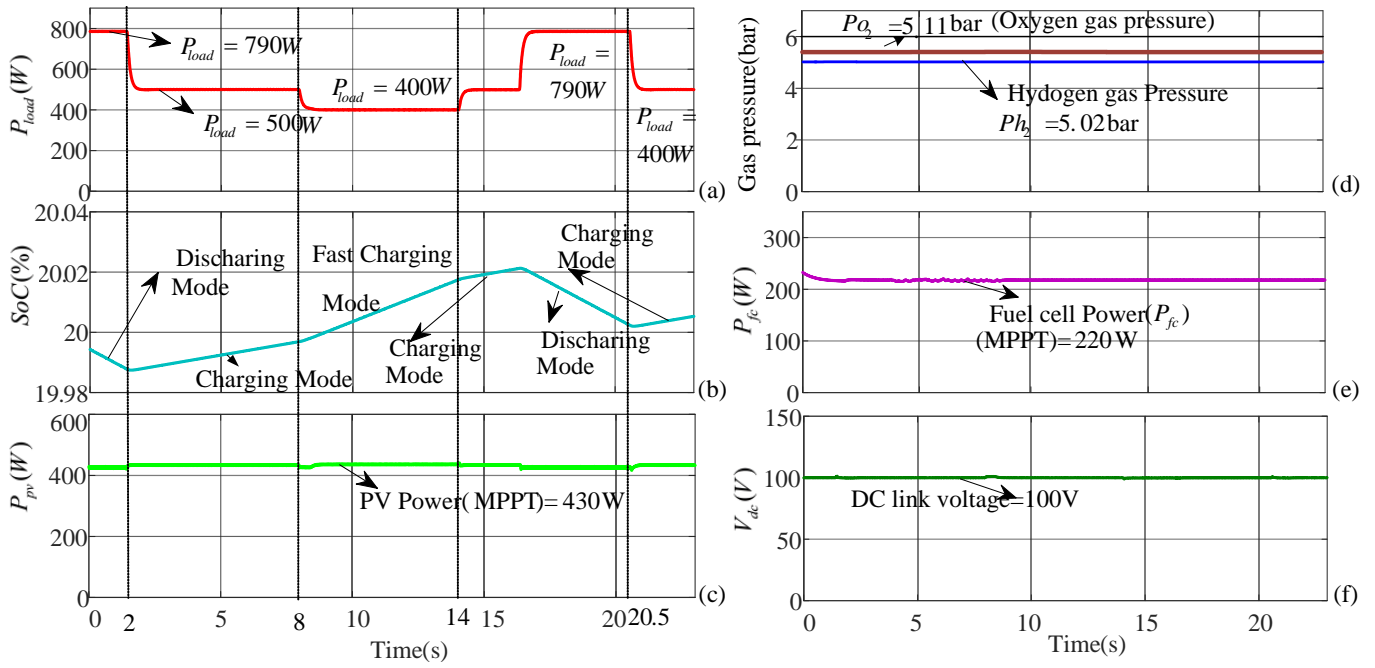
Figure 5.13: Minimum BESS $SoC = 20\%$ with load changes: (a) Load power (P_{load}), (b) Battery $SoC(\%)$, (c) PV power (P_{pv}), (d) Hydrogen pressure (P_{h_2}), and Oxygen gas pressure (P_{o_2}), (e) Fuel cell power (P_{fc}), and (f) DC link voltage (V_{dc})

5.5.2   Case-(ii) ($SoC = 20\%$):

In this case, the battery SoC is near its lower limit (SoC_{min}) as shown in Figure.5.13(b). Under these conditions, the performance of the proposed EMS is evaluated for varying load conditions. The initial load on the DC microgrid was $P_{load} > P_{pv} + P_{fc}$, and battery SoC was at 20% as shown in Figures.5.13(a) and 5.13(b).The proposed EMS operated PV and fuel cell system in MPPT mode and fuel pressure was maintained in minimum mode as shown in Figure.5.13(c),(d), and (e), and the battery discharged to maintain the load demand while also avoiding deep discharging of the batteries. The optional load was shed at $t = 2s$ with the net load being $P_{load} = 500W$. The battery started to charge. Further, the charge at $t = 8s$ led the load to being further reduced to $P_{load} = 400W$ battery at a faster rate. At $t = 14s$ the load increased and reached $P_{load} = 790W$, During this time, BESS discharged to maintain the load demand. At $t = 20.5s$, to avoid deep discharging, the load demand was again reduced as shown in Figure.5.13.
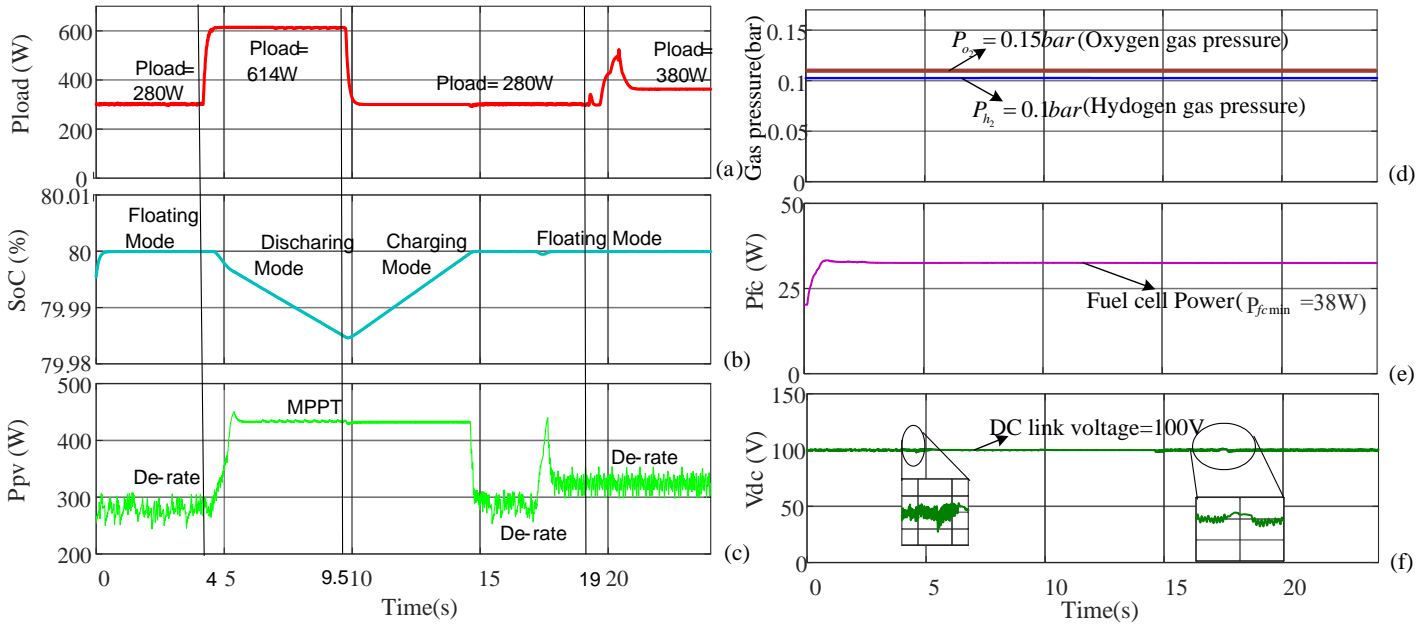
103
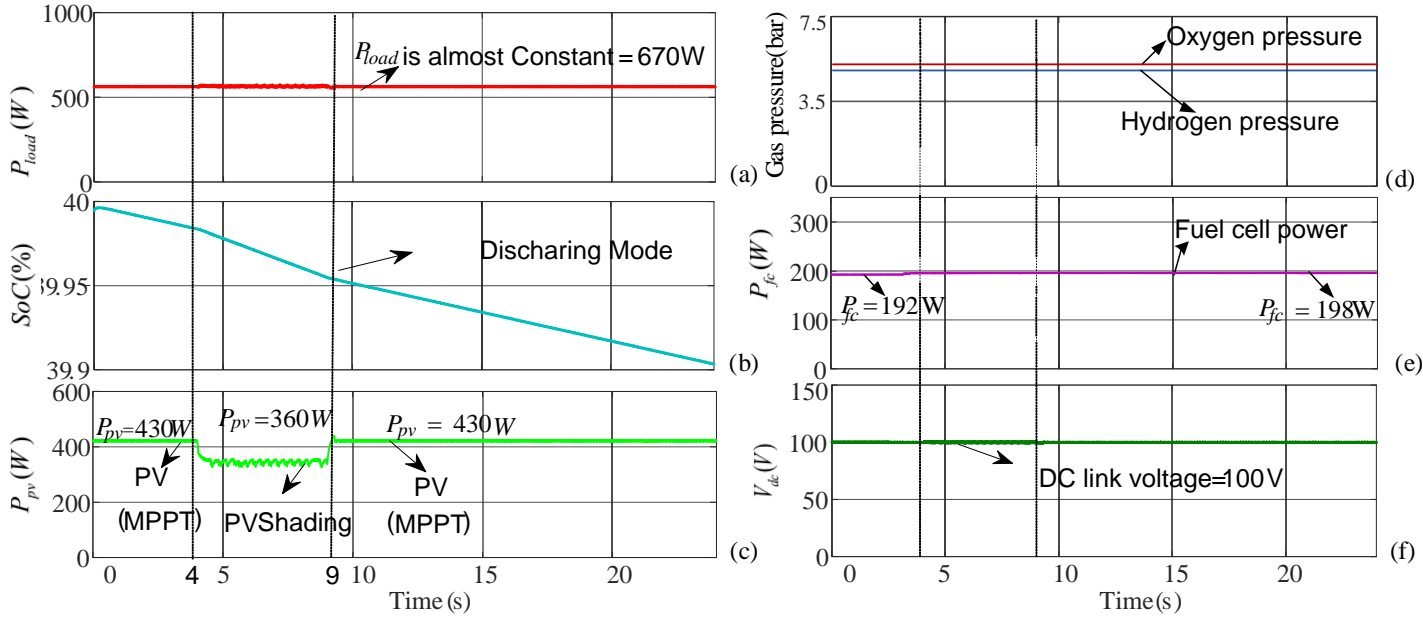
Figure 5.14: Minimum BESS $SoC = 40\%$ with PV Shaded Condition: (a) Load power (P_{load}), (b) Battery $SoC(\%)$, (c) PV power (P_{pv}), (d) Hydrogen pressure (P_{h_2}),& Oxygen gas pressure (P_{o_2}), (e) Fuel cell power (P_{fc}) , and (f) DC link voltage (V_{dc})

5.5.3   Case-(iii) ($SoC = 40\%$):

In this case, load demand was maintained constant $(P_{load} = 670W)$ as shown in Figure.5.14(a). Initially, the battery SoC was considered at 40% within limits of SoC_{min} and SoC_{max} as shown in Figure.5.14(b). During this phase, PV was operated in MPPT mode, and the fuel cell power reference was obtained from reverse sigmoidal function of BESS SoC at $P_{fc}^* \approx 0.84 P_{fcmax} = 193.2W$. BESS was operated in discharging mode with $P_{bat} = 51W$ to maintain the load demand as shown in Figure.5.14(f). At 4s, due to cloud shade, PV output power was reduced to $P_{pv} = 360W$ as shown in Figure. 5.14(c), and fuel cell output was held at $P_{fc} = 193.5W$ as shown in Figure. 5.14(e). The additional load demand was met the battery $P_{bat} = 120W$ with increased rate of discharge as shown in Figure .5.14(b). At time $t = 9s$, the solar PV system irradiance was restored due to which the battery discharging rate reduced as depicted in Figure.5.14(b).

5.6   Experimental results

The proposed EMS was validated using a hardware DC microgrid prototype model shown in Figure.5.15. The schematic diagram of the hardware prototype is the same as shown in Figure.5.1 with different ratings, tabulated in Table.5.1. A programmable PV simulator (Magna power electronics XR 250-6.0/200+PPPE+SL) was used to replace the PV system; PEMFC (H-50 Horizon) with hydrogen pressure (P_{h_2}) ranging from 1-5.02 (Bar) performed at 12V,
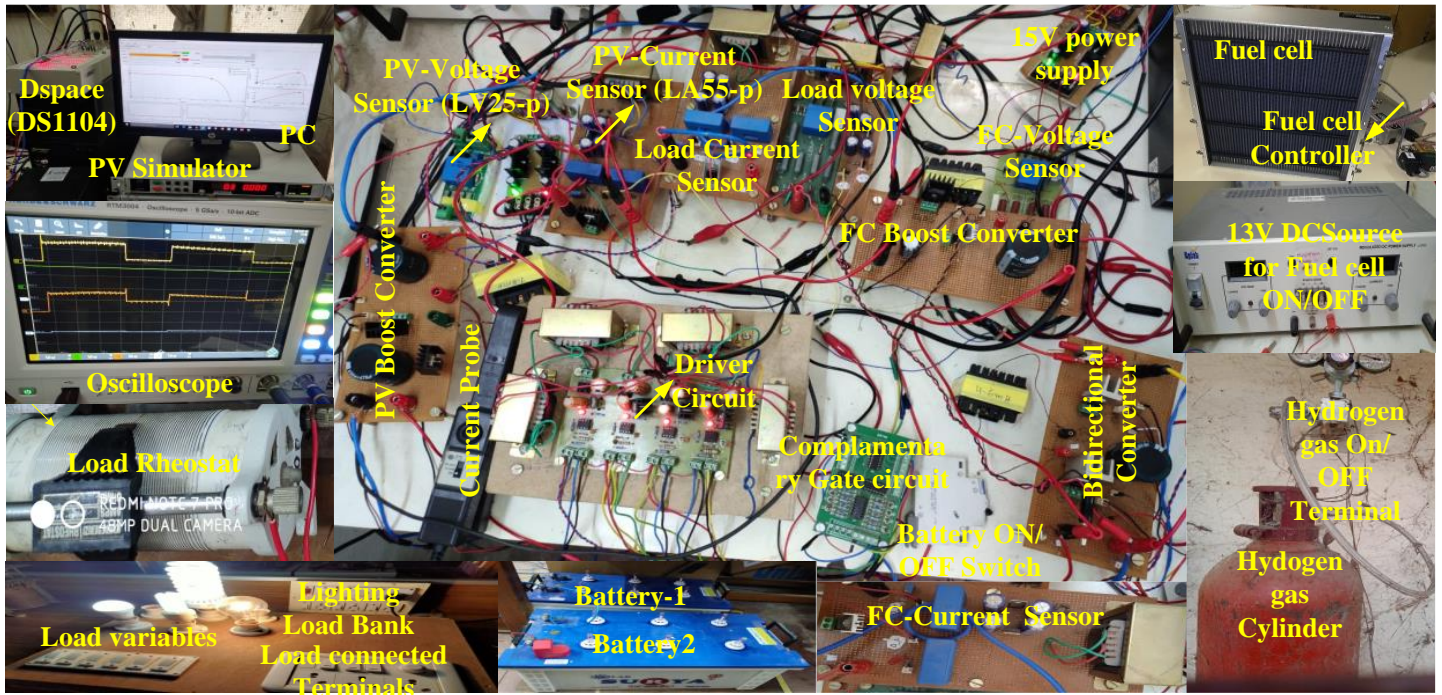
Figure 5.15: Experimental setup.

$4.1A$, and 40% efficiency, and two series-connected $12V/120Ah$ lead–acid batteries were used as sources, The local controllers of the individual source and the proposed EMS were implemented in dSPACE-DS1104 controller. The system was designed to maintain DC-link voltage at reference $V_{dcref} = 48V$. Further, LEDs and incandescent bulbs were used as the DC loads in this system as shown in Figure.5.15.

5.6.1 Case-(i) ($SoC = 80\%$):

In this case, the performance of the proposed EMS was evaluated for varying load conditions while the battery SoC was near its upper limit with $SoC \approx 80\%$, as shown in Figure.5.16. Initial $P_{load} \approx 80W$, $P_{pv} \approx 70W$, and $P_{fc} \approx 2W$. As $P_{load} > P_{pv} + P_{fc}$ and $SoC \approx 80\%$, the proposed EMS ensured that MPPT operation for PV and fuel cell was in minimum power operation mode so that the battery discharged by supplying additional power $P_{bat} \approx 8W$. At the time, t_1, the total load was P_{load} in DC microgrid, and it decreased to $73W$(Figure. 5.16 (a)). Even though the load decreased, $P_{load} > P_{pv} + P_{fc}$, the PV and fuel cell showed similar operation to that in the pre-disturbance phase. However, the battery output power (P_{bat}) reduced to $1W$. At time t_2, the load was brought back to its initial value, which made all sources deliver the same output power as provided during the initial operation.

Figure 5.16: BESS $SoC = 80\%$ with load changes:(a) Load power (P_{load}) PV power (P_{pv}) Fuel cell power (P_{fc}), and (b) Battery $SoC(\%)$, DC link Voltage(V_{dc})

5.6.2 Case-(ii) ($SoC = 80\%$:

In this case, the load demand was held constant at $(P_{load} = 72W)$ and PV was shaded from t_1 to t_2 as shown in Figure.5.17 (a). Initially, as $P_{load} > P_{pv} + P_{fc}$ and $SoC \approx 80\%$, the PV was operated in MPPT with output power $P_{pv} = 70W$; the fuel cell was operated at minimum power with $P_{fc} = 2W$ and the battery was in floating mode. At t_1, PV irradiance reduced which also decreased PV MPP to $P_{pv} = 60W$. As $P_{load} > P_{pv} + P_{fc}$ and $SoC \approx 80\%$, the battery supplied power of $P_{bat} = 10W$ to meet the load demand as shown in Figure. 5.17 (b). At t_2, PV irradiance was restored to initial value due to which the battery was operated in floating mode.

5.6.3 Case-(iii) ($SoC = 20\%$):

Initially, $P_{load} \approx 82W$, $P_{pv} \approx 70W$, $P_{fc} \approx 50W$, and $SoC \approx 20\%$. The recommended EMS assured MPPT operations for PV, and fuel cell for maximum power operations to sustain load demand and charge the battery with a power rating of $P_{bat} = 38W$, which was done by delivering additional power from the fuel cell, as $P_{load} < P_{pv} + P_f c$ and $SoC \approx 21\%$. The load demand P_{load} in DC microgrid was reduced to $74W$ at time t_1, as illustrated in Figure. 5.18 (a). Even though the load was reduced, PV was unable to meet the load requirement; thus, the fuel cell inputs hydrogen to the maximum in supply mode ($P_{fc} = 46W$) in combination with PV to meet the
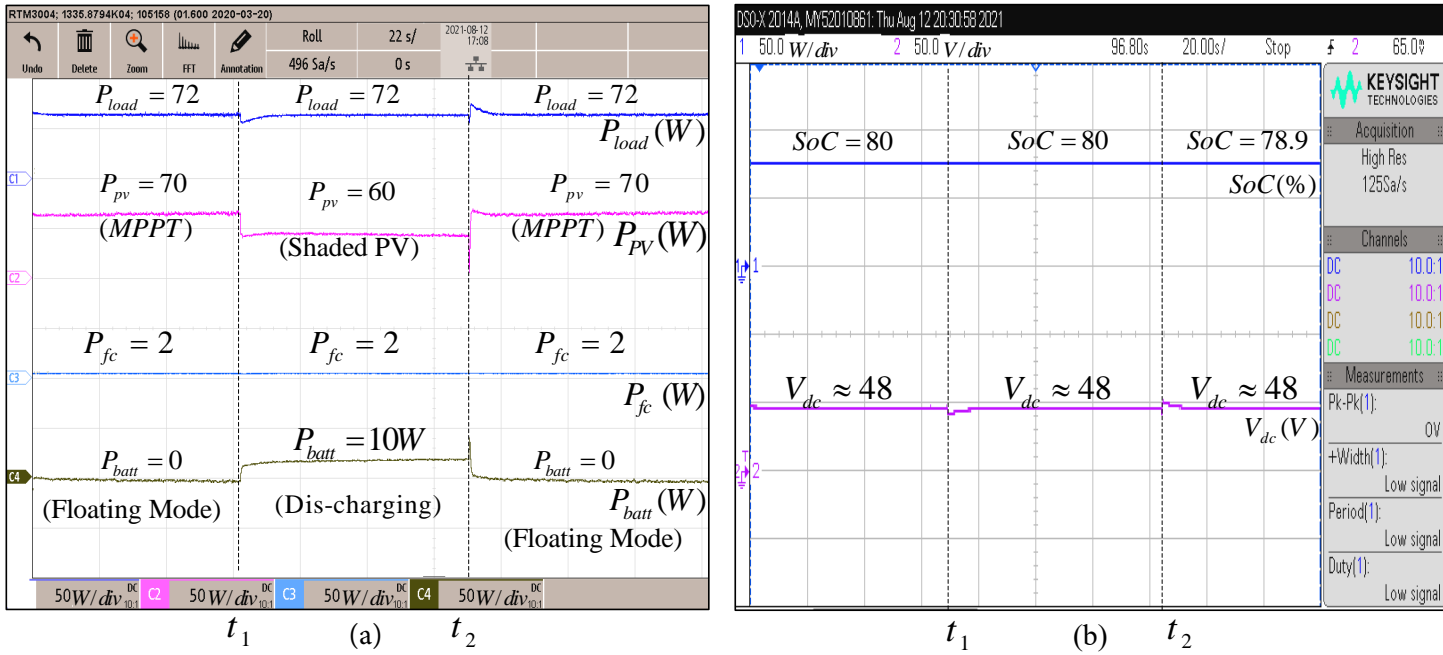
Figure 5.17: BESS $SoC = 80\%$ with PV shaded Condition: (a) Load power (P_{load}) PV power (P_{pv}) Fuel cell power (P_{fc}), and (b) Battery $SoC(\%)$, DC link Voltage(V_{dc})

load demand, and charge the battery. At time t_2, the load is reset to power output as shown in Figures.5.18 (a),and (b). as all sources generate the same power in initial operation.

5.6.4   Case-(iv): ($SoC = 20\%$

As illustrated in Figure.5.19 (a), the total load is kept constant at ($P_{load} = 82W$), and PV is shaded from t_1 to t_2.At first, because $P_{load} > P_{pv}$ and $SoC \approx 20\%$, the PV functioned in MPPT with a power output of $P_{pv} = 70W$, and the fuel cell was required to implement maximum output power mode with $P_{fc} = 50W$ to sustain power demands and recharge the battery with an output power of $P_{fc} = 38W$. At t_1 instant, PV irradiation was lowered from $1000W/m^2$ to $700W/m^2$ which also lowered PV MPP to $P_{pv} = 60W$. Because of $P_{load} > P_{pv}$ and $SoC \approx 20\%$, a fuel cell with a power rating of $P_{fc} = 50W$ was required to fulfil the load demand and charge the battery, as shown in Figures.5.19 (a) and (b). The PV irradiation was returned to its initial value at t_2, allowing the battery to function in charging mode.

5.7   Comparative studies

In this chapter, the PI control in MATLAB was configured with three input signals to PV, FC, and battery. The efficacy of the proposed EMS was evaluated by comparing it against existing approaches developed in [149] and [150] and their comparison is tabulated in 5.2. Strategy I and II were taken from [149] and [150], respectively.They isolate microgrid with PV, fuel cell,
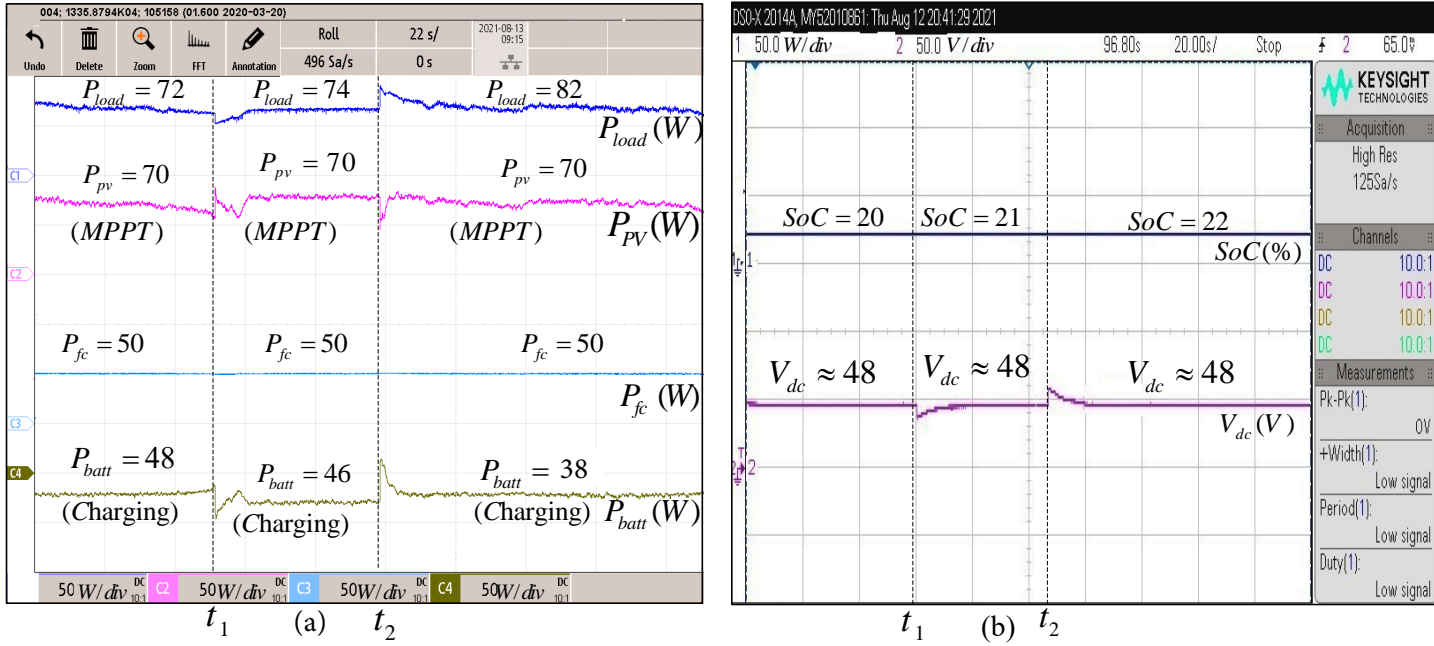
Figure 5.18: BESS $SoC = 20\%$ with load changes (a) Load power (P_{load}) PV power (P_{pv}) Fuel cell power (P_{fc}), and(b) Battery $SoC(\%)$, DC link Voltage(V_{dc})
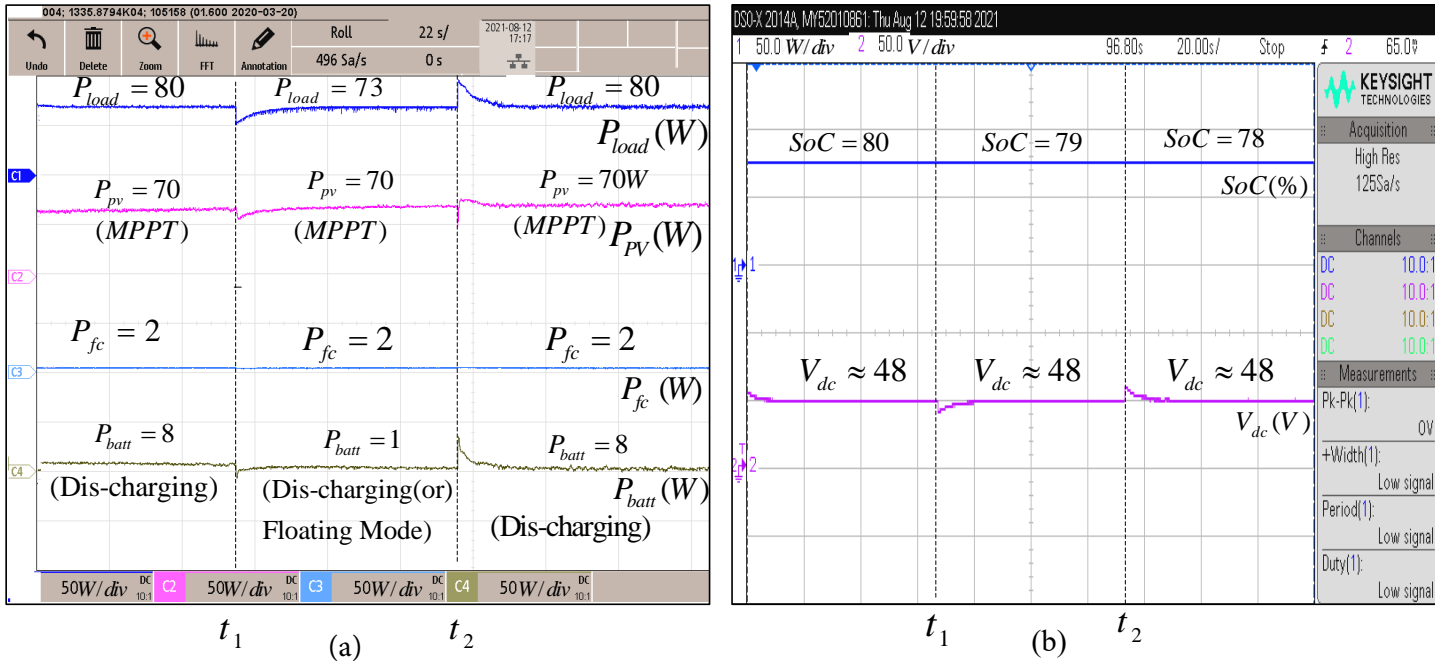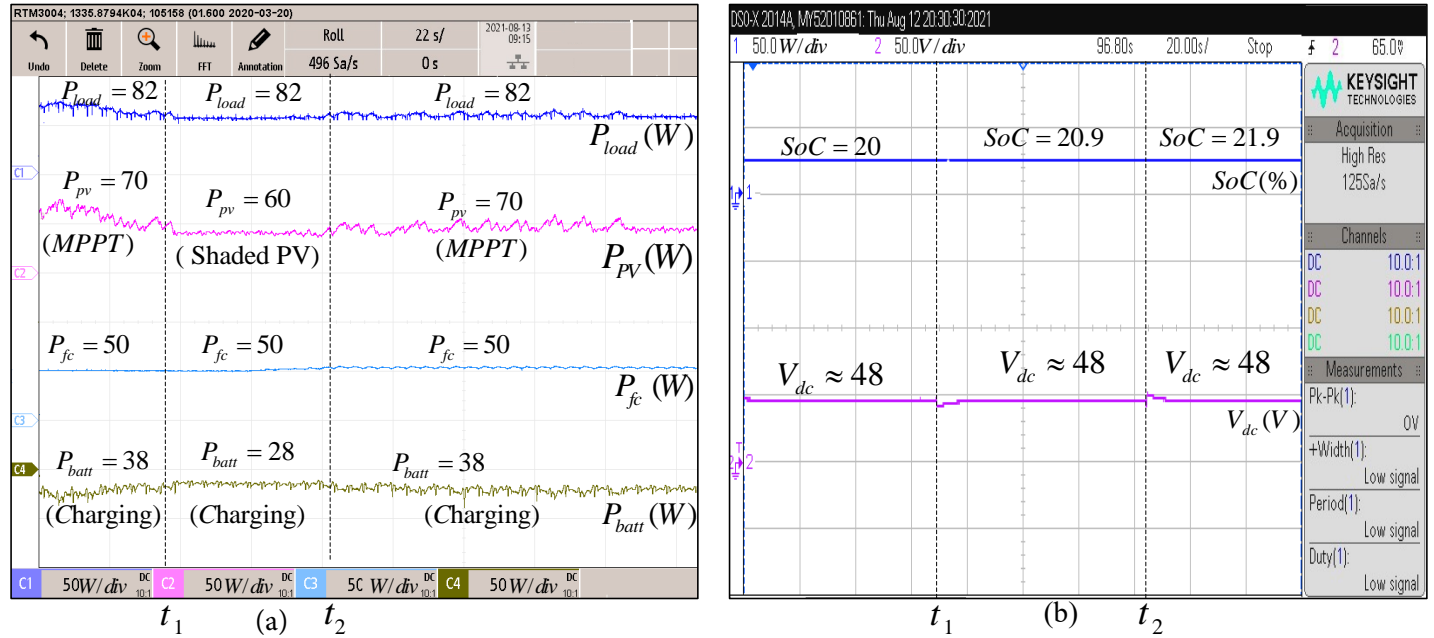

Figure 5.19: BESS $SoC = 20\%$ with PV shaded condition: (a) Load power (P_{load}) PV power (P_{pv}) Fuel cell power (P_{fc}), and (b) Battery $SoC(\%)$, DC link Voltage(V_{dc})
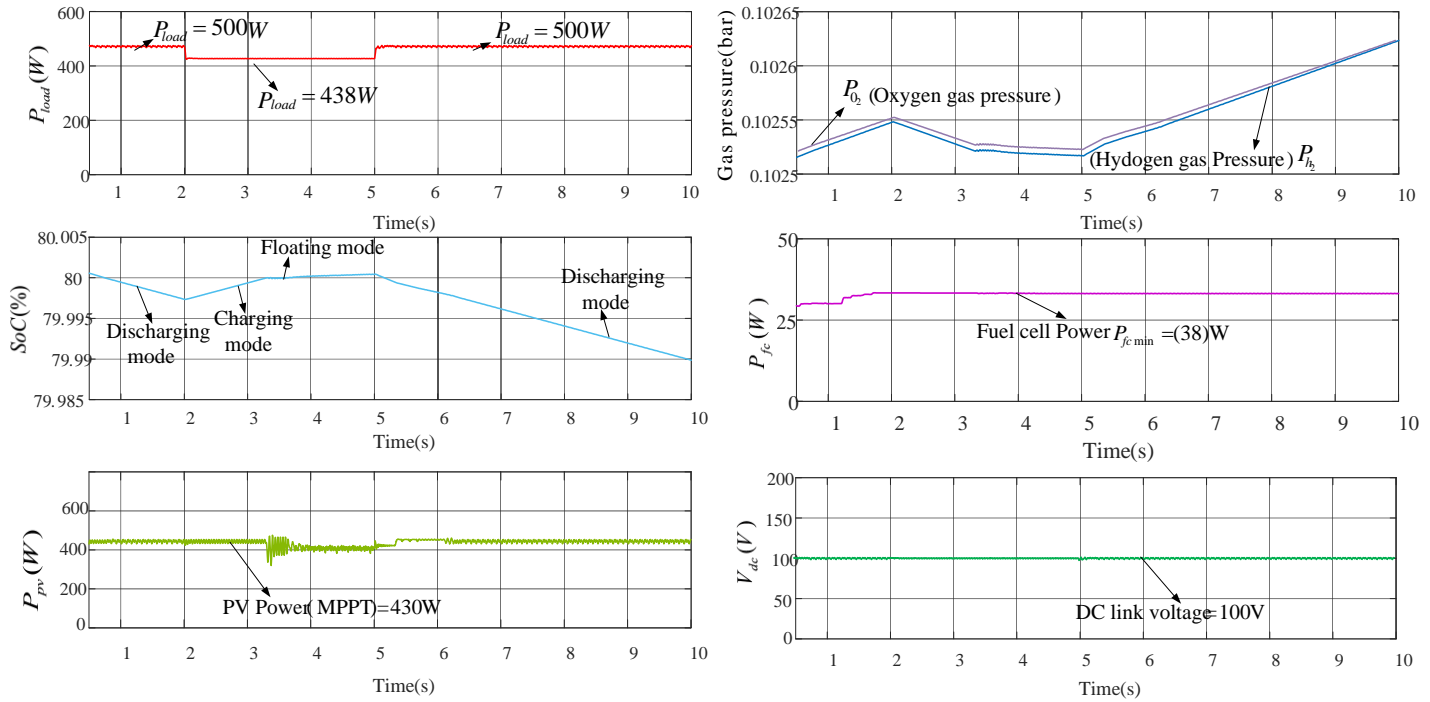
Figure 5.20: BESS $SoC = 80\%$, load changes with proposed EMS (a) Load power (P_{load}) (b) Battery $SoC(\%)$ (c) PV power (P_{pv}) (d) Hydrogen pressure (P_{h2}), and Oxygen gas pressure (P_{o2}) (e) Fuel cell power (P_{fc}) (f) DC link voltage(V_{dc})

battery, and load power under two different operating conditions with battery SoC were maximum condition ($SoC_{max} = 80\%$) and minimum condition ($SoC_{min} = 20\%$) which considered for direct comparative analysis. In Table 5.2, an analytical comparison of existing techniques under various operating scenarios with load fluctuation is presented.

5.7.1   Energy management strategy comparison with conventional method:

Figure.5.21 and Figure 5.22 show the system operation with EMS in [149] and the proposed strategy. In Figure. 5.21, initially, from $t = 0s$ to $2s$,$P_{load} = 700W$, and PV was operated at MPPT with $P_{pv} = 430W$, and fuel cell supplying power of $220W$ as load was greater than generation, and the battery was in discharging mode. When the load was suddenly reduced to ($P_{load} = 600W$) in 2 seconds, the battery started charging and went beyond maximum SoCmax, i.e. 80%, leading to deep charging mode as shown in Figure 5.22. At t=5s, the load was again increased to 700W, thus discharging the battery. But with the proposed EMS technique (shown in Figure. 5.22), at $t = 2s$, when the load demand falls to $P_{load} = 435W$, the total demand was less than the generation. This enables the charging of battery, however, battery SoC reached to 80%, PV was automatically derated to 400W to avoid deep charging as shown in Figure 5.22.
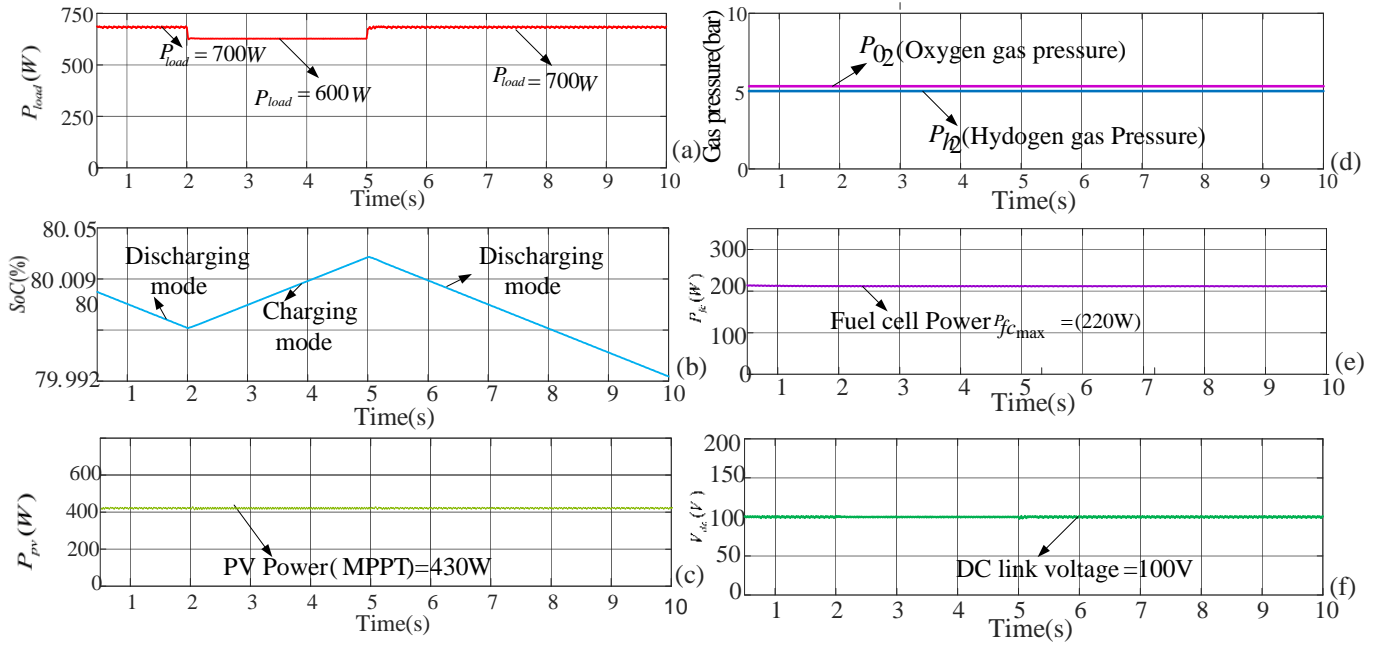
Figure 5.21: BESS $SoC = 80\%$, load changes without EMS (a) Load power (P_{load}) (b) Battery $SoC(\%)$ (c) PV power (P_{pv}) (d) Hydrogen pressure (P_{h2}), and Oxygen gas pressure (P_{o2}) (e) Fuel cell power (P_{fc}) (f) DC link voltage(V_{dc})
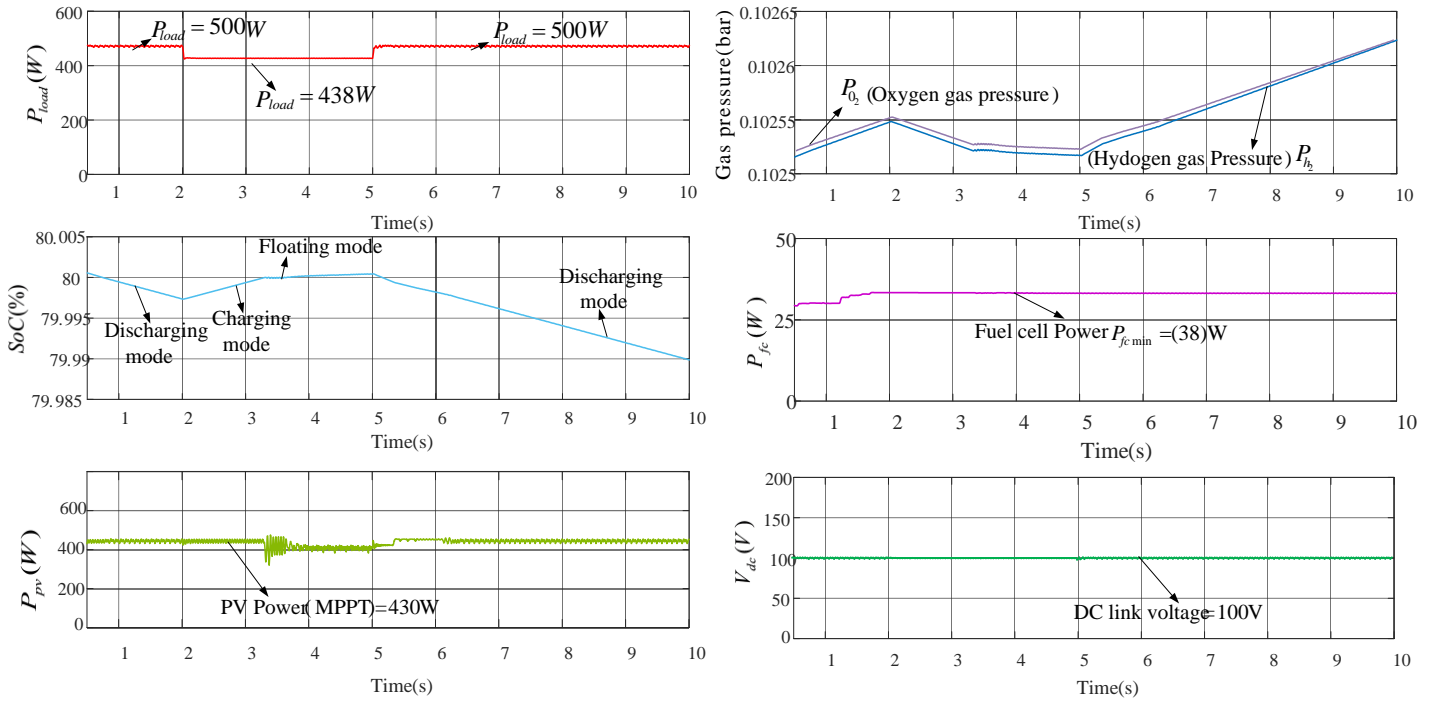
Figure 5.22: BESS $SoC = 80\%$, load changes with proposed EMS (a) Load power (P_{load}) (b) Battery $SoC(\%)$ (c) PV power (P_{pv}) (d) Hydrogen pressure (P_{h2}), and Oxygen gas pressure (P_{o2}) (e) Fuel cell power (P_{fc}) (f) DC link voltage(V_{dc})

110

Table 5.2: Comparison of the proposed method against strategies [149] and [150]

Operation condition of DC microgrid and status of battery	Strategy-I [150]	Strategy-II [149]	Proposed EMS method
Case.1 (SoC >= 80%), under load variation	The PV controller is not designed to have derating mode.	The PV controller is not designed to have derating mode.	The PV system can operate in derating mode as per requirement.
	The battery can be over charged beyond safe limits under light load.	The battery can be over charged beyond safe limits under light load	The battery SoC is maintained at maximum limit, by derating PV.
Case.2 (20%<SoC<80%), under load variation	The fuel cell operates at constant power with no control over the Ph2 and Po$_2$ pressure.	The fuel cell operates output power is varied by using addition control command from the controller. But no control over the Ph2 and Po2 pressure	The fuel cell power output is regulated using reverse sigmoidal function SoC, without loosing much of fuel cell efficiency
	The PV system is operating in MPPT Mode	The PV system is operating in MPPT Mode.	The PV system is operating MPPT Mode.
Case.3 (SoC <= 20%), under load variations	The battery can be deeply discharged.	The battery can be deeply discharged.	The battery SoC maintains (discharging, charging, and floating modes) by regulating the Ph2 and Po2 pressures within limitations.

111

5.8   Conclusions

In this chapter, an effective EMS was proposed for standalone DC microgrid with PV/fuel cell/energy storage Systems. The EMS was developed for improved longevity of battery by maintaining the battery's *SoC* in an acceptable range and also for reduced hydrogen fuel intake in a fuel cell without compromising system reliability. In normal operation, the PV system operates in MPPT mode to maximize the utilization of renewable energy. The fuel cell is operated as a function of battery *SoC* to avoid deep charging/discharging of the battery, which also improves the fuel cell efficiency. The battery bank is managed by EMS to ensure balanced power distribution across sources and loads while regulating DC link voltage. The improved functionality of EMS manages the power flow between the fuel cell generating system and the storage battery under various operating conditions.

The operating conditions are classified into 9 operational states based on BESS *SoC*, the system's total demand power, as well as optimal working points of distributed generators. These operational modes enable the de-rated operation of PV system under light load and high SoC conditions, MPPT operation of fuel cell under heavy load and low *SoC*. This avoids deep charging/discharging of batteries, thereby improving their longevity, efficiency of the fuel cell under normal conditions, and increasing reliability of the system under extreme conditions. The proposed EMS was validated in simulation and on hardware DC microgrid prototype under various battery *SoC* levels and loading conditions. According to the results, this method is able to regulate diverse distributed generation systems while maintaining power balance, as well as optimizing DC microgrid system. Further, the EMS can be slightly modified for effective operation of the system under transient conditions while limiting the battery discharge rate within acceptable limits using super-capacitor. Additionally, the application of the proposed EMS algorithm can be extended to microgrids with heterogeneous distributed generators.

Chapter 6

Optimal Coordinated Energy Management Strategy for Standalone Solar Photovoltaic System with Hybrid Energy Storage

6.1 Introduction

In nanogrid, energy storage systems (ESS) are commonly employed to compensate power imbalance between generation and load demand. ESSs are also used to address issues like energy management, peak(or)maximum shaving, power quality, transient stability response, load levelling, voltage control, and provide uninterrupted power supply. Various energy storage devices are classified according to factors such as energy and power density, life cycle, ramp limit, and so on [151]. Battery energy storage systems (BESS), and Supercapacitor(SC) are the most commonly used ESS technologies. With advancements in battery technology, BESS has a wide range of applications in electric and hybrid vehicles, aeroplanes, DC shipboards, and other applications of DC and AC microgrids.

To address these issues, an adaptive charge discharge rate limit regulation with optimization technique has been developed. The key contributions of the proposed control schemes are:

- Optimise the amount of energy charge/discharge from BESS during the transient condition using EMS.

- Optimise BESS's charge/discharge rate limitation.

- Optimise the time period in which BESS is discharging and charging at its greatest possible rate with EMS, and

- A PV system de-rating approach was intended to successfully overcome deep charging of the battery under light load situations.

6.2 System configuration and control

A DC nanogrid consists of a photovoltaic (PV) system, a battery energy storage system (BESS), a supercapacitor (SC), and power electronic converters, as shown in Figure.6.1. The PV system is the major energy source that is designed to meet the maximum load demand in the system during day daytime. A boost converter is used to control the PV output power (mostly to track
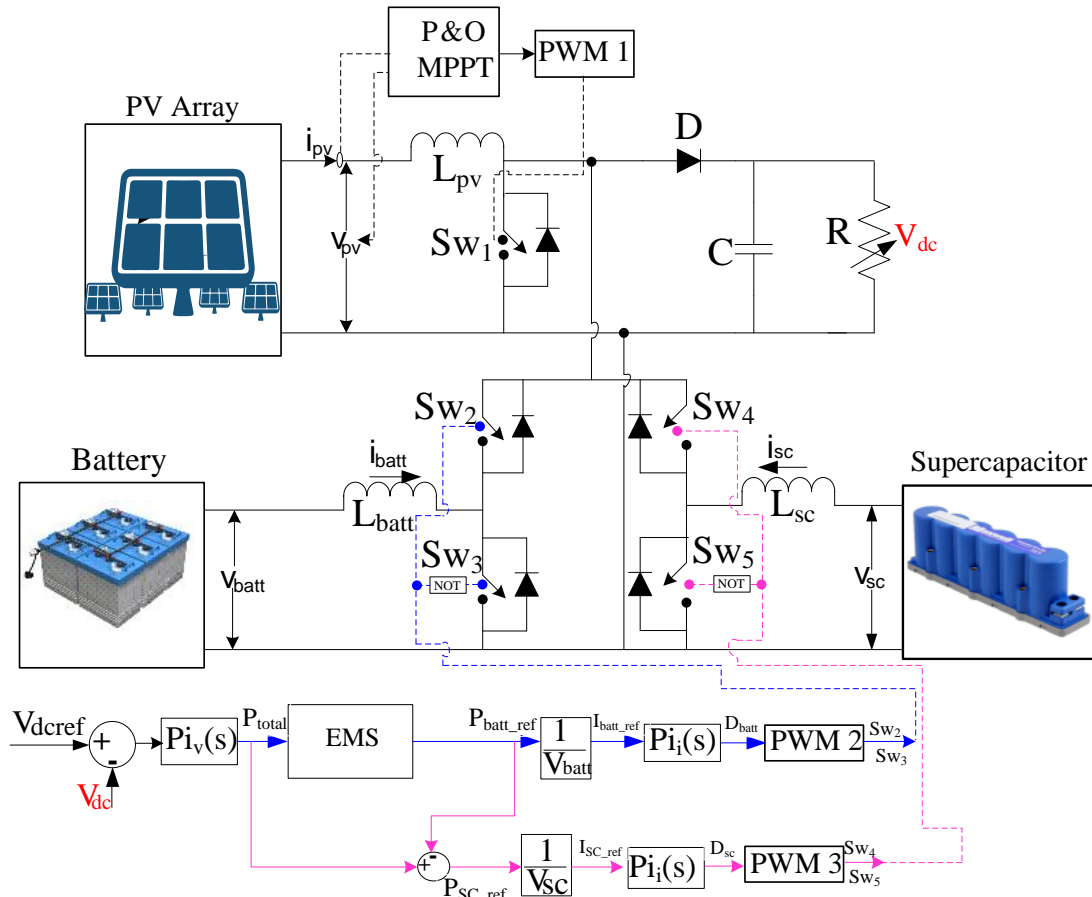
Figure 6.1: Standalone solar PV-BESS-SC nanogrid with energy management system

the maximum power point) and feed the net output power into the network. HESS is linked to a common DC bus through an individual DC-DC bi-directional converter for each storage source. HESS is utilized to regulate the DC voltage (V_{dc}) at the common DC link while supplying power to meet any imbalances between generation and load. The DC–DC bi-directional converter has two operating modes. 1) charging mode if the power generation is greater than the load demand, and 2) discharging mode if generation is lower than the load requirement. The HESS detailed here is capable of fulfilling average power requirements for a long time, and can fulfil the transient power variations for a short duration.

In Figure.6.1, V_{pv}, V_{batt} , and V_{sc} are the terminal voltages, i_{pv}, i_{batt}, i_{sc}, and i_{load} indicate currents, L_{pv}, L_{batt} , and L_{sc} are inductor variables, respectively. The resistance R represents the DC load. SW_1,SW_2, SW_3 ,SW_4, and SW_5 are the controllable switches used in DC–DC power converters. The DC-link voltage is denoted by the symbol V_{dc}. The converters of solar PV systems, BESS, and SC sources are controlled with their respective local controllers as per the commands provided by the proposed energy management strategy (EMS).

114
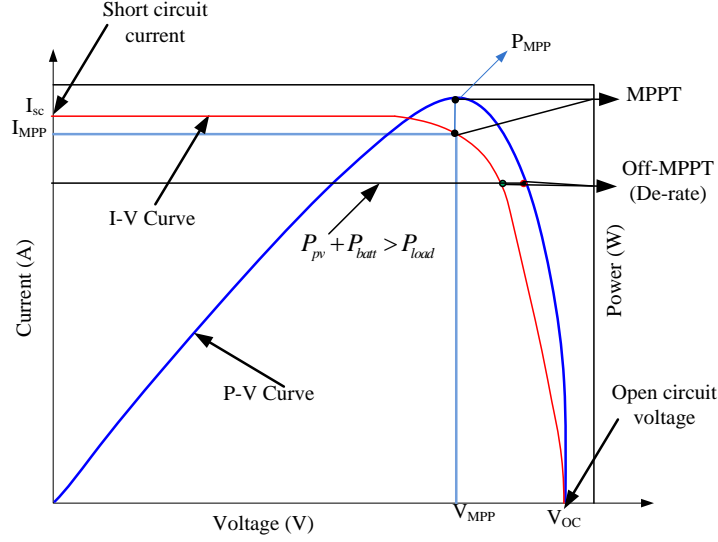
Figure 6.2: Solar P-V and V-I Characteristics

6.2.1 Solar photovoltaic (PV) system

The PV array is modelled using equations given in [152]. Each module is capable of producing power of $80.18W/m^2$ at V_{oc} =21.1V and I_{sc}=3.8A. The PV array is formed by connecting 3 modules in series and one such row in parallel. The standard temperature and irradiance are considered to be 25°C and $1000W/m^2$, respectively. Solar PV systems [91] are usually expected to operate at MPP. However, in the standalone DC nanogrid systems, the PV system is expected to operate either in MPPT mode or off-MPPT (de-rated) mode, based on load. For PV MPPT operation, the conventional perturb-and-observe MPPT [144] is used to track the maximum power point by taking V_{pv} and I_{pv} as inputs. For off-MPPT mode, the operating point of the PV system is shifted to the right side of the MPP (as shown in Figure.6.2) which curbs PV output power to meet energy balance requirements in the system. This is achieved by varying the boost converter duty cycle (D_{pv}) using conditional logic given by equation(6.1).

$$D_{pv} = \begin{cases} D_{pv}^{old} + \Delta D_{pv}, & \text{if } P_{pv} - P_{load} < 0 \\ D_{pv}^{old} - \Delta D_{pv}, & \text{else if } P_{pv} - P_{load} > 0 \\ D_{pv}^{old} & \text{otherwise} \end{cases} \tag{6.1}$$

The PV systems are operating on the right side of MPP in off-MPPT, the difference in PV voltage V_{pv} is low, guaranteeing stable voltage operation in the nano grid. In general, during a normal operation, whenever the battery $SoC < SoC_{max}$, the PV system works in MPPT mode, obtaining maximum power possible. $SoC \geq SoC_{max}$, signifies an off-MPPT operation, decreasing PV output power to prevent deep charging of the battery, as illustrated in the flowchat shown in Figure.6.3.

115

Start

Initialize $D_{pv}^{old}, V_{pv}^{old}, I_{pv}^{old}$

Read V_{pv}, I_{pv}, P_{load}

Calculate $P_{pv} = V_{pv} I_{pv},\ P_{pv}^{old} = V_{pv}^{old} I_{pv}^{old}$
$\Delta P_{pv} = P_{pv} - P_{pv}^{old},\ \Delta V_{pv} = V_{pv} - V_{pv}^{old}$

Assign $D_{pv}^{old} = D_{pv}$,
$V_{pv}^{old} = V_{pv}, I_{pv}^{old} = I_{pv}$

Full load

No (Off-MPPT)

Yes (MPPT)

$P_{pv} - P_{load} > 0$

No

Yes

$D_{pv} = D_{pv}^{old} - \Delta D$

$D_{pv} = D_{pv}^{old} + \Delta D$

$\Delta P_{pv} = 0$

Yes

$D_{pv} = D_{pv}^{old}$

No

$\Delta P_{pv} > 0$

No

Yes

$\Delta V_{pv} < 0$

No

Yes

$\Delta V_{pv} < 0$

No

Yes

$D_{pv} = D_{pv}^{old} + \Delta D$

$D_{pv} = D_{pv}^{old} - \Delta D$

$D_{pv} = D_{pv}^{old} - \Delta D$

$D_{pv} = D_{pv}^{old} - \Delta D$
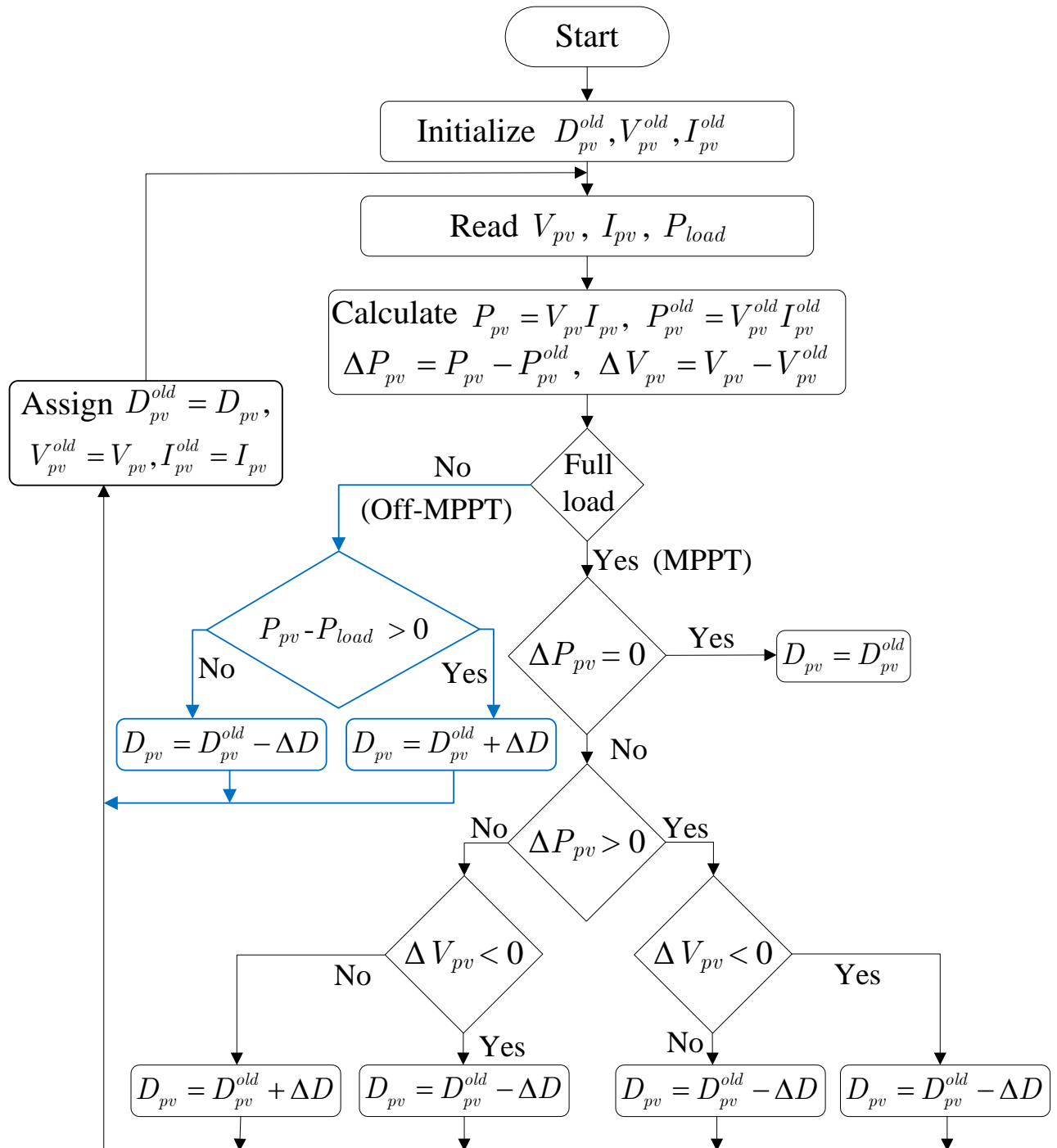
Figure 6.3: Flow Chart of P&O MPPT for PV System

116

6.2.1.1 Design process of PV system

The solar radiation availability, its allowance area, and the PV module efficiency all affect how much electricity solar PV systems can produce [153]. A PV device's hourly output of electrical power may be calculated as:

$$P_{pv} = A_{pv} * H_{t(AV)} * \eta_{pv} \tag{6.2}$$

where P_{pv} is the hourly electrical power generated, $H_{t(AV)}$ is the place's daily hour solar irradiance, η_{pv} is the PV panels' efficacy, and A_{pv} is the zone of the PV panel. The size of the PV panels required to satisfy a specific load requirements is given by:

$$A_{pv} = \frac{E_L}{H_{t(AV)} * \eta_{pv} * \eta_{batt} * A_{Tcf}} \tag{6.3}$$

where E_L is the expected overall energy requirement, $\eta_{(batt)}$ is the efficacy of BESS, and A_{Tcf} is the temperature adjustment factor. This variable corrects for testing conditions and takes into account the temperature-related reduction in cell voltage. In this work, the value is estimated to be 0.8. The number of PV panels($P_{pv)}$ required to provide the required power may be estimated using the equation below:

$$\eta_{pv} = \frac{P_{pv}}{PV_{peak}} \tag{6.4}$$

where the terms η_{pv} and PV_{peak} refer to the quantity of PV panels and their individual peak powers, respectively. The International Institute of Tropical Agriculture in Ibadan provided the solar irradiance data employed in this chapter's modeling. Table.6.1 presents the PV module's specifications, which were employed in this study.

6.2.2 Battery energy storage system (BESS)

A 12V, 120Ah lead-acid BESS is considered for nanogrid operation. The battery model is changed to suit the datasheet parameters provided in the manufacturer's catalog [154]. The battery is critical to the effectiveness of HESS because it supplies consistent power to the DC link. The mathematical formulation of a lead-acid battery bank is adapted from [155], as illustrated in Figure.6.4. Battery functioning is dependent on SoC of battery bank, and BESS SoC variations slower than SC. SoC was maintained between 20% and 80% for the safety of HESS. The BESS model equations are presented in Equations. (6.5), (6.6), and (6.7).
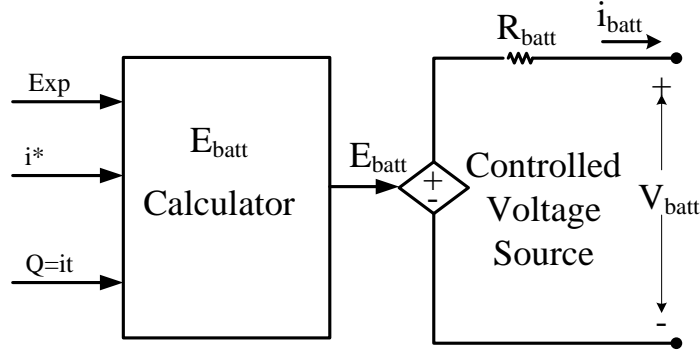
Figure 6.4: Mathematical model of lead acid battery [156]

$$E_{batt} = E_o - K\frac{Q}{i_{batt}t - 0.1Q}(i_{batt}t + i_{batt}^* + Exp(t) \tag{6.5}$$

$$V_{batt} = E_{batt} - i_{batt}R_{batt} \tag{6.6}$$

$$Exp(t) = B.|i(t)|.(-Exp(t) + A.u(t)) \tag{6.7}$$

Where i_{batt} = BESS current(A), i_{batt}^* = filtered BESS current (A), Exp denotes BESS's exponentially zone voltage(V), and Q = BESS capacity (Ah), i_{batt} = actual BESS charge. A = exponential voltage (V), B = exponential capacity Ah^{-1}, R_{batt} = BESS internal resistance (Ω), E_{batt} = Energy released by BESS(W).

6.2.2.1 Design process of BESS

Considering the voltage level (V_s), the BESS's depth of discharge (DoD), and its efficacy, the total capacity of BESS (Wh) required for a certain application may be computed [153] as follows:

$$A_{pv} = \frac{D_d x E_L}{\eta_{batt} * DoD * V_s} \tag{6.8}$$

wherein D_d is the total number of autonomous days. The system's needed battery count may be calculated using the equation given below:

$$\eta_{batt} = \frac{C_{batt}}{C_{sg}} \tag{6.9}$$

Where C_{sg} is the storage capacity of a single battery in Ah. The parameters of the battery are furnished in Table.6.1
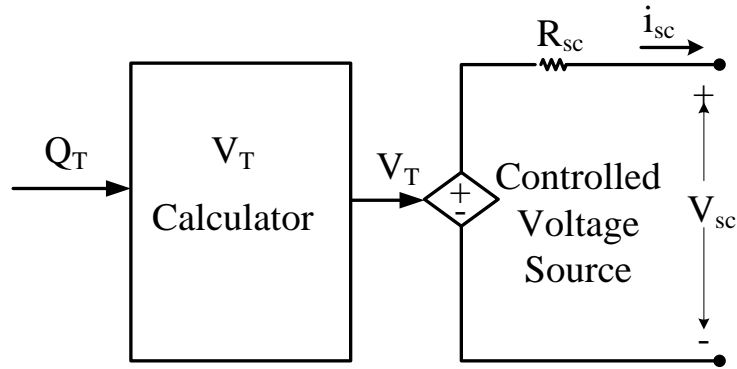
Figure 6.5: Mathematical model of supercapacitor [159]

6.2.3   Supercapacitor(SC) energy storage system

Under changing loads that require great instantaneous power, having a single energy supply for such purposes would lead to thermal as well as power quality difficulties. Most of these difficulties are mitigated and power stability is improved by including SC. In this approach, changing loads are established by connecting various power loads in parallel via regulated switches [157]. The supercapacitor (SC) serves as a link between the conventional capacitor and also BESS. SC is well suited for transitory applications because of its quick response time and capacitance of a few hundred Farads. For SC evaluation, the SC modeling provided in math works [158] was employed. The SC numerical analysis is a hybrid of Helmholtz and Gouy–Chapman models as shown in Figure.6.5. Equations. (6.10), (6.11) and (6.12). provide the formula for SC inner voltage with SoC. The maximal amount of energy that may be stored in SC is given by

$$E_{sc,max} = \frac{1}{2} C_{sc} V_{sc,max}^2 \tag{6.10}$$

The amount of energy saved by SC at every particular time,$E_{sc}(t)$ is given by:

$$E_{sc,max} = \frac{1}{2} C_{sc} V_{sc}^2(t) \tag{6.11}$$

The following are the relationships between SC's energies and SoC:

$$SoC_{sc} = \frac{E_{sc}(t)}{E_{sc,max}} \tag{6.12}$$

As a result, the SoC of SC depicts the fluctuations in energy over time. As a result, SoC is provided in the form of charge, as shown in equation.(6.13)

$$SoC_{sc} = \frac{Q_{int} - \int_0^t i(t)dt}{Q_T} \tag{6.13}$$

119

Here, Q_T is the total charge stored by internal SC (Coulomb).

One of the goals of this chapter is to determine the right combination of system components that will have minimum life cycle cost and meet the power demand requirement.

6.2.3.1   Design process of supercapacitor

When switched on, supercapacitors may be employed to supply higher current needed by induction machines since they are high-density power storage systems [153]. They are not suitable for this application by themselves due to the low energy density. Hence, they are compatible with BESS. Although SC typically have low voltage, they must be linked in series when used in applications where the voltage level is higher than that of a single capacitor. SC is linked in parallel to enhance the amount of energy that may be stored. The total capacitance C of any combination of supercapacitors in series and in parallel is given in equation.6.14.

$$C = \frac{n}{m} C_f, \tag{6.14}$$

where m refers to the amount of SC operating in parallel and n refers to the amount of SC operating in series. Each supercapacitor has a capacitance C_f. The SC's maximum potential energy output in joules is given by

$$Q_{sc} = 0.5C * (V_{scmax}^2 - V_{scmin}) \tag{6.15}$$

where V_{scmax} and V_{scmin} stand for the SC's maximum and minimum voltages, respectively. Using the formula $1J = 2.78 * 10^{-7} kWh$, the energy supplied by the SC may be translated to kWh. Table. 6.1 provides the SC parameters utilized in this study.

6.3   Cost analysis of PV/battery and supercapacitor:

In the simulation test system, the daily residential average load is considered to be around $240W$, with the peak load being around $P_{loadmax}=610W$. The daily energy load demand is $E_{load}=210W * 24hr=5.04kWh$. To meet this load demand, the installed capacity of PV and batteries is calculated, as given in [153], which comes to $P_{pv}=205W$ and $E_{battery}=7200VAh$. But additionally, if a supercapacitor is used along with PV and Battery system, the net required installed capacities of each component is $P_{pv}=205W$, $E_{battery}=5760VAh$ and $C_{sc}=99F$ (at $V_{sc}=24V$). To give a complete economic analysis, three cost components are considered: (i)the initial cost, (ii)the cost of repairs at current value, and (iii)the expense of use and service [153].
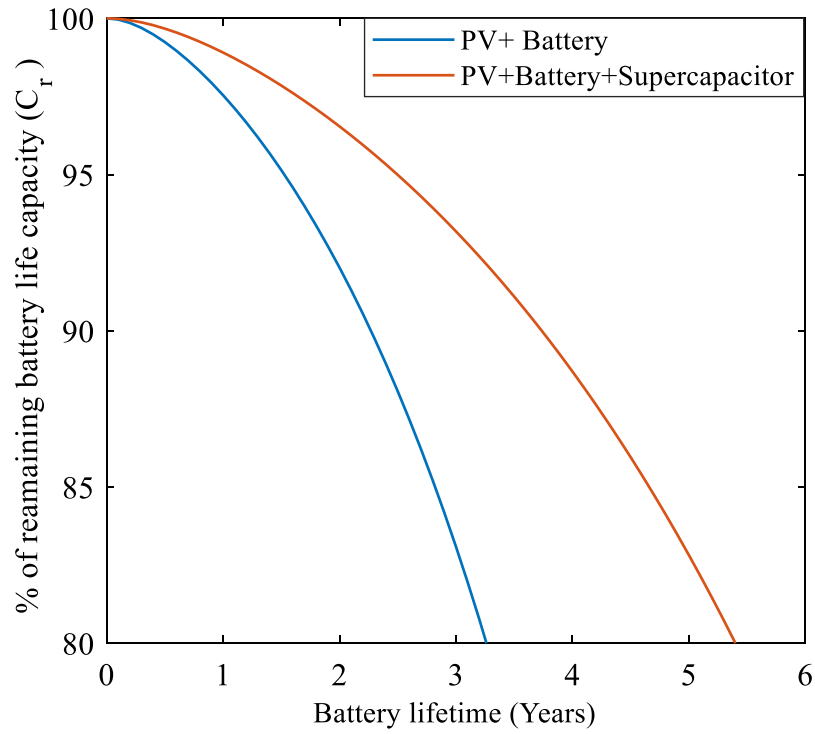
Figure 6.6: Battery Life time comparison without and with supercapacitor

Table 6.1: Starting cost of the source

System components	PV ($C_{(pv(init))}$) (80 INR/W)	Battery ($C_{batt}(init)$)	Supercapacitor ($C_{sc}(init)$)	Total ($C_{i}nit$)
Unit cost (INR)	19,200	63,860	0	83,060
Unit cost (INR)	19,200	31,200	31,200	102,400

6.3.1 Initial cost:

The initial investment expense incurred while purchasing parts of the system for the very first time is known as "startup cost." The price of device upon launch is listed as

$$C_{init} = C_{pv(init)} + C_{batt(init)} + C_{sc(init)} \tag{6.16}$$

where $C_{(pv(init))}$ is the PV modules' starting cost, $C_{(batt(init))}$ is the initial amount of BESS, and $C_{(sc(init))}$ is the initial amount of SC (Table.6.1).

6.3.2   Present value replacement cost:

The cost of repairing system components as they approach the limit of their service life is considered in the current value purchase price of such components. Inflation and rate of interest, which might affect the system's current value, are considered in this cost as well. The formula for calculating the cost of repairs C_{rep} is:

$$C_{rep} = C_{unit}C_{nom} \sum_{i=1}^{Nrep} \left[\frac{1+f_o}{1+K_d} \right]^{\frac{N_i}{N_{rep+1}}} \tag{6.17}$$

Where f_o is the inflation rate of the replacing unit, k_d is the rate of interest of the replaced element, N_i is the couple of year, and C_{nom} is the value of a system component. using the Schiffer balanced Ah capacity model, the effect of SC on BESS life is determined. By taking into consideration the corrosive loss (C_c) and (C_{deg}) of BESS materials, this method computes BESS's lifespan. When a BESS's capacity (C_r) is less than 80% of its rated capacity (C_0), it is said to have achieved the end of its useful life. The BESS's remaining capacity may be calculated using equation (6.18).

$$C_r = C_0 - C_c - C_{deg} \tag{6.18}$$

where is C_c and C_{deg} are calculated as given in [160];, Figure.6.7 shows the remaining battery capacity with and without the supercapacitor. It is evident that the replacement of the battery was carried out with 3.5 years when the battery alone was used in the system, whereas if the super capacitor is used, then battery life time is increased by almost 2 more years. This reduces the replacement cost C_{rep}.

6.3.3   Present value of operation and maintenance cost:

This cost includes the cost of running and maintaining every element of the device over the duration of the device. It is given by

$$C_{(0\&m)}o = \begin{cases} C_{(0\&m)}o, \left[\frac{1+f_o}{1+K_d} \right] \left[1 - \frac{(1+f_o)}{1+K_d})^n \right], k_d \neq f_1 \\ C_{(0\&m)}o, xn, k_d \neq f_1 \end{cases} \tag{6.19}$$

where $C_{(0m)o}$ represents the initial operating cost and maintenance, f_1 represents the inflation rate for costs, and n represents the lifespan in years. It should be noted that the operation of a supercapacitor requires the bare minimum cost, as there are no dynamic or moving components.
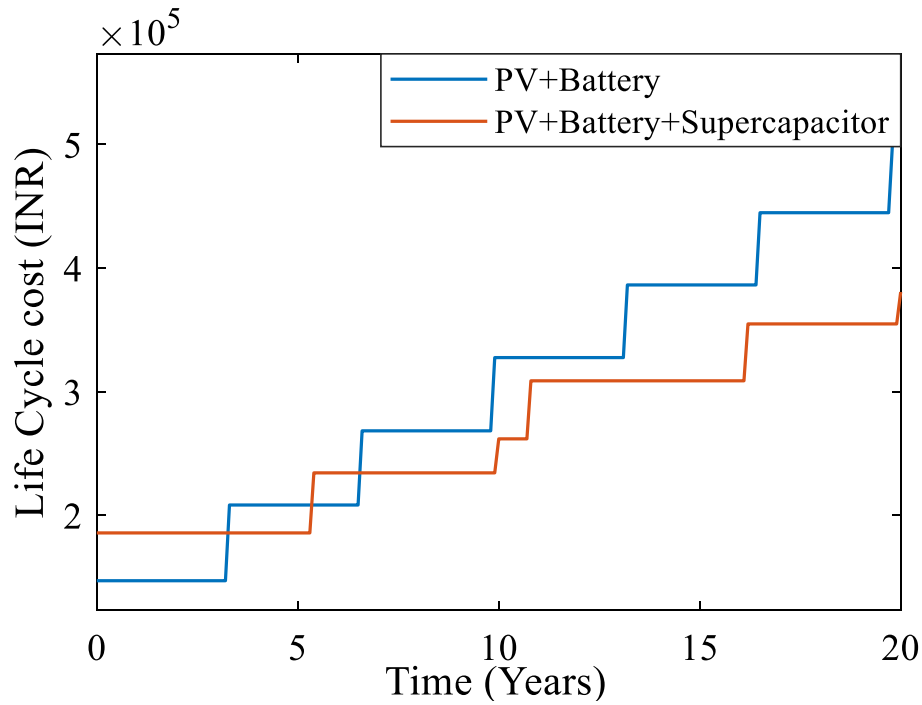
Figure 6.7: Total Cost incurred in the system life time of 20years

6.3.4   Life cycle cost:

The life cycle cost (LCC) includes the initial capital cost of the system, the present value replacement cost of the system component throughout the system's lifetime, and the present value of operation and maintenance cost throughout the system's lifetime. Hence, the life cycle cost is given as equation.(6.20).

$$LCC = C_{init} + C_{crep} + C_{o\&m} \qquad (6.20)$$

Although the initial cost of PV with HESS (INR 102,400) is larger when compared to the PV with BESS (INR 83,060), on inclusion of replacement and maintenance costs, the PV with BESS has becomes more expensive after 6 years, as observed in Figure. 6.6. Here, in our case study, the life of a supercapacitor is pessimistically considered to be 10 years, even though many data sheets claim to have a 10–15 year life span. The comparison in Figure.6.7 shows that PV with HESS is less expensive in the long time if the selected design specifications and control strategy is a fair indicator.

6.4   HESS supported RES configuration

The HESS arrangement that is most frequently utilized to achieve individual control over both BESS and SC is shown in Figure.6.8. The element ESSs under actively parallel arrangement of

123
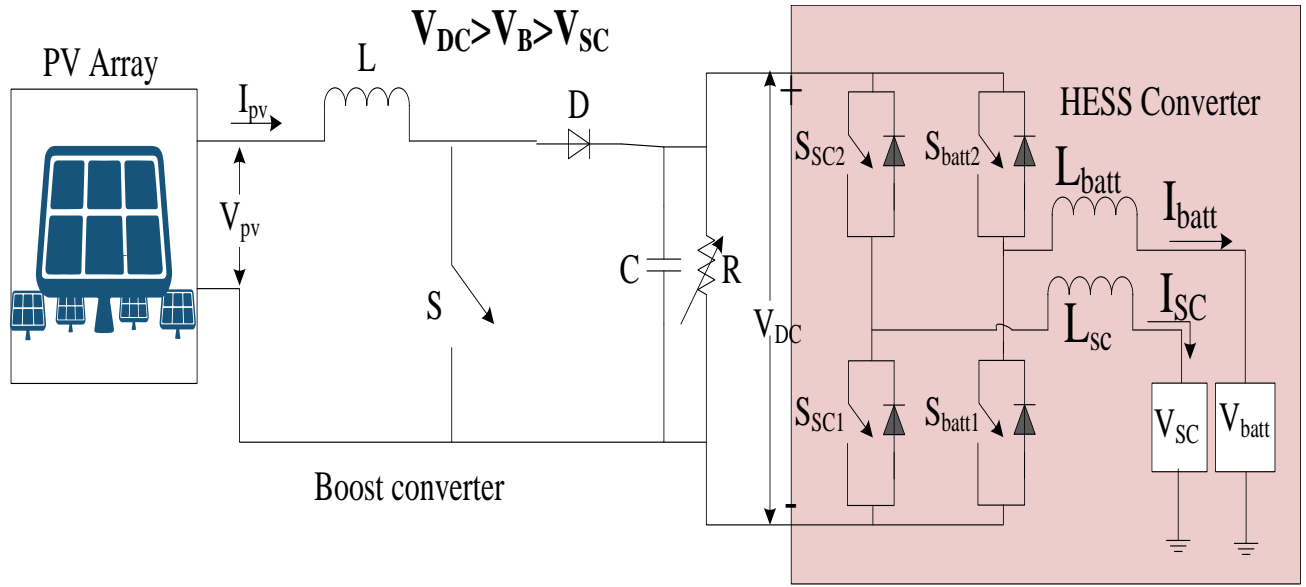
Figure 6.8: DC microgrid setup powered by PV source and supplemented by HESS

HESS might interchange energy, for instance, so,that BESS store the SC ESS or vice-versa. PV serves as the primary power supply for such DC nanogrid and is coupled with a BESS and a SC. The MPP tracking and DC grid interface of PV are done using the DC-DC converter. The PV supply used in this study has an MPP of $80.18W/m^2$ at $21.1V$ and $3.8A$, with a solar irradiation of $1000W/m^2$ and a module temperature of $25°C$. It is possible to correct the mismatch between source power and load power using HESS device, which includes a BESS-SC bank. To link HESS to DC nanogrid, a two-input, four-switch H-bridge DC-DC bidirectional converter is employed. HESS discharge and charge are regulated by two - input bidirectional DC-DC converter. HESS manages the excess or deficiency power at the predetermined reference of DC grid voltage at the location of discrepancy among source power with load power.

6.4.1   Operation of microgrid with HESS

In this part, the functioning of the nanogrid with HESS is described, and the two-input DC-DC bidirectional converter is utilised to regulate HESS (battery management). As shown in Figure.6.8, the system consists of four switching devices arranged in an H-bridge configuration. With this converter design, the battery voltage is chosen to be lower than DC utility grid but more than SC voltage. The BESS and SC legs are linked, accordingly, to higher frequency inductance L_{batt} and L_{sc}. The following sections discuss several types of operations.
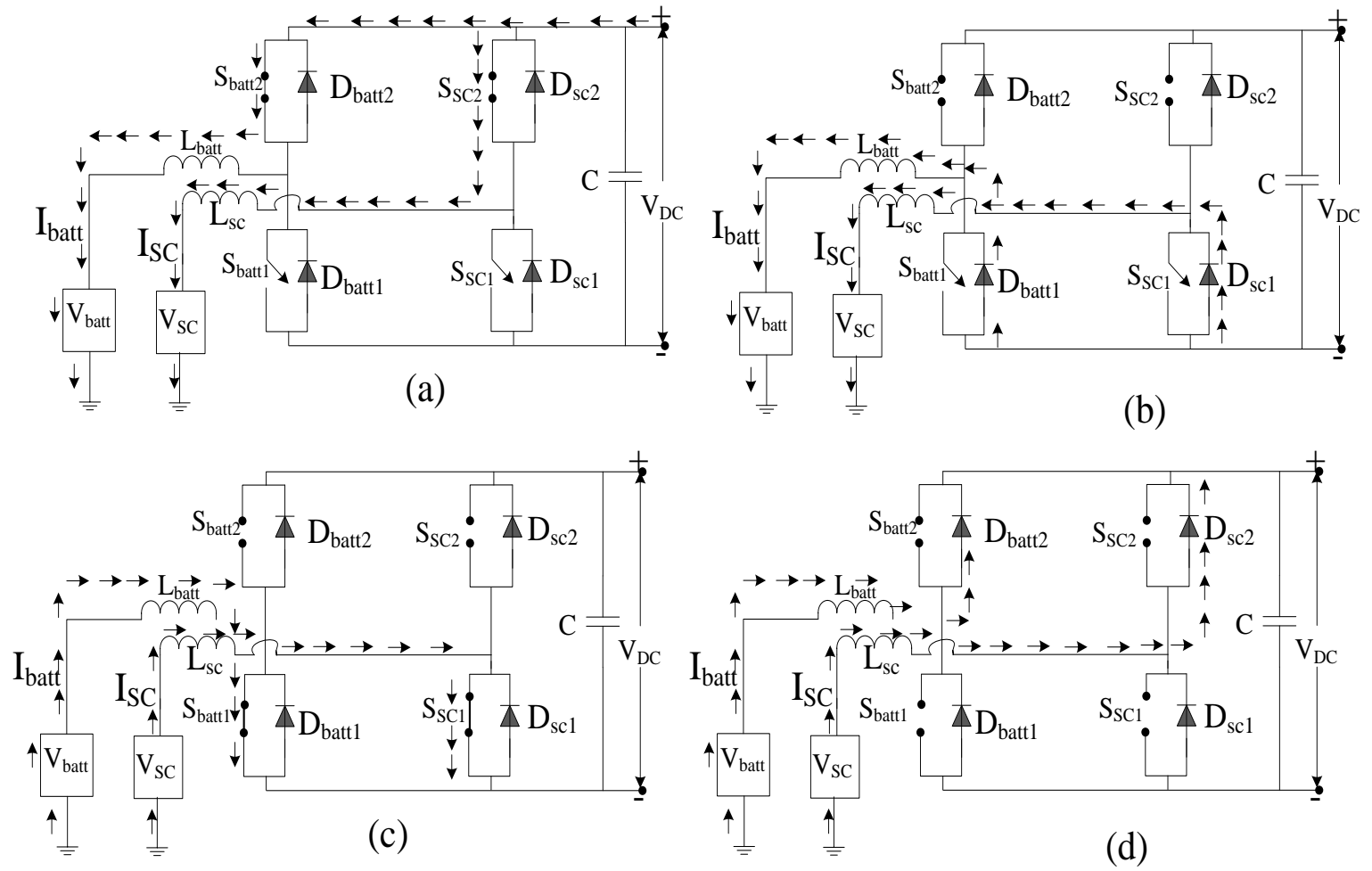
Figure 6.9: Equivalent circuit of bidirectional DC–DC converter:(a),(b) charging mode and (c),(d)discharging mode

6.4.1.1   HESS charging mode

When PV power produced exceeds the necessary load or even when the load reduces, there is extra power, as in a DC nanogrid, which causes the DC grid level voltage to rise. The extra power is used to charge SC and BESS, balancing the DC nanogrid. As a result, electricity from the DC grid is sent to HESS in this state. As indicated in Figure.6.9, the DC-DC converter operations in this state can be split into two time periods. Switches S_{batt2} and S_{sc2} are actuated with a duty ratio throughout the time period T_1, charging the inductances L_{batt} and L_{sc} with respective sources V_{batt} and V_{SC}. As shown in Figure.6.10, current rises with a profile of $(V_{DC}$ $-V_{batt})/ L_{batt}$ and $(V_{DC}-V_{SC})/ L_{sc}$, respectively. After this time (during T_2), two switch devices are switched off, allowing i_{LB} and i_{LS} to freely go via D_{batt1} and D_{sc1}, respectively.

$$V_{batt} = d_{batt}.V_{DC} \qquad\qquad (6.21)$$

$$V_{SC} = d_{SC}.V_{DC} \qquad\qquad (6.22)$$

Where d_{batt} and d_{SC} are now the duty cycles, respectively. Energy is transferred from the DC grid to HESS. More potential exists for the DC grid network than for the HESS. The bidirectional converter is then used in buck mode to recharge HESS.

6.4.1.2   Discharging mode of HESS

DC nanogrid voltage drops when PV generating power reduces owing to decreased irradiance or when demand exceeds PV generating capacity. For this time period, HESS must provide power. Under this state, electricity is transferred from HESS to DC grid by appropriately managing S_{batt1} and S_{sc1} devices. As shown in Figure.6.9, when switches S_{batt1} and S_{sc1} are controlled during each time period T_3, inductors (L_{batt} and L_{sc}) accumulate energy mostly in reverse way, and reversal current flow (i_{Lbatt} and $i-Lsc$) grows with a gradient of V_{batt}/ L_{batt} and V_{SC}/ L_{sc}, respectively.Power flows through HESS to DC grid in the directions shown in Figure.6.10 after its time span T_3 (during time span T_4) as the total of BESS and inductance voltages surpasses DC grid voltage.

$$V_{DC} = \frac{V_{batt}}{1 - d_{batt}} \qquad\qquad (6.23)$$

$$V_{DC} = \frac{V_{SC}}{1 - d_{SC}} \qquad\qquad (6.24)$$

126

since switches S_{batt1}, S_{batt2}, S_{sc1}, and S_{sc2} are operated in a complementary manner. There is just a single gate circuit needed for each switching leg.

6.5   Calculate the converter efficiency

The power efficiency of the system is dependent on power electronic converter losses, which are used in PV and HESS systems. The power efficiency of the standalone system is calculated from the net power loss of individual converters. The power efficiency of PV boost converter is given by:

$$\eta_P^{PV} = \frac{i_{pvo}.v_{dc}}{i_{pv}.v_{pv}} \tag{6.25}$$

Similarly, the power efficiency of the bi-directional converter used for BESS and SC is η_P^{batt}, and η_P^{SC}, respectively. The power efficiency is as follow:

$$\eta_P^{batt} = \frac{i_{batto}.v_{dc}}{i_{batt}.v_{batt}} \tag{6.26}$$

$$\eta_P^{sc} = \frac{i_{sco}.v_{dc}}{i_{sc}.v_{sc}} \tag{6.27}$$

The total power loss in the standalone system is calculated as:

$$P_{loss} = (i_{pv}v_{pv} - i_{pv0})v_{dc}) + (i_{batt}v_{batt} - i_{batt0}v_{dc}) + (i_{SC}v_{SC} - i_{sc0}v_{dc}). \tag{6.28}$$

However, the efficiency that the authors claimed in the manuscript is referred to as "energy efficiency," which depends on the charge and discharge cycles of BESS and SC [161]. The energy efficiency of the storage device is defined by:

$$\eta_{\text{energy}} = \frac{\text{energy (Wh) discharged}}{\text{energy (Wh) required for complete charge}} \tag{6.29}$$

In practice the lead acid battery has an efficiency of η_{energy}^{bat}=70 − 85% while the supercapacitor has an efficiency of η_{energy}^{SC}=85 − 98%. For our system, the battery efficiency was nearly η_{energy}^{bat}=79.4% and for supercapacitor, efficiency was around η_{energy}^{SC}=92.3% for one complete charge-discharge cycle.

6.6   Dynamic modelling of the standalone system:

In this section, the complete small signal modelling (SSM) of the standalone microgrid is devel-
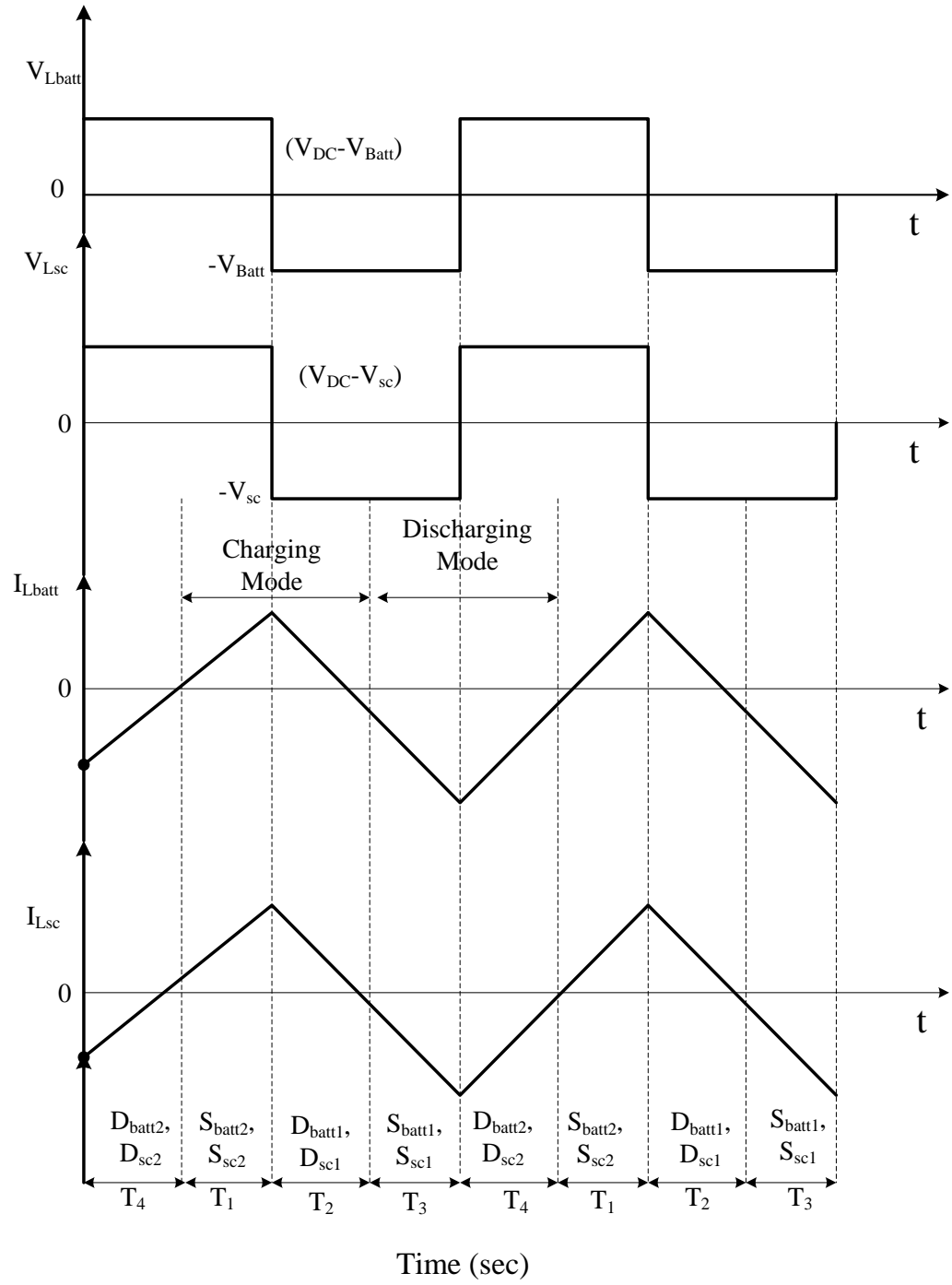
Figure 6.10: Steady state wave forms for HESS charging discharging mode

(a)   (b)
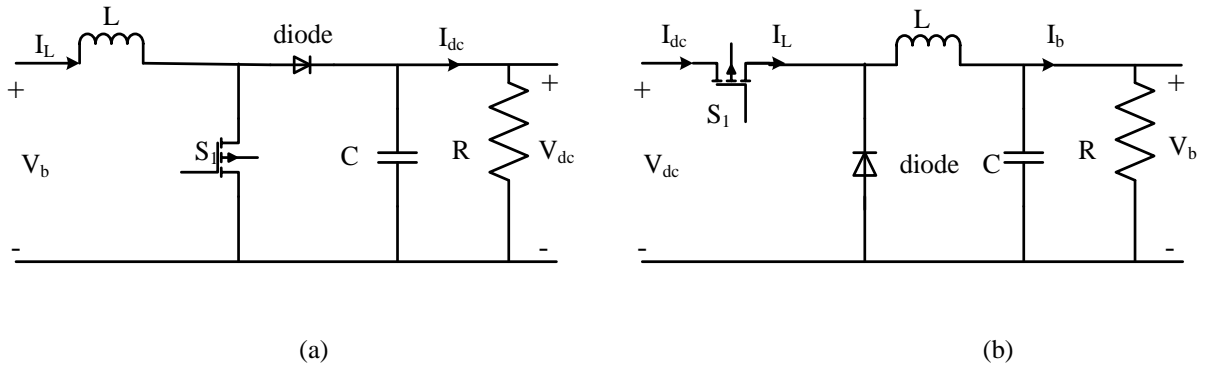
Figure 6.11: Circuit of the DC–DC bidirectional converter in (a) boost-mode and (b) buck-mode operation.

oped. As the switching ripples of the state variables are equal to zero over one switching period of the power converters for both PV and HESS, the small signal averaged model is considered to assume continuous conduction mode. Moreover, the nonlinearities caused by the averaging procedure are eliminated before linearizing the small signal dynamic model.

Small-signal analysis: determining the dynamic behavior of a DC-DC converter is essential for the development of regulation [162]. The resultant LTI model for small signals allows for the use of all common circuit analysis methods. In order to describe the time-domain dynamics in the case of small-signal activation, a continuous variant- time small signal design has been developed. The frequency-spectral (s-domain) small-signal concept is then created by changing the time-spectral small-signal model. The power stage dynamical transfer functions are generated by this transformation, which is necessary for the stability design.

6.6.1   DC-DC bidirectional converter:

The DC-DC bidirectional converter combines boost and buck conversions, with the EMS choosing the proper mode. With such a converter, the BESS and SC are discharged and charged, with the current control system determining the appropriate duty cycles, or d_1 and d_2, of the switches S_1 and S_2, accordingly. In the follow-up, a thorough small-signal design is provided for the instance of boost and buck operating modes.

6.6.2   Boost-mode operation:

The boost-mode is applied for the discharging procedure of the storage (battery or supercapacitor). Figure.6.11(a) shows the circuit of the boost-mode operation of the converter, where the direction of the inductor current is from lower voltage side to higher voltage side. The av-

eraged large signal inductor current, i_L , and the DC-bus output voltage, v_{dc} , in a continuous conduction mode (CCM) of operation can be found using the equations below.

$$\frac{di_L}{dt} = \frac{1}{L}(v_b - (1-d_1)v_{dc}), \frac{d_{vdc}}{dt} = \frac{1}{C}((1-d_1)i_L - i_{dc}) \tag{6.30}$$

where L is the inductance of the converter, C is the capacitance of the converter, v_b is the input voltage (i.e., battery voltage), and i_{dc} is the output current of the converter. Thus, the input voltage and the duty cycle $(v_b(t), d_1(t))$ can be represented by the sum of their quiescent values (V_b, D_1) and small variations in time $(\hat{V}_b(t), \hat{d}_1(t))$.

$$v_b(t) = V_b + \hat{u}_b(t), d_1(t) = D_1 + \hat{d}_1(t). \tag{6.31}$$

$$i_{dc(t)} = I_{dc} + \hat{i}_d c(t), v_{dc}(t) = V_{dc} + \hat{v}_{dc(t)}, i_L(t) = I_L + \hat{i}_L(t) \tag{6.32}$$

Thus, equations in (6.30) can be linearized by expanding and separating the steady-state terms and small-signal terms.

$$L\frac{di_L}{dt} + \frac{di_L\hat{(t)}}{dt} = V_b - \hat{D}_1 V_{dc} + \hat{V}_b(t) + v_{dc}\hat{d}_1(t) - \hat{D}_1\hat{v}_{dc}(t) + \hat{v}_{dc}(t)\hat{d}_1(t) \tag{6.33}$$

$$C\frac{dv_{dc}}{dt} + \frac{dv_d\hat{c}(t)}{dt} = \hat{D}_1 I_L - I_{dc} + \hat{D}_1\hat{i}_L(t) - i_L\hat{d}_1(t) - \hat{i}_{dc}(t) + (-\hat{i}_L(t)\hat{d}_1(t) \tag{6.34}$$

Where $\hat{D}_1 = 1 - D_1$ In state space form:

$$\begin{bmatrix} \frac{d\hat{i}L(t)}{dt} \\ \frac{d\hat{u}dc(t)}{dt} \end{bmatrix} = \begin{bmatrix} 0 & \frac{\hat{D}_1}{L} \\ \frac{\hat{D}_1}{C} & \frac{-1}{RC} \end{bmatrix} \begin{bmatrix} \hat{i}L(t) \\ \hat{u}dc(t) \end{bmatrix} + \begin{bmatrix} \frac{1}{L} & 0 & \frac{v_{dc}}{L} \\ 0 & \frac{-1}{C} & \frac{-I_L}{C} \end{bmatrix} \begin{bmatrix} \hat{u}_b(t) \\ \hat{i}_{dc}(t) \\ \hat{d}_1(t) \end{bmatrix} \tag{6.35}$$

The state vector $\hat{x}(t)$ input vector $\hat{u}(t)$ and output vector $\hat{y}(t)$ are defined by equation.6.36 below.

$$\hat{x}(t) = \begin{bmatrix} \hat{i}L(t) \\ \hat{u}dc(t) \end{bmatrix}, \hat{u}(t) = \begin{bmatrix} \hat{u}_b(t) \\ \hat{i}_{dc}(t) \\ \hat{d}_1(t) \end{bmatrix}, \hat{y}(t) = \begin{bmatrix} \hat{v}dc(t) \\ \hat{i}L(t) \end{bmatrix} \tag{6.36}$$

The above vectors in state-space equation form are written as:

$$\hat{x}(t) = A\hat{x}(t) + B\hat{u}(t), \hat{y}(t) = C\hat{x}(t) + D\hat{u}(t) \tag{6.37}$$

The next step is the conversion of the time-domain small signal model into a frequency-domain (s-domain) small-signal model. Taking Laplace transforms (with zero initial conditions) in equation. 6.38, yields:

$$\hat{x}(s) = (sI - A)^{-}1B\hat{u}(s), \hat{y}(s) = C(sI - A)^{-}1B\hat{u}(s) \tag{6.38}$$

The last step is to export the small-signal transfer functions of the boost converter.

$$G_{id}(s) = \frac{\hat{i}_L(S)}{\hat{d}(s)} = \frac{2V_{dc}}{R\hat{D}_1^2}\left(\frac{1 + s\frac{RC}{2}}{1 + s\frac{L}{R\hat{D}^2}} + S^2\frac{LC}{\hat{D}_1^2}\right) \tag{6.39}$$

6.6.3   Buck-mode operation:

The buck-mode is operated for the charging process of the storage. Figure.6.11(b) presents the circuit of the buck-mode converter. In contrast to boost-mode operation, the inductor current flows from higher voltage side to lower voltage side. The averaged large signal inductor current, i_L, and the output battery voltage, v_b are calculated using equations 6.40, and describe the buck-mode operation in a CCM of the converter.

$$\frac{di_L}{dt} = \frac{1}{L}(v_{dc}d_2 - v_b), \frac{d_{vb}}{dt} = \frac{1}{C}(i_L - \frac{v_b}{R}) \tag{6.40}$$

Thus, equations in 6.40 can be linearized by expanding and separating the steady-state terms and small-signal terms.

$$L\frac{di_L}{dt} + \frac{d\hat{i_L}(t)}{dt} = (V_{dc}D_2 - V_b + Vdc\hat{d}_2(t) + D_2\hat{v}_{dc}(t) - \hat{v}_b(t) + \hat{v}_{dc}(t)\hat{d}_2(t)) \tag{6.41}$$

$$C\frac{dv_b}{dt} + \frac{d\hat{v_{b(t)}}}{dt} = (I_L - \frac{v_b}{R} + (i_L(t) - \frac{v_b(t)}{R}) \tag{6.42}$$

In state space form:

$$\begin{bmatrix} \frac{d\hat{i_L}(t)}{dt} \\ \frac{d\hat{v}_b(t)}{dt} \end{bmatrix} = \begin{bmatrix} 0 & \frac{-1}{L} \\ \frac{1}{C} & \frac{-1}{RC} \end{bmatrix} \begin{bmatrix} \hat{i_L}(t) \\ \hat{v}_b(t) \end{bmatrix} + \begin{bmatrix} \frac{D_2}{L} & \frac{v_{dc}}{L} \\ 0 & 0 \end{bmatrix} \begin{bmatrix} \hat{v}_dc(t) \\ \hat{d}_2(t) \end{bmatrix} \tag{6.43}$$

131

The state vector $\hat{x}(t)$ input vector $\hat{u}(t)$ and output vector $\hat{y}(t)$ are defined by equation.6.44 below.

$$\hat{x}(t) = \begin{bmatrix} \hat{i}_L(t) \\ \hat{u}dc(t) \end{bmatrix}, \hat{u}(t) = \begin{bmatrix} \hat{u}_b(t) \\ \hat{d}_2(t) \end{bmatrix}, \hat{y}(t) = \begin{bmatrix} \hat{v}b(t) \\ \hat{i}L(t) \end{bmatrix} \tag{6.44}$$

As before, the last step is to determine the required small signal transfer function of the buck converter using Laplace transforms. The above vectors in state-space equation form are written as

$$G_{id}(s) = \frac{\hat{i}_L(S)}{\hat{d}(s)} = \frac{v_b}{R\hat{D}_2}\left(\frac{1+sRC}{1+s\frac{L}{R}+S^2LC}\right) \tag{6.45}$$

6.7 Conventional control strategy:

The control strategy maintains the DC link voltage (V_{dc}) at a reference value (V_{dcref}). In this case, fluctuations in load power (P_{load}), and generation of ($P_{PV)}$ are reflected on V_{dc}; the voltage error is passed through the PI controller of the battery to maintain voltage. Adjustment for load power (P_{total}) is provided by HESS. The overall power (P_{total}) is split into high-frequency potions and low-frequency portions; the lower frequencies part is provided to BESS converter as ($P_{battref}$); meanwhile, the high frequencies part is provided to SC as (P_{scref}).

BESS and/or SC provide imbalance in generation and load requirement (ΔP_{load}) at any moment in time using the controller (figure.6.12), as indicated in equation(6.46).

$$\Delta P_{diff} = \Delta P_{pv} - \Delta P_{load} = P_{batt} + P_{sc} \tag{6.46}$$

where P_{batt} represents the amount of power provided by BESS, and P_{sc} denotes power provided by SC. As a result, the factor of (ΔP_{diff}) is constituted of high-frequency element fulfilled by SC as also the lower frequency element attained by BESS. The need for a low pass filter enables a low-frequency element, which seems to be the deficit reference power, to be obtained using the equation provided by (6.47).

$$\Delta P^* = f_{LPF}(\Delta P_{diff}) \tag{6.47}$$

where f_{LPF} signifies the low-pass filter's transfer function. A charge/discharge time limit is provided for BESS's reference power [163], which is given by:

$$P_{battref} = f_{LPF}(\Delta P^*) \tag{6.48}$$

132
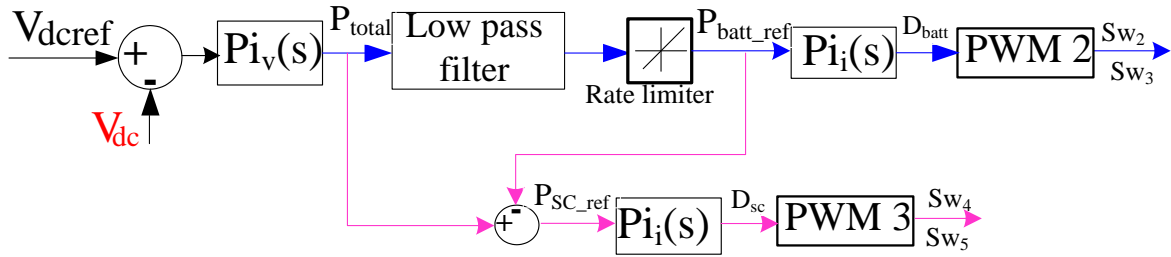
Figure 6.12: Conventional PI control diagram

The SC's function is to provide uncompensated required power from BESS. As a result, SC's reference power value becomes:

$$P_{scref} = P_{total} - P_{battref} \tag{6.49}$$

The reference value (P_{scref}) is compared with the actual value (P_{sc}), and thus the standard error is passed to the PI controller, which produces the duty cycle D_{sc} towards the PWM control signaling of SC converter switches (SW_4 and SW_5).

Figure.6.13 displays the graph of $P_{sc}+P_{batt}$ response while separating the high frequency and low-frequency component changes in (ΔP_{load}). The region under each curve, i.e., the $P_{sc}+P_{batt}$ curve, represents the amount of energy delivered by SC & BESS respectively; the energy released by BESS is calculated as

$$E_{batt} = \int_0^t P_{batt}dt = \int_0^t V_{batt}I_{batt}dt \tag{6.50}$$

where V_{batt}, I_{batt}, and P_{batt} denote BESS voltage, current, and power respectively. Based on energy levels, the SoC in the battery rises, falls, or remains unchanged. The battery's bank % of SoC is expressed by the equation given below [157].

$$\%SoC = (1 - \frac{1}{Q}\int I_{batt}dt) * 100 \tag{6.51}$$

Here, Q is the battery capacity. When I_{batt} is positive, it represents battery discharging, while negative represents battery charging. Because energy as well as SoCs, are factors of I_{batt}, BESS SoC may be shown in the form of energy.

$$SoC = f(E_{batt}) \tag{6.52}$$

As a result, SoC is determined by the amount of energy stored in/discharged from BESS, and the battery's power flow is performed to match the specific power requirement.
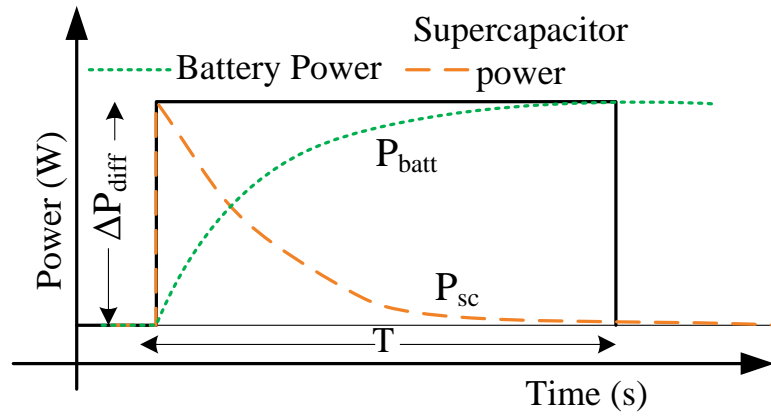
Figure 6.13: BESS and SC respond to increased load requirements
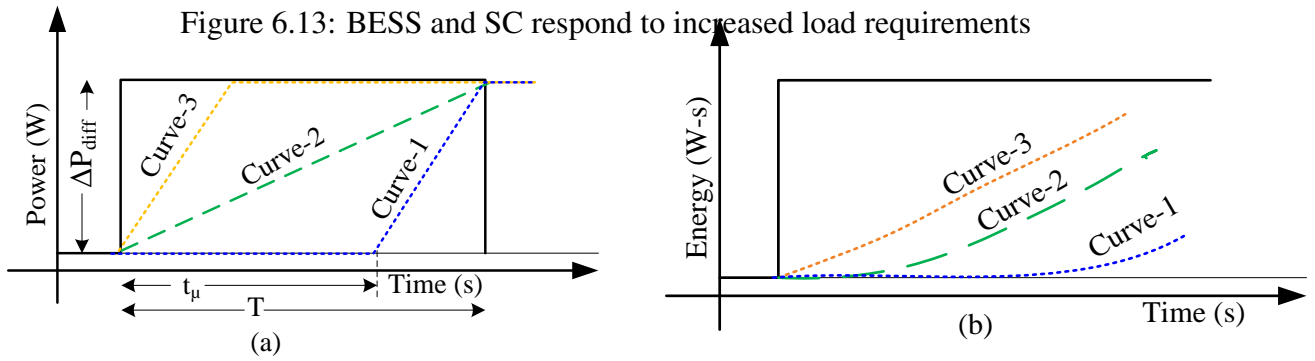
Figure 6.14: BESS response curve: (a) power, and (b) energy

6.8 Proposed control strategy

In this approach, during the transient interval, the power path of BESS is fully dependent on PI variables, the error supplied to the PI controller, and LPF. The power path is non-linear, generally as shown in Figure.6.13. To explain the influence of power curve on BESS, we assume that the maximum discharge rate specified by the designer is (μ_{max}) and the BESS response to changes in load requirements is linear instead of nonlinear.

Figure.6.14 displays three different power curves adopted by BESS to fulfill the change in (ΔP_{diff}) load requirement. Curve-1, in Figure.6.14(a), delivers the load requirement at zero a discharge rate of till t_μ, then it drains at the discharging rate (μ_{max}); curve-2 is designed to deliver the load requirement at a linear rate $=(\Delta P_{diff}/T)$. Similarly, curve-3 initially delivers the load requirements at a higher discharge rate (μ_{max}), and then delivers the load at zero flow rates after fulfilling the necessary load requirements. From the curves, curve-2 provides the lowest discharge rate while fulfilling the load requirements. Here, curve -1 and curve-3 discharge at maximum rate. So all non-linear power curves are produced by using PI controller between

134
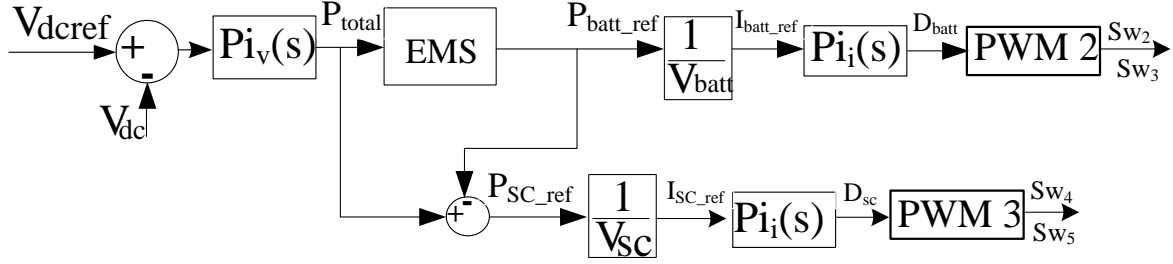
Figure 6.15: A diagram of a proposed control method.

curve-1 and curve-3 under load demand (ΔP_{diff}) and settling time(T). Figure.6.14(b) shows the energy supplied by the battery under these power curves. It explains that, for a given load requirement and settling time, the power provided by these curves is provided in the order listed: $curve-1 < curve-2 < curve-3$. curve-3 discharges at a higher energy rate than other two curves, which is undesirable. However, curve-2 produces higher energy with a lower discharge flow rate, while curve-1 provides lower energy with a higher discharge rate. As a result, a trade-off scenario should occur between both the discharge flow rate as well as energy discharged. As a function, curves 1 and 2 are taken into account to develop the energy management operating strategy to optimize battery energy management strategy with a fixed time duration,

6.8.1 Energy management strategy (EMS)

The basic requirement of optimal battery management is a component of disturbance to BESS and disturbance to SC.Using Meta-heuristic Jaya algorithm with fixed-time SC operation an optimal BESS system has been developed to provide a reference to the traditional PI controller. To develop the proposed battery energy management system, it is assumed that:

- The BESS system's maximum allowable charge/discharge ratio is μ_{max}.

- The positive direction shows that BESS is being discharged, while the negative orientation shows that BESS is being charged.

- The SC maintains a balance between load requirement and BESS power, $P_{sc}(t)=\Delta P_{diff}(t)$ -$P_{batt}(t)$,

- The standard powers are accurately tracked by power converter.

- During the operating condition, the SC's SoC is maintains within oprational limit.

The EMS generated using Meta-heuristic Jaya algorithm with a fixed flow rate limit is shown in Figure.6.16; adding a new power curve as an opt-curve, with a flexible flow rate limit
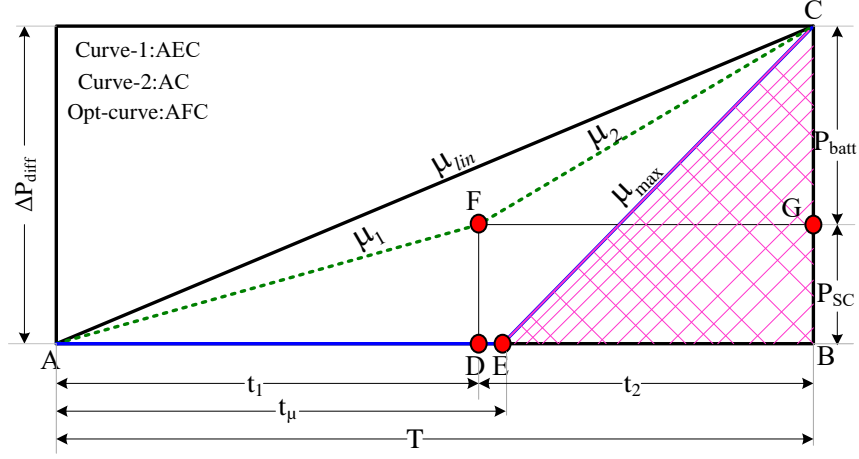
Figure 6.16: Proposed method rate-limit control for the BESS

$(\mu_1 and \mu_2)$, within curve-1 and curve-2 leads to [164]

Curve-1's power is defined as follows:

$$P_1(t) = \begin{cases} 0, & \text{for} 0 < t \leq t_\mu \\ \mu_{max}(T - t_\mu), & \text{for } t_\mu < t \leq T \end{cases} \tag{6.53}$$

Where, T denotes the settling time, and

$$t_\mu = T - \frac{\Delta P_{diff}}{\mu_{max}} \tag{6.54}$$

curve-2's functionality is defined as

$$P_2(t) = \mu_{lin}t \tag{6.55}$$

where

$$\mu_{lin} = \frac{\Delta P_{diff}}{T} \tag{6.56}$$

For any change in load condition, BESS operation is used to study the battery and SC operation. The same can be extended for load decrease. Curve-1 performs the AEC pathway with a fixed flow rate limit of μ_{max}, curve-2 takes the AC pathway with a fixed flow rate limit of μ_{lin}, while optimum curve (opt-curve) employs the AFC pathway with a fixed flow rate limit of μ_1 and μ_2. The fixed flow rate limits μ_1 and μ_2 are defined as follows:

$$\mu_1 = \frac{P_{batt}(t)}{t_1} \tag{6.57}$$

136

$$\mu_2 = \frac{P_{sc}(t)}{t_2} \tag{6.58}$$

$$P_{batt}(t) = \frac{\Delta P_{diff}(t)}{3} \tag{6.59}$$

$$P_{sc}(t) = \Delta P_{diff}(t) - P_{batt}(t), \tag{6.60}$$

$$t_2 = T - t_1, \tag{6.61}$$

The span of such rate limitations is given as

$$0 \leq \mu_1 \leq \mu_{lin} \tag{6.62}$$

$$\mu_{lin} \leq \mu_2 \leq \mu_{max} \tag{6.63}$$

opt-curve provides the following power:

$$P_{opt}(t) = \begin{cases} \mu_1(t), & \text{for} 0 < t \leq t_1 \\ P_{batt} + \mu_{2(T-t_1)}, & \text{for } t_1 < t \leq T \end{cases} \tag{6.64}$$

The energy saved by certain curve-1 is given by:

$$E_1 = Area of \Delta EBC = \frac{1}{2}(T - t_\mu)\Delta P_{diff} \tag{6.65}$$

The energy saved by certain curve-2 is:

$$E_2 = Area of \Delta ABC = \frac{1}{2}T\Delta P_{diff} \tag{6.66}$$

Likewise, the energy saved by opt-curves is :

$$E_{opt} = Area of ABCFA \tag{6.67}$$

$$= Area of \Delta ADF + FDBGF + \Delta FGC \tag{6.68}$$

$$= E_{opt1} + E_{opt2} + E_{opt3} \tag{6.69}$$

$$E_{opt1} = \frac{1}{2}t_1 P_{batt} = \frac{1}{2}\mu_1 t_1^2 = \frac{P_{batt}^2}{2\mu_1} \tag{6.70}$$

137

$$E_{opt2} = \frac{1}{2} t_2 P_{sc} = \frac{1}{2} \mu_2 t_2^2 = \frac{P_{sc}^2}{2\mu_2} \tag{6.71}$$

$$E_{opt3} = t_2 P_I = \mu_1 t_1 t_2 = \frac{P_{batt} P_{sc}}{\mu_2} \tag{6.72}$$

The proposed control strategy is aimed to satisfy three optimum requirements listed below.

(i) During a transitory period, BESS is stored/discharged and (E_{opt}) is optimised.

(ii) The maximum discharge/charge rate (μ_2) is optimised.

(iii) The period (t_2) during which the battery discharges/charges at its maximum flow rate (μ_2) is optimised.

The optimum point as presented in Figure.6.16 is 'F', E_{opt}, is obtained using the proposed Meta-heuristic minimization of Jaya algorithm given below.

6.8.2   Jaya algorithm

Let $f(x)$ be the objective function to determine the values of $x_i \in \{\mu_1, \mu_2, P_{batt}, P_{sc}\}$ that minimize the value of power [27]. The population size of 10 (i.e. candidate solutions), for each variable $x \in \{\mu_1, \mu_2, P_{batt}, P_{sc}\}$ is initialized as shown in flow chart Figure.6.17.

$$min f(x_i) = \left[\frac{P_{batt}^2}{2\mu_1(i)} + \frac{P_{sc}^2}{2\mu_2(i)} + \frac{P_{batt} P_{sc}}{\mu_2(i)} \right] \tag{6.73}$$

Subject to the conditions privided below:

$$P_{batt} + P_{sc} = \Delta P_{diff} \tag{6.74}$$

$$\frac{P_{batt}}{\mu_1} + \frac{P_{sc}}{\mu_2} = T \tag{6.75}$$

$$0 \le \mu_1 \le \frac{\Delta P_{diff}}{T} \tag{6.76}$$

$$\frac{\Delta P_{diff}}{T} \le \mu_2 \le \mu_{max} \tag{6.77}$$

138

The initial population of the variables is randomly generated within their respective upper and lower limits, and correspondingly the objective function is computed for each population candidate $f(x_i)$. As it is a minimization function, the lowest value of $f(x)$ is considered the best solution, and the highest value of $f(x)$ is considered the worst solution. Let the best candidate obtain the best value of $f(x)$ (i.e. $f(x)_{best}$) in the entire candidate solutions and the worst candidate obtain the worst value of $f(x)$ (i.e. $f(x)_{worst}$) in the entire candidate solutions as per the following eq.(6.73).

The variables within the limit having the lowest objective values at the end of the iteration are maintained and these values become the input for the next iteration.

6.8.3   Analysis of energy management strategy

An EMS scheme has been proposed to efficiently utilize sources (PV,BESS,and SC) for supplying the load demand,improve longevity of BESS,reduce transients and ensure battery is within the limits while regulating DC-link voltage at nominal value, Here, a rule-based controller scheme is implemented for EMS by considering PV power, P_{pv} load (P_{load}), SC, and battery SoC level. The proposed system for EMS is shown in Figure.6.18.

In all operating conditions, Spv represents PV MPPT status that is fed to the PV local controller ($S_{pv} = 1$), which represents MPPT operation. ($S_{pv} = 0$) represents the derating operation. Under normal conditions, the PV is typically operated at MPP, extracting the maximum available power. The SC charge/discharge time constant (T) is selected by the operator, which decides the operational time of SC during the transient period.

Based on the variation in power generation and load demand, the DC nano grid operation can be broadly classified into two different modes of operation, (i) Positive change in power ($\Delta P_{diff} > 0$). (ii) Negative change in power ($\Delta P_{diff} < 0$) as shown in Figure.6.19 .

6.8.4   For negative change in power $(\Delta P_{diff} < 0)$

This occurs mainly if generation falls ($\Delta P_{PV} < 0$) or load increases ($\Delta P_{load} > 0$). Under this condition, the system operation can be classified into four operating modes as shown in Figure.6.19.

Mode: (i)($SoC_{batt} \leq SoC_{batt_{min}}$),($SoC_{sc} \leq SoC_{sc_{min}}$): In this case, the SC and battery SOC are in minimal condition mode. In this condition, PV is running in MPPT mode and the minimum
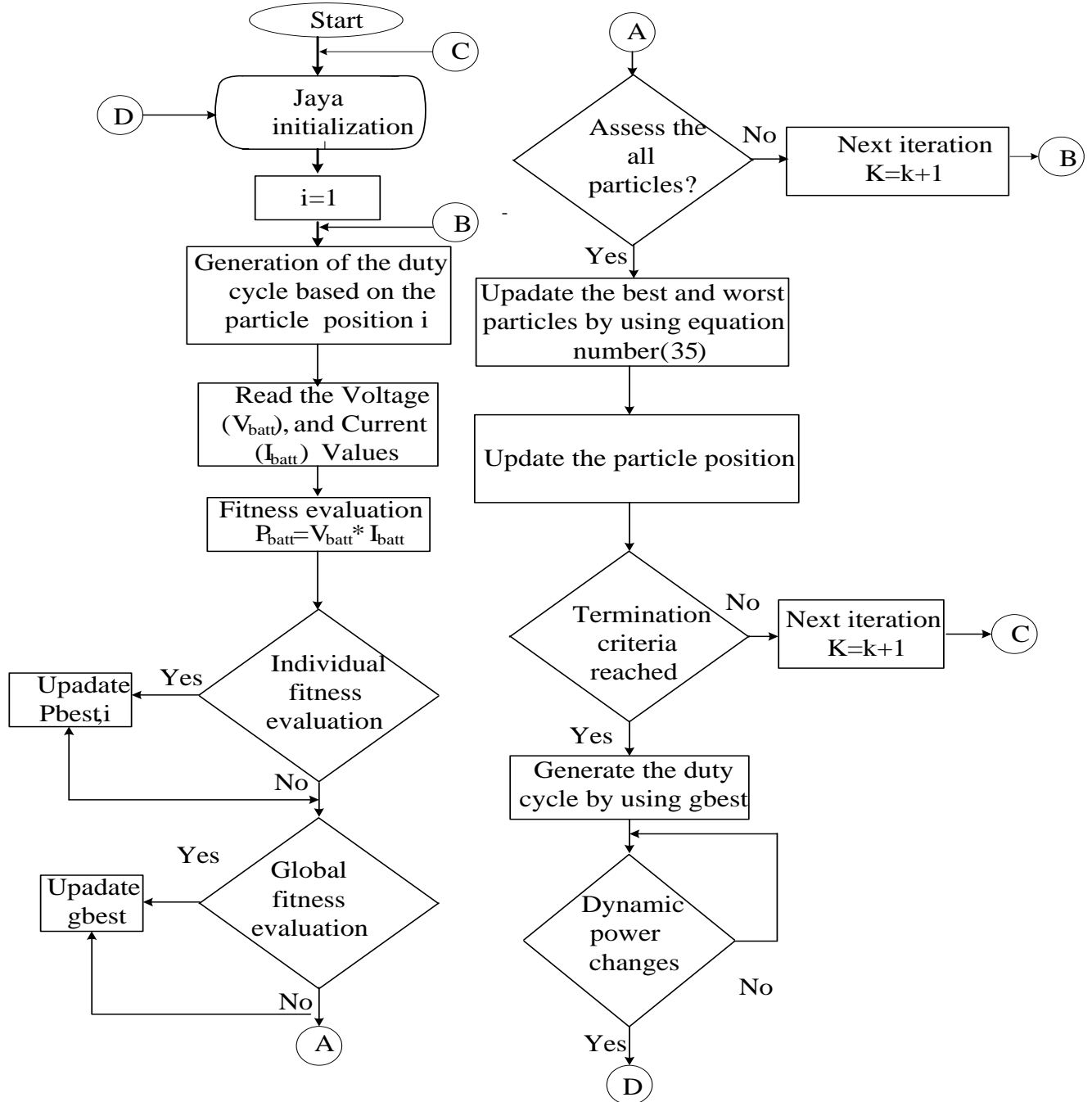
Figure 6.17: Flow chart for Jaya algorithm.
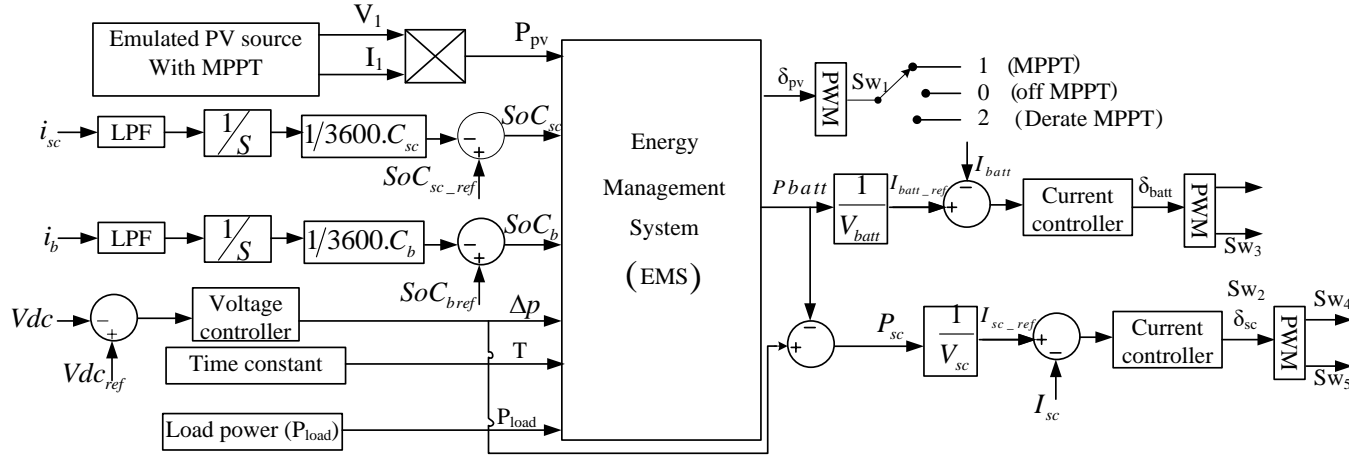
Figure 6.18: Proposed System for Energy Management

SoC of battery and SC is insufficient to meet the load requirement. Under this condition, the load is shed depending on generation.

Mode: (ii)$(SoC_{batt} \leq SoC_{batt_{min}}),(SoC_{sc} \geq SoC_{sc_{min}})$: In this mode SoC is the minimum mode, and SC SoC level is more than the minimum condition, so PV and SC discharge as per load requirement, and the battery is in floating mode.

Mode: (iii)$(SoC_{batt} \geq SoC_{batt_{min}}),(SoC_{sc} \leq SoC_{sc_{min}})$:In this mode, the battery SoC is greater than the minimum, but SC SoC is minimum. Under this condition,PV, and battery can supply the load needed as the load varies, and SC is in floating mode.

Mode: (iv)$(SoC_{batt} \geq SoC_{batt_{min}}),(SoC_{sc} \geq SoC_{sc_{min}})$: In this mode, the SC and battery SoCs are greater than the minimal value; under this situation, the PV, battery, and SC provide the load demand as per equations ((6.59)) and ((6.60).)

6.8.5 For positive change in power $(\Delta P_{diff} > 0)$.

This condition arises if there is an increase in PV output power, $(\Delta P_{PV} > 0)$, or when the load demand decreases, $(\Delta P_{load} < 0)$. Based on SC and battery SoC level, in the proposed EMS strategies, the system operation can be classified into four operating modes as shown in Figure.6.19.

Mode: (v)$(SoC_{batt} \leq SoC_{batt_{max}}),(SoC_{sc} \leq SoC_{sc_{max}})$:When the battery is under light load and SC SoC is in maximal mode; as a result, the PV is running in derating mode, which is equivalent to

141

load demand, while the battery and SC are in floating mode.

Mode: (vi)$(SoC_{batt} \leq SoC_{batt_{max}})$,$(SoC_{sc} \geq SoC_{sc_{max}})$: In this case, the battery SoC is in maximum mode and SC SoC is in minimum mode; thus, the PV operates in MPPT mode to charge SC to the maximum SoC level and meet the demand; the battery remains in floating mode.

Mode: (vii)$(SoC_{batt} \geq SoC_{batt_{max}})$,$(SoC_{sc} \leq SoC_{sc_{max}})$: In this condition, the battery SoC is in minimal condition while SC SoC is in maximum condition. Under light loads, the PV can run in MPPT mode to charge the battery and fulfil the load requirement; in this scenario, the SC continues in floating mode.

Mode: (viii)$(SoC_{batt} \geq SoC_{batt_{max}})$,$(SoC_{sc} \geq SoC_{sc_{max}})$:In this situation, the battery and SC SoC are in minimal mode under light load conditions, and the PV is operating in MPPT mode to meet the load requirement and charge the battery and SC according to equations ((6.59)) and ((6.60)).

6.9   Discussion on simulation outcomes

The efficacy of the proposed EMS was evaluated by simulating the DC nano grid system as shown in Figure.6.1 in MATLAB/Simulink. The specifications of the PV systems, BESS, and SC, along with their respective converter and control parameters used in simulation studies, are detailed in Table.6.3. The PV generates a maximum output power $(P_{pv} = 205W)$, and BESS is controlled using the cascaded control loop method to regulate DC link voltage. In this, the inner current controller is tuned using the pole-zero placement approach, and the outer voltage controller is tuned using the symmetrical optimal method. The upper and lower limits for SoC of BESS and SC are assumed to be $SoC_{max} = 80\%$ and $SoC_{min} = 20\%$. The EMS is designed to operate BESS and SC within the limits of SoC. Further, for all test scenarios, the resistive loads are considered across the DC link. The local controller of BESS is designed to maintain the DC link voltage at a reference nominal value of $Vdc_{ref} =100V$, and thus to manage the charge/discharge periods of BESS using EMS. The outcomes of the proposed method analysis, established using three major test scenarios, are discussed in this section.

  Case (i): Energy management under load demand increases $\Delta P_{diff} < 0$.

  Case (ii): Energy management under load demand decreases $\Delta P_{diff} > 0$,and

  Case (iii): Energy management when PV is in derating mode

142
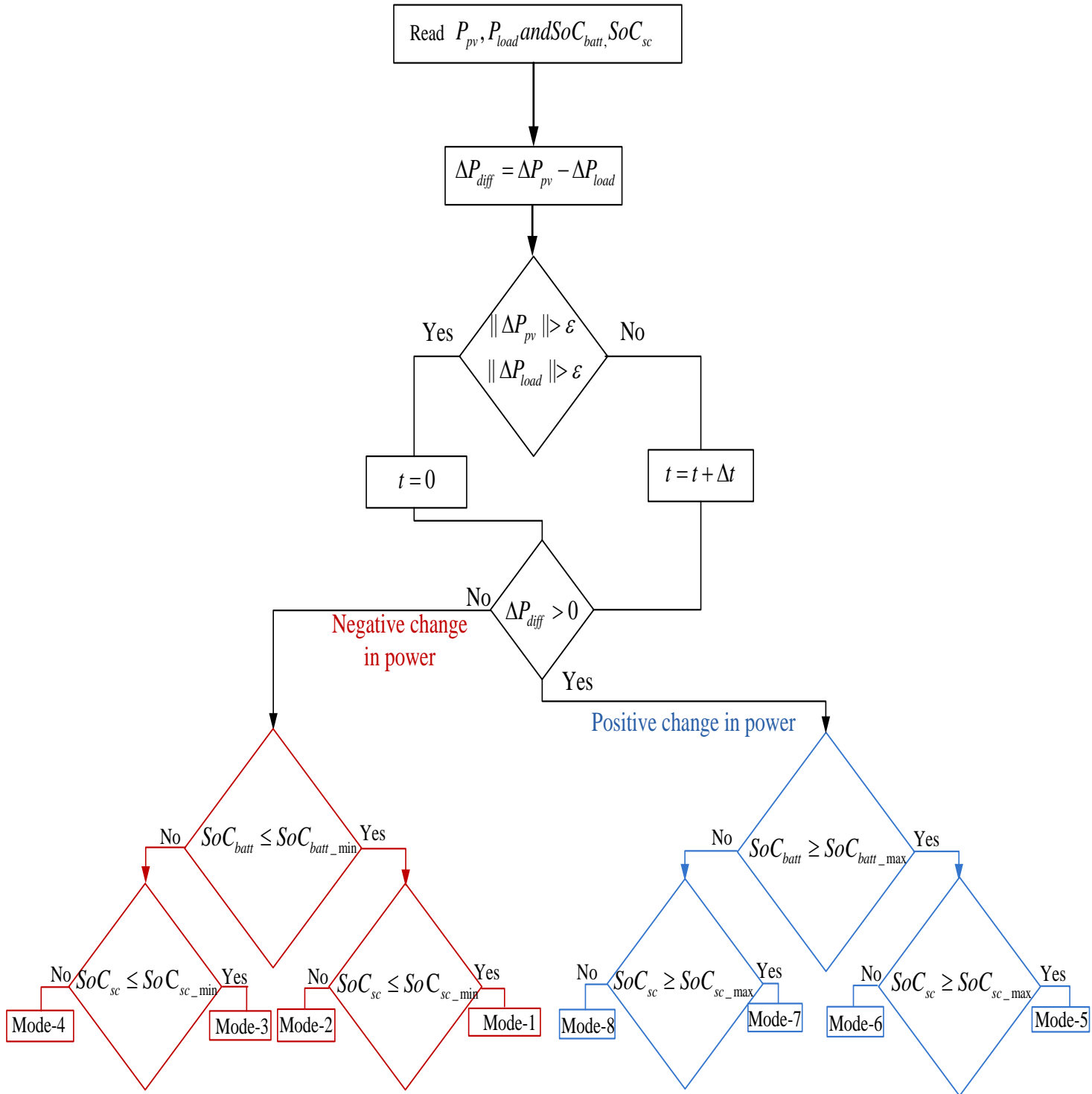
Figure 6.19: Flowchart for Modes of Operation in PV, BESS and SC System with Proposed Energy Management Strategy.

6.9.1 Case (i): Energy management under load demand increases $(\Delta P_{diff} < 0)$.

HESS using the traditional voltage control technique for a sudden change in load demand is considered as shown in Figure.6.20(i). In this scenario, PV is operated in MPPT mode and any changes in load demand are met by BESS and SC. The SC acts for a short period to reduce the effect of transient discharge on the battery. In the case study, four scenarios were considered, as shown in Figure.6.20. In all these scenarios, initially, PV generation was operating at MPPT, extracting power of, $(205W)$, with a total connected load of $200W$. The *SoC* of BESS and SC were considered to be 50.0575% and 51.425%, respectively, and in floating mode as $P_{diff} - P_{loss} \approx 0$. At $2sec$, the load is increased to $(620W)$, and BESS and SC started to discharge to meet the load that suffers a shortfall by PV generation. In Figure. 6.20(a), with the conventional approach, the SC was able to take the sudden load transients. However, this approach could not limit the battery discharge to an optimal rate and led to sudden discharges beyond the maximum discharge rate. This might cause overheating of the battery and diminish the battery life span. To improve BESS's discharge rates, the proposed EMS with optimal rate limit strategy was applied, whose responsibility for different operating time constants of SC is shown in Figure.6.20(b) - 6.21(d).

Similar to the conventional approach scenario (6.20(a)), a sudden increase in load demand was considered for all other three scenarios, to demonstrate the efficacy of the proposed approach. Under comparable test conditions, the performance of the proposed control method when applied to the system with SC operational time constants being $1sec$, $2sec$, and $3sec$ is shown in Figure. 6.20(b), 6.21(c), and 6.21(d), respectively. In these scenarios, the energy released by BESS is more than the energy released by traditional voltage control approach. As a result, BESS quickly exceeds the SoC limit in traditional techniques, as shown in Figure.6.20(i), Although, in all these scenarios, the initial SoC is 50.0575, based on the selected operating time constant of SC, the slope of the discharge varies and SoC at the end of $10sec$ is different, as seen in Figures 6.20(a)(iv), 6.20(b)(iv), 6.21(c)(iv),6.21(d)(iv). With the conventional approach, the battery has seen a larger discharge for a value of *SoC*=50.0428% (6.20(a)(iv)), While with the proposed approach and with an SC time constant of $T = 3sec$, the battery SoC is smaller and discharged to a value of 50.046% as shown in fgure(Figure.6.21(d)(iv)).

(a)

(b)

Figure 6.20: Simulation results of an increase in load demand: (a) Conventional method, (b) Proposed method with T = 1 sec.

Figure 6.21: Simulation results of an increase in load demand: (c) Proposed method with T = 2 sec, (d) Proposed method with T = 3 sec.   146

6.9.2   Case (ii): Energy management under the load demand decreases ($\Delta P_{diff} > 0$)
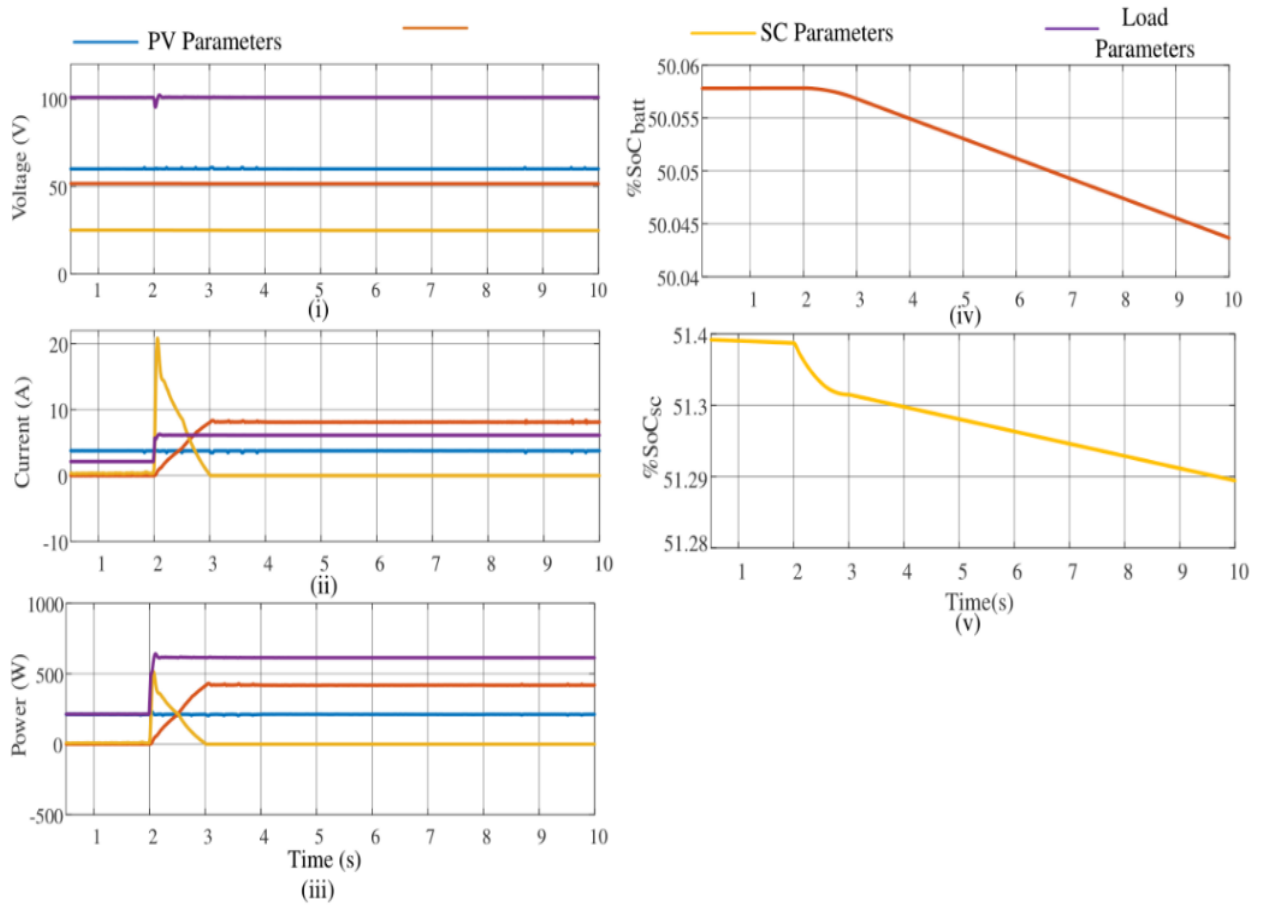
The HESS using traditional voltage control techniques for sudden decrease in load demand is considered, as shown in Figure.6.22(i). To start with, four scenarios were considered, as shown in Figure.6.22(a),(b),(c),and(d). In this case, PV was initially operating in MPPT power mode (P_{pv}=205W) to satisfy the load requirement (P_{load}=200W). The *SoC* of BESS and SC were considered to be at 50.16278 and 52.0875, respectively, and in floating mode as $P_{diff} - P_{loss} \approx 0$. When the load was lowered to ($100W$) at t=2s, BESS and SC begin to charge to compensate for surplus PV generation. In Figure.6.22(i), the conventional approach allowed the SC to absorb rapid load transients; however, this approach did not limit the battery charge to an optimal rate, resulting in a sudden charge that exceeded the maximum charge rate. This may have an effect on the battery's durability and shorten its life cycle the response ofBESS and SoC to varied operating time constants of SC is shown in Figure.6.22(b)-6.23(d).

In all three scenarios, a sudden fall in load demand was considered, as in the traditional method scenario (Figure.6.22(a)), to show the superiority of the proposed approach. The performance of the proposed control approach when applied to systems with SC operating time constants of 1*sec*, 2*sec*, and 3*sec* is shown in Figures.6.22(b), 6.23(c) and 6.23(d), respectively, under comparable test conditions. In such cases, the energy absorbed by BESS is slower than the energy absorbed by the traditional voltage control approach. As a result, in the traditional technique, BESS rapidly reaches the SoC limit, as seen in Figure.6.22(iv), Although, in all these scenarios, the initial SoC is 50.1617, based on the selected operating time constant of the SC, the slope of the charge is varied, and the SoC at the end of 10*s* is different as seen in Figure. 6.22(a)(iv), 6.22(b)(iv), 6.23(c)(iv),6.23(d)(iv). With conventional approach, the battery has seen larger charge attaining a value of SoC = 50.1658 (as shown in Figure6.22(a)(iv)), while with the proposed approach and with SC time constant of $T = 3sec$, the battery's SoC is smaller charged to a value of 50.1638 (Figure. 6.23(d)(iv))

6.9.3   Case (iii): Energy management when PV is derating mode

As shown in Figure.6.24(d), the SC and battery SoC approach the upper limits ($SoC_{batt} \leq SoC_{batt_{max}}$), ($SoC_{sc} \leq SoC_{sc_{max}}$. Under these conditions, the proposed EMS method is evaluated for varied load conditions. The DC nanogrid's initial load is P_{load} =205W, SC, and the battery SoC is at 80%. Under this condition, to avoid deep charging of the batteries, the proposed EMS sends an S_{pv}= 1 signal from EMS to PV local control, which causes the PV to operate in load
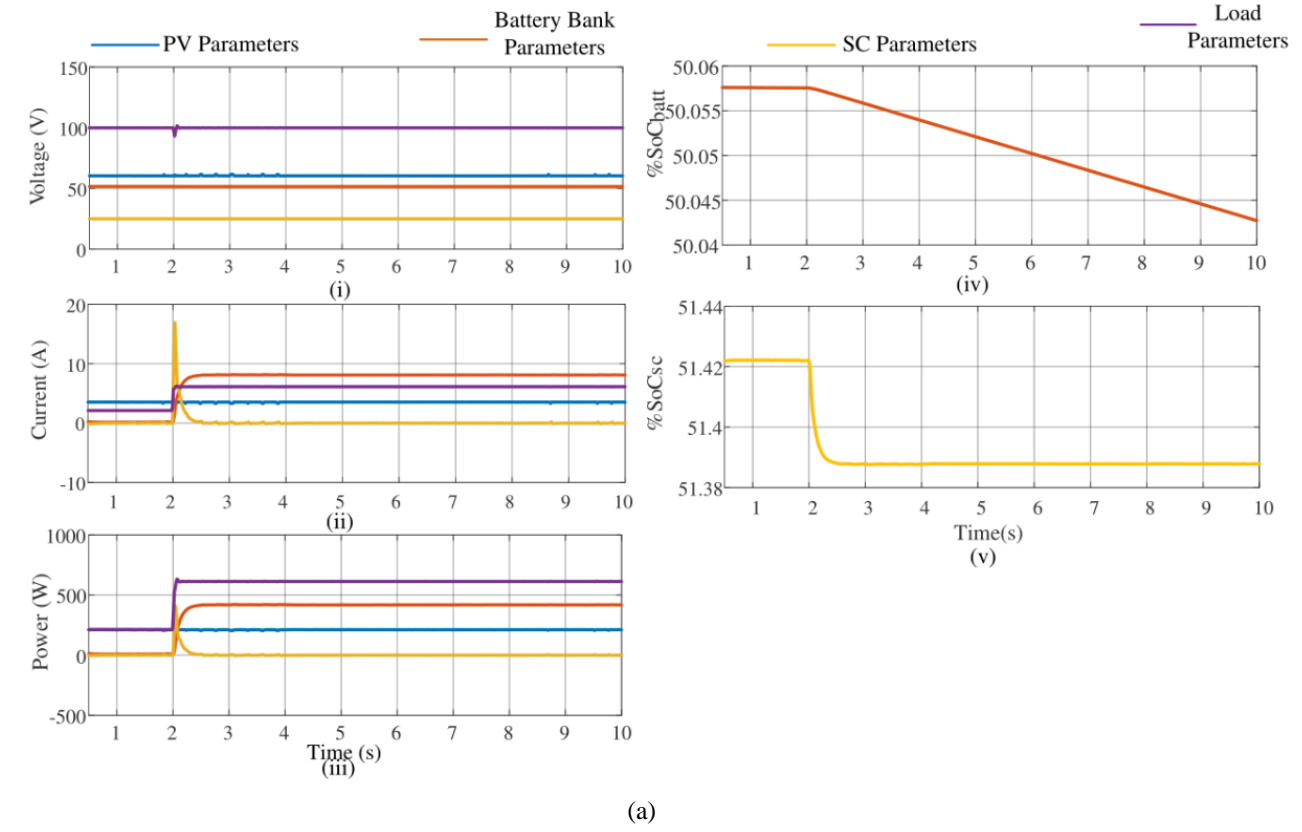
(a)

(b)

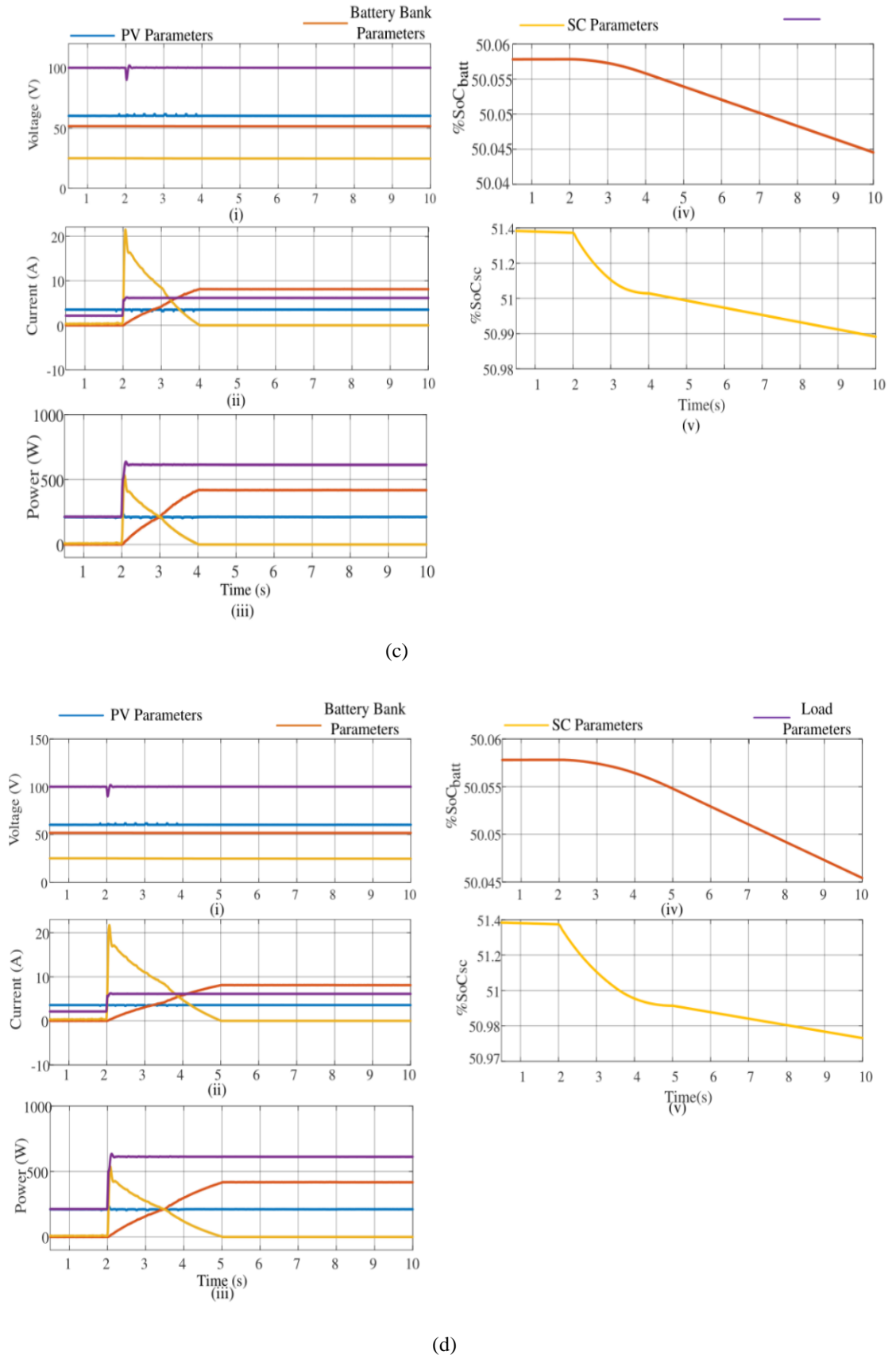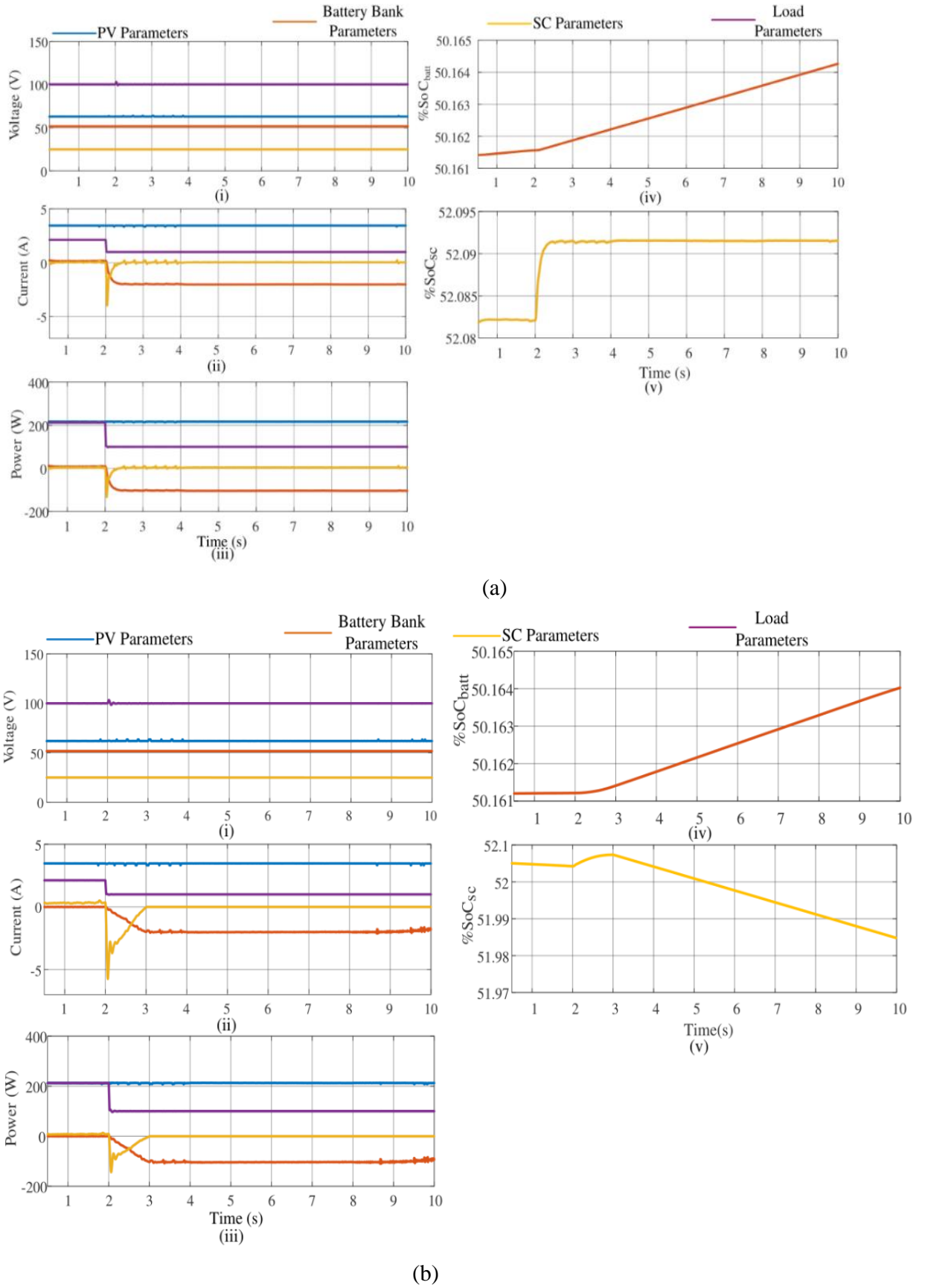Figure 6.22: Simulation results of decrease in load demand: (a) Conventional method, (b) Proposed method with T = 1 sec.
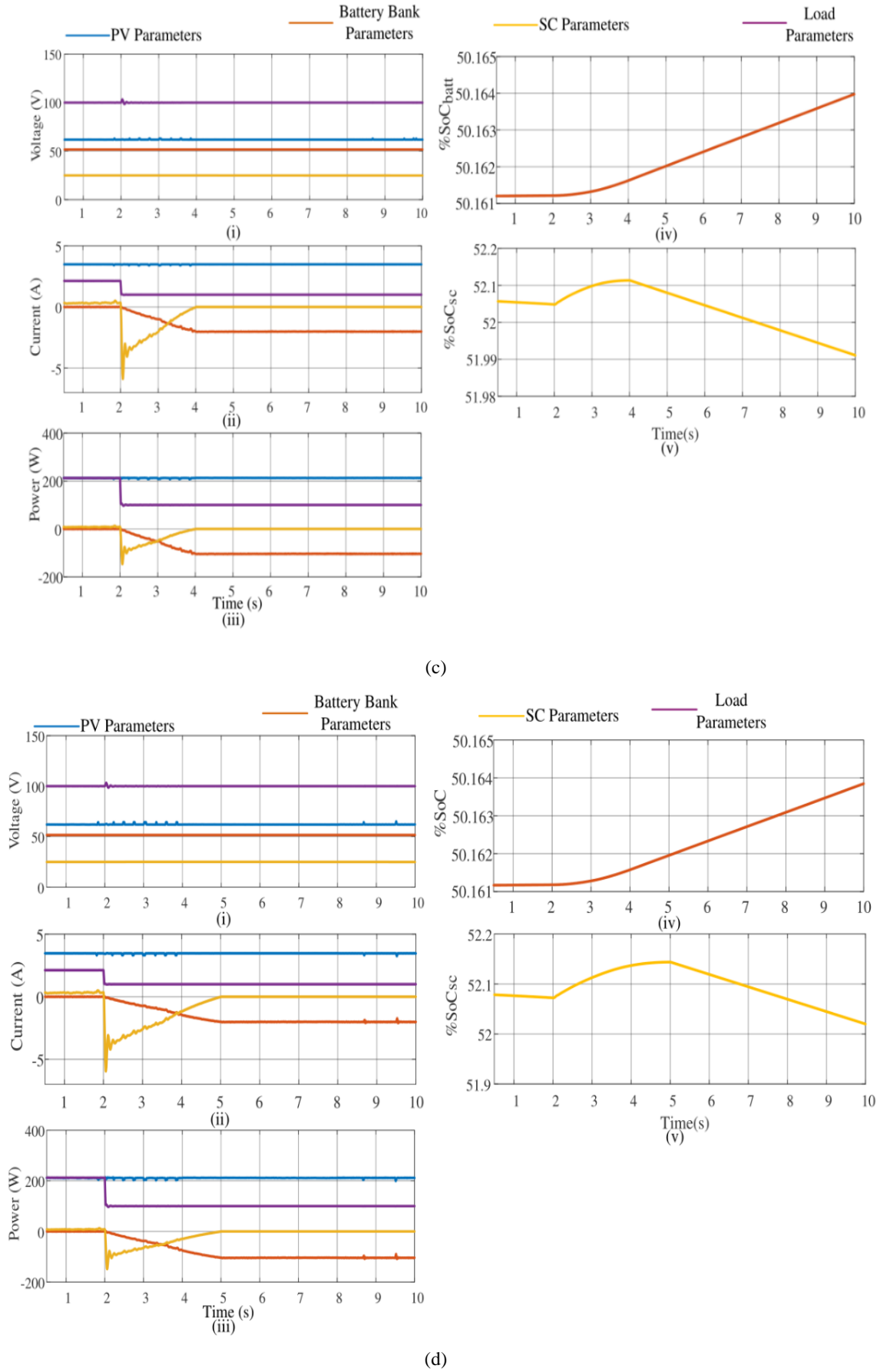
Figure 6.23: Simulation results of decrease in load demand: (c) Proposed method with T = 2 sec, (d) Proposed method with T = 3 sec .   149
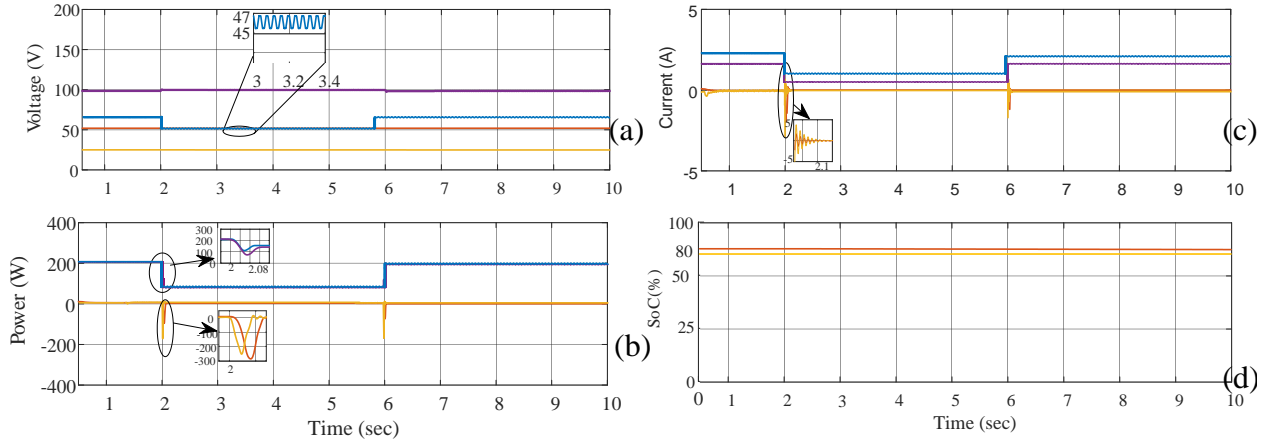
Figure 6.24: Simulation results of derating mode: (a) Voltage (b) Current (iii) Power (iv) SoC

follower mode to avoid further charging of the battery. At $t = 2sec$, the load demand is lowered to $100W$, causing the battery and SC to charge till $SoC \leq SoC_{max}$. When the proposed EMS detects that BESS SoC has reached its maximum capacity, it sends an off-MPPT signal of $S_{pv}=$ 2 to the PV controller, allowing the PV to operate in a derated mode with an output power of $P_{pv} = P_{load}$, shown in Figure.6.24 (c). At $t =6sec$, the load demand increases again to $205W$. As $SoC \leq 80\%$, the PV runs as MPPT to match the load demand. The battery and SC were in floating mode under these circumstances, as indicated in Figure. 6.24(d).

6.10 Experimental study

Figure.6.25 shows an experimental model of a HESS system, which includes a programming PV emulator, BESS, supercapacitor, boost, and bi-directional converters. The proposed EMS controller is realized using a real-time controller, dSPACE 1104. In this experiment, the PV array is simulated using programming PV emulators, while the $12V$, $120Ah$ lead-acid battery with a bi-directional converter is used as a BESS system. A Maxwell supercapacitor ($BMOD0058$) of capacitance $58F$, $16V$ is used in HESS system. The detailed specifications of all components used in the hardware prototype are tabulated in Table.6.3. The controller in dSPACE is designed to control voltage across the DC link using a cascaded voltage and current controller. The reference to the current controller was obtained using the optimization technique used in EMS controller developed in dSPACE. The hardware prototype developed was used to validate the practical feasibility of the proposed EMS under different conditions.

6.10.1 Case (i): Energy management under the load demand increases $(\Delta P_{diff} < 0)$.

In this case, the efficacy of the proposed EMS is validated for increased load demand condi-

Table 6.2: Parameters of the proposed method and boost converter

Particulars	Specifications
Jaya	Maximum iteration = 100, population size = 3
Boost Converter	$L_{pv} = 0.4mH$, $C_{in} = C_{out} = 100\mu F$, $F_s = 10kHz$, Variable Rheostat :100Ω 10A
Sampling Period	For Simulation $T_s = 10ms$, For Experimental $T_s = 200ms$
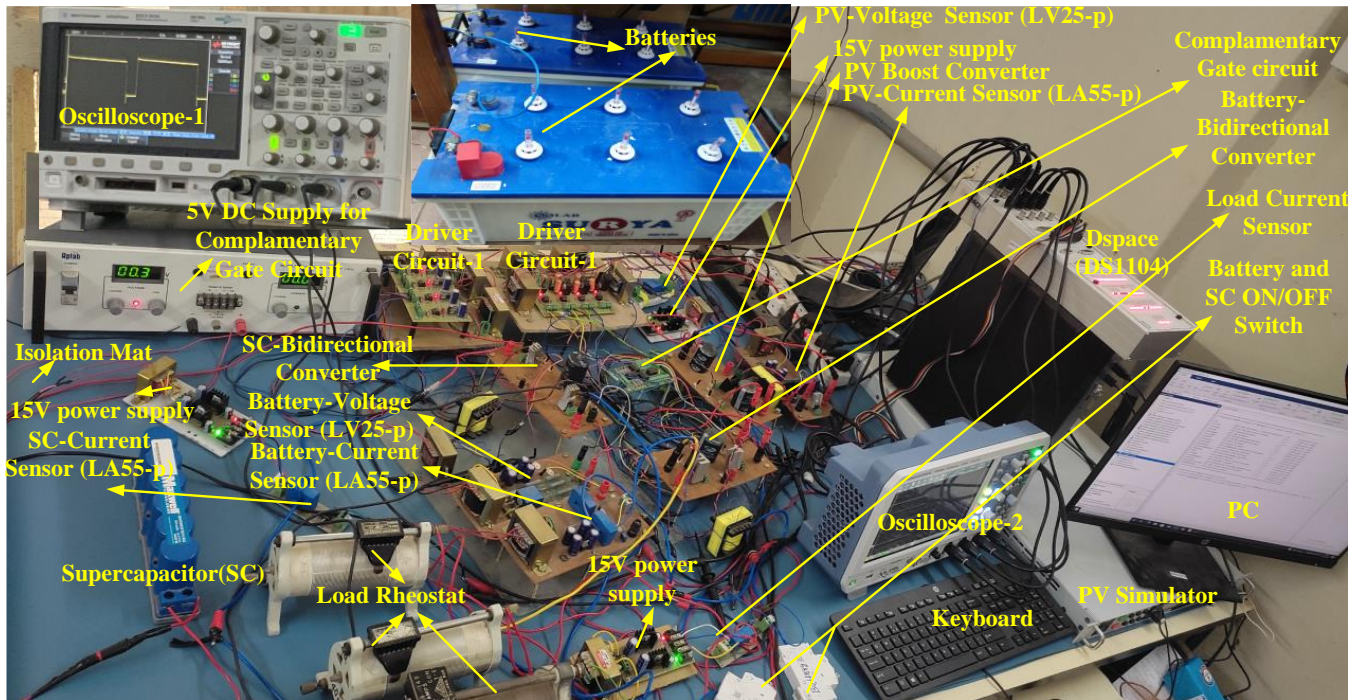
Figure 6.25: Experimental Setup for HESS

tions (Figure.6.26(b), Figure.6.27(c), and Figure.6.27(d)). The proposed approach is compared against the traditional voltage controller developed. Under this case study, four scenarios were considered.

Scenario (i)- HESS system operation with conventional voltage controller (Figure.6.26(a))

Scenario (ii)- HESS system operation with proposed EMS for SC time constant T=1s (Figure.6.26(b))

Scenario (iii))- HESS system operation with the proposed EMS for SC time constant T=2s (Figure.6.27(c)) and

Scenario (iv))- HESS system operation with the proposed EMS for SC time constant T=3s (Figure.6.27(d))

Table 6.3: System Parameters

Parameters Name	Simulation Parameters	Experimental Parameters
Specification for Solar PV at STC ($1000W/m^2, 25°C$)		
Power at MPP (W)	54.69	70.2
Voltage at MPP (V)	16.88	31.2
Current at MPP (A)	3.24	2.25
Voltage at Voc (V)	21.1	39.36
Current at Isc (A)	3.6	2.5
No of cells	48	96
Each cell Voltage (V)	0.44	0.41
Specifications of Supercapacitor		
Rated capacitance(Farads)	99	58
Number of series capacitors	1	1
Number of Parallel Capacitors	50	6
Initial voltage (V)	50	16
Operating Temp(celsius)	25	+65
Capacitor (C_{sc})	$2000\mu F$	$500\mu F$
Inductor (L_{sc})	4mH,0.001X	8.5 mH
Specification of BESS		
Battery choice	lead–acid battery	lead–acid battery
Rating in Ampere hour	120 Ah	120 Ah
Nominal Voltage	12 V	12 V
Charging rate	C/10	C/10
Capacitor (C_{batt})	$2000\mu F$	$500\mu F$
Inductor (L_{batt})	$4.8mH, 0.001X$	$7.2mH$

In all four scenarios, load demand is greater than PV generation, EMS sends signal MPPT operation command to PV and supplies power P_{pv}=222W. At nearly 2*sec*, the load is increased to 280W. As the P_{pv} falls short of the load demand, BESS and SC begin to discharge power to fulfill to meet the load demand while maintaining the DC link voltage at 48V. The results of the traditional voltage controller (scenario1) are shown in Figure.6.26(b), as well as the results of the proposed method; various settling periods of 1sec (scenario2), 2sec (scenario3), and 3sec (scenario4), are shown in Figure.6.26(b), Figures ref320(c),6.27(d). The results indicate that in scenario 1, BESS is nearly at the maximum permissible discharge limit; however, in scenarios 2 to 4, the discharge levels are reduced, as shown in Figure.6.26(b) Figures6.27(c),6.27(d). Comparing all scenarios, the traditional approach has shown the highest battery discharge rate while the proposed approach with $T = 3s$ has displayed low discharge rate. Moreover, the energy released by BESS is lower with the proposed control scheme compared to a traditional voltage controller. From Figures 6.26(b), and Figure.6.27(c),6.27(d), the SoC of BESS for Scenario 1 is lower than its Soc for Scenarios- 2, 3, and 4, showing that comparatively higher energy is released.

6.10.2   Case (ii): Energy management under the load demand decreases. $(\Delta P_{diff} > 0)$

In this case, the superiority of the proposed EMS is validated for decreased load demand condition Figure.6.28, The proposed method is evaluated with the conventional voltage controller described in [36]. In this test case, four scenarios were considered.

scenario.(i): HESS system operation with conventional voltage controller 6.28(a)

scenario.(ii): HESS system operation with the proposed EMS for SC time constant T = 1s 6.28)(b)

scenario.(iii): HESS system operation with the proposed EMS for SC time constant T = 2s 6.28(c) and

scenario.(iv): HESS system operation with the proposed EMS for SC time constant T = 3s 6.28(d)

In all four scenarios, load demand was lower than PV generation. As a result, surplus energy was supplied to BESS and SC while maintaining power balance and DC grid voltage at 48 V. In this case, in all scenarios, initially, the PV system supplies MPP power of $P_{pv} = 222W$ and a supplying load of around $P_{load} = 220W$ up to 2 sec. At $t = 2s$, the load is reduced to 162W, as P_{pv} is more than the load demand, and the surplus energy is immediately fed to SC while maintaining the DC link voltage at 48V. The energy stored in SC is slowly transferred to

153

(a)

(b)
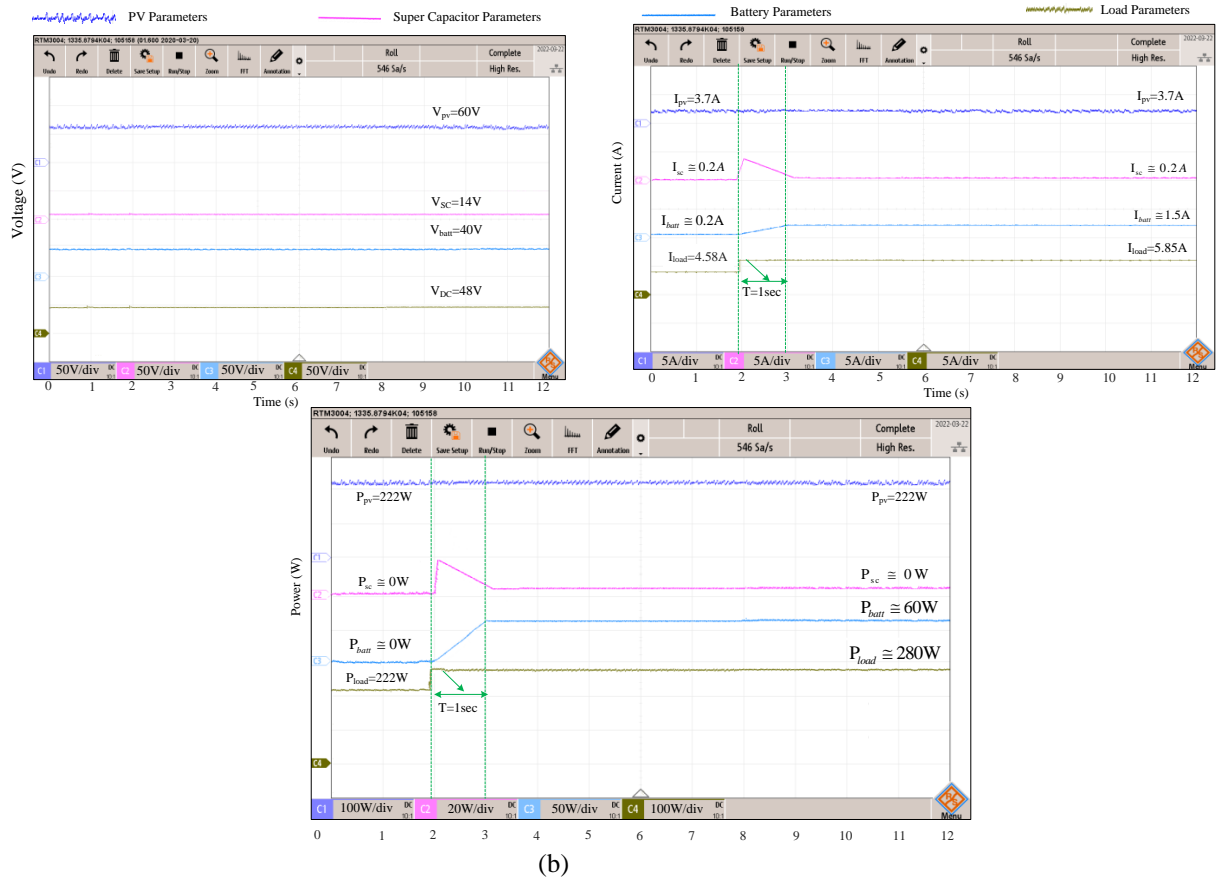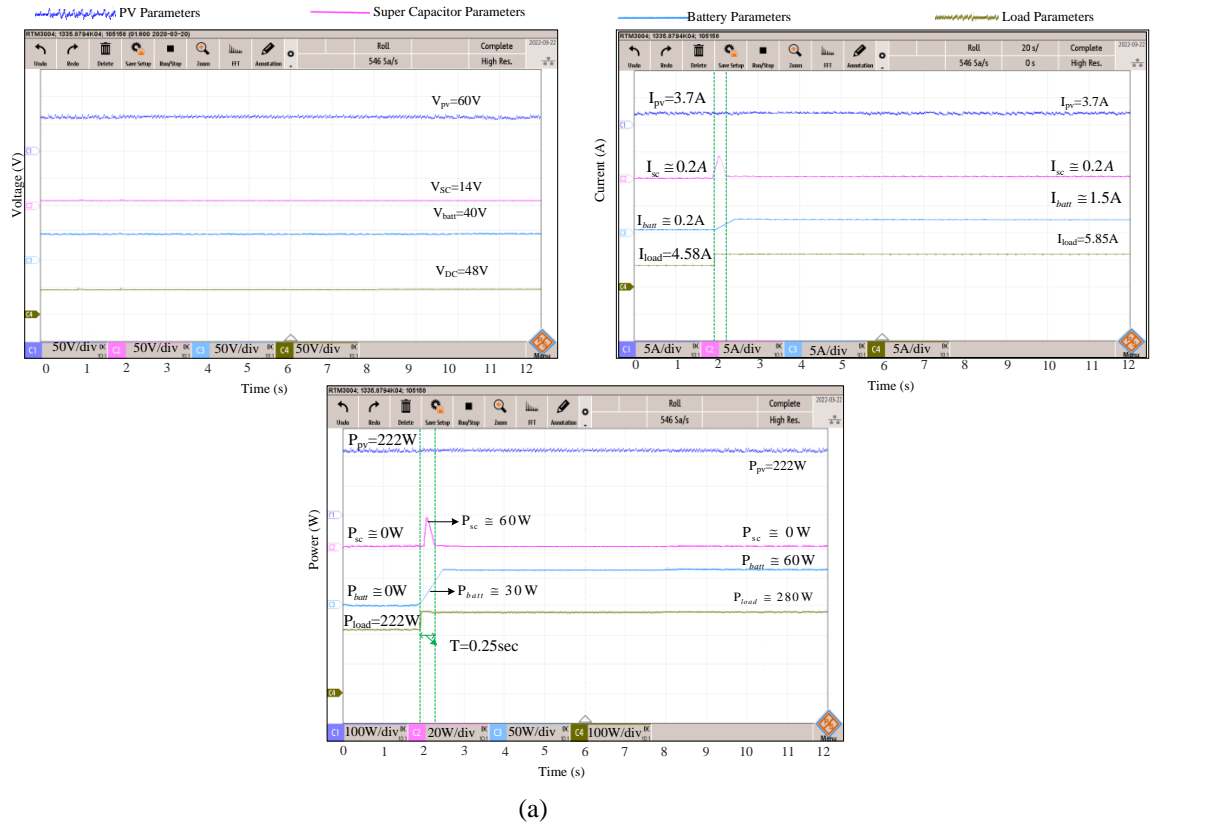
Figure 6.26: Experimental results of increase in load demand: (a) conventional method (scenario 1) , (b)proposed method with T = 1 sec (scenario 2)

(c)

(d)
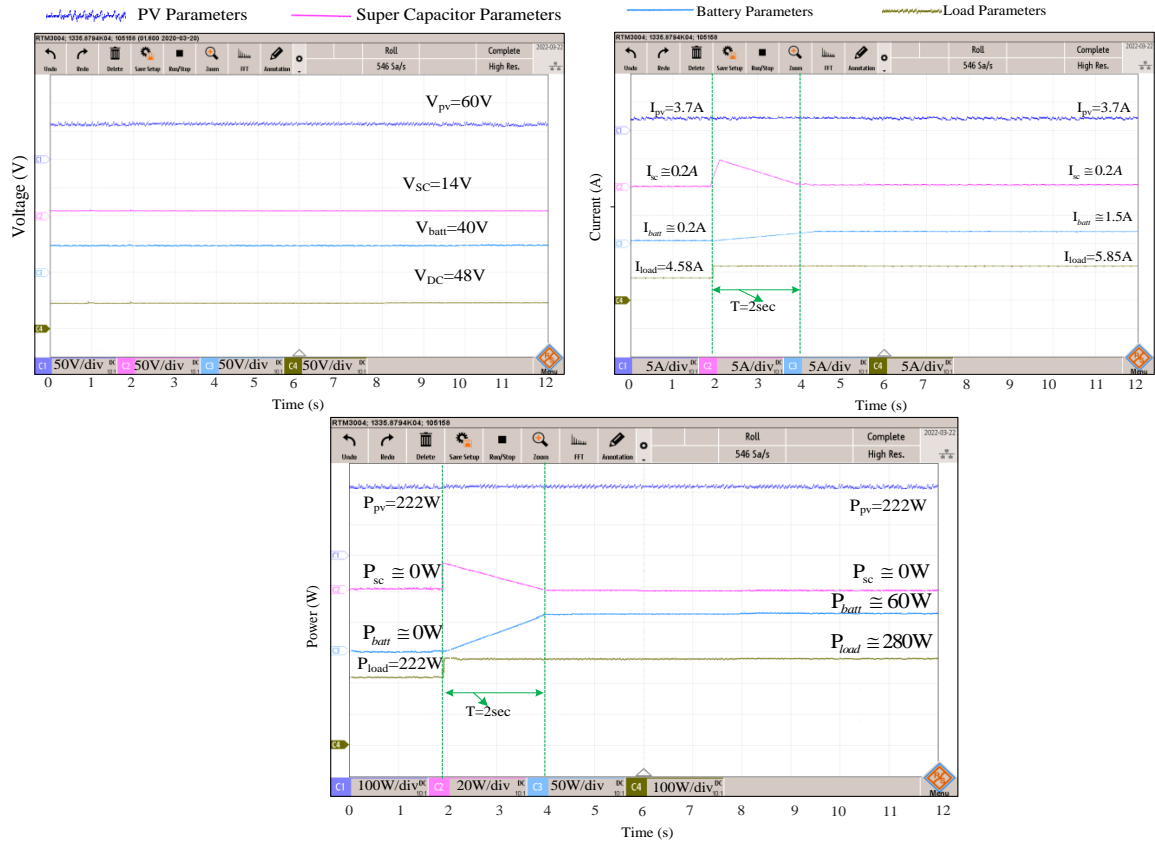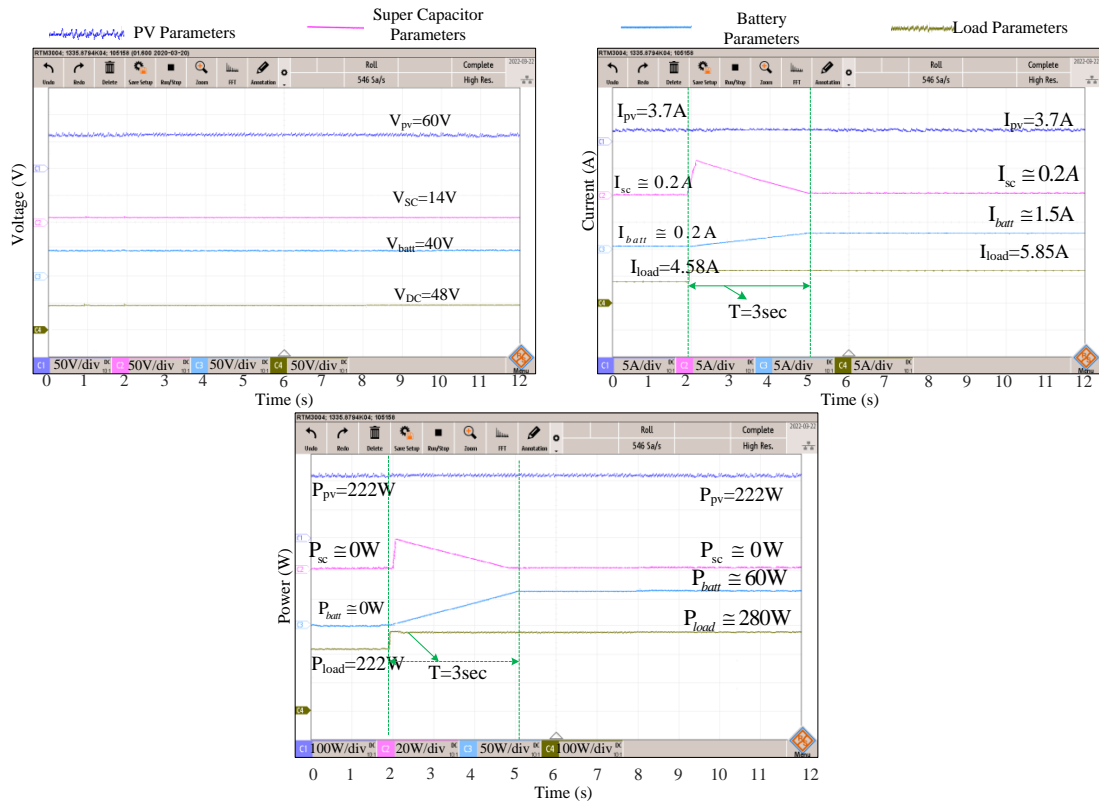
Figure 6.27: Experimental results of increase in load demand: (c)proposed method with T = 2 sec (scenario 3), (d)proposed method with T = 3 sec (scenario 4)
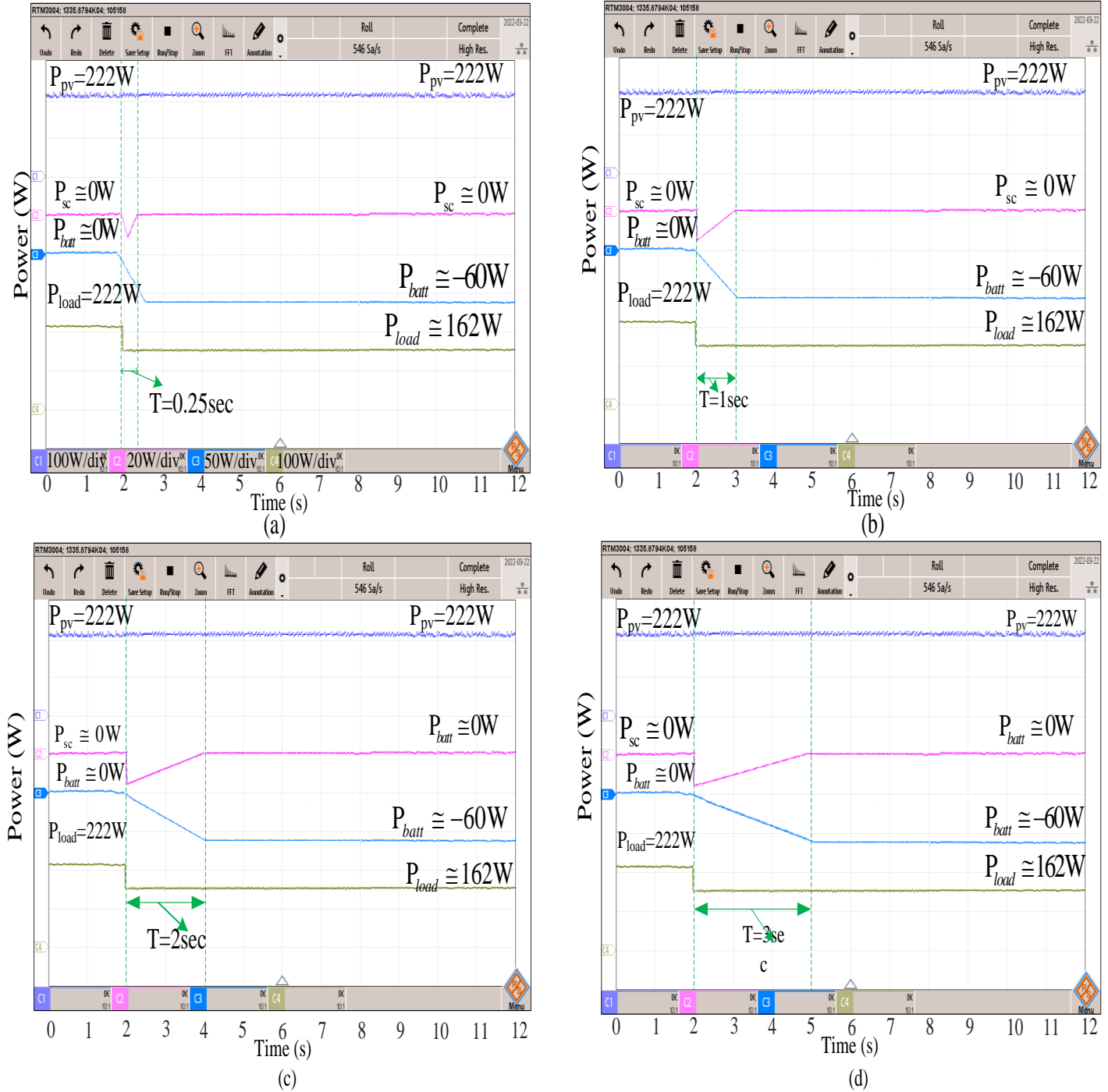
Figure 6.28: Experimental results of decrease in load demand: (a) power of conventional method (scenario 1),(b) power of proposed method with T = 1 sec(scenario 2),(c) power of proposed method with T = 2 sec (scenario 3),(d) power of proposed method with T = 3 sec (scenario 4)

BESS, and excess power from PV is taken by the battery after T seconds of post disturbance. With traditional voltage controllers, as observed in Figure.6.28(a), the response time of SC and BESS is quick, and they are charged with faster charge rate limit within a short duration of time (scenario1). The results of the proposed controller with different settling periods of 1sec (scenario2), 2sec (scenario3), and 3sec (scenario4) are shown in Figure.6.28(b)–(d). It indicates that the proposed control BESS charges at a slower rate than the traditional voltage controller method.

6.11   Conclusions

In this chapter, an energy management system for DC nanogrid has been proposed to optimize charge/discharge rates of the battery with SC. A Jaya-based optimization algorithm was used to optimally to calculate the charge/discharge rate constants of HESS for a given desired operational time constant and load/PV generation perturbation. Further, to improve the longevity of BESS, the EMS was designed to avoid deep charging and discharging. The PV generation derated especially under light load (no-load) conditions and when battery SoC$\geq$ SoC$_{max}$. Similarly, the SC charging and optional load shedding were used when SoC$\leq$ SoC$_{min}$ to avoid deep discharging.

In the proposed EMS, the DC voltage of the nanogrid was maintained constant by HESS system, which also enables instantaneous power balance. The effectiveness of the proposed EMS was validated through both simulation studies and by developing the hardware prototype. The results were compared with conventional control method, and it was observed that energy charge/discharge rates by the battery were optimized during the transient period compared to conventional scheme.

Chapter 7

Conclusions and Scope for Future Work

7.1 Conclusions

To understand the principles and advancements in the history of hybrid systems, a study of earlier chapters on hybrid systems included a PV panel, an FC, a battery, SC and amanagement. Furthermore, a complete comparison, analysis, and integration of management topology was carried out.
The following conclusions have been drawn from the research work.

A solar photovoltaic (PV) controller based on Bayesian Fusion Techinique (BFT) was developed for better tracking of global maximum power point in partially shaded environments. Comparing the recommended approach to PSO, Jaya, and incremental conductance-based tracking techniques, the proposed method is easier to use, highly cost-effective, and could provide quicker and more effective tracking performance.To help the controller overcome stagnancy at the nearby peak location in a partially darkened state, BFT is created. A reverse probability that represents uncertainty depending on available observations is a feature of BFT. The approach suggested is more effective than many current state-of-the-art methods in that it minimizes the number of repetitions while still achieving GMPP. This work might be expanded to include more features of renewable energy, such as utilising machine learning to quickly distinguish between temperature differences and enable effective control of various hybrid renewable energy sources, such as solar energy, wind energy, etc.

A static as well as dynamic model of fuel cell(FC) was examined and simulated at various gas flows using a maximum power tracker. Static and dynamic models verified the mathematical concepts. Extra overshoots appeared in the simulation of the dynamic FC model. The device that tracks it extracts maximum power while being efficient. The constant step applied to or removed from the present amount can be used to regulate the time required to achieve MPP. An increase in constant step decreases tracking time while increasing output power fluctuations. Another advantage of adopting MPPT is its capacity to prevent FC from deteriorating and improve its lifetime by preventing the FC voltage drop and current from exceeding critical limits. The compensator's work is to keep the voltage that it outputs at the level specified by the user's specification. We may conclude that the proposed approach has certain benefits by managing

current, hydrogen gas flow, and oxygen gas flow in a single MPP tracker while all parameters are associated with the current demanded by the load.We may use it to create a controller for the hydrogen gas valves and oxygen gas values described by the proposed method.

Typically, Fuzzy Logic Controller (FLC) [129], artificial neural network (ANN) algorithms [165], An adaptive neuro-fuzzy inference system (ANFIS) [45] method was used for decision-making problems. The major drawback of these controllers is that they require large amounts of training data and intense computational facilities. However, the implementation of rules-based heuristic strategies is fairly simple and straight forward. In these approaches, there is no requirement for a large data set for training and no need for huge computational facilities, and control actions are highly reliable. This makes it more feasible for real-world problems and can be implemented using already available computational facilities. Owing to these advantages, the rule-based heuristic approach scores over other artificially, intelligent approaches. However, these approaches also have a few challenges, especially; to frame the rules, for which expert knowledge is required.

The major contributions of a successful EMS for a standalone DC microgrid with PV/fuel cell/energy storage systems were suggested. The EMS is designed to increase battery longevity by keeping the battery's SoC within an acceptable range, as well as to limit hydrogen fuel input in a fuel cell without affecting system dependability. In normal operation, the PV system runs in MPPT mode to maximise renewable energy use. To minimise deep charging/discharging of the battery, the fuel cell operates as a function of the battery SoC, which also enhances fuel cell efficiency. EMS manages the battery bank to guarantee balanced power distribution sources and loads while managing DC link voltage.Furthermore, utilising a super-capacitor, the EMS may be significantly changed for effective system functioning under transient situations while keeping the battery depletion rate below acceptable ranges. Furthermore, the proposed EMS algorithm's use may be extended to microgrids with heterogeneous distributed generators.

To optimize the charge/discharge rate and energy stored/discharged by the storage device, a dynamic rate-limit controller has been developed. Depending on the load requirement and settling time, two distinct rate-limits were established to charge/discharge electricity from the battery. To validate the control scheme's efficacy, it was implemented to an independent photovoltaic system with HESS by establishing a control hardware-in-loop dSPACE. When the findings have been compared to the usual control method, it was discovered that charge/discharge evaluations and energy stored/discharged by the battery were optimized over the transient phase. The amount of stress on the battery was also optimized as the charge/discharge incidences were optimized, thereby minimizing the life-time restriction effects of high charge/discharge amounts. Furthermore, because the energy stored/discharged through the battery was optimized, the bat-

tery's state of charge can remain within limits for a longer period of time, resulting in low overcharging/discharging of the batteries. Because the recommended control approach preserves the characteristics of the traditional control scheme, the energy balance stays constant under steady-state operating circumstances with the assistance of supercapacitor.

7.2   Scope for Future Research

A prospective researcher has the opportunity to expand on the current research effort:

- The proposed EMS is subject to control the microgrid in grid-connected mode. However, during the period of disconnection from the grid (islanded mode) the microgrid needs a different operating strategy in order to sustain its stability. In islanded mode, voltage magnitude and system frequency drifts away from their nominal values and hence the stability of microgrid highly depends on the balance between generation and consumption. In this case, role of droop control mechanisms is very important to keep the frequency and voltage in microgrid at a certain level.

  At the same time, there exists power fluctuations due to non-linearity of load and the stochastic behavior of solar PV plant. This matter exacerbates the situation and pushes the microgrid forward to become unstable. Therefore, a sophisticated energy management approach must be adopted to maintain the microgrid during the islanded operating mode.

- The methods recommended in the present investigation may be employed on PV integration to grid-tied systems in order to increase PV system tracking efficiency.

- Improved adaptive optimisation approaches can be used in hybrid systems to enhance efficiency while providing consistent power to the DC grid.

- Maximum power point tracking strategies can be used to increase wind power generating efficiency. etc.

Publications

SCI International Journal Publications:

[1] Ramesh Gugulothu and Bhookya Nagu, "**A Bayesian fusion technique for maximum power point tracking under partial shading condition**," in *SN Applied. Science-Springer nature(ESCI).*, volume. 3, no. 539, pp. 2865-2884, 2021. **Impact facor:2.11.**.

[2] Ramesh Gugulothu, Bhookya Nagu Deepak Pullaguram, " **A computationally efficient Jaya optimization for fuel cell maximum power tracking, Energy Sources**," in *Part A: Recovery, Utilization, and Environmental Effects-.Taylor and Francis online(SCI)*, volume. 44, no. 1, pp. 1541-1565, 2022. **Impact facor:2.902**

[3] Ramesh Gugulothu, Bhookya Nagu Deepak Pullaguram, " **Energy management strategy for standalone DC microgrid system with photovoltaic/fuel cell/battery storage**," in *Journal of Energy Storage-Elsevier (SCI)*, volume. 57, pages. 106274, pp.2352-152X, 2023.**Impact facor:8.907**.

[4] Ramesh Gugulothu, Bhookya Nagu Deepak Pullaguram, " **Optimal coordinated energy management strategy for standalone solar photovoltaic system with hybrid energy storage**," in *Journal of Energy Storage-Elsevier (SCI)*, volume. 67, pages. 107628,, pp.2352-152X, 2023.**Impact facor:8.907**.

References

References

[1] N. Femia, G. Petrone, G. Spagnuolo, and M. Vitelli, "Optimization of perturb and observe maximum power point tracking method," *IEEE Transactions on Power Electronics*, vol. 20, no. 4, pp. 963–973, 2005.

[2] S. K. Kollimalla and M. K. Mishra, "Variable perturbation size adaptive po mppt algorithm for sudden changes in irradiance," *IEEE Transactions on Sustainable Energy*, vol. 5, no. 3, pp. 718–728, 2014.

[3] N. Femia, D. Granozio, G. Petrone, G. Spagnuolo, and M. Vitelli, "Predictive adaptive mppt perturb and observe method," *IEEE Transactions on Aerospace and Electronic Systems*, vol. 43, no. 3, pp. 934–950, 2007.

[4] K. S. Tey and S. Mekhilef, "Modified incremental conductance algorithm for photovoltaic system under partial shading conditions and load variation," *IEEE Transactions on Industrial Electronics*, vol. 61, no. 10, pp. 5384–5392, 2014.

[5] W. Xiao and W. Dunford, "A modified adaptive hill climbing mppt method for photovoltaic power systems," in *2004 IEEE 35th Annual Power Electronics Specialists Conference (IEEE Cat. No.04CH37551)*, vol. 3, 2004, pp. 1957–1963 Vol.3.

[6] I. R. Balasubramanian, S. Ilango Ganesan, and N. Chilakapati, "Impact of partial shading on the output power of pv systems under partial shading conditions," *IET Power Electronics*, vol. 7, no. 3, pp. 657–666, 2014. [Online]. Available: https://ietresearch.onlinelibrary.wiley.com/doi/abs/10.1049/iet-pel.2013.0143

[7] A. Harrag and S. Messalti, "Variable step size modified po mppt algorithm using ga-based hybrid offline/online pid controller," *Renewable and Sustainable Energy Reviews*, vol. 49, pp. 1247–1260, 2015. [Online]. Available: https://www.sciencedirect.com/science/article/pii/S1364032115004475

[8] F. M. de Oliveira, S. A. Oliveira da Silva, F. R. Durand, L. P. Sampaio, V. D. Bacon, and L. B. Campanhol, "Grid-tied photovoltaic system based on pso mppt technique with active power line conditioning," *IET Power Electronics*, vol. 9, no. 6, pp. 1180–1191,

2016. [Online]. Available: https://ietresearch.onlinelibrary.wiley.com/doi/abs/10.1049/iet-pel.2015.0655

[9] S. Lyden and M. E. Haque, "A simulated annealing global maximum power point tracking approach for pv modules under partial shading conditions," *IEEE Transactions on Power Electronics*, vol. 31, no. 6, pp. 4171–4181, 2016.

[10] W. Zhu, L. Shang, P. Li, and H. Guo, "Modified hill climbing mppt algorithm with reduced steady-state oscillation and improved tracking efficiency," *The Journal of Engineering*, vol. 2018, no. 17, pp. 1878–1883, 2018. [Online]. Available: https://ietresearch.onlinelibrary.wiley.com/doi/abs/10.1049/joe.2018.8337

[11] K. Ishaque and Z. Salam, "A deterministic particle swarm optimization maximum power point tracker for photovoltaic system under partial shading condition," *IEEE Transactions on Industrial Electronics*, vol. 60, no. 8, pp. 3195–3206, 2013.

[12] T. Sudhakar Babu, N. Rajasekar, and K. Sangeetha, "Modified particle swarm optimization technique based maximum power point tracking for uniform and under partial shading condition," *Applied Soft Computing*, vol. 34, pp. 613–624, 2015. [Online]. Available: https://www.sciencedirect.com/science/article/pii/S1568494615003294

[13] L. L. Jiang, D. L. Maskell, and J. C. Patra, "A novel ant colony optimization-based maximum power point tracking for photovoltaic systems under partially shaded conditions," *Energy and Buildings*, vol. 58, pp. 227–236, 2013. [Online]. Available: https://www.sciencedirect.com/science/article/pii/S0378778812006366

[14] K. Sundareswaran, P. Sankar, P. S. R. Nayak, S. P. Simon, and S. Palani, "Enhanced energy output from a pv system under partial shaded conditions through artificial bee colony," *IEEE Transactions on Sustainable Energy*, vol. 6, no. 1, pp. 198–209, 2015.

[15] G. Li, Y. Jin, M. Akram, X. Chen, and J. Ji, "Application of bio-inspired algorithms in maximum power point tracking for pv systems under partial shading conditions – a review," *Renewable and Sustainable Energy Reviews*, vol. 81, pp. 840–873, 2018. [Online]. Available: https://www.sciencedirect.com/science/article/pii/S1364032117311760

[16] S. Daraban, D. Petreus, and C. Morel, "A novel mppt (maximum power point tracking) algorithm based on a modified genetic algorithm specialized on tracking the global maximum power point in photovoltaic systems affected

by partial shading," *Energy*, vol. 74, pp. 374–388, 2014. [Online]. Available: https://www.sciencedirect.com/science/article/pii/S0360544214008184

[17] S. Mohanty, B. Subudhi, and P. K. Ray, "A new mppt design using grey wolf optimization technique for photovoltaic system under partial shading conditions," *IEEE Transactions on Sustainable Energy*, vol. 7, no. 1, pp. 181–188, 2016.

[18] J. Prasanth Ram and N. Rajasekar, "A novel flower pollination based global maximum power point method for solar maximum power point tracking," *IEEE Transactions on Power Electronics*, vol. 32, no. 11, pp. 8486–8499, 2017.

[19] H. Li, D. Yang, W. Su, J. Lü, and X. Yu, "An overall distribution particle swarm optimization mppt algorithm for photovoltaic system under partial shading," *IEEE Transactions on Industrial Electronics*, vol. 66, no. 1, pp. 265–275, 2019.

[20] J. Prasanth Ram and N. Rajasekar, "A new robust, mutated and fast tracking lpso method for solar pv maximum power point tracking under partial shaded conditions," *Applied Energy*, vol. 201, pp. 45–59, 2017. [Online]. Available: https://www.sciencedirect.com/science/article/pii/S0306261917306049

[21] S. Malathy and R. Ramaprabha, "Maximum power point tracking algorithm of spva under inhomogeneous irradiation conditions: A modified fibonacci search based approach," in *2017 IEEE 12th International Conference on Power Electronics and Drive Systems (PEDS)*, 2017, pp. 487–492.

[22] X. Li, Y. Li, and J. E. Seem, "Maximum power point tracking for photovoltaic system using adaptive extremum seeking control," *IEEE Transactions on Control Systems Technology*, vol. 21, no. 6, pp. 2315–2322, 2013.

[23] L. M. Elobaid, A. K. Abdelsalam, and E. E. Zakzouk, "Artificial neural network-based photovoltaic maximum power point tracking techniques: a survey," *IET Renewable Power Generation*, vol. 9, no. 8, pp. 1043–1063, 2015. [Online]. Available: https://ietresearch.onlinelibrary.wiley.com/doi/abs/10.1049/iet-rpg.2014.0359

[24] D. A. Nugraha, K. L. Lian, and Suwarno, "A novel mppt method based on cuckoo search algorithm and golden section search algorithm for partially shaded pv system," *Canadian Journal of Electrical and Computer Engineering*, vol. 42, no. 3, pp. 173–182, 2019.

[25] M. Kermadi, Z. Salam, J. Ahmed, and E. M. Berkouk, "An effective hybrid maximum power point tracker of photovoltaic arrays for complex partial shading conditions," *IEEE Transactions on Industrial Electronics*, vol. 66, no. 9, pp. 6990–7000, 2019.

[26] J. P. Ram, D. S. Pillai, N. Rajasekar, and S. M. Strachan, "Detection and identification of global maximum power point operation in solar pv applications using a hybrid elpso-po tracking technique," *IEEE Journal of Emerging and Selected Topics in Power Electronics*, vol. 8, no. 2, pp. 1361–1374, 2020.

[27] R. Venkata Rao, "Jaya: A simple and new optimization algorithm for solving constrained and unconstrained optimization problems," *International Journal of Industrial Engineering Computations*, vol. 7, pp. 19–34, 01 2016.

[28] I. Shams, S. Mekhilef, and K. S. Tey, "Maximum power point tracking using modified butterfly optimization algorithm for partial shading, uniform shading, and fast varying load conditions," *IEEE Transactions on Power Electronics*, vol. 36, no. 5, pp. 5569–5581, 2021.

[29] M. Seyedmahmoudian, T. K. Soon, B. Horan, A. Ghandhari, S. Mekhilef, and A. Stojcevski, "New armo-based mppt technique to minimize tracking time and fluctuation at output of pv systems under rapidly changing shading conditions," *IEEE Transactions on Industrial Informatics*, pp. 1–1, 2019.

[30] A. Ali, K. Almutairi, M. Z. Malik, K. Irshad, V. Tirth, S. Algarni, M. H. Zahir, S. Islam, M. Shafiullah, and N. K. Shukla, "Review of online and soft computing maximum power point tracking techniques under non-uniform solar irradiation conditions," *Energies*, vol. 13, no. 12, 2020. [Online]. Available: https://www.mdpi.com/1996-1073/13/12/3256

[31] A. K. Podder, N. K. Roy, and H. R. Pota, "Mppt methods for solar pv systems: a critical review based on tracking nature," *IET Renewable Power Generation*, vol. 13, no. 10, pp. 1615–1632, 2019. [Online]. Available: https://ietresearch.onlinelibrary.wiley.com/doi/abs/10.1049/iet-rpg.2018.5946

[32] e. a. Srinivas N, Krause A, "Gaussian process optimization in the bandit setting: no regret and experimental design," in *Proceedings of international conference on machine learning (ICML)*, 2010, pp. 1015–1022.

[33] L. Egiziano, A. Giustiniani, G. Petrone, G. Spagnuolo, and M. Vitelli, "Optimization of perturb and observe control of grid connected pem fuel cells," in *2009 International Conference on Clean Electrical Power*, 2009, pp. 775–781.

[34] N. Karami, L. E. Khoury, G. Khoury, and N. Moubayed, "Comparative study between p amp;o and incremental conductance for fuel cell mppt," in *International Conference on Renewable Energies for Developing Countries 2014*, Nov 2014, pp. 17–22.

[35] H. Rezk and A. Fathy, "Performance improvement of pem fuel cell using variable step-size incremental resistance mppt technique," *Sustainability*, vol. 12, no. 14, 2020.

[36] P.-Y. Chen, K.-N. Yu, H.-T. Yau, J.-T. Li, and C.-K. Liao, "A novel variable step size fractional order incremental conductance algorithm to maximize power tracking of fuel cells," *Applied Mathematical Modelling*, vol. 45, pp. 1067 – 1075, 2017.

[37] Q. Li, W. Chen, Z. Liu, A. Guo, and S. Liu, "Control of proton exchange membrane fuel cell system breathing based on maximum net power control strategy," *Journal of Power Sources*, vol. 241, pp. 212–218, 2013.

[38] N. Bizon, "On tracking robustness in adaptive extremum seeking control of the fuel cell power plants," *Applied Energy*, vol. 87, no. 10, pp. 3115–3130, 2010.

[39] Bizon, "Energy optimization of fuel cell system by using global extremum seeking algorithm," *Applied Energy*, vol. 206, pp. 458–474, 2017.

[40] "Ieee/caa journal of automatica sinicae," *IEEE/CAA*, 2017.

[41] S. M. Nasiri Avanaki I, "A new maximum power point tracking method for pem fuel cells based on water cycle algorithm," *J Renew Energy Environ*, 2016.

[42] M. Aly and H. Rezk, "A differential evolution-based optimized fuzzy logic mppt method for enhancing the maximum power extraction of proton exchange membrane fuel cells," *IEEE Access*, vol. 8, pp. 172 219–172 232, 2020.

[43] A. Fathy, M. A. Abdelkareem, A. Olabi, and H. Rezk, "A novel strategy based on salp swarm algorithm for extracting the maximum power of proton exchange membrane fuel cell," *International Journal of Hydrogen Energy*, vol. 46, no. 8, pp. 6087–6099, 2021, developments of Hydrogen Fuel Cell Technologies.

[44] M. Derbeli, O. Barambones, M. Y. Silaa, and C. Napole, "Real-time implementation of a new mppt control method for a dc-dc boost converter used in a pem fuel cell power system," *Actuators*, vol. 9, no. 4, 2020.

[45] K. Reddy and D. S. Natarajan, "Anfis-mppt control algorithm for a pemfc system used in electric vehicle applications," *International Journal of Hydrogen Energy*, vol. 44, 04 2019.

[46] A. Harrag and H. Bahri, "Novel neural network ic-based variable step size fuel cell mppt controller: Performance, efficiency and lifetime improvement," *International Journal of Hydrogen Energy*, vol. 42, no. 5, pp. 3549–3563, 2017.

[47] N. Harrabi, M. Souissi, A. Aitouche, and M. Chaabane, "Modeling and control of photo-voltaic and fuel cell based alternative power systems," *International Journal of Hydrogen Energy*, vol. 43, no. 25, pp. 11 442–11 451, 2018, alternative Energies for Sustainability.

[48] S. Ahmadi, S. Abdi, and M. Kakavand, "Maximum power point tracking of a proton exchange membrane fuel cell system using pso-pid controller," *International Journal of Hydrogen Energy*, vol. 42, 07 2017.

[49] D. N. Luta and A. K. Raji, "Fuzzy rule-based and particle swarm optimisation mppt techniques for a fuel cell stack," *Energies*, vol. 12, no. 5, 2019.

[50] Shashikant and B. Shaw, "Comparison of sca-optimized pid and p&o-based mppt for an off-grid fuel cell system," in *Soft Computing in Data Analytics*, J. Nayak, A. Abraham, B. M. Krishna, G. T. Chandra Sekhar, and A. K. Das, Eds. Singapore: Springer Singapore, 2019, pp. 51–58.

[51] S. Kumar and B. Shaw, "Design of off-grid fuel cell by implementing alo optimized pid-based mppt controller," in *Soft Computing in Data Analytics*, J. Nayak, A. Abraham, B. M. Krishna, G. T. Chandra Sekhar, and A. K. Das, Eds. Singapore: Springer Singapore, 2019, pp. 83–93.

[52] N. Priyadarshi, F. Azam, S. Solanki, A. Sharma, A. K. Bhoi, and D. Almakhles, *A Bio-Inspired Chicken Swarm Optimization-Based Fuel Cell System for Electric Vehicle Applications*, 01 2021, pp. 297–308.

[53] M. Derbeli, O. Barambones, and L. Sbita, "A robust maximum power point tracking control method for a pem fuel cell power system," *Applied Sciences*, vol. 8, no. 12, 2018.

[54] K. Rana, V. Kumar, N. Sehgal, and S. George, "A novel dpdi feedback based control scheme using gwo tuned pid controller for efficient mppt of pem fuel cell," *ISA Transactions*, vol. 93, pp. 312–324, 2019.

[55] S. Samal, R. Makireddi, and P. K. Barik, "Modeling and simulation of interleaved boost converter with mppt for fuel cell application," 03 2018, pp. 1–5.

[56] C. Wang and M. H. Nehrir, "Power management of a stand-alone wind/photovoltaic/fuel cell energy system," *IEEE Transactions on Energy Conversion*, vol. 23, no. 3, pp. 957–967, 2008.

[57] G. Janssen, E. Sitters, and A. Pfrang, "Proton-exchange-membrane fuel cells durability evaluated by load-on/off cycling," *Journal of Power Sources*, vol. 191, no. 2, pp. 501–509, 2009. [Online]. Available: https://www.sciencedirect.com/science/article/pii/S0378775309002729

[58] M. Marrony, R. Barrerab, S. Quenet, S. Ginocchio, L. Montelatici, and A. Aslanides, "Durability study and lifetime prediction of baseline proton exchange membrane fuel cell under severe operating conditions," *Journal of Power Sources - J POWER SOURCES*, vol. 182, pp. 469–475, 08 2008.

[59] G. T. Samson, T. M. Undeland, O. Ulleberg, and P. J. S. Vie, "Optimal load sharing strategy in a hybrid power system based on pv/fuel cell/ battery/supercapacitor," in *2009 International Conference on Clean Electrical Power*, 2009, pp. 141–146.

[60] K. Agbossou, M. Kolhe, J. Hamelin, and T. Bose, "Performance of a stand-alone renewable energy system based on energy storage as hydrogen," *IEEE Transactions on Energy Conversion*, vol. 19, no. 3, pp. 633–640, 2004.

[61] A. Frances, R. Asensi, o. Garcia, R. Prieto, and J. Uceda, "Modeling electronic power converters in smart dc microgrids—an overview," *IEEE Transactions on Smart Grid*, vol. 9, no. 6, pp. 6274–6287, 2018.

[62] V. Vega-Garita, M. F. Sofyan, N. Narayan, L. Ramirez-Elizondo, and P. Bauer, "Energy management system for the photovoltaic battery integrated module," *Energies*, vol. 11, no. 12, 2018.

[63] A. A. A. Alahmadi, Y. Belkhier, N. Ullah, H. Abeida, M. S. Soliman, Y. S. H. Khraisat, and Y. M. Alharbi, "Hybrid wind/pv/battery energy management-based intelligent non-integer control for smart dc-microgrid of smart university," *IEEE Access*, vol. 9, pp. 98 948–98 961, 2021.

[64] D. Lu, H. Fakham, T. Zhou, and B. François, "Application of petri nets for the energy management of a photovoltaic based power station including storage units," *Renewable Energy*, vol. 35, no. 6, pp. 1117–1124, 2010.

[65] M. Marzband, S. S. Ghazimirsaeid, H. Uppal, and T. Fernando, "A real-time evaluation of energy management systems for smart hybrid home microgrids," *Electric Power Systems Research*, vol. 143, pp. 624–633, 2017.

[66] N. Mebarki, T. Rekioua, Z. Mokrani, and D. Rekioua, "Supervisor control for stand-alone photovoltaic/hydrogen/ battery bank system to supply energy to an electric vehicle," *International Journal of Hydrogen Energy*, vol. 40, no. 39, pp. 13 777–13 788, 2015.

[67] H. Hassani, F. Zaouche, D. Rekioua, S. Belaid, T. Rekioua, and S. Bacha, "Feasibility of a standalone photovoltaic/battery system with hydrogen production," *Journal of Energy Storage*, vol. 31, p. 101644, 2020.

[68] M. F. Elmorshedy, M. Elkadeem, K. M. Kotb, I. B. Taha, and D. Mazzeo, "Optimal design and energy management of an isolated fully renewable energy system integrating batteries and supercapacitors," *Energy Conversion and Management*, vol. 245, p. 114584, 2021.

[69] C. Serir, D. Rekioua, N. Mezzai, and S. Bacha, "Supervisor control and optimization of multi-sources pumping system with battery storage," *International Journal of Hydrogen Energy*, vol. 41, no. 45, pp. 20 974–20 986, 2016.

[70] L. Valverde, F. Rosa, A. del Real, A. Arce, and C. Bordons, "Modeling, simulation and experimental set-up of a renewable hydrogen-based domestic microgrid," *International Journal of Hydrogen Energy*, vol. 38, no. 27, pp. 11 672–11 684, 2013.

[71] P. Thounthong, V. Chunkag, P. Sethakul, S. Sikkabut, S. Pierfederici, and B. Davat, "Energy management of fuel cell/solar cell/supercapacitor hybrid power source," *Journal of Power Sources*, vol. 196, no. 1, pp. 313–324, 2011.

[72] E. G. Shehata, M. S. Gaber, K. A. Ahmed, and G. M. Salama, "Implementation of an energy management algorithm in dc mgs using multi-agent system," *International Transactions on Electrical Energy Systems*, vol. 29, no. 4, p. e2790, 2019.

[73] Amin, R. T. Bambang, A. S. Rohman, C. J. Dronkers, R. Ortega, and A. Sasongko, "Energy management of fuel cell/battery/supercapacitor hybrid power sources using model predictive control," *IEEE Transactions on Industrial Informatics*, vol. 10, no. 4, pp. 1992–2002, 2014.

[74] R. Sathishkumar, S. K. Kollimalla, and M. K. Mishra, "Dynamic energy management of micro grids using battery super capacitor combined storage," in *2012 Annual IEEE India Conference (INDICON)*, 2012, pp. 1078–1083.

[75] Y. Jia, R. Shibata, N. Yamamura, and M. Ishida, "Characteristics of smoothed-power output topology of stand-alone renewable power system using edlc," in *2006 37th IEEE Power Electronics Specialists Conference*, 2006, pp. 1–7.

[76] M. Glavin, P. K. Chan, S. Armstrong, and W. Hurley, "A stand-alone photovoltaic supercapacitor battery hybrid energy storage system," in *2008 13th International Power Electronics and Motion Control Conference*, 2008, pp. 1688–1695.

[77] P. T. Moseley, "Energy storage in remote area power supply (raps) systems," *Journal of Power Sources*, vol. 155, no. 1, pp. 83–87, 2006, selected papers from the 88th Bunsenkolloquium.

[78] N. Mendis, K. M. Muttaqi, and S. Perera, "Management of battery-supercapacitor hybrid energy storage and synchronous condenser for isolated operation of pmsg based variable-speed wind turbine generating systems," *IEEE Transactions on Smart Grid*, vol. 5, no. 2, pp. 944–953, 2014.

[79] U. B. P. S. Arunkumar, C. R.Manthati, "Supercapacitor-based transient power supply for dc microgrid applications," *Electrical Engineering*, vol. 104, no. 2, pp. 1432–0487, 2022.

[80] N. Mendis, K. M. Muttaqi, and S. Perera, "Active power management of a super capacitor-battery hybrid energy storage system for standalone operation of dfig based wind turbines," in *2012 IEEE Industry Applications Society Annual Meeting*, 2012, pp. 1–8.

[81] A. M. Gee and R. W. Dunn, "Novel battery / supercapacitor hybrid energy storage control strategy for battery life extension in isolated wind energy conversion systems," in *45th International Universities Power Engineering Conference UPEC2010*, 2010, pp. 1–6.

[82] O. Laldin, M. Moshirvaziri, and O. Trescases, "Predictive algorithm for optimizing power flow in hybrid ultracapacitor/battery storage systems for light electric vehicles," *IEEE Transactions on Power Electronics*, vol. 28, no. 8, pp. 3882–3895, 2013.

[83] M. Ding, B. Wang, Z. Chen, Z. Chen, Y. Luo, and G. Zheng, "Stabilizing control strategy of complementary energy storage in renewable energy system," in *IEEE PES Innovative Smart Grid Technologies*, 2012, pp. 1–5.

[84] A. Mohamed, V. Salehi, and O. Mohammed, "Real-time energy management algorithm for mitigation of pulse loads in hybrid microgrids," *IEEE Transactions on Smart Grid*, vol. 3, no. 4, pp. 1911–1922, 2012.

[85] P. Singh and J. s. Lather, "Variable structure control for dynamic power-sharing and voltage regulation of dc microgrid with a hybrid energy storage system," *International Transactions on Electrical Energy Systems*, vol. 30, no. 9, p. e12510, 2020.

[86] H. Fakham, D. Lu, and B. Francois, "Power control design of a battery charger in a hybrid active pv generator for load-following applications," *IEEE Transactions on Industrial Electronics*, vol. 58, no. 1, pp. 85–94, 2011.

[87] B. Hredzak, V. G. Agelidis, and M. Jang, "A model predictive control system for a hybrid battery-ultracapacitor power source," *IEEE Transactions on Power Electronics*, vol. 29, no. 3, pp. 1469–1479, 2014.

[88] B. Hredzak, V. G. Agelidis, and G. D. Demetriades, "A low complexity control system for a hybrid dc power source based on ultracapacitor–lead–acid battery configuration," *IEEE Transactions on Power Electronics*, vol. 29, no. 6, pp. 2882–2891, 2014.

[89] Z. Zheng, X. Wang, and Y. Li, "A control method for grid-friendly photovoltaic systems with hybrid energy storage units," in *2011 4th International Conference on Electric Utility Deregulation and Restructuring and Power Technologies (DRPT)*, 2011, pp. 1437–1440.

[90] D. Wu, R. Todd, and A. J. Forsyth, "Adaptive rate-limit control for energy storage systems," *IEEE Transactions on Industrial Electronics*, vol. 62, no. 7, pp. 4231–4240, 2015.

[91] M. G. Villalva, J. R. Gazoli, and E. R. Filho, "Comprehensive approach to modeling and simulation of photovoltaic arrays," *IEEE Transactions on Power Electronics*, vol. 24, no. 5, pp. 1198–1208, 2009.

[92] P. A. Lynn, "Electricity from sunlight: An introduction to photovoltaics," *John Wiley and Sons*, vol. 9, no. 11, 2010.

[93] Øystein Ulleberg, "Stand-alone power systems for the future: optimal design, operation control of solar-hydrogen energy systems," *NTNU, Trondheim, Norv'ege,*, vol. 12, 1998.

[94] C. Wang, M. Nehrir, and S. Shaw, "Dynamic models and model validation for pem fuel cells using electrical circuits," *IEEE Transactions on Energy Conversion*, vol. 20, no. 2, pp. 442–451, 2005.

[95] Z. Ural Bayrak, M. Gençoğlu, and B. Gumus, "Dynamic simulation of a pem fuel cell system," pp. 13–15, 08 2007.

[96] W. Saeed and G. Warkozek, "Modeling and analysis of renewable pem fuel cell system," *Energy Procedia*, vol. 74, pp. 87–101, 08 2015.

[97] I. Papagiannakis, "Studying and improving the efficiency of water electrolysis using a proton exchange membrane electrolyser," 2005.

[98] J. Correa, F. Farret, L. Canha, and M. Simoes, "An electrochemical-based fuel-cell model suitable for electrical engineering automation approach," *IEEE Transactions on Industrial Electronics*, vol. 51, no. 5, pp. 1103–1112, 2004.

[99] R. R. K.W. Harrison and G. Martin, "Hydrogen production: Fundamentals and cas study summaries," *National Renewable Energy Laboratory, 8th World Hydrogen Energy Conference Essen, Germany NREL/CP-550-47302*, vol. CP, pp. 550–47 302, 2010.

[100] E. T. Services, "Fuel cell handbook," *USA: Solid State Energy Conversion Alliance.*, 2002.

[101] W. Winkler, "Thermodynamics, in high temperature solid oxide fuel cells: Fundamentals,design and applications," *S.C. Singhal and K. Kendall, Editors. lsevier Ltd.: Oxford,UK*, pp. 53–82, 2003.

[102] F. Huet, "A review of impedance measurements for determination of the state-of-charge or state-of-health of secondary batteries," *Journal of Power Sources*, vol. 70, no. 1, pp. 59–69, 1998. [Online]. Available: https://www.sciencedirect.com/science/article/pii/S0378775397026657

[103] R. C. Kroeze and P. T. Krein, "Electrical battery model for use in dynamic electric vehicle simulations," in *2008 IEEE Power Electronics Specialists Conference*, 2008, pp. 1336–1342.

[104] S. Barsali and M. Ceraolo, "Dynamical models of lead-acid batteries: implementation issues," *IEEE Transactions on Energy Conversion*, vol. 17, no. 1, pp. 16–23, 2002.

[105] M. Uzunoglu and M. Alam, "Dynamic modeling, design, and simulation of a combined pem fuel cell and ultracapacitor system for stand-alone residential applications," *IEEE Transactions on Energy Conversion*, vol. 21, no. 3, pp. 767–775, 2006.

[106] R. Spyker and R. Nelms, "Analysis of double-layer capacitors supplying constant power loads," *IEEE Transactions on Aerospace and Electronic Systems*, vol. 36, no. 4, pp. 1439–1443, 2000.

[107] P. C. Tang H, He S, "A short progress report on highefciency perovskite solar cells," *Nanoscale Res Lett*, vol. 12, no. 1, 2017.

[108] A. Safari and S. Mekhilef, "Simulation and hardware implementation of incremental conductance mppt with direct control method using cuk converter," *IEEE Transactions on Industrial Electronics*, vol. 58, no. 4, pp. 1154–1161, 2011.

[109] K. S. Tey and S. Mekhilef, "Modified incremental conductance algorithm for photovoltaic system under partial shading conditions and load variation," *IEEE Transactions on Industrial Electronics*, vol. 61, no. 10, pp. 5384–5392, 2014.

[110] B. Yang, T. Zhu, J. Wang, H. Shu, T. Yu, X. Zhang, W. Yao, and L. Sun, "Comprehensive overview of maximum power point tracking algorithms of pv systems under partial shading condition," *Journal of Cleaner Production*, vol. 268, p. 121983, 2020. [Online]. Available: https://www.sciencedirect.com/science/article/pii/S0959652620320308

[111] Y. Wang, Y. Li, and X. Ruan, "High-accuracy and fast-speed mppt methods for pv string under partially shaded conditions," *IEEE Transactions on Industrial Electronics*, vol. 63, no. 1, pp. 235–245, 2016.

[112] Z. Yang, Z. Yang, and J. Yin, "Realising advanced risk-based port state control inspection using data-driven bayesian networks," *Transportation Research Part A: Policy and Practice*, vol. 110, pp. 38–56, 2018. [Online]. Available: https://www.sciencedirect.com/science/article/pii/S0965856417309047

[113] F. Keyrouz, "Enhanced bayesian based mppt controller for pv systems," *IEEE Power and Energy Technology Systems Journal*, vol. 5, no. 1, pp. 11–17, 2018.

[114] T. Z. Zinola, Carlos F. Fahidy, "Some applications of bayes' rule in probability theory to electrocatalytic reaction engineering," *International Journal of Electrochemistry Hindawi Access to Research*, vol. 6, no. 19, pp. 2090–3529, 2011.

[115] Y. A. Mahmoud, W. Xiao, and H. H. Zeineldin, "A parameterization approach for enhancing pv model accuracy," *IEEE Transactions on Industrial Electronics*, vol. 60, no. 12, pp. 5708–5716, 2013.

[116] T. Shimizu, O. Hashimoto, and G. Kimura, "A novel high-performance utility-interactive photovoltaic inverter system," *IEEE Transactions on Power Electronics*, vol. 18, no. 2, pp. 704–711, 2003.

[117] C. Olalla, D. Clement, M. Rodriguez, and D. Maksimovic, "Architectures and control of submodule integrated dc–dc converters for photovoltaic applications," *IEEE Transactions on Power Electronics*, vol. 28, no. 6, pp. 2980–2997, 2013.

[118] R. C. N. Pilawa-Podgurski and D. J. Perreault, "Submodule integrated distributed maximum power point tracking for solar photovoltaic applications," *IEEE Transactions on Power Electronics*, vol. 28, no. 6, pp. 2957–2967, 2013.

[119] A. Safari and S. Mekhilef, "Incremental conductance mppt method for pv systems," in *2011 24th Canadian Conference on Electrical and Computer Engineering(CCECE)*, 2011, pp. 000 345–000 347.

[120] J.-t. Yu, C.-H. Kim, A. Wadood, T. Khurshaid, and S.-B. Rhee, "Jaya algorithm with self-adaptive multi-population and lévy flights for solving economic load dispatch problems," *IEEE Access*, vol. 7, pp. 21 372–21 384, 2019.

[121] C. Huang, L. Wang, R. S.-C. Yeung, Z. Zhang, H. S.-H. Chung, and A. Bensoussan, "A prediction model-guided jaya algorithm for the pv system maximum power point tracking," *IEEE Transactions on Sustainable Energy*, vol. 9, no. 1, pp. 45–55, 2018.

[122] S. Padmanaban, N. Priyadarshi, M. S. Bhaskar, J. B. Holm-Nielsen, E. Hossain, and F. Azam, "A hybrid photovoltaic-fuel cell for grid integration with jaya-based maximum power point tracking: Experimental performance evaluation," *IEEE Access*, vol. 7, pp. 82 978–82 990, 2019.

[123] P. Larranaga, C. Kuijpers, R. Murga, and Y. Yurramendi, "Learning bayesian network structures by searching for the best ordering with genetic algorithms," *IEEE Transactions on Systems, Man, and Cybernetics - Part A: Systems and Humans*, vol. 26, no. 4, pp. 487–493, 1996.

[124] urphy KP, "Machine learning—a probabilistic perspective," *The MIT Press, Cambridge Massachusetts London England*, 2012.

[125] K. Teo, P. Lim, B. L. Chua, H. H. Goh, and M. K. Tan, "Particle swarm optimization based maximum power point tracking for partially shaded photovoltaic arrays," *International Journal of Simulation: Systems, Science and Technology*, vol. 17, pp. 20.1–20.7, 01 2016.

[126] Z. Yang, M. Ghadamyari, H. Khorramdel, S. M. Seyed Alizadeh, S. Pirouzi, M. Milani, F. Banihashemi, and N. Ghadimi, "Robust multi-objective optimal design

of islanded hybrid system with renewable and diesel sources/stationary and mobile energy storage systems," *Renewable and Sustainable Energy Reviews*, vol. 148, p. 111295, 2021. [Online]. Available: https://www.sciencedirect.com/science/article/pii/S1364032121005827

[127] W. Cai, R. Mohammaditab, G. Fathi, K. Wakil, A. G. Ebadi, and N. Ghadimi, "Optimal bidding and offering strategies of compressed air energy storage: A hybrid robust-stochastic approach," *Renewable Energy*, vol. 143, pp. 1–8, 2019. [Online]. Available: https://www.sciencedirect.com/science/article/pii/S0960148119306603

[128] M. Zhang, T. Yan, and J. Gu, "Maximum power point tracking control of direct methanol fuel cells," *Journal of Power Sources*, vol. 247, pp. 1005 – 1010, 2014.

[129] N. E. Benchouia, A. Derghal, B. Mahmah, B. Madi, L. Khochemane, and E. Hadjadj Aoul, "An adaptive fuzzy logic controller (aflc) for pemfc fuel cell," *International Journal of Hydrogen Energy*, vol. 40, no. 39, pp. 13 806 – 13 819, 2015.

[130] G. M. P. M. e. a. Akbary, P., "Extracting appropriate nodal marginal prices for all types of committed reserve," *Comput Econ*, vol. 53, pp. 1–26, 2019.

[131] M. Dargahi, M. Rezanejad, J. Rouhi, and M. Shakeri, "Maximum power point tracking for fuel cell in fuel cell/battery hybrid systems," in *2008 IEEE International Multitopic Conference*, 2008, pp. 33–37.

[132] A. Kirubakaran, S. Jain, and R. Nema, "A review on fuel cell technologies and power electronic interface," *Renewable and Sustainable Energy Reviews*, vol. 13, no. 9, pp. 2430–2440, 2009.

[133] H. Ye, G. Jin, W. Fei, and N. Ghadimi, "High step-up interleaved dc/dc converter with high efficiency," *Energy Sources, Part A: Recovery, Utilization, and Environmental Effects*, vol. 0, no. 0, pp. 1–20, 2020.

[134] S. W. Cha, R. O'Hayre, Y.-I. Park, and F. Prinz, "Electrochemical impedance investigation of flooding in micro-flow channels for proton exchange membrane fuel cells," *Journal of Power Sources*, vol. 161, no. 1, pp. 138 – 142, 2006.

[135] L. Bhukya and S. Nandiraju, "A novel photovoltaic maximum power point tracking technique based on grasshopper optimized fuzzy logic approach," *International Journal of Hydrogen Energy*, vol. 45, no. 16, pp. 9416 – 9427, 2020.

[136] Y.-M. Chen, H.-C. Wu, Y.-C. Chen, K.-Y. Lee, and S.-S. Shyu, "The ac line current regulation strategy for the grid-connected pv system," *IEEE Transactions on Power Electronics*, vol. 25, no. 1, pp. 209–218, 2010.

[137] P. Mohamed, K. Chandrakala, and S. Subramani, "Comparative study of maximum power point tracking techniques for fuel cell powered electric vehicle," *IOP Conference Series: Materials Science and Engineering*, vol. 577, p. 012031, 12 2019.

[138] H. Myneni and S. K. Ganjikunta, "Energy management and control of single-stage grid-connected solar pv and bes system," *IEEE Transactions on Sustainable Energy*, vol. 11, no. 3, pp. 1739–1749, 2020.

[139] S. Kotra and M. K. Mishra, "A supervisory power management system for a hybrid microgrid with hess," *IEEE Transactions on Industrial Electronics*, vol. 64, no. 5, pp. 3640–3649, 2017.

[140] F. Nejabatkhah and Y. W. Li, "Overview of power management strategies of hybrid ac/dc microgrid," *IEEE Transactions on Power Electronics*, vol. 30, no. 12, pp. 7072–7089, 2015.

[141] M. Marzband, E. Yousefnejad, A. Sumper, and J. L. Domínguez-García, "Real time experimental implementation of optimum energy management system in standalone microgrid by using multi-layer ant colony optimization," *International Journal of Electrical Power & Energy Systems*, vol. 75, pp. 265–274, 2016.

[142] A. Fathy, H. Rezk, and A. M. Nassef, "Robust hydrogen-consumption-minimization strategy based salp swarm algorithm for energy management of fuel cell/supercapacitor/batteries in highly fluctuated load condition," *Renewable Energy*, vol. 139, pp. 147–160, 2019.

[143] S. Li, C. Gu, P. Zhao, and S. Cheng, "Adaptive energy management for hybrid power system considering fuel economy and battery longevity," *Energy Conversion and Management*, vol. 235, p. 114004, 2021.

[144] Z. Zhao, R. Cheng, B. Yan, J. Zhang, Z. Zhang, M. Zhang, and L. L. Lai, "A dynamic particles mppt method for photovoltaic systems under partial shading conditions," *Energy Conversion and Management*, vol. 220, p. 113070, 2020.

[145] N. Mezzai, D. Rekioua, T. Rekioua, A. Mohammedi, K. Idjdarane, and S. Bacha, "Modeling of hybrid photovoltaic/wind/fuel cells power system," *International Journal of Hydrogen Energy*, vol. 39, no. 27, pp. 15 158–15 168, 2014.

[146] S. Aissou, D. Rekioua, N. Mezzai, T. Rekioua, and S. Bacha, "Modeling and control of hybrid photovoltaic wind power system with battery storage," *Energy Conversion and Management*, vol. 89, pp. 615–625, 2015.

[147] a. D. Erickson Robert W Maksimovic, *Fundamentals of Power Electronics*. Springer, 2020.

[148] . P. S. Arunkumar C R, Manthati U B, "Supercapacitor-based transient power supply for dc microgrid applications," *Springer-part of Springer Nature 2021*, vol. 21, no. 5, 2021.

[149] A. A. Kamel, H. Rezk, N. Shehata, and J. Thomas, "Energy management of a dc microgrid composed of photovoltaic/fuel cell/battery/supercapacitor systems," *Batteries*, vol. 5, no. 3, 2019. [Online]. Available: https://www.mdpi.com/2313-0105/5/3/63

[150] Y. Han, W. Chen, and Q. Li, "Energy management strategy based on multiple operating states for a photovoltaic/fuel cell/energy storage dc microgrid," *Energies*, vol. 10, no. 1, 2017. [Online]. Available: https://www.mdpi.com/1996-1073/10/1/136

[151] A. Khaligh and Z. Li, "Battery, ultracapacitor, fuel cell, and hybrid energy storage systems for electric, hybrid electric, fuel cell, and plug-in hybrid electric vehicles: State of the art," *IEEE Transactions on Vehicular Technology*, vol. 59, no. 6, pp. 2806–2814, 2010.

[152] N. B. Gugulothu, R., "A bayesian fusion technique for maximum power point tracking under partial shading condition," *SN Applied sciences*, vol. 3, no. 539, 2021.

[153] T. R. Ayodele, A. S. O. Ogunjuyigbe, and B. E. Olateju, "Improving battery lifetime and reducing life cycle cost of a PV/battery system using supercapacitor for remote agricultural farm power application," *Journal of Renewable and Sustainable Energy*, vol. 10, no. 1, 01 2018, 013503. [Online]. Available: https://doi.org/10.1063/1.4999780

[154] landportbv.com, "https://www.landportbv.com/media/pdfs," *IEEE Transactions on Power Electronics*.

[155] .Mathworks., "Implement generic battery model-simulink-mathworks united kingdom," *http:// www. mathw orks. co. uk/ help/ physm od/ power sys/ ref/ batte ry. html*, 09 Feb 2020.

[156] S. Kotra and M. K. Mishra, "Design and stability analysis of dc microgrid with hybrid energy storage system," *IEEE Transactions on Sustainable Energy*, vol. 10, no. 3, pp. 1603–1612, 2019.

[157] M. M. S. Khan, M. O. Faruque, and A. Newaz, "Fuzzy logic based energy storage management system for mvdc power system of all electric ship," *IEEE Transactions on Energy Conversion*, vol. 32, no. 2, pp. 798–809, 2017.

[158] .Mathworks., "Implement generic supercapacitor model-simulink-mathworks india," *https:// in. mathw orks. com/ help/ physm od/ sps/ power sys/ ref/ super capac itor. html.*, 09 Feb 2020.

[159] O. Tremblay and L.-A. Dessaint, "Experimental validation of a battery dynamic model for ev applications," *World Electric Vehicle Journal*, vol. 3, no. 2, pp. 289–298, 2009.

[160] S. Lu, Z. Yin, S. Liao, B. Yang, S. Liu, M. Liu, L. Yin, and W. Zheng, "An asymmetric encoder–decoder model for zn-ion battery lifetime prediction," *Energy Reports*, vol. 8, pp. 33–50, 2022, 2022 7th International Conference on Green Energy Technologies. [Online]. Available: https://www.sciencedirect.com/science/article/pii/S2352484722019357

[161] L. C. Augustin McEvoy, Tom Markvart, "Practical Handbook of Photovoltaics," *2nd Edition, Academic Press*, vol. 10, no. 1, pp. 721–776, 01 2012.

[162] M. C. Argyrou, C. C. Marouchos, S. A. Kalogirou, and P. Christodoulides, "Modeling a residential grid-connected pv system with battery–supercapacitor storage: Control design and stability analysis," *Energy Reports*, vol. 7, pp. 4988–5002, 2021. [Online]. Available: https://www.sciencedirect.com/science/article/pii/S235248472100603X

[163] S. K. Kollimalla, M. K. Mishra, and N. L. Narasamma, "Design and analysis of novel control strategy for battery and supercapacitor storage system," *IEEE Transactions on Sustainable Energy*, vol. 5, no. 4, pp. 1137–1144, 2014.

[164] S. K. Kollimalla, A. Ukil, H. B. Gooi, U. Manandhar, and N. R. Tummuru, "Optimization of charge/discharge rates of a battery using a two-stage rate-limit control," *IEEE Transactions on Sustainable Energy*, vol. 8, no. 2, pp. 516–529, 2017.

[165] N. Mallick and V. Mukherjee, "Maximum power point tracking supported proton exchange membrane fuel cell based intelligent dynamic voltage restorer," *International Journal of Hydrogen Energy*, vol. 45, no. 53, pp. 29 271–29 287, 2020.

Curriculum - Vitae

Name   :   G Ramesh
Date of Birth   : $15^{nd} May 1985$
Marital Statue   :   Married
Gender   :   Male
Contact number   :   +91 9533153668
Email id   :   rameshphd@student.nitw.ac.in

Academic Qualifications:

Program	Institute	% of Marks	Year
M.Tech. (Power Systems)	National Institute of Technology Kurukshetra	6.7(CGPA)	2010
B.Tech. (EEE)	PRRM College of Engg.&technology Shabad	62	2007